A comprehensive approach for the efficient acquisition and processing of hyperspectral images and sequences

Método integral para la adquisición y procesamiento eficiente de imágenes y secuencias hiperespectrales

Author/Autora: Blanca María Priego Torres

Doctoral Thesis / Tesis Doctoral / 2016

Advisor/Director:

Richard J. Duro Fernández

Programa Oficial de Doctorado en Computación[1]

[1]Programa regulado por el R.D. 1393/2007

UNIVERSIDADE DA CORUÑA

D. Richard J. Duro Fernández, Catedrático de Universidad del Departamento de Computación de la Universidade da Coruña,

CERTIFICA:

Que la memoria titulada:

"A comprehensive approach for the efficient acquisition and processing of hyperspectral images and sequences"

"Método integral para la adquisición y procesamiento eficiente de imágenes y secuencias hiperespectrales"

ha sido realizada por **Dña. Blanca María Priego Torres** bajo mi dirección en el Departamento de Computación de la Universidade da Coruña, y constituye la Tesis que presenta para optar al grado de Doctor.

Fdo. Richard J. Duro Fernández
Director de la Tesis Doctoral

Abstract

Despite the scientific and technological developments achieved during the last two decades in the hyperspectral field, some methodological, operational and conceptual issues have restricted the progress, promotion and popular dissemination of this technology. These shortcomings include the specialized knowledge required for the acquisition of hyperspectral images, the shortage of publicly accessible hyperspectral image repositories with reliable ground truth images or the lack of methodologies that allow for the adaptation of algorithms to particular user or application processing needs.

The work presented here has the objective of contributing to the hyperspectral field with procedures for the automatic acquisition of hyperspectral scenes, including the hardware adaptation of our own imagers and the development of methods for the calibration and correction of the hyperspectral datacubes, the creation of a publicly available hyperspectral repository of well categorized and labeled images and the design and implementation of novel computational intelligence based processing techniques that solve typical issues related to the segmentation and denoising of hyperspectral images as well as sequences of them taking into account their temporal evolution.

Resumen

A pesar de los desarrollos tecnológicos y científicos logrados en el campo hiperespectral durante las dos últimas décadas, algunas limitaciones de tipo metodológico, operacional y conceptual han restringido el progreso, difusión y popularización de esta tecnología, entre ellas, el conocimiento especializado requerido en la adquisición de imágenes hiperespectrales, la carencia de repositorios de imágenes hiperespectrales con etiquetados fiables y de acceso público o la falta de metodologías que posibiliten la adaptación de algoritmos a usuarios o necesidades de procesamiento concretas.

Este trabajo doctoral tiene el objetivo de contribuir al campo hiperespectral con procedimientos para la adquisición automática de escenas hiperespectrales, incluyendo la adaptación hardware de cámaras hiperespectrales propias y el desarrollo de métodos para la calibración y corrección de cubos de datos hiperespectrales; la creación de un repositorio hiperespectral de acceso público con imágenes categorizadas y con verdades de terreno fiables; y el diseño e implementación de técnicas de procesamiento basadas en inteligencia computacional para la resolución de problemas típicamente relacionados con las tareas de segmentación y eliminación de ruido en imágenes estáticas y secuencias de imágenes hiperespectrales teniendo en consideración su evolución temporal.

Resumo

A pesar dos desenvolvementos tecnolóxicos e científicos logrados no campo hiperespectral durante as dúas últimas décadas, algunhas limitacións de tipo metodolóxico, operacional e conceptual restrinxiron o progreso, difusión e popularización desta tecnoloxía, entre elas, o coñecemento especializado requirido na adquisición de imaxes hiperespectrales, a carencia de repositorios de imaxes hiperespectrales con etiquetaxes fiables e de acceso público ou a falta de metodoloxías que posibiliten a adaptación de algoritmos a usuarios ou necesidades de procesamento concretas.

Este traballo doutoral ten o obxectivo de contribuír ao campo hiperespectral con procedementos para a adquisición automática de escenas hiperespectrais, incluíndo a adaptación hardware de cámaras hiperespectrales propias e o desenvolvemento de métodos para a calibración e corrección de cubos de datos hiperespectrais; a creación dun repositorio hiperespectral de acceso público con imaxes categorizadas e con verdades de terreo fiables; e o deseño e implementación de técnicas de procesamento baseadas en intelixencia computacional para a resolución de problemas tipicamente relacionados coas tarefas de segmentación e eliminación de ruído en imaxes estáticas e secuencias de imaxes hiperespectrais tendo en consideración a súa evolución temporal.

Acknowledgements

First and foremost I would like to offer my sincerest gratitude to my research advisor, Dr. Richard J. Duro, who has supported me throughout this thesis with knowledge, patience and enthusiasm, whilst giving me room to develop my own ideas.

I am very grateful to Dr. Jocelyn Chanussot for his encouragement, contributions and the pleasant working environment at GIPSA-lab Grenoble that he has created. I also thank Drs. Lorenzo Bruzzone and Francesca Bovolo for giving me the opportunity to collaborate with them and making my stay in Trento a memorable one.

Muchas gracias, en general, a todos los miembros del Grupo Integrado de Ingeniería de la Universidad de la Coruña por haberme tratado tan afectuosamente durante esos años.

Agradecer a Fran la guía y supervisión en el inicio de este trabajo doctoral.

Andrés, gracias por tu amistad, reforzada con matices de 'momentos hardware', cafés y cañas.

Quiero agradecer a Juan, en todas sus versiones, el disparatado sentido del humor con el que me ha animado en la escritura de este trabajo.

Muchas gracias, Daniel, por el tiempo invertido en afanosas calibraciones, pero sobre todo, por hacer de la rutina un continuo de buen humor y risas.

Quiero también mostrar mi agradecimiento a Juan Carlos, además de por la espléndida portada que arropa esta tesis doctoral, por sus sugerencias y consejos (a punta de dedos).

Gracias, Abraham, por todas las conversaciones alrededor de té, un bolígrafo y servilletas, por mantener tu apoyo y por haber compartido tal sinfín de buenos momentos durante tantos años.

Para finalizar, quiero expresar el más profundo agradecimiento a mis padres Pepe y Blanca, por cuidarme en la distancia y ser mi mejor ejemplo de dedicación, esfuerzo y constancia.

Este trabajo has sido parcialmente financiado por el MECD mediante una ayuda del Programa Nacional de Formación de Profesorado Universitario (FPU); por la Universidad de la Coruña e Inditex S. A. mediante una ayuda Inditex-UDC para la realización de estancias predoctorales en el extranjero; por la Unidad Mixta de Investigación Universidad de la Coruña - Navantia mediante un contrato de investigador en formación; y por el MICINN y MINECO a través de los proyectos TIN2011-28753-C02-01 y TIN2015-63646-C5-1-R.

Publications

For the development of the present work, the following articles related with the main topic of the thesis have been published:

- López-Fandiño, J., Priego, B., Heras, D. B., Arguello, F., and Duro, R. J. GPU Projection of ECAS-II Segmenter for Hyperspectral Images Based on Cellular Automata. Accepted for IEEE Journal of Selected Topics in Applied Earth Observations and Remote Sensing (2016).

- Priego, B. ,Duro, R. J., López-Fandiño, J., Heras, D. B., and Argüello F. (2016, July). Evolutionary cellular automata based approach to high-dimensional image segmentation for GPU projection. In 2016 International Joint Conference on Neural Networks (IJCNN). IEEE.

- Priego, B., Bellas, F., and Duro, R. J. (2015, June). Evolving cellular automata to segment hyperspectral images using low dimensional images for training. In International Work-Conference on the Interplay Between Natural and Artificial Computation (IWINAC) (pp. 117-126). Springer International Publishing.

- Priego, B., Bellas, F., and Duro, R. J. (2015, July). ECAS-II: A hybrid algorithm for the construction of multidimensional image segmenters. In 2015 International Joint Conference on Neural Networks (IJCNN) (pp. 1-8). IEEE.

- Priego, B., Souto, D., Bellas, F., and Duro, R. J. (2014). Training cellular automata for hyperspectral image segmentation. Advanced Data Acquisition and Intelligent Data Processing (pp. 271-292).

- Priego, B., Souto, D., Bellas, F. and Duro, R. J. (2013). Hyperspectral image segmentation through evolved cellular automata. Pattern Recognition Letters, 34(14), 1648-1658.

- Priego, B., Veganzones, M. A., Chanussot, J., Amiot, C., Prieto, A., and Duro, R. (2013, September). Spatio-temporal cellular automata-based filtering for image sequence denoising: Application to fluoroscopic sequences. In 2013 IEEE International Conference on Image Processing (pp. 548-552). IEEE.

- Priego, B., Souto, D., Bellas, F., and Duro, R. J. (2013, September). Addressing the training problem in cellular automata based hyperspectral image segmentation. In Intelligent Data Acquisition and Advanced Computing Systems (IDAACS), 2013 IEEE 7th International Conference on (Vol. 1, pp. 382-387). IEEE.

- Priego, B., Souto, D., Bellas, F., López-Peña, F., and Duro, R. J. (2013). An Evolved Cellular Automata Based Approach to Hyperspectral Image Processing. In Advanced Techniques for Knowledge Engineering and Innovative Applications (pp. 115-135). Springer Berlin Heidelberg.

- Priego, B., Souto, D., Bellas, F., Duro, R. J., and Lopez-Pena, F. (2012). A Temporal Based Process Classification Approach Using Hyperspectral Image Sequences. Digital Image and Signal Processing for Measurement Systems, 267.

- Heras, D. B., Arguello, F., Gomez, J. L., Priego, B., and Becerra, J. A. (2012). Towards Real-Time Image Processing: A GPGPU Implementation of Target Identification. Digital Image and Signal Processing for Measurement Systems, 235.

- Priego, B., Souto, D., Bellas, F., and Duro, R. J. (2012). Unsupervised segmentation of hyperspectral images through evolved cellular automata. Advances in Knowledge-Based and Intelligent Information and Engineering Systems (KES), 243, 2160-2169.

- Priego, B., Bellas, F., Souto, D., López-Peña, F., and Duro, R. J. (2012, June). Evolving cellular automata for detecting edges in hyperspectral images. In Fuzzy Systems (FUZZ-IEEE), 2012 IEEE International Conference on (pp. 1-6). IEEE.

- Priego, B. , Duro, R. J., Bellas, F., and Souto, D. (2012). Neural based rotation and scale independent detection of targets in a hyperspectral waterway monitoring system. In Proceedings of the 1st International Conference on Pattern Recognition Applications and Methods (ICPRAM 2012) (pp. 419-425).

- Priego, B., Souto, D., Peña, F. L., and Duro, R. J. (2011, September). An ANN based hyperspectral waterway control and security system. In 2011 IEEE International Conference on Computational Intelligence for Measurement Systems and Applications (CIMSA) Proceedings (pp. 1-6). IEEE.

- Priego, B., Souto, D., Bellas, F., Duro, R. J., and López-Peña, F. (2011, September). Time in hyperspectral processing: a temporal based classification approach. In Intelligent Data Acquisition and Advanced Computing Systems (IDAACS), 2011 IEEE 6th International Conference on (Vol. 1, pp. 341-346). IEEE.

Contents

Chapter 1

Introduction

Hyperspectral images are made up of hundreds of contiguous and narrow spectral bands within a broad range of the electromagnetic spectrum, providing both spatial and spectral representations of scenes. Hyperspectral technology exploits the fact that materials reflect electromagnetic radiation differently depending on their shape and molecular composition, giving rise to distinct patterns of specific wavelengths. This particularity leads to a vastly improved ability to extract relevant information about objects in the scene based on their spectral properties. The potential of this technology has meant that hyperspectral image processing is currently a solid and active research line, with a large backing in the scientific literature over the past 25 years.

The concept of hyperspectral technology emerged in the 1980s from the development of the Airborne Visible-Infrared Imaging Spectrometer (AVIRIS) at NASA's Jet Propulsion Laboratory [Goetz et al., 1985]. Hence, at the beginning of the development of this technology, its applicability was mainly focused on the field of Remote Sensing (RS) and images were acquired from satellites or airborne platforms. Since then, the hyperspectral field has undergone rapid growth due to the hardware improvements in hyperspectral sensors, which has brought new challenges for the scientific community, including the design and development of new algorithms to represent, process and analyze hyperspectral data. Concurrently and related to the technological advances in digital image acquisition, new commercial hyperspectral imagers of smaller sizes have appeared over the last ten years, pressing the application frontiers of hyper-

spectral technology. The philosophy behind the development of hyperspectral systems for satellites or airborne remote sensing platforms rests on the improvement of the spectral-spatial resolution and precision, also keeping the acquired spectral range as wide as possible, so that depending on the final application, one or another segment of spectrum is selected. Conversely, the philosophy supporting the development of commercial sensors is geared towards the design and implementation of hyperspectral cameras whose spectral, spatial and temporal characteristics are more closely directed to a particular final application.

Hyperspectral technology has great potential to be applied to new areas. In general, in order to promote the dissemination and popularization of this technology, some methodological, operative and conceptual limitations have to be solved. Among them:

- Commercially available hyperspectral imagers are, even in our days, relatively cumbersome to use and expensive. Normally, specialized knowledge and experience in the field are required in order to produce adequate results.

- There is a lack of publicly accessible hyperspectral image repositories with their images that are properly labeled and characterized. This fact has conditioned the design of algorithms, highly skewed towards the properties of the few hyperspectral images that are available and are, therefore, more frequently used, which has restricted the applicability of hyperspectral technology to new fields.

- The state of the art of processing techniques and hyperspectral data analysis is highly focused on the processing of still hyperspectral images captured from airborne platforms or satellites. Spaceborne and airborne hyperspectral imagery produce images with low spatial resolution, and for this reason most of the processing techniques developed deal with the *endmember* extraction problem, that is, the estimation of the contributions of different materials in each pixel of the image. This fact is evidenced by searching *"hyperspectral and (endmembers or unmixing)"* and *"hyperspectral and segmentation"* in the Scopus citation database. The number of published documents from 2010 to 2014 related to endmember extraction algorithms is 4.23 times the documents devoted to segmentation methods.

However, when images are captured from short and medium distances, the combined analysis of spectral and spatial information gains a greater weight for the processing techniques.

- Reviewing the existing works in the literature that perform general tasks such as segmentation, classification, anomaly detection, etc., a remarkable aspect that arises is the lack of methodological procedures that allow algorithms to adapt to the particular requirements of different users or final applications. For instance, considering the segmentation task, it would be desirable to follow a methodology that enables adjusting the operation of the segmentation algorithm in terms of level of detail in the delimitation of regions of the image under analysis.

- A high percentage of algorithms in the literature are based on the extension or extrapolation of methods conceived for processing single-band or red-green-blue (RGB) images, by projecting the high dimensional image onto a lower dimension, leading to the possible loss of valuable information. General image processing techniques that exploit the inherent multidimensional nature of hyperspectral data are therefore required.

- Finally, there is little research on the processing and analysis of temporal image sequences. In many cases, a still image does not provide enough information to solve classification, segmentation or anomaly detection problems, since the relevant information may be contained in the evolution of spatio-spectral characteristics over time.

It is our vision that an impulse is required in three main directions for the technology to become commonplace and popular: the development of affordable, small, and light imagers that operate as autonomously as possible, require low maintenance, are simple to calibrate and easy to use by non-expert users; the design of new hyperspectral image processing methods that analyze and interpret the multidimensional data automatically, taking into account the final application requirements, allowing real time processing and exploiting the inter-dimensional diversity; and finally, in order to unify and strengthen the hyperspectral field, it is necessary to establish a methodology for the validation of methods and techniques. This entails the availability of hyperspectral repositories with properly labeled images and standard assessment criteria, that facilitate the comparison between different processing algorithms.

In this context, the main objective of this doctoral thesis is to make a contribution to the hyperspectral field in terms of instrumentation, image datasets and processing techniques based on computational intelligence that further promote this field and open it up to new applications and a more ubiquitous use of hyperspectrometry.

With this aim in mind, we have started by adapting and making operational two hyperspectral imager prototypes. Using these hyperspectral sensors, a repository of labeled images has been created with the purpose of validating and testing algorithms. From a processing point of view, this work deals with the treatment of hyperspectral data through the integration of computational intelligence based techniques, aiming to address the following general issues:

- Provide a methodology that allows obtaining spatio-spectral processing structures, specially segmenters. These structures must be computationally efficient, effective and able to adapt to the processing requirements of different users.
- Provide a methodology that allows obtaining processing structures that enables the filtering of hyperspectral image sequences by intrinsically considering spatial, spectral and temporal aspects.

The work carried out for the achievement of these goals has been divided into three main packages:

The first one aims to continue a research line previously undertaken within the Integrated Group for Engineering Research of the University of A Coruña for the development of compact hyperspectral imagers. In a first phase of this research line, a hyperspectral imager prototype was designed and implemented, with high sensitivity to light and low noise. It was conceived to acquire images for applications with high spatial and spectral reliability requirements. Afterwards, a second hyperspectral prototype was developed with specifications related to lightness, portability, inexpensiveness and low maintenance, but with lower image quality requirements, such as, spectral noise or distortion. Having the possibility of using both devices enables to cover the applicability of hyperspectral technology over multiple fields depending on the scene characteristics or the type of processing task. Specifically, the work carried out in this first package has consisted in the adaptation of the two prototypes with the purpose of facilitating their use by any type of user. This has been achieved by

implementing several methods for the simple and intuitive calibration of the sensors and a tool for the easy acquisition and visualization of hyperspectral captures. These hyperspectral prototypes are *pushbroom* based, which means that the imager captures consecutive 2-dimensional images with spectral and 1-dimensional spatial information of a single spatial line of the scene. Thus, it is necessary to enable a system that sweeps the scene to produce a 3-dimensional datacube. In this regard, the work carried out in this thesis deals with providing the prototypes with synchronization and control systems that allow performing the complete datacube acquisition process.

The second work package is devoted to the creation of a repository of labeled and characterized synthetic and real hyperspectral images. This initiative emerged out of the need of having hyperspectral data for training and testing algorithms, thus mitigating the lack of benchmark libraries of hyper-photographic material with reliable labeling. Here we have addressed the issue through the creation of synthetic and real hyperspectral image repositories. For the creation of synthetic hyperspectral images, a software tool was developed following a procedure based on spectral and spatial features. With regard to real hyperspectral images, these were captured using the calibrated and operational hyperspectral prototypes. A relevant aspect of this repository is that all the hyperspectral images have been characterized based on spectral and spatial properties. This facilitates the selection of images for validating algorithms. The repository is publicly available[1], being licensed under the Creative Commons Atributtion & Share alike license.

Finally, the third and more ambitious work package deals with the design and implementation of computational intelligence based algorithms for the processing of hyperspectral images. These algorithms have been conceived considering the following five requirements that may contribute to their posterior application to different areas:

- The processing methods should solve generic tasks (segmentation, classification, edge detection, denoising, etc.), in contrast to *ad-hoc* algorithms. This would provide the algorithms the possibility to adapt to different needs.

[1] Synthetic and real hyperspectral images are available at http://gii.udc.es/gii_hyperspectral_repository

- The processing methods should work based on knowledge acquired through a learning process guided directly or indirectly by a user, which would lead to adaptability and flexibility advantages.
- The algorithms should be supported by a methodology that simplifies their training/learning process in a way that the cost and computational time is reduced and the procedure is accessible to non-expert users.
- The multi-dimensional nature of hyperspectral images should be exploited, avoiding the projection of spectral information onto lower dimensions.
- The algorithms should be based on structures susceptible to be easily implemented in a concurrent fashion over hardware such as Graphic Processing Units (GPUs).

Taking these issues into account, we have firstly addressed the segmentation of still hyperspectral images, aiming to transform the hyperspectral datacubes into modified versions that are easier to process by, for example, subsequent classification or anomaly detection methods. The proposed approach is based on Cellular Automata (CA) structures, motivated by their suitability to the five conditions laid down originally. Thus, in this first approximation, we have dealt with the processing of spatio-spectral information jointly. Once this approach was analyzed and validated, we have increased the complexity of the multi-dimensional processing by adding the temporal dimension for the processing of sequences of both multi-temporal single-band and hyperspectral images. In this case, we have addressed the denoising of multidimensional image sequences, using also for this case cellular automata structures and taking into account the inter-dimensional diversity by processing the spatial, spectral and temporal information jointly.

CAs are dynamic systems consisting of a regular spatially distributed grid of cells, each of which can be in a certain state. The state of every cell is updated synchronously or asynchronously based on the their current state, the state of neighboring cells and a set of transition rules. The crux for achieving a particular result in the execution of CA lies in the adequate selection of this set of transition rules, so that after successive changes of state, the CA generates the desired behavior. Thus, the critical point in the use of CA is to adequately determine its set of transition rules, which is far from being a straightforward task. Indeed, the selection of the transition rules involves solving the so called

inverse problem, that is, to infer a set of local rules from a global behavior, which is highly complex. The inverse problem has been addressed from different points of view by the scientific community dedicated to CA analysis [Ganguly et al., 2003], being evolutionary techniques the most popular method used to obtain the set of transition rules that make up the CA.

Concerning the application of CAs to process still hyperspectral images, we can find some works in the literature dedicated to the segmentation of low dimensional images [Gallego et al., 2012, Wang et al., 2011, Kauffmann and Piché, 2010] or edge detection of multidimensional images [Lee and Bruce, 2010] but, in most cases, the rules are set manually and in an ad-hoc manner and, in order to be applied over hyperspectral data, the datacube is usually projected onto a lower dimension.

In this work, we propose a method for the segmentation of hyperspectral images based on CAs, whose details and advantages are summarized in the following points:

- In each iteration of the CA, the multi-dimensionality of the datacube is preserved, avoiding any projection of the spectral information onto a vectorial base of lower dimensionality. This prevents the loss of information contained in the spectral dimension. The segmentation result is achieved by iteratively and gradually modifying the spectrum associated to each cell (pixel) of the CA. Thus, after a number of iterations, the spectral information converges to clearly distinct spectral clusters, so that all the cells that belong to the same region or cluster present a very similar spectrum.

- The behavior of the CA in its application to a hyperspectral image depends on how the set of transition rules has been constructed. This rule adjustment is performed through the use of evolutionary algorithms and following a methodology that simplifies the training process. This methodology allows for obtaining distinct segmenters that are adapted to different user or application requirements, giving rise to segmentations with higher or lower level of detail.

- The training process of the evolutionary method for selecting the set of transition rules has been addressed following a methodology that avoids, on the one hand, a computationally intensive processing and, on the other

hand, the use of real hyperspectral images. This methodology consists in the extraction of parametric descriptors from the objective type of image and segmentation; the creation of synthetic low-dimensional images consistent with the extracted parameters; and finally, the use of these synthetic images as the training image datasets for the evolutionary algorithm. The steps of this methodology are totally automatic and can be adjusted without difficulty by any user.

- Since cellular automata are intrinsically distributed models, the method can be easily implemented by distributing it over high speed GPU based platforms, thus increasing significantly its suitability to be used in real time applications.

The second method we propose is a first step in the introduction of the temporal dimension within the spatio-spectral processing of hyperspectral datacubes. This requires extending the CA-based method to sequences of hyperspectral images. In this case, the CA performs a denoising (noise filtering) task over a whole sequence of hyperspectral images. The inclusion of temporal information improves the performance of the denoising task, since temporal correlations between hyperspectral frames add a new source of information which is taken into account.

In the processing of hyperspectral image sequences, the cells of the CA are distributed over three dimensions and neighborhood relations appear in both the spatial and temporal planes. The temporal denoising method differs from the CA-based segmentation approach in the encoding of the rules that direct the behavior of the CA, how the cell states are updated and the methodological procedure followed to determine the set of transition rules that make up the CA.

In a similar way to the CA-based segmentation method, the proposed CA-based filtering approach fulfills the five requirements that were initially defined. The main characteristics of this method are summarized in the following points:

- The CA-denoising method processes each frame of a hyperspectral image sequence explicitly and jointly taking the temporal, spectral and spatial information into account.

- The selection of the transition rules that make up the CA is performed through the use of evolutionary algorithms, making the method adaptive to hyperspectral image sequences exhibiting distinct spatial, spectral and temporal features or different types of noise models.

- The methodology followed to evolve the CA-based filters is based on the construction of a proper training dataset used in the evaluation step of the evolutionary algorithms. This process is totally automatic once the type of noise model that corrupts the real sequence to denoise is identified.

- The CA-based method presents intrinsically parallel low-level processing operations, which enables its implementation in a concurrent fashion over hardware such as GPUs.

These three work packages are structured in this thesis as follows:

The global objectives of this PhD thesis are established in **chapter 2**.

Chapter 3 is devoted to reviewing the background for the research presented in this thesis. The first part of this chapter reviews the fundamentals of hyperspectral imaging, including the basics of hyperspectral imagers. The second part presents the state-of-the-art of segmentation and classification methods.

Chapter 4 describes the procedures followed to operationalize two prototypes of pushbroom hyperspectral imagers built in the Integrated Group for the Engineering Research of the University of A Coruña (GII), including the hardware and the design of calibration and correction methods.

Chapter 5 is dedicated to the presentation of the GII-SEG repository of synthetic and real hyperspectral images. A methodology to categorize real hyperspectral images based on parametric spatio-spectral features is outlined, as well as the procedure followed for the creation of synthetic hyperspectral images based on those parameters.

In **chapter 6**, the CA-based approach for the customized segmentation of hyperspectral images is introduced. The particular encoding of the CA structures is presented, as well as the strategy followed for the proper selection of the transition rules that determine the segmentation behavior of the CA. Examples

of application of the method over benchmark hyperspectral images and those selected from the GII-SEG repository are presented and compared to the results obtained with classification algorithms extracted from the literature.

Chapter 7 introduces a novel CA-based filtering method for the denoising of both single-band and hyperspectral image sequences. The encoding of the rules particularized to this problem and the methodology followed to learn the set of transition rules are described. The proposed method is compared over both simulated and real sequences to several state-of-the-art algorithms.

Finally, **chapter 8** draws the main conclusions of this work and provides a view of the most prominent future research directions that could be derived from this thesis.

Chapter 2

Objectives

The research work presented in this dissertation aims to contribute to the hyperspectral field in terms of instrumentation, hyper-photographic material and computational intelligence based processing techniques that help promote this field, boosting its applicability to different domains.

Three main objectives guide the work carried out in this PhD thesis. The first one has to do with the full operationalization of two prototypes of push-broom hyperspectral imagers built in the Integrated Group for Engineering Research of the University of A Coruña (GII), with the purpose of facilitating their use by any type of user. The achievement of this objective involves:

- The hardware adaptation of the prototypes that allows sweeping the scene to produce a 3-dimensional datacube.
- The development of methods for the simple and intuitive calibration and distortion correction of the sensors.
- The implementation of software tools for the easy acquisition and visualization of hyperspectral captures.

The second objective addresses the creation of a repository of synthetic and real hyperspectral images that can help in training and testing algorithms. This implies addressing the following concerns:

- The design of a method for the creation of synthetic multi-dimensional images based on parametrized spatial and spectral features.
- The design of a procedure for the categorization of real hyperspectral images in accordance to spatial and spectral descriptors.
- The creation of a publicly accessible repository of categorized hyperspectral images with reliable labeling.
- The implementation of software tools for the creation of multidimensional images and the aiding in the labeling of real images.

The third objective deals with the design and implementation of computational intelligence based techniques for the processing of hyperspectral images and sequences. In this regard, this dissertation seeks to address the following list of sub-objectives:

- The design and implementation of a method for the segmentation of still hyperspectral images that avoids projecting the spectral information and is amenable to be implemented over high speed GPU based platforms.
- The design of a methodology that allows simplifying the training/learning process of the segmentation method and enables the adaptation to different use cases or types of segmentation.
- The design and implementation of a method for the noise filtering of hyperspectral image sequences that avoids projecting the spectral information and is suitable to be used in real time applications.
- The design of a methodology that allows simplifying the training/learning process of the denoising method and enables the adaptation to different types of sequences or noise models.

Chapter 3

Background

This chapter aims to provide background knowledge about hyperspectral imaging. It is organized in two sections. The first one sets forth the fundamental concepts of this technology. Starting from the basics of hyperspectral imaging, through the fundamentals of hyperspectral cameras, to the particular characteristics and calibration procedures of pushbroom imagers. The second section reviews the state of the art of processing techniques applied to hyperspectral images, in particular those dedicated to segmentation and classification tasks. A final section provides an overview of tools and hyperspectral image datasets available to validate and test image processing algorithms.

3.1 Fundamentals of Hyperspectral Imaging

Spectral imaging refers to the collection of optical images in one or more wavelength bands, resulting in an N-dimensional data cube where the information unit is a pixel, also viewed as a vector containing the response to the same spatial location for different wavelengths. Panchromatic and RGB imaging systems have dominated electro-optical sensing in the visible region, but more recently, spectral imaging systems have evolved to include a higher number of spectral bands composing a wider spectrum range, giving rise to *Multispectral* (MSI) and *Hyperspectral Imaging* (HSI). There are three main distinguishing features between MSI and HSI: the number of spectral bands, up to 10 bands and on

the order of 100 respectively; the spectral resolution, ten times higher in the case of HSI; and the regular spacing and continuity of the spectral bands, being widely and irregularly spaced in MSI systems and leading to a continuous and regular spaced spectrum for each pixel in HSI (Fig. 3.1).

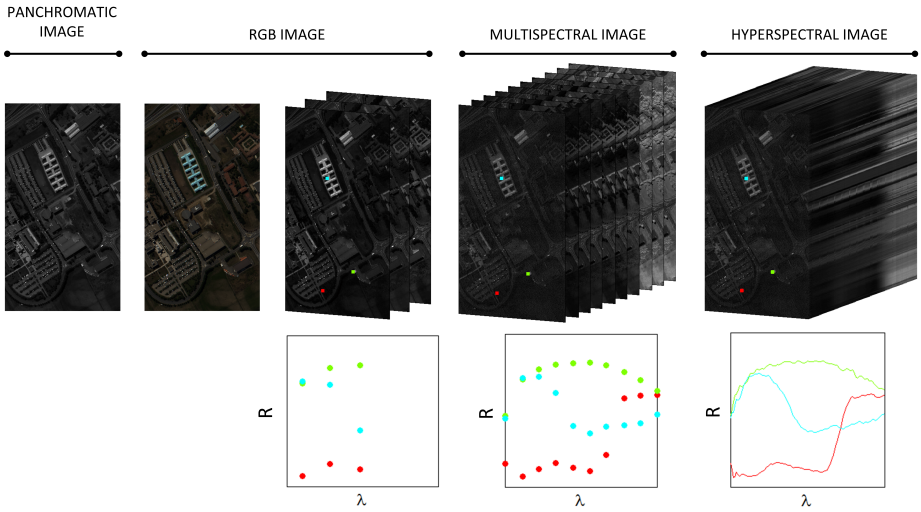

Figure 3.1: From left to right: Panchromatic image of University of Pavia scene; pseudocolor composite of the red, green and blue channels; grayscale images, that are used in the red, green and blue channels to create the illusion of color; multispectral data cube; hyperspectral data cube

This thesis is focused on hyperspectral imaging and, in order to comprehend this technology, it is worth understanding how its sensors work, the different existing technologies for hyperspectral data acquisition, the problems related to the acquisition process and the main features of hyperspectral cubes.

In general, sensors collect data passively or actively. Active sensors require an external source of power to operate, while passive sensors, such as hyperspectral imaging systems, collect and record electromagnetic energy that is reflected or emitted by objects or surfaces. To better understand the type of radiometric measure acquired by hyperspectral imagers, it is convenient to distinguish among three different terms: *irradiance*, *radiance* and *reflectance*.

Irradiance refers to the radiant flux incident per unit area of a surface, normalized by the surface area (W/m^2). Reflectance is the ratio of the intensity of reflected radiation to that of the radiation incident on a surface (unitless). Finally, radiance is the amount of light that passes through or is emitted from

a particular area and falls within a given solid angle in a specified direction ($W/m^2/steradian$), and this is the radiometry measure acquired by hyperspectral sensors. Reflectance is a property of the material being observed, whereas radiance depends on the illumination and the orientation and position of the target. The great applicability of the hyperspectral technology is due to the assumption that the reflectance spectrum of every material is unique and, therefore, represents a means for identifying materials. This unique reflectance spectrum is called *spectral signature* and suggests a one to one correspondence with a particular material.

Table 3.1: Applications of hyperspectral imaging

		λ	Applications
VNIR	Visible + near infrared	400-1000 nm	Quality control Food and vegetation research On-line sorting and quality monitoring Plant and vegetation research Environmental monitoring Counterfeit detection
eNIR	Visible (orange, red) + near infrared	600 - 1600 nm	Vegetation research Food analysis Semiconductors
NIR	Near infrared	900 - 1700 nm	Moisture profiling Food analysis Chemical sorting Recycling Pharmaceutical QA Medical imaging Cosmetics
SWIR	Short-wavelength infrared	1000 - 2500 nm	Chemical and Material Sorting Pharmaceutical manufacture Recycling Mineral mapping Food and agriculture Moisture content distribution Art research and archiving Forensics
MWIR	Mid-wavelength infrared	3 - 5 μm	Black polymer sorting Geology Gas detection
LWIR	Long-wavelength infrared	8 - 12.4 μm	Geological mapping Mineral classification Volcanology Water temperature Camouflage detection Gas detection Flame analysis Land cover type recognition

Hyperspectral imagers collect information of radiated electromagnetic energy (Fig. 3.2) in one or more spectral regions. The suitability for applying HSI to different fields depends, amongst other things, on the portion of the electromagnetic spectrum captured by the hyperspectral sensor. Although HSI was originally developed for mining, geology, ocean observation, etc., new applications have arisen during the last decade. For instance, some of the applications with more potential in the VNIR spectral region are quality control, food and vegetation research and environmental monitoring. Table 3.1 shows more examples of applications of HSI associated with different regions of the electromagnetic spectrum.

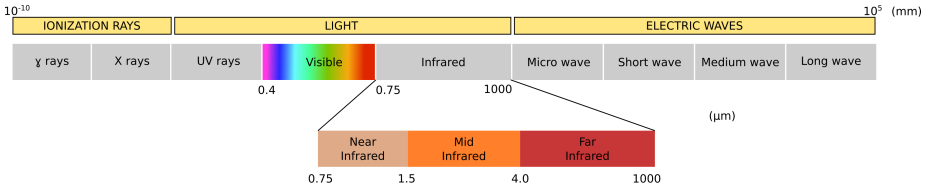

Figure 3.2: Electromagnetic spectrum

3.1.1 Basics of Hyperspectral Imagers

From the beginning of HSI, different spectral imaging methods and related technologies have arisen to acquire spectral image data or hypercubes. HSI acquisition technology is divided into four basic camera configurations based on the type of spatial information acquired: whiskbroom, pushbroom, staring, and snapshot.

In *whiskbroom* imagers, also known as point-scanning imagers, each 1D partial capture measures the spectrum on a small spot, making it necessary to scan the scene from side to side perpendicular to the direction of the sensor platform. The spatial scanning is normally carried out by hardware, leading to complex and also highly time-consuming systems.

Pushbroom imagers, also called line-scanning imagers, capture a slit image from the scene dispersed by a prism or grating onto a 2D detector. Each partial 2D capture contains the spatial information displayed along one axis and the spectral information along the other. In this configuration, it is necessary to scan the spatial dimension which is perpendicular to the one acquired in each partial capture.

With *staring* imagers, also known as band sequential imagers, a single band 2D image is acquired with full spatial information at once. The spectral selection is performed by using filters instead of a grating or prism. Then, the entire hypercube is completed by tuning the output wavelength of the filter as a function of time.

Finally, *snapshot* imagers collect both the spatial and the spectral information in a single shot [Hagen et al., 2012]. The complete hypercube is acquired by simultaneously remapping and dispersing image areas onto a 2D detector .

Table 3.2: Comparison of whiskbroom, pushbroom, staring and snapshot imagers

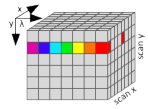

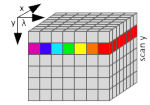

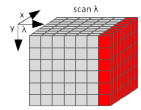

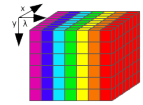

Criterion	Whiskbroom	Pushbroom	Staring	Snapshot
Scanning	Both spatial dim.	Along-track dim.	Spectral dim.	-
Dispersion element	Prism/grating	Prism/grating	Tunable filters	Prims/grating
λ ranges	Wide	Wide	Mediate	Wide
λ selectability	Partial	Partial	Yes	No
Spectral resolution	High	High	Mediate	Low
Band numbers	High	High	High	Low
Collection time	Long	Long	Short	Fast
Complexity	Complex	Complex	Simple	Mediate
Cost	Low	Low	High	Mediate

Each one of these acquisition modes present advantages and drawbacks [Li et al., 2013b] (summarized in table 3.2) that reveal that there is not an unquestionably best mode for hyperspectral acquisition. Actually, the most appropriate hyperspectral imaging configuration will depend on the restrictions imposed by the different types of applications.

From another point of view, there are three basic methods of acquiring hyperspectral images: ground-based, airborne and spaceborne imaging. Each procedure has associated peculiarities, problems and shortcomings.

Spaceborne imaging enables the observation of the Earth's surface providing a periodic monitoring of the areas of interest during the satellite revisits. The spatial resolution of the hyperspectral images strongly depends on the satellite orbital parameters, such as the satellite altitude. An advantage of spaceborne missions is that for satellites there are no political borders, so they can collect information from any part of the Earth's surface. Conversely, the weakness of

spaceborne imagery is the high cost of developing the whole system, including the ground support facilities. Some of the currently operational and planned satellite hyperspectral instruments are Hyperion (EO-1), FTHSI (MightySatII), OMI (AURA), HICO, COIS (NEMO), HIS (SIMSA), Warfighter-1 (OrbView-4), EnMAP, HypSEO (MITA), MSMI (SUNSAT), PRIMSA and WFIS [Thenkabail et al., 2011]. Fig. 3.3 shows the main features of the mentioned satellite hyperspectral instruments.

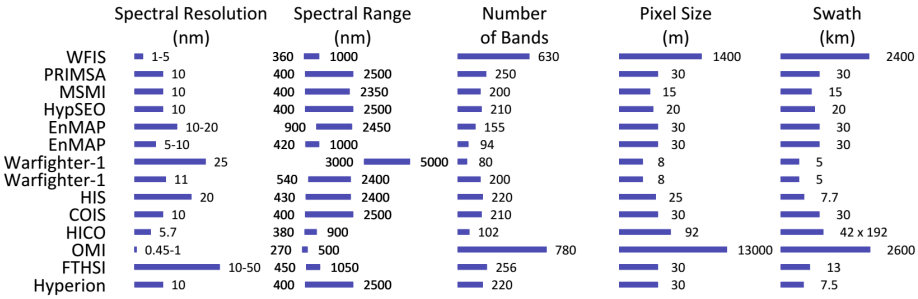

Figure 3.3: Operational and Planned Satellite Hyperspectral Instruments

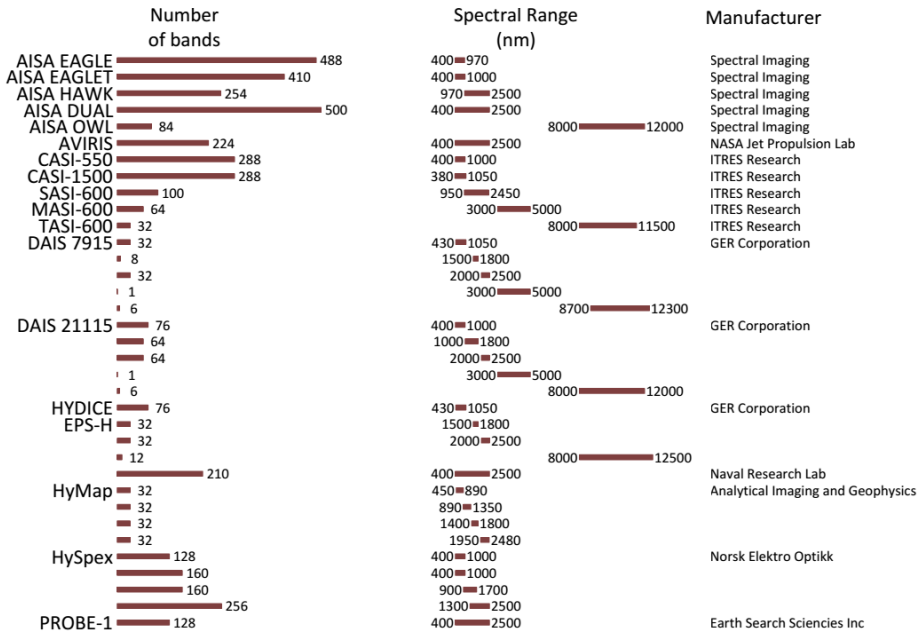

Figure 3.4: Current Airborne Sensors and Data Providers

Airborne hyperspectral imagery is becoming more accessible thanks to the increasing number of companies operating hyperspectral spectrometers. Most airborne hyperspectral imagers are pushbroom sensors, so that it is necessary to scan lines along flight direction. Consequently, the quality of airborne images can be affected by environmental conditions and flight operations, leading to more complex post-processing tasks. This post-flight processing step involves the inertial navigation system (INS) which provides the information to assign the corresponding geographical coordinates to each pixel of the hyperspectral cube. On the other hand, airborne hyperspectral sensors are more flexible than spaceborne imagers: the spatial resolution and swath are adjustable and the acquisition is easier to schedule. Some of the state-of-the-art hyperspectral airborne imagers are AVIRIS, HYDICE, AISA, HyMAP, ARES, CASI 1500, and AisaEAGLET [Thenkabail et al., 2011]. Table 3.4 provides a review of these instruments and some other current airborne hyperspectral sensors showing their main spectral characteristics.

Over the last five years, there has been a remarkable increase in the number of companies dedicated to the research and development of *ground-based* hyperspectral systems. Fig. 3.5 shows the main features of some of the commercially available ground-based hyperspectral cameras found on the market [Bayspec, Bodkin, Brimrose, CI Systems, Cubert, Eba Japan, Evk, Gamaya, Gilden photonics, HeadwallPhotonics, Imec, LLa instruments GmbH, Middleton spectral vision, Photon Etc, Resonon, Rikola, Specim, Surfaceoptics, Tattile, Ximea, Zolix]. Their light weight and small size enable mounting these systems on ground platforms or holding them by hand, allowing both field-based and in-lab spatio-spectral measurements. Specifications on the operating system requirements, software support, data storage, etc., vary from camera to camera and from manufacturer to manufacturer. In Fig. 3.5, it is immediately noticeable that the great majority of available hyperspectral cameras are of the pushbroom-type. Pushbroom systems are more suited to applications that require a high number of bands, high spectral and spatial resolutions, or when low frequencies are needed. However, there is a trend towards the design and development of snapshot systems, motivated by their smaller size, lighter weight and a better adaptation to real-time acquisition. On the contrary, the limitations of snapshot systems are the spectrum range covered, normally restricted to VNIR and the lower spatial and spectral resolutions associated to this technology.

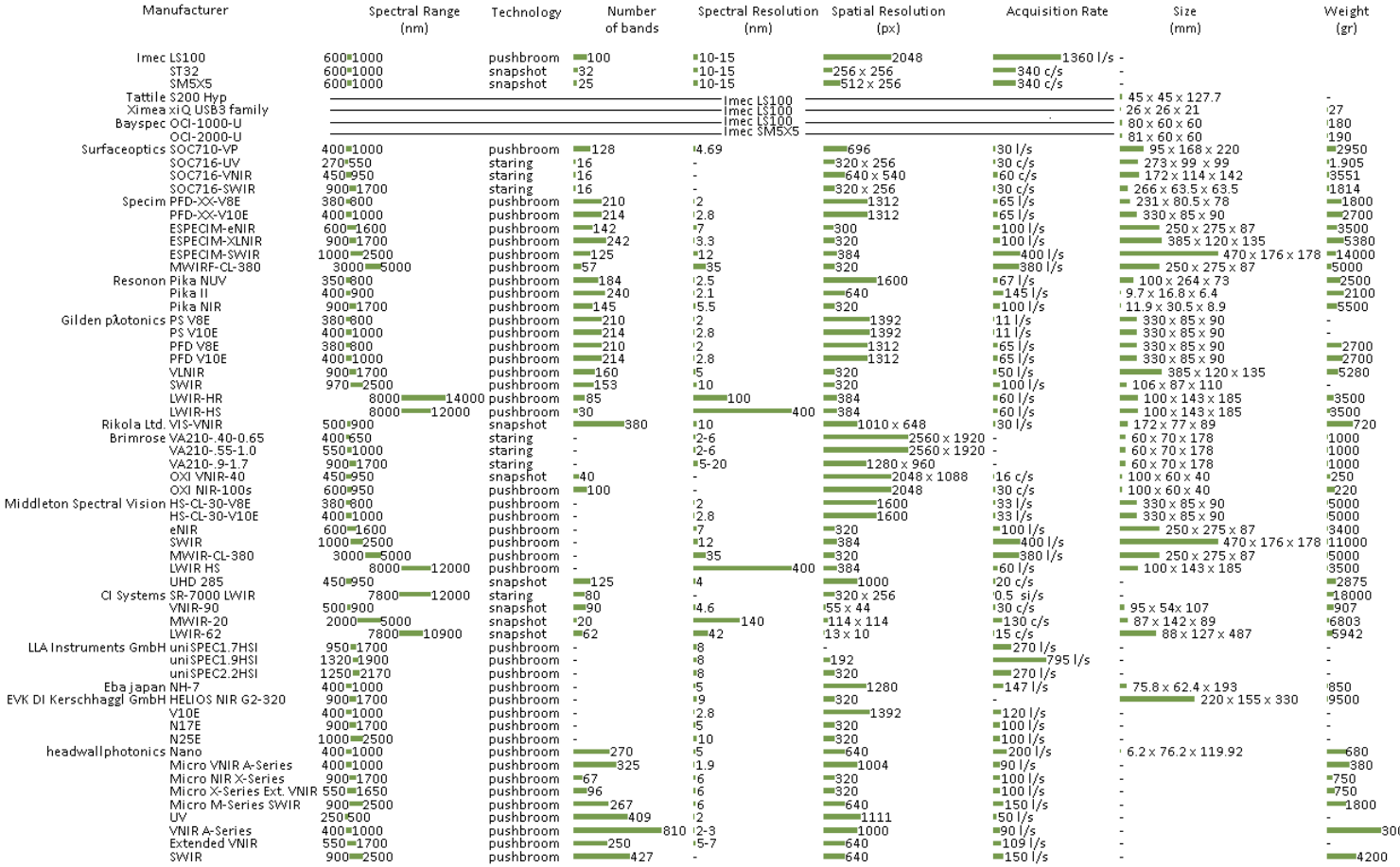

Figure 3.5: Commercial ground-based Sensors and Data Providers

Part of this thesis work treats the reconditioning, calibration, start-up and operation of two ground-based pushbroom imagers based on dispersing elements, designed and built by the Integrated Group for Engineering Research of the University of A Coruña. The next subsection provides a detailed overview of this imaging technology, analysing the optical design of this configuration and the distortion and artifacts associated with the optic mechanical elements and the acquisition process.

3.1.2 Pushbroom Hyperspectral Imagers

The basic optical scheme of a Pushbroom Hyperspectral Imager (PHI) based on dispersing elements is shown in Fig. 3.6a. The observed object is illuminated by a light source, such as the sun (outdoors) or a halogen lamp (indoors). The input objective optics collect the diffused or transmitted light and form an image on the image plane, where a narrow slit (15-30μm) is located. Afterwards, the radiation is collimated and dispersed by a dispersing element, i.e. a prism, a grating or a prism-grating-prism (PGP). The dispersion step basically modifies the direction of propagation of the radiation according to its wavelength. Both the entrance slit width and the characteristics of the dispersing element will determine the spectral resolution of the imager. Finally, the radiation is focused through the focusing optics so that it is detected by a 2D detector array such as a CCD or CMOS sensor. Thus, one axis of the 2D detector corresponds to the imaged spatial positions along the slit height and the second axis corresponds to spectral wavelength. By scanning the object, the second spatial dimension is incorporated, resulting in a 3D datacube. This spatial scan is provided either by a flight platform, a sliding platform or a panning mirror.

In order to facilitate the extraction of accurate spectroscopic information from a scene, it is necessary to characterize and calibrate the hyperspectral sensors with good accuracy in both the spectral and the spatial dimensions. In general, image quality and fidelity in pushbroom imagers are affected by various Point Spread Function (PSF) non-uniformity artefacts [Schläpfer et al., 2007]. It is widely assumed that the PSF has a gaussian shape, so that its position is parametrized by the local maximum response, and its width is measured at full width at half maximum (FWHM), as shown in Fig. 3.6b. Thus, in an ideal image, the PSFs would be aligned with the image columns (spatial channels) and rows (spectral channels), respectively, and the FWHMs would

remain homogeneous. However, due to optical aberrations of the integrated lens and the dispersing element, inaccurate alignments, fabrication imperfections, etc. artifacts or deviations from the ideal image appear in form of PSF non-uniformities.

In general, hyperspectral sensor characterization can be divided into [Davis et al., 2002]:

- *Image quality*: The spectral and spatial resolution is defined as the FWHM of the PSF following both the spatial and the spectral directions. Image quality is also affected by the existence of spatial or spectral discontinuities, i.e. bad pixels.

- *Spatial-Spectral fidelity*: including PSF non-uniformities, area artifacts (stray light, ghost reflections, multiple orders, and frame transfer smear) and linearity. Two uniformity terms are commonly used for the description of image fidelity:

  - *Spatial PSF uniformity*: it is the uniform spatial response between pixels at different wavelengths. The artefacts and mis-registration related to the spatial PSF uniformities are denoted as *keystone* and can be described by the position and width of the spatial response function (SiRF) in the across track dimension.

  - *Spectral PSF uniformity*: it is the uniform spectral response in the across-track direction of the 2D detector. In this case, the artefacts and mis-registration related to the spatial PSF uniformities are denoted as *smile* and the non-uniformity level is described also by the position and width of the spectral response function (SRF).

- *Radiometric performance*: including linearity, signal-to-noise ratio (SNR), dynamic range and temporal and thermal stability.

Several different techniques have been designed and put into practice in order to characterize and correct hyperspectral imagers.

The correction of spatial discontinuities effects, i.e. missing pixels, is analysed by Kieffer [1996] and Schläpfer et al. [2000, 2007], where they test how the use of interpolation (nearest neighbour and bilinear interpolation) affects image quality.

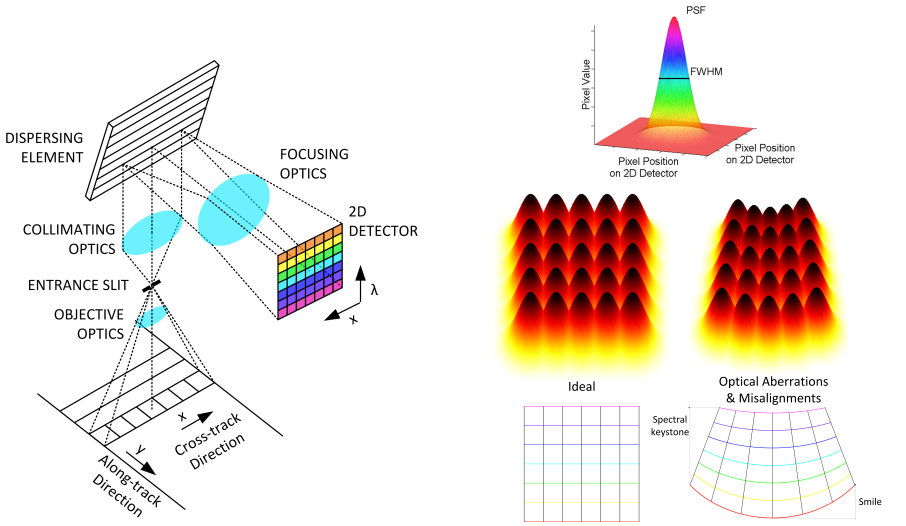

(a) Typical pushbroom optics

(b) Point Spread Function and Smile and keystone distortions

Figure 3.6: Typical pushbroom optics and associated distortions

To characterize the spectral fidelity of hyperspectral systems, it is common to use gas-discharge lamps, calibrated monochromators, laser light sources and precise mechanical actuators. Schläpfer et al. [2000] and Lenhard et al. [2015] use a monochromator coupled with a collimator as a source to take measurements and characterize spectral PSF uniformity. To determine the two relevant parameters of the SRF, the center wavelength and the bandwidth, a Gaussian function is fitted to the data measured for each channel. Polder et al. [2003] perform the spectral calibration by finding the polynomial relation between measured peak locations of several known spectra and the corresponding real spectral line wavelengths. In the work of Mouroulis and McKerns [2000], a slit is imaged on the focal plane and illuminated by various spectral lamps. For each particular emitted wavelength, the PSF centroids are calculated and fitted to a quadratic and linear curves. Then, the smile is measured as the difference between each pair of fitted lines. Similarly, regarding spatial uniformity, keystone is also estimated following analogous approaches consisting in the observation of a physically thin light source at predetermined positions [Mouroulis and McKerns, 2000, Baumgartner et al., 2012].

In general, these first methods do not consider the spatial-spectral dependency in the characterization process or require complex measurement setups or very specific instrumentation. In later works, Lin et al. [2011] and Skauli [2012] propose methods to characterize PSF non-uniformities by combining smile and keystone, considering the spatial and spectral coupling. Furthermore, some other methods, [Kosec et al., 2013, Jemec et al., 2014], suggest the use of a set of affordable reference objects for the measurements in order to simplify the instrumentation necessary for the spatial-spectral fidelity characterization.

Once the smile and keystone distortions have been characterized, only a few works propose resampling correction methods to improve the spatial-spectral image fidelity of the calibrated imagery. Fridman et al. [2013] show that the performance of a resampling camera is comparable to that of a hardware corrected camera with 0.1 pixel residual keystone. It is also proven that the use of an advanced resampling method, such as high-resolution cubic splines, is highly beneficial for the data quality of the resampled image. Lawrence et al. [2003] propose a resampling method based on Geometric Control Points (GCP), with which a transformation that maps distinct points in an image to known locations is developed considering a two–dimensional quadratic polynomial distortion model. Also Van Der Heijden and Glasbey [2003] use an optimization procedure based on the penalized maximum likelihood to determine the most likely warping function between an acquired image and the corresponding synthetic image of a calibration target.

The mentioned works deal with the characterization and the subsequent correction of non-uniformities that mainly depend on the alignment and properties of the components that make up the hyperspectral camera. Despite the expectation that laboratory calibrations should provide the best method for processing pushbroom imagery, there are some other non-uniformities that need to be characterized and corrected based on individual captured scenes. Several works treat vertical disturbance patterns known as vertical stripping VS, which come from the image formation process and are due to the spatial scan, to sensitivity deviations between neighbouring elements of the 2D detector and to variations in the width of the slit along its length. Leathers et al. [2005] deal with VS denoising using an in-scene mean-spectrum non-uniformity correction assuming constant-static noise patterns, which is not realistic and should only be used on uniform regions of the hyperspectral datacube. Statistical methods account for the assumption that the inputs of all sensors have the same statis-

tical characteristics [Gadallah et al., 2000, Sun et al., 2008]. Then, destripping is performed by adjusting the distributions of values acquired by each sensor to some reference distribution by means of a histogram or moment matching, which is not adequate for high spatial resolution imagery or small images. More complex image statistics of log transformed slopes are used in [Carfantan and Idier, 2010], where they assume a linear response of each detector gain and the VS denoising approach is based on a Markov random field model for the logarithm of pixel intensities. The basis of filtering methods, [Garcia and Moreno, 2004, Srinivasan et al., 1988, Chen et al., 2003], is that pixel-to-pixel high frequency variations are due to noise contributions, while the surface contribution presents smoother profiles. These methods assume that the imaged surface does not contain structures with spatial frequencies of the same order as noise, which is not always the case. Oh the other hand, in the work of Gómez-Chova et al. [2008], also based on considering noise as pixel-to-pixel high frequency variations, a technique is introduced for excluding the contribution of the spatial high frequencies of the surface from the process of noise removal.

After reviewing the state of the art on characterization and correction techniques for hyperspectral pushbroom imagers, it is apparent that how to measure, quantify and correct image non-uniformities is currently not well defined. Nevertheless, methods and algorithms tend to fulfill the following requirements:

- In-house/in-lab methods:
  - Fast, simple, dependable and easily repeatable procedures.
  - Consider the spatial-spectral dependency in the characterization process.
  - Employ affordable instrumentation.
- Scene-based methods:
  - Automatic (self-calibration).
  - Sufficiently fast to allow real-time processing.
  - Independent of image size.
  - Work properly regardless of the image and noise statistics.

3.1.3 Summary

In this first section, the basics of hyperspectral imaging from the acquisition process perspective are presented. Hyperspectral images can be captured from different acquisition platforms and through distinct capturing modes. The specific characteristics, advantages and difficulties that make each one suited for different particular applications have been presented.

As part of this thesis focuses on the reconditioning, calibration and operation of pushbroom imagers, the optical design of this capturing mode has been analysed, showing the typical non-uniformities or artifacts associated with the integrated optical mechanical elements that make up these imagers.

Several approaches have been addressed to characterize and correct the related non-uniformities or artifacts. However, it has been shown that there are still no well defined methods to follow. Thus, in-lab and scene-based methods that attempt to achieve a calibration and correction in a robust, fast, simple, affordable and automatic manner need to be established.

3.2 Hyperspectral Image Processing

Before the design and implementation of image processing methods, it is essential to know the nature of the data to be processed. In hyperspectral images, the spectral information of every pixel is collected in a large number of contiguous discrete spectral bands. The wealth of information implied by the large amount of data produced in a single scene is a great help in solving a variety of processing tasks. However, hyperspectral data cubes exhibit restricting characteristics that need to be taken into account, and which present a challenge for the development of processing algorithms. The main drawbacks of hyperspectral image processing are related to:

- *Data storage and transmission:* The large volume of data collected by hyperspectral imagers require large storage capacities and entail a problem in transmitting hyperspectral data in the case of on-board acquisition. The economics of storage and transmission of hyperspectral images lies

in the coding of hyperspectral images, so that efficient compression techniques become an essential feature in hyperspectral imagery [Motta et al., 2006].

- *Data processing time:* Practical hyperspectral applications typically require large amounts of data to be processed in (near) real-time. Decreasing the data processing time involves, on the one hand, the design of time-efficient data analysis techniques. On the other hand, it is desirable that these algorithms can be easily processed in a concurrent fashion within hardware such as GPUs [Plaza et al., 2011, Priego et al., 2016].

- *Data management:* The specific features of hyperspectral images demand the definition of new strategies for the maintenance and automated search within collections of hyperspectral images.

- *Data redundancy:* High dimensional information often leads to collinearity between neighbouring features, which can limit the performance of the data analysis.

- *Hughes phenomenon:* Hyperspectral data are subject to the Hughes phenomenon. In the context of supervised processing methods, with a limited training set, accuracy increases gradually as the number of spectral bands or dimensions grows, but tends to decrease dramatically when the band number reaches some value [Hughes, 1968].

- *Data visualization:* As hyperspectral data contain hundreds of spectral bands, traditional data visualization techniques, such as a standard red, green and blue (RGB) displays, can't be directly applied to represent hyperspectral images. New simple and quick display methods are needed to visualize data consistently, preserve natural contours of features and highlight targets or objects of interest. [Jacobson et al., 2007].

In the early days of spectral imagery, hyperspectral images were mainly acquired from high flying airplanes and on-board platforms. Hence, the spatial resolution of the sensors was too coarse to contain information of only one material of the scene. This results in mixed pixels which contain contributions from distinct signal signatures corresponding to pure materials. On the contrary, when the spatial resolution is fine enough, as usually occurs with ground-based sensors, it is considered that a single pixel covers only one type of pure material

or homogeneous mixture of materials. This leads to addressing the different processing tasks through *mixed-pixel (or subpixel)* and *full-pixel (or per-pixel)* techniques.

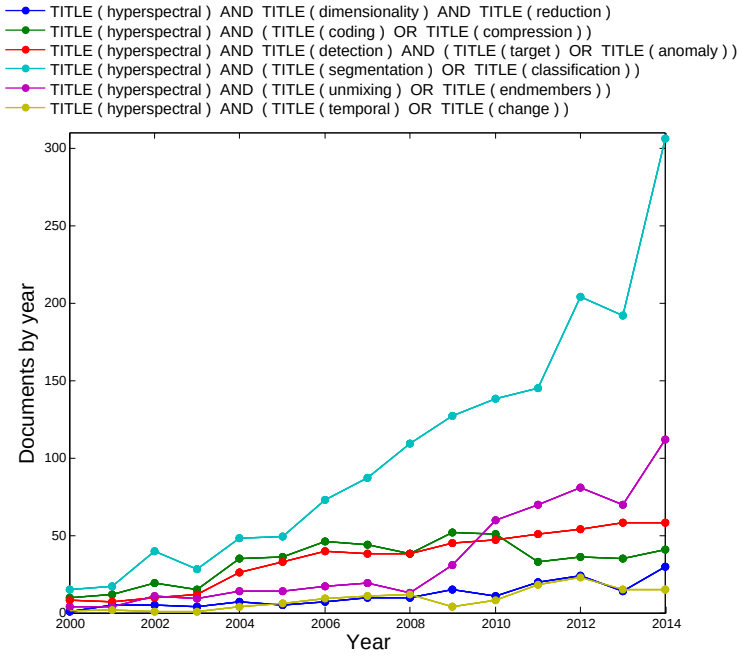

Figure 3.7: Number of documents published per year related to hyperspectral processing. The legend indicates the keywords used in the search engine provided by Scopus (http://www.scopus.com/)

Furthermore, the spatio-spectral features of hyperspectral images lead to different processing problems which, due to the special nature of the data, must be addressed under specific mathematical formalisms and computational conditions. Most of the processing problems considered in hyperspectral imagery can be organized according to the following specific tasks (Fig. 3.7) :

- *Dimensionality reduction:* Dimensionality reduction methods transform data from a high dimension to a low dimension retaining the original information in order to facilitate subsequent processing tasks. This preprocessing step is relevant when the Hughes phenomenon jointly affects the data and the algorithm being applied [Plaza et al., 2005].

- *Image coding:* The amount of data contained in hyperspectral images or sequences makes compression and coding necessary for their storage or transmission. Typically, the compression is required not to degrade the data quality. Two desirable features in hyperspectral image coding is SNR and resolution scalability. SNR scalability allows for a single embedded code stream to generate images at a variety of precision levels without repeating coding. Resolution scalability enables the decoding of different resolution images from the compressed stream of the hyperspectral data [Tang et al., 2005, Christophe, 2011].

- *Target/Anomaly detection:* Target detection consists in searching for sets of pixels (spectral vectors) in a hyperspectral image that do not correspond to some model of the background spectral signature or do correspond to a target model. When the spectral signature of the target to detect is unknown, the detection task is called anomaly detection [Van Der Heijden and Glasbey, 2003].

- *Segmentation/Classification:* Segmentation is defined as an exhaustive partitioning of the input image into non-overlapping regions, each of which is considered to be homogeneous with respect to some criterion of interest (homogeneity criterion, e.g., intensity or texture). Classification assigns to each pixel or object in the hyperspectral image a specific class. Segmentation and classification are usually mixed up, since both are inter-linked: a classifier implicitly segments an image, and a segmentation generally implies a classification.

- *Unmixing:* Unmixing divides each pixel spectrum from a hyperspectral image into a set of spectral signatures called *endmembers* and their corresponding fractional abundances. The endmembers represent pure materials present in the pixel and the abundances indicate the percentage of each endmember that is present in the pixel [Bioucas-Dias et al., 2012].

- *Multi-temporal change detection:* Multi-temporal change detection searches for the variation of a set of pixels that have experienced a significant change relative to a previous data sequence. Temporal changes are typically studied between two sets of data acquired at different times and are usually due to object movement, insertion, deletion, removal or deformation.

This thesis is particularly focused on the problem of segmenting and classifying hyperspectral images and sequences. The next subsection presents the particularities and challenges of hyperspectral image segmentation and classification and reviews in detail the state of the art of these specific hyperspectral processing tasks.

3.2.1 Hyperspectral Image Segmentation and Classification

In the last decade, even though a lot of methods for hyperspectral image segmentation and classification have been proposed, the resolution of these tasks continues to be a challenging problem. There exist some particular aspects of segmentation or classification of hyperspectral images that complicate the partitioning or labelling of the data:

- Philosophical problems
  - *What is considered a homogeneous region or a class?* Images can be segmented or classified in different ways depending on the requirements of the user. One could, for instance, want to segment a hyperspectral image into regions corresponding to fields, urban areas and water or into more detailed regions such as different types of vegetation, distinguish roads from buildings or differentiate between rivers and the sea.
- Methodological problems
  - *High dimensionality of the images and very limited labelled data.* Increasing the number of spectral bands in hyperspectral images requires that the number of labelled pixels (training samples) grow exponentially in order to maintain statistical integrity for supervised classification purposes.
  - *Integration of spectral, spatial and temporal information.* Hyperspectral images are highly correlated in the spatial, spectral and temporal dimensions. It is essential to develop spectral-spatial segmentation/classification techniques (spectral-spatial-temporal techniques

when processing image sequences) capable of considering dependencies between neighbouring pixels. This complicates the process of designing new algorithms and increases the processing times.

- Practical and operational problems
  - *Very few labelled hyperspectral datasets are publicly available.* Acquiring hyperspectral data and building reliable labelled datasets is quite costly in terms of economics, time and resources.
  - *Building the datasets.* Labelling is a controversial procedure because of the subjectivity involved in the interpretation of the data.
  - *Distortion and noise.* The acquisition process is highly likely to be corrupted by distortions and noise. Atmospheric and illumination variations may spoil the dataset, making it necessary to design robust methods to segment and classify hyperspectral images.
  - *Pre-processing steps are usually required*: sometimes, preprocessing methods are required, for instance, to apply dimensionality reduction or denoising algorithms. These added steps increase the complexity and processing time of the whole process but, conversely, make the post segmentation and classification simpler and more efficient.
  - *Expert knowledge is needed.* Typically, segmentation and classification methods need an initial parameter set up to adapt the algorithms to a particular problem or application. This first stage is usually performed by expert users, which limits the applicability of the methods.

Common segmentation and classification procedures can be decomposed into three main groups based on prior information used to infer the function that emulates a certain behaviour: supervised, unsupervised and semi-supervised methods.

In a **supervised** technique, an expert user or analyst recognizes in a scene representative samples of different surfaces or materials of interest based on prior knowledge. These samples are labelled making up the *reference data* or *training data* of the image being analysed. This identification process is subject to an inherent subjectivity and depends heavily on the cognition and skills of

the image analyst. Once the image is properly labelled, the reference data is used to train or adjust the parameters of the classification method so that it can later be used for mapping new samples.

Unsupervised methods do not require prior information from the image which is being analysed. The classification procedure is performed by the examination and categorization into a number of classes of a large set of unknown samples based on natural spectral features. The basic principle is that equally labelled samples are close in terms of a particular similarity measurement.

Semi-supervised methods typically make use of a small set of labelled data in conjunction with a large set of unlabelled data in order to improve the classification performance.

From another point of view, most classification methods process hyperspectral images in a **pixel-wise** manner. This means that each pixel is processed independently without considering contextual (spatial or temporal) information. Traditional classification methods ruled by this model, used since the nineties, comprise maximum-likelihood-based (ML) [Zenzo et al., 1987, Jia et al., 1994, Jackson et al., 2001], minimum-distance-based, spectral angle based [Kruse et al., 1993], subspace projection-based methods as Orthogonal Subspace Projection (OSP) [Harsanyi and Chang, 1994, Althouse, 1998, Chang et al., 1998, Chang, 1998] or Principal Component Transformation (PCT) [Jia and Richards, 1999, Rodarmel and Shan, 2002], Fisher's linear discriminant analysis (LDA) [Du and Chang, 2001],Linearly Constrained Discriminant Analysis (LCDA), shape filtering [Cochrane, 2000] and fuzzy methods [Bárdossy and Samaniego, 2002].

Alongside the previous approaches, classification methods based on Artificial Neural Network (ANN) models emerged. ANNs are considered to be powerful classification tools because of their non-linear properties [Guilfoyle et al., 2001] and the fact that they make no assumptions about statistical information of the data [Moon and Merenyi, 1995, Du and Chang, 1999, Plaza et al., 2009a].

In [Gualtieri and Cromp, 1998], a Support Vector Machine (SVM) technique was applied to hyperspectral data for the first time. SVM consists in finding the optimal separation surface between classes through the identification of the most representative training sample, called support vector, of each class. SVM has shown very good performances for classifying high-dimensional data when a limited number of training samples is available. Furthermore, a feature selection

step to reduce the dimensionality of the image cube is not required. If the training samples are not linearly separable, a kernel method is usually employed to project the data into a higher dimensional space where the classes become linearly separable. Due to the suitability of this technique for hyperspectral data, it has been repeatedly applied in numerous works [Gualtieri and Chettri, 2000, Melgani and Bruzzone, 2002, Mercier and Lennon, 2003, Camps-Valls et al., 2003, 2004, Camps-Valls and Bruzzone, 2005].

The aforementioned methods consider hyperspectral data as a set of spectral measurements without meaningful arrangement. That means that each spectral vector will be classified in the same manner regardless of its spatial position within the hyperspectral cube. This is the reason why pixel-wise classifiers may lead to "salt and pepper" noise in classification maps.

However, taking into account correlations between spatially or temporally neighbouring pixels may significantly improve the performance of the classification algorithm. Moreover, the combination of spectral, spatial and temporal information makes it possible to classify images according to spectral textures, spatial patterns, shapes, temporal changes, etc. Methods that follow this methodological line are called **spectral-contextual** techniques [Lu and Weng, 2007].

The design of spectral-contextual methods when dealing with single hyperspectral images, hereafter **spectral-spatial** methods, normally entails the application of a multi-stage classification procedure. The pioneer work in introducing spatial context into a multivariate image classification is the Extraction and Classification of Homogeneous Objects (ECHO) classifier [Landgrebe, 2005]. Since then, many studies have been carried out to propose new algorithms to perform spectral-spatial classification.

There are mainly two approaches to include the spatial information:

- The first approach processes each pixel using spatial information within a *fixed/adaptive window size* centred on the pixel which is being analysed.

  Markov Random Fields (MRF) in conjunction with an adaptive ML approach were proposed by Jackson et al. [2002]. For a Markov random field, the conditional distribution of a point in the field, given all other points, is only dependent on its neighbours. The first-order neighborhood system is usually defined as the four pixels surrounding a given pixel, and

higher orders are defined by adding corner pixels to a lower order neighbourhood system. Jackson et al. [2002] showed that this method improves the performance of a ordinary ML technique. However, using a standard neighbourhood may not be sufficient to contain enough spatial information of structures present in the image and, unfortunately, increasing the size and shape of the spatial window is, in most cases, computationally intractable. Moreover, MRF normally requires an iterative optimization step, such as simulated annealing, which is extremely time consuming.

Several approaches based on mathematical morphology have been widely treated in the literature. These techniques are focused on image structural information, which is obtained through the application of morphological operators (erosion/dilation, opening/closing, top-hat/bot-hat, rank filters, etc.). Morphological operators are applied to each pixel using a multi-scale approach, thus obtaining what are called Morphological Profiles (MP), which serve as inputs to a posterior classification step. The first works based on MP were applied over panchromatic images [Pesaresi and Benediktsson, 2001, Benediktsson et al., 2003]. Afterwards, Benediktsson et al. [2005] extended the approach to hyperspectral images by building Extended Morphological Profiles (EMP) from several first components of a PCT transformation applied to the data cube. Later, Plaza et al. [2009b] followed the same procedure of reducing the dimensionality of hyperspectral images through a PCT or a MNF transform. In this case, the classification step was performed by means of a SVM applied to the morphological features. In [Falco et al., 2015, Dalla Mura et al., 2010], the concept of MP and EMP was enhanced by extracting additional spatial features, leading to the notion of Attribute Profiles (AP). In [Falco et al., 2015], advanced pre-processing steps are carried out to reduce the dimensionality. In this case the dimensionality reduction step is addressed by applying Independent Component Analysis (ICA), prior to the extraction of contextual information for spatial features based on APs. Then, a compact optimized representation of the extracted spatial-spectral attributes is proposed.

Generally, mathematical morphology based approaches provide good classification accuracy results, but most of the methods still suffer from the high dimensionality of the data. Furthermore, morphological operators were originally defined for single-band images. The extension to hyper-

spectral data has been addressed by extracting and processing independently one or a few representative grayscale images, which leads to significant information losses.

Another related technique makes use of SVM with composite kernels (SVM-CKs). A pixel-wise classification is performed based on a kernel formulation where the spatial information is incorporated as an operation among spatial, spectral and spatial-spectral kernels. In SVM-CKs, the spatial feature is usually represented as the mean or standard deviation of the gray value distribution of pixels in a fixed spatial neighborhood [Camps-Valls et al., 2006]. In [Camps-Valls and Bruzzone, 2009], the hyperspectral image is filtered using a flat zone area filter which removes all the structures of the image that contain fewer pixels than a given parameter. Then, the neighbourhood of each pixel is considered as the set of pixels belonging to the same flat labelled zone. As in [Camps-Valls et al., 2006], the information is merged using a combination of kernels during the classification process. A framework for generalized-composite-kernel-based classification is proposed in [Li et al., 2013a], that differs from the previous ones in relying on a Sparse Multinomial Logistic Regression (SMLR) classifier to produce the final classification results and in modeling the spatial information using Extended Multiattribute Profiles (EMAPs).

- The second procedure for the inclusion of spatial information starts with a preliminary *spatial/spectral clustering/segmentation* followed by an area fusion stage based on a supervised criterion.

  Segmentation is defined as an exhaustive partitioning of an image into non-overlapping regions, each of which is considered to be homogeneous with respect to some criterion of interest. Then, a segmentation step provides sets of connected pixels that share particular properties. Usually, the supervised classification is performed by means of a SVM classifier and a majority voting rule is used to merge the spectral and spatial information. The segmentation step has been addressed through different techniques: ECHO [Landgrebe, 2005], partitional clustering methods [Tarabalka et al., 2009], watershed transformation [Tarabalka et al., 2010], hierarchical segmentation (HSeg) or region growing [Tilton et al., 2012].

> The classification accuracy of the previously cited works is conditional on the performance of the selected segmentation approach, which is normally highly sensitive to the measure of region homogeneity and the inherent parameters of the segmentation algorithm [Fauvel et al., 2013].

Spectral-spatial classification methods have been shown to improve the performance of pixel-wise techniques and provide more homogeneous classification maps. However, these improvements normally have restrictive implications, such as scale limitations and algorithmic and computational complexity.

Up to now, the processing of single hyperspectral images has been considered. When dealing with image sequences, a new dimension has to be added to the hyperspectral processing stage. This leads the algorithms to acquire a greater degree of complexity, but conversely, it allows hyperspectral imagery to meet important applications in monitoring natural environments and human activities, such as change detection, temporal classification, tracking, etc.

Before implementing multi-temporal analysis, two conditions must be satisfied: precise co-registration and radiometric calibration between multi-temporal images. Once the hyperspectral image sequences have been correctly coregistered and calibrated, there are two ways to incorporate temporal information in processing methods: by combining spectral and temporal information in a temporal pixel-wise fashion (spectral-temporal methods) or by merging the spectral, spatial and temporal information (spectral-spatial-temporal methods).

In general, **spectral-temporal methods** can be divided into two broad categories [Singh, 1989]: those that simultaneously analyse multi-temporal data (pre-classification methods) and those that comparatively analyse independently produced classifications for different times (post-classification methods).

Spectral-temporal methods based on post-classification consist in independently producing spectral classification maps from each frame of the multi or hyperspectral image sequence, followed by a pixel-by-pixel comparison to detect changes [Yuan et al., 2005, Ji et al., 2006, Ghosh et al., 2011]. Advantages of post-classification methods are the insensitivity to the problem of uncompensated radiometric calibration between frames and the feasibility of multi-change detection. However, the performance of the comparison is highly dependent on the accuracy of the initial classifications.

The first spectral-temporal methods in simultaneously analysing multitemporal data operate through the pixel-wise comparison of selected spectral bands (or particular components after a transformation) of two co-registered multi or hyperspectral images.

The simplest comparative methods comprise image differencing [Serneels et al., 2001] (0 means no change) and image rationing [Howarth and Wickware, 1981] (1 means change). Then, to detect the change a simple thresholding has to be applied [Rosin and Ioannidis, 2003].

Other methods perform a linear transformation of the original co-registered images after their arrangement in $2n$-dimensional space (n is the spectral dimension). Some examples of linear transformations are PCA [Ortiz-Rivera et al., 2006], multivariate alteration detection (MAD) [Nielsen et al., 1998], iterative re-weighted MAD (IR-MAD) [Nielsen, 2007] and Kauth-Thomas Transformation (KT) [Jin and Sader, 2005]. These methods have been proven to accurately detect changes, but, as in the case of image differencing and rationing, they are designed for detecting just the presence or absence of change.

In order to enable the analysis and classification of the change, the Change Vector Analysis (CVA) technique involves multiple image bands in the temporal processing [Johnson and Kasischke, 1998, Baker et al., 2007, Wen and Yang, 2009]. CVs are calculated by pixel-wise subtracting vectors as in image differencing. The magnitude of the CV is used for change and no-change classification, meanwhile the CV direction can be used for classifying the change. Bovolo et al. [2012] have addressed multiple-change detection problems in low spectral resolution imagery through Compressed Change Vector Analysis C^2VA. Recently, Sequential Spectral Change Vector Analysis (S^2VA) and Hierarchical Spectral Change Vector Analysis (HSCVA) [Liu et al., 2015a] have been proposed as alternatives to the previous C^2VA when dealing with high spectral resolution images [Liu et al., 2015b].

Machine Learning based methods, such as ANNs and SVMs, have also been applied to process multi-temporal data in a pixel-wise manner [Liu and Lathrop Jr, 2002, Huang et al., 2008]. But, as with spectral-spatial classification methods, ANNs and SVMs suffer the same drawbacks related to the need of large amounts of reference data when training the methods.

A step further in the processing of hyperspectral image sequences is the inclusion of spatial information in the analysis of the spectral-temporal data, giving rise to **spectral-spatial-temporal methods**.

Most of the spectral-spatial-temporal methods found in the literature are focused on Object-Based Change Detection OBCD [Hussain et al., 2013]. Techniques encompassed under OBCD incorporate spectral, spatial, temporal and geometrical information, and their aim is "to identify differences in geographic objects at different moments using object-based image analysis" [Chen et al., 2012]. Some OBCD approaches perform direct object change detection by comparing geometrical properties (width, area and compactness) [Zhou et al., 2008, Lefebvre et al., 2008], spectral information (mean band values) or extracted features (e.g. texture) [Tomowski et al., 2011] of the image objects. Other methods classify the change based on a post-classification of the image objects [Blaschke, 2005, Stow, 2010, Hansen and Loveland, 2012].

OBCD methods overcome the limitations of pixel-based approaches. However, there are still some associated issues that should be improved [Hussain et al., 2013]: the automatic selection of the most appropriate parameters for object extraction when dealing with multi-sized objects and the definition of a standard procedure for accuracy assessment.

The validity of all the aforementioned processing methods should be subject to an unified criterion for partial and rigours comparisons. Furthermore, it would be highly desirable that algorithms were validated using assorted images from a repository of standardized benchmark images. The next subsection reviews the most common evaluation criteria employed in the validation of classification methods. It also provides a compendium of publicly available repositories found on-line.

3.2.2 Evaluation of Hyperspectral Classification methods

Although the classification of hyperspectral images has gained great importance in the remote sensing field, the evaluation of classifications methods is, however, a problematic issue.

The first problem to mention is that classification errors are of more or less significance depending on the point of view of each different user. This leads to asserting that the validity and utility of a particular classification should be assessed by its ability to be used for a particular purpose.

Assuming that there exists an indisputable ground truth image to compare to the classified one, most of the works conduct the classification assessment through single accuracy metrics. Classification accuracy is typically taken to mean the degree to which the derived image classification agrees with reality or conforms to the "truth" [Campbell, 2002]. Accuracy metrics that have been systematically used to assess classification methods are overall accuracy, average accuracy, class-specific accuracies and kappa coefficient. These measures derive from a confusion matrix and are defined as:

- Overall Accuracy (OA): percentage of correctly classified pixels.
- Average Accuracy (AA): mean of the percentage of correctly classified pixels for each class.
- Kappa coefficient (κ): percentage of agreement (correctly classified pixels) corrected by the number of agreements that would be expected purely by chance.
- Class-specific accuracies: percentage of agreement of each class.

Nevertheless, some authors [Foody, 1992, Turk, 2002, Pontius Jr and Millones, 2011] maintain that accuracy metrics are not sufficient to reflect the diverse attributes of the classified image. κ is generally thought to be a more robust measure than a simple percentage of correctly classified pixels, since it takes into account the agreement occurring by chance. However, κ is considered [Viera et al., 2005] as a too-conservative measure of agreement, since it tends to underestimate the agreement on the less frequent categories. As an alternative, new measures have been introduced. For instance, Pontius Jr and Millones [2011] suggest employing two new measures related to quantity disagreement and allocation disagreement. Quantity disagreement relates to disagreement in the overall proportions of map classes in two maps, while allocation disagreement relates to the disagreement in spatial allocation of map classes, given the proportions of the classes in the two maps. In this regard, it seems necessary to reconsider the assessment method in the classification of hyperspectral images, as well as to converge to an unified criterion.

Table 3.3: Free datasets found on-line

Reference	Imager	λ (nm)	N. of bands	N. of images	Themes	Ground Truth
Scyllarus	Staring (LCTF)	400-700	31	75	·Portraits ·Office scenes ·Close-ups ·Fruit ·Vegetables ·Flowers ·Landscapes	No
Foster et al.	Staring (LCTF)	400-720	33	16 3	·Rural scenes from the Minho region (Portugal) ·Earth and urban scenes from the cities of Porto and Braga ·Medieval and Early Modern Manuscripts	No
Chakrabarti et al. 2011	Staring (LCTF)	420-720	31	77	·Indoor and outdoor images under daylight ·Indoor images under artificial and mixed illumination	No
Parraga et al. 1998	Staring (LCTF)	400-700	31	29	·Natural images	No
Di et al. 2010	Staring (LCTF)	400-720	33	300	·Neutral facial expressions from 25 individuals	No
Brainard	Staring (LCTF)	400-700	31	9	·Indoor images	No
Skauli et al. 2013	HySpex	415-950	148	44 6 1	·Faces ·Landscapes ·Memorial Church Facade	No
MultiSpec	HYDICE	401-2473	191	1	·Washington DC Mall	No
Baumgardner et al.	AVIRIS	400-2500	220	1	·Indian Pine Test Site 3	Yes
UPV/EHU	AVIRIS AVIRIS ROSIS Hyperion	400-2500 400-2500 430-860 400-2500	224 224 102 242	2 1 2 1	·Valley of Salinas (Southern California) ·Kennedy Space Center (Florida) ·Pavia Scenes (Italy) ·Okavango Delta (Botswana)	Yes
Gader et al. 2013	CASI-1500	367-1043	72	3	·Gulfport campus (Florida)	Yes
HICO website	HICO	400-900	87	6400	·Coastal regions (five years of operations)	No
AVIRIS website	AVIRIS	400-2500	224	1 1 1 1	·Moffett Field ·Cuprite ·Lunar Lake ·Low Attitude	No
JPL	AVIRIS HYPERION	400-2500 400-2500	224 242	12 1 1 1	·Yellowstone, Hawaii and Maine Scenes ·Lake Monona ·Mt. St. Helens ·Erta Ale	No
Spectir	AISA	395-2450	360	9	·Agriculture, Vegetation, Aquatic, Urban and Mixed Environment Samples	No
SPECIM dataset	SPECIM	400-700	49	52 37 57	·Outdoor Scenes ·Indoor Scenes ·Fruits	No

Finally, the majority of classification methods found in the literature are applied and then evaluated using no more than five or six different hyperspectral images. This becomes a major issue, since it may lead to the efficiency of the developed and future algorithms being highly dependent on specific features (particular signatures, spatial and spectral resolution, etc.) of these repeatedly used hyperspectral images. This fact is a consequence of a lack of publicly available repositories of labelled hyperspectral images. Table 3.3 shows a compendium of hyperspectral images databases found on-line, which reveals that, despite the fact that there are hundreds of hyperspectral images available, only a dozen of them have an associated ground truth with a more or less reliable labelling.

3.2.3 Summary

This second section has been devoted to introducing the basics of hyperspectral image processing. The particular characteristics of hyperspectral images, mainly related to the multidimensional nature of the data, have been presented. It has been shown that dealing with the large amount of data produced in a single hyperspectral scene involves facing difficulties in its processing, but also allows solving a variety of processing tasks.

The main research work of this thesis is focused on providing a methodology, along with an algorithm to segment and classify both single and multi-temporal hyperspectral images. Focusing on this point, this section serves as a review of the most relevant works found in the literature that aim to solve these tasks.

Finally, the problem of the classification assessment has been discussed. There exists a significant issue in validating the classification of hyperspectral images due to he lack of a unified assessment criterion and the unavailability of a repository of standardized benchmark images with reliable associated ground truths.

3.3 Discussion

Although hyperspectral imaging has a clear potential in multiple fields, the popularization of this technology is still not a reality. From the review provided in this chapter, it can be extracted that there exist some limitations that hinder taking the leap of hyperspectral technology to a major spread and roll-out.

Firstly, today's hyperspectral imagers are less expensive and have experienced an improvement in terms of spatial and spectral resolution, noise level, etc. However, they are not "affordable enough" and their operating mode is not intended to be used by a non specialist user. Moreover, most of the hyperspectral cameras, particularly pushbroom imagers, require reconditioning and calibration procedures that should be applied periodically, which presupposes having available appropriate calibration instruments as well as the technical know-how that these processes demand.

In this sense, it appears necessary to:

- Adapt the manipulation of hyperspectral imagers for a widespread use.
- Provide low-cost instrumentation together with simple methods to calibrate hyperspectral imagers, so that this calibration can be carried out by any final user.

Concerning the processing of hyperspectral images, it is found that most of the methods presented until now, specifically those designed to address segmentation and classification tasks, do not consider the subjectivity involved in the interpretation of the data. In this regard, it is desirable to provide processing methods with the capacity of adapting to what the user desires, contemplating the fact that there are multiple ways of segmenting or classifying images. That is why it is considered pertinent to:

- Facilitate a new methodology that allows non expert users to provide their own segmentation/classification criteria in a simple and low-expertise fashion.
- Design processing algorithms able to learn from and adapt to different segmentation/classification criteria.

- Propose a method to conduct the learning process that is as simple and less-time consuming as possible.

Regarding the effectiveness of the proposed methods, it has been evidenced that spectral-contextual techniques improve the results of segmentation or classification methods that operate in a pixel-wise manner. Furthermore, it has been proven desirable to preserve all the spectral information in the processing of hyperspectral images, avoiding projecting the spectral data onto lower dimensional spaces. With regard to the foregoing, it appears advantageous to:

- Include and process the spatial, spectral and (if it is the case) temporal information in the hyperspectral data.
- Propose methods that work with the entire spectrum obtained by the hyperspectral sensor.

In general, the majority of methods found in the literature are not designed taking into consideration that their application to real scenarios would certainly have requirements of real-time operation. That leads to the necessity of:

- Designing new methods based on parallel low-level processing operations, making them attractive for their implementation in a concurrent fashion within hardware such as GPUs. This would allow hyperspectral systems to keep pace with real-world activities, responding appropriately to them.

Finally, it has been found a non-negligible issue in validating processing algorithms in the hyperspectral field. It is considered fundamental to:

- Converge to an unified assessment criterion in the classification of hyperspectral images.
- Have a repository of standardized benchmark images with reliable associated ground truths at disposal of the hyperspectral community.

Once some of the possible action points for the popularization of hyperspectral technology have been presented, the next chapter describes the specific contributions of this thesis for the reconditioning and calibration treatment of pushbroom hyperspectral imagers.

Chapter 4

Calibration and Operationalization of Two Pushbroom Imagers

4.1 Introduction

This chapter is devoted to the presentation of the procedures followed to operationalize two prototypes of pushbroom hyperspectral imagers built in the Integrated Group for the Engineering Research of the University of A Coruña (GII), and designed in collaboration with the Department of Applied Physics of the University of Santiago de Compostela, Spain. These procedures embrace the electro-mechanical mechanisms that enable them to acquire a whole hyperspectral datacube, the spatio-spectral characterization of the hyperspectral images obtained using the prototypes, the methods designed to minimize the distortions associated with these imagers and the implementation of software tools that facilitate the operation with the hyperspectral cameras.

A comprehensive approach for the efficient acquisition and processing of hyperspectral images and sequences

Método integral para la adquisición y procesamiento eficiente de imágenes y secuencias hiperespectrales

Author/Autora: Blanca María Priego Torres

Doctoral Thesis / Tesis Doctoral / 2016

Advisor/Director:

Richard J. Duro Fernández

Programa Oficial de Doctorado en Computación[1]

[1]Programa regulado por el R.D. 1393/2007

4.2 Hyperspectral Camera Prototypes

In the beginning of this thesis project, a first hyperspectral sensor (PHI V.1) was at the prototype phase within the GII. This work took as its starting point a prototype of a hyperspectral camera with the optical and mechanical design finished and the elements that constructed the imager assembled.

Initially, this prototype was conceived to be small, lightweight, portable, with high-quality spatial and spectral specifications, at the same time as relatively cheap compared to other commercial cameras found at that moment. Fig. 4.1 shows the first prototype after being assembled in indoor and outdoor operation.

(a) (b) (c)

Figure 4.1: First prototype of pushbroom hyperspectral imager

(a) (b)

Figure 4.2: Second prototype of pushbroom hyperspectral imager

The second prototype (PHI V.2) emerged because of the need to have an even smaller and more economic hyperspectral camera. This new model was devised to be used for the acquisition of hyperspectral images from ground-level or aircraft platforms such as Unmanned Aerial Vehicle (UAVs). Consequently, this new prototype improves the previous one in terms of size and weight, while slightly decrementing its spatial-spectral characteristics. Some images of this new prototype are shown in Fig. 4.2.

The main physical, spatial and spectral features of the two prototypes are summarized in Table 4.1

Since both camera prototypes are pushbroom-based systems, it was necessary to face the problem of scanning lines along the dimension perpendicular to the one acquired in each partial capture. The next section describes the established and implemented mechanisms that make the acquisition of whole hyperspectral datacubes possible.

Table 4.1: Features of the two hyperspectral imagers developed

	PHI V.1	PHI V.2
Size	$37 \times 12 \times 8.5$ cm	$21 \times 5 \times 6$ cm
Weight	2120 g	680 g
Spectral Range	$[413, 1030]$ nm	$[385, 950]$ nm
N. of Spectral Bands	342	360
Sensor Resolution (along track)	1392	20848

4.3 Hardware Conditioning of Pushbroom Hyperspectral Imagers

Prototype PHI V.1 was designed with an autonomous and automatic system in mind. This means that the casing of the hyperspectral camera should include the subsystem that enables de spatial scanning of the scene. The implementation of the scanning subsystem covers the mobile mechanical elements and electronics that synchronize these mechanical elements with the camera in the acquisition process.

On the other hand, prototype PHI V.2 was intended to operate from airborne platforms. In this case, the movement of the airborne platform itself is responsible of the spatial scanning of the scene.

The next subsection enumerates the particular steps involved in acquiring complete hyperspectral datacubes for PHI V.1.

4.3.1 PHI V.1

As stated earlier, a prerequisite for the design of PHI V.1 was to be fully automatic. In order to spatially scan the scene and then obtain a whole hyperspectral datacube, a module has been designed that is attached to the end of the hyperspectral sensor. The main elements of this new module are (Fig. 4.3a):

- A rotating mirror: A first reflection mirror rotates with respect to an axis which is aligned with the slit contained in the optical module. The mirror can be rotated from $-30°$ to $+30°$, allowing a FOV of $+60°$ (along-track).
- A servomotor along with a gear-and-chain system that enables the movement of the mirror.
- A mechanical structure with the purpose of focusing a scene without the need to disassemble any module of the whole hyperspectral system.

The automatic control of the mechanical elements has required the development of a printed circuit board (PCB), which is integrated in the camera casing itself (Fig. 4.3b). The functions of the developed PCB are:

- Receive control signals from the PC (initiate/finish acquisition and configuration parameters such as exposure time).
- Modify the rotation of the mirror by sending the appropriate signal to the servomotor, which is engaged with the gears-mirror.
- Send a trigger signal to the camera to initiate the capture of an image.
- Read two signals, *sync A* and *sync B*, coming from the camera. The state of these signals changes when the exposure time (*sync A*) and the data reading time (*sync B*) have been initiated or finished.

The PCB board has an Arduino nano v3.0 platform attached; a 1.3.mm Jack connector through which the PCB board is powered; a MiniDin connector to communicate with the camera; and a 4-pin connector to control and power the servomotor (see Fig. 4.3). A 12 V to 5 V converter is also integrated in order to power the servo with the appropriate voltage level.

The main steps involved in the capture of a whole hyperspectral data, from the point of view of the mirror and the image capture timing control, are described in B.

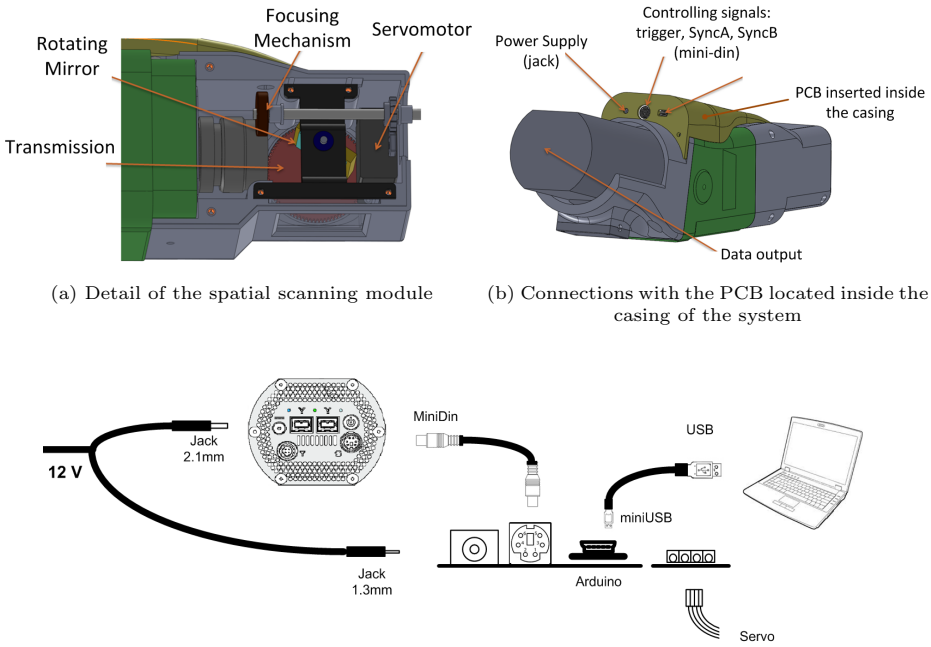

(a) Detail of the spatial scanning module

(b) Connections with the PCB located inside the casing of the system

Figure 4.3: PCB connections

4.4 Characterization and Calibration procedures

As stated in the background section, the hyperspectral sensor characterization covers aspects such as image quality, spectral fidelity, and radiometric performance. In this work, the particular tasks carried out in relation to the characterization and calibration/correction of the developed sensors are restricted to

spectral range determination, smile and keystone correction (spectral fidelity) and destripping (image quality). Through the application of these procedures, we seek to reconstruct the hyperspectral datacube preserving high-quality spatial and spectral specifications.

4.4.1 Smile and Keystone Correction

The objective here is to keep the position of the PSF uniform between pixels at different wavelengths and in the across-track direction of the 2D detector. To achieve this spatial-spectral uniformity, in this work a simple and automatic method that operates with low-cost and accessible materials for which specialist knowledge is not required is proposed. Specifically, the material resources to carry out smile and keystone correction are:

- Printed black and white lined pattern, for setup 1 (Fig. 4.4a).
- Lamp with an approximately flat spectral emission curve.
- Set of one or two gas discharge lamps with emission lines covering the spectral range of the hyperspectral sensor, for setup 2 (Fig. 4.4b).
- Light diffuser, for setup 2 (Fig. 4.4b).

The calibration procedure starts by setting up the black and white lined pattern and the hyperspectral sensor, as shown in Fig. 4.4a, and by illuminating using a lamp with an approximately flat spectral emission curve. Several partial captures are acquired without moving any element of the setup. A pixel-wise average is carried out using all the captures, which leads to an image with an appearance similar to the one shown in Fig. 4.4c. Afterwards, an edge-based line detection algorithm is applied in order to determine the position of the black and white transitions present in the captured pattern (Fig. 4.4e). In case of an ideal system, these lines should appear totally straight and vertical.

A second setup is then constructed. Several captures of emitted light from two gas-discharge lamps are acquired. In order to get more spatially homogenized images, a light diffuser is placed between the camera and the lamps. Again, a pixel-wise average is applied to the captures. By using at the same time Mercury and Argon Lamps, respectively, the resulting averaged image will

be similar to the one shown in Fig. 4.4d. Next, an automatic line detection algorithm is applied by fitting the spatio-spectral responses to lines following the model: $(x_i - x_o)^2 + (y_i - y_o)^2 \leq r^2$ (Fig. 4.4f).

The next step consists in extracting the intersection points between the spatial and spectral lines that were previously detected. Each one of these points will have an associated correspondence point which reflects its final spatio-spectral position in the corrected image. Then, considering both sets of input (non-corrected) and output (corrected) points, a 2-dimensional transformation based on a polynomial of degree two is estimated:

$$\begin{aligned} x_f(x_0, y_0) &= a_1 + a_2 \cdot x_0 + a_3 \cdot y_0 + a_4 \cdot x_0 \cdot y_0 + a_5 \cdot x^2 + a_6 \cdot y^2 \\ y_f(x_0, y_0) &= b_1 + b_2 \cdot x_0 + b_3 \cdot y_0 + b_4 \cdot x_0 \cdot y_0 + b_5 \cdot x_0^2 + b_6 \cdot y_0^2 \end{aligned} \tag{4.1}$$

where x_0 and y_0 are the coordinates in the non-corrected image, x_f and y_f are the coordinates in the corrected image and a_i and b_i are the estimated parameters of the 2-dimensional transformation.

Finally, each capture acquired by means of the hyperspectral sensor must be processed using the estimated spatio-spectral transformation, in order to obtain a corrected version of it (Fig. 4.4h).

The advantages of the method presented here are:

- It is fully automatic
- Only low-cost instrumentation is required
- It is easily reproducible
- Both keystone and smile distortions are corrected simultaneously

4.4.2 Spectral Range Determination

Once the keystone and smile distortions have been corrected, we can determine the spectral range of the hyperspectral sensor, in other words, establish a correspondence between y_f and spectral band or wavelength, λ.

The instrumentation required to determine the spectral range of the sensor is reduced to:

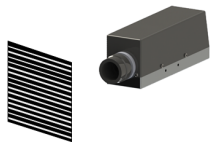

(a) Setup 1

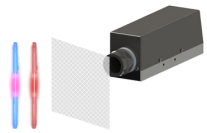

(b) Setup 2

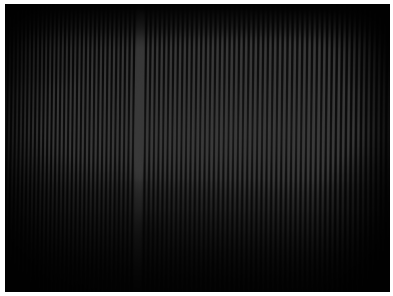

(c) Spatial lines

(d) Spectral lines

(e) Detected spatial lines

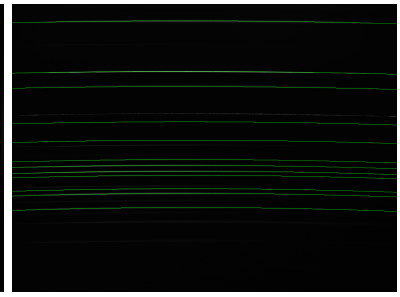

(f) Detected spectral lines

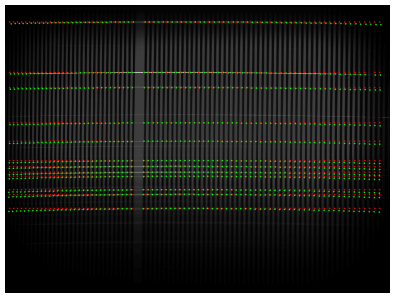

(g) Intersection of spatial and spectral lines. Input and output points are colored in green and red respectively

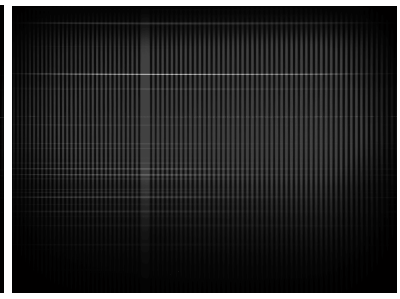

(h) Corrected capture

Figure 4.4: Smile and Keystone correction. X-axis and Y-axis map the across-track spatial and spectral dimensions respectively

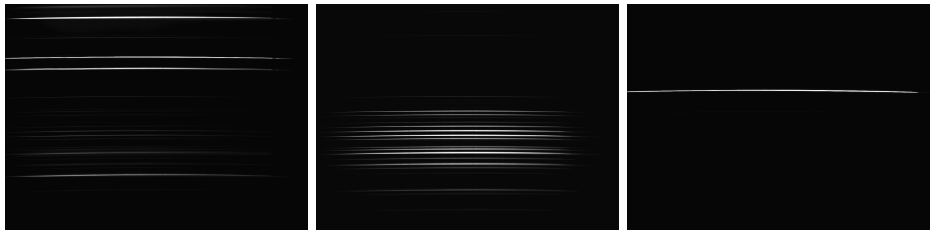

(a) Hg Tube Spectrum (b) Ar Tube Spectrum (c) 635nm Laser Spectrum

Figure 4.5: Captures of spectral Tubes

- A set of several gas discharge lamps with emission lines covering the spectral range of the hyperspectral sensor.
- A light diffuser.

The procedure for determining the spectral range begins by arranging the setup showed in Fig. 4.4b. The idea here is to acquire images using different gas discharge lamps, for which the theoretical emitted spectrum is known (Fig. 4.6a), and then relate the y-axis pixel position in the image to the corresponding wavelength.

Then, a set of captures are obtained using each available gas discharge lamp, such as those showed in Fig. 4.5. After that, the smile and keystone correction is applied considering the 2-dimensional transformation that was previously estimated.

Subsequently, for each capture, a horizontal histogram is calculated by summing all the intensity values in every row of the image (Fig. 4.6c). At this point, the y-axis position of the peaks found in the horizontal histogram should fit the theoretical spectrum lines. For each capture, a first estimation is performed using the peaks of the horizontal histograms and the theoretical information. Later, using those preliminary correspondences between y-axis positions, y_i, and wavelengths, λ, a linear regression is fit to the data:

$$\lambda(y_f) = y_f \cdot p_1 + p_2 \tag{4.2}$$

Thus, the determination of p_1 and p_2 will delimit the spectral range of the hyperspectral sensor.

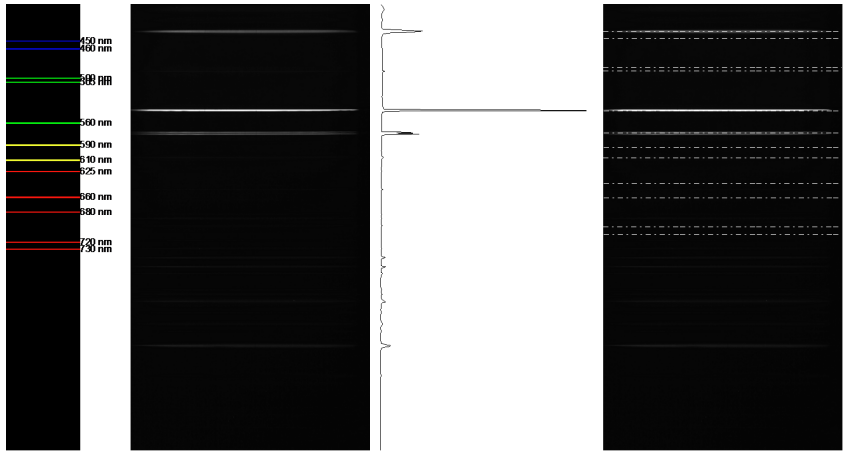

Figure 4.6: Spectral range determination: (a) theoretical spectral lines emitted by the gas-discharge lamp; (b) spectral response of the gas-discharge lamp captured using the hyperspectral sensor; (c) horizontal histogram; (d) superposition of theoretical and captured spectral lines once the range determination is performed

4.4.3 Destripping

Another important source of noise present in pushbroom imagers is due to physical deviations in some elements of the optical system and appears in the form of horizontal lines with different intensity values compared to the background of the hyperspectral scene (Fig. 4.7a). This effect, known as stripping, normally has to do with the fact that the narrow slit, which is in charge of selecting the light arriving from a strip of the surface, reveals non-uniformities in width along its length (Figs. 4.7b and 4.7c). The stripping effect is scene-based and highly dependent on the temperature, which makes it convenient to follow a correction procedure that adapts to different hyperspectral captures.

The destripping method proposed in this work proceeds on two main assumptions. The first one is that stripes may not be correlated band to band. The second one assumes that the stripping correction of all the pixels in every row should be performed by multiplying each pixel intensity value by an across-track and band-dependent factor. Thus, the destripping method consists

in estimating those across-track and band-dependent factors ($f_{k,b}$) that, once applied to each row of the data-cube, k, achieve the across-track homogenization of the hyperspectral scene.

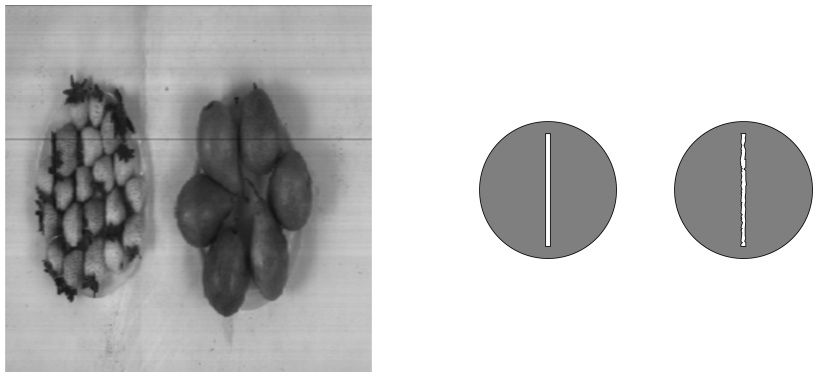

(a) (b) (c)

Figure 4.7: (a) 682 nm band of a real hyperspectral image showing the stripping effect; representation of a ideal slit (b) and a real slit (c)

Going into detail on the proposed method, it is applied row by row along the across-track direction, operates in two separated steps and requires the setting of two calibration parameters, M_a and N_a.

Letting k be the row that is being corrected, the first step seeks to select a set of N_a columns or segments that exhibit, on the one hand, high intensity values and, on the other, low variance following the across-track direction within a window of M_a rows in which row k is centered. This step enables the method to be insensitive to pixel-to-pixel high frequency variations due to surface contributions. Then, in order to perform segment selection, a 3D subdatacube of M_a rows, N columns and B spectral bands is extracted from the hyperspectral scene, where M_a is a calibration parameter, and N and B are the along-track size and the number of spectral bands of the image, respectively. From this 3D-datacube, and for each spatial column, the spectral band that presents higher intensity values is selected to construct a new 2D data-matrix (see Fig. 4.8a). After that, two vectors of size N are obtained by calculating the variance and mean of the 2D matrix along its first dimension. Considering the values of these two vectors, the selected segments will be the first N_a columns

that exhibit lower variance and higher mean intensity values. This procedure is schematized in Fig. 4.8b, Fig. 4.9a plots using red dots the segments selected for each row in the sample scene.

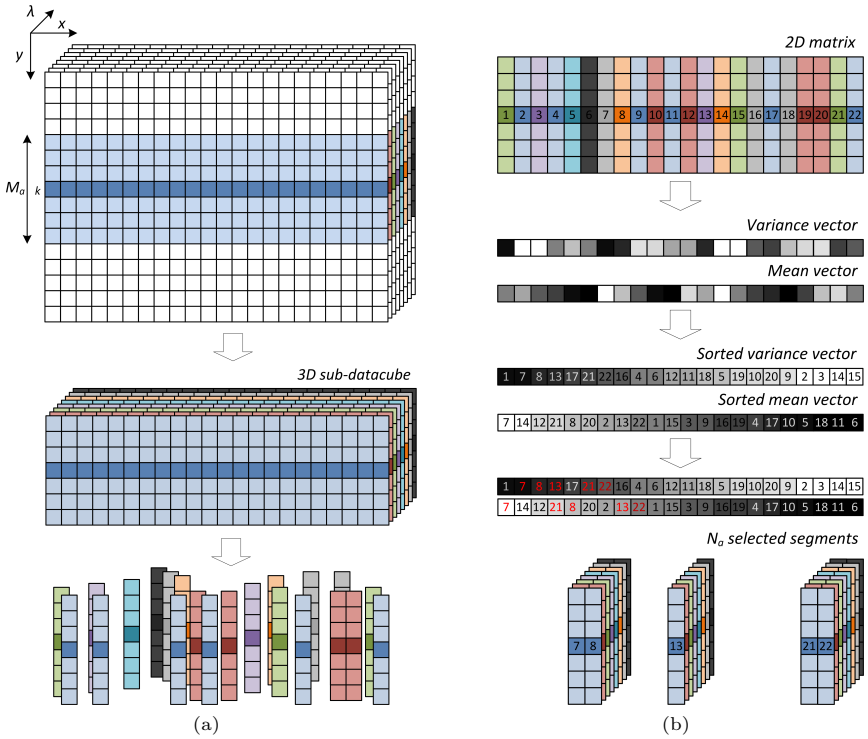

Figure 4.8: Segment selection procedure

The second step makes use of the segments selected in each row, k, to estimate the band-dependent destripping factors, $f_{k,b}$. With the purpose of easily describing the process, let's consider that we are correcting the row of the image shown in Fig. 4.9a as darker. For this row, we have previously selected 15 ($N_a = 15$) segments in a window of 23 pixels ($M_a = 23$). We pick one out of the N_a selected segments, denoted as segment j, and represent the spectral values for pixels contained in a window of size 23 centered in row k of the sample image. These values are represented in Fig. 4.10a, where a valley corresponding to the darkest strip in the image of Fig. 4.9a can be observed. Let us denote these values as $s_{k+i,j,b}$ with $i \in \{-\lfloor M_a/2 \rfloor, ..., \lfloor M_a/2 \rfloor\}$ and $b \in \{1, 2, ..., B\}$.

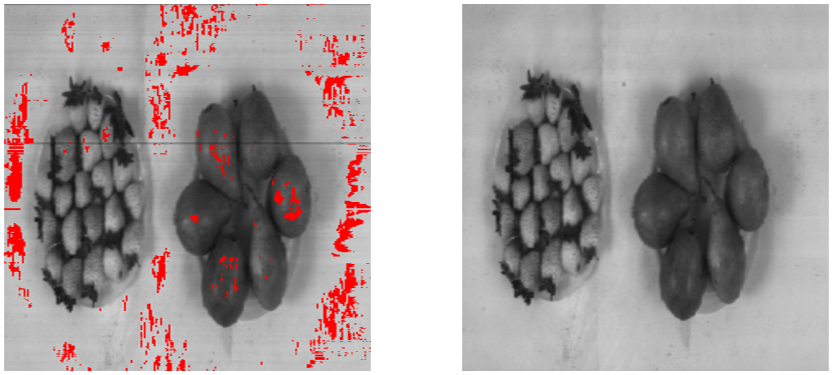

(a) (b)

Figure 4.9: (a) 682 nm band of a real hyperspectral image with the selected segments for each row marked in red; (b) 682 nm band once the hyperspectral image has been corrected

A median filtering is performed for each spectral band using the M_a values of the across-track neighborhood of $s_{k,j,b}$, obtaining then a set of filtered spectral values denoted as $s'_{k+i,j,b}$. The graphical result of this operation is shown in 4.10b. After that, the band-dependent correcting factors for row k and the selected segment j are obtained as:

$$f_{k,j,b} = \frac{s'_{k,j,b}}{s_{k,j,b}} \tag{4.3}$$

After repeating this process for all the selected segments $j \in \{1, 2, ..., N_a\}$, the final band-dependent correcting factors are obtained:

$$f_{k,b} = median(f_{k,1,b}, f_{k,2,b}, ..., f_{k,N_a,b}) \tag{4.4}$$

Finally, the destripping process consists in multiplying each element of the hyperspectral datacube $s_{i,j,b}$ by the corresponding correcting factor $f_{i,b}$. The result of the destripping correction over the sample image is shown in Fig. 4.9b.

The advantages of the proposed method can be summarized as:

- It is fully automatic.
- It is independent of image size.
- It avoids the blurring effect.

- It is insensitive to variations of image and noise statistics.

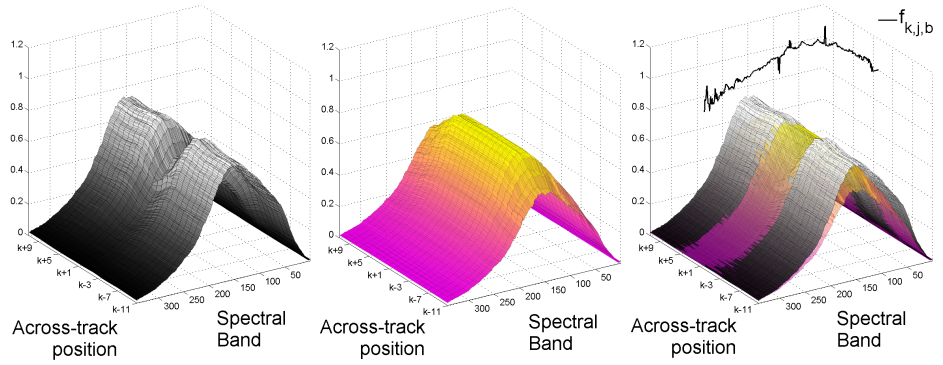

(a) (b) (c)

Figure 4.10: Original (a) and filtered (b) spectral values of a selected segment, j, in an across-track window of size 23 centered in row k of the sample image shown in Fig. 4.7a; (c) Superposition of graphs (a) and (b), including the value of the band-dependent correcting factors $f_{k,j,b}$

4.5 Acquisition Tools

With the aim of making the hyperspectral image acquisition automatic and straightforward for expert or non-expert users, two different tools have been implemented in this work. The first one is devoted to the acquisition itself, and the second one to facilitating the visualization of hyperspectral captures. The hyperspectral acquisition tool is programmed in C language and uses the windows interface (*WinApi*) to interact with the user, allowing setting and modifying several parameters in the acquisition process. Conversely, the hyperspectral visualization tool is programmed in *Matlab*, as are the processing algorithms designed and implemented in this PhD work. Both tools are described in the following subsections.

4.5.1 Hyperspectral Acquisition Tool

The software tool implemented for the acquisition of hyperspectral images consists of two panels: one to adjust the exposure time for each partial capture of the datacube, and one to configure and launch the acquisition. The exposure

time can be adjusted manually or automatically and the number of lines or partial captures for the acquisition, that is, the dimension of the hyperspectral capture in the along-track direction must be set up to a maximum of 450 lines.

Fig. 4.11 shows a capture of the hyperspectral acquisition tool.

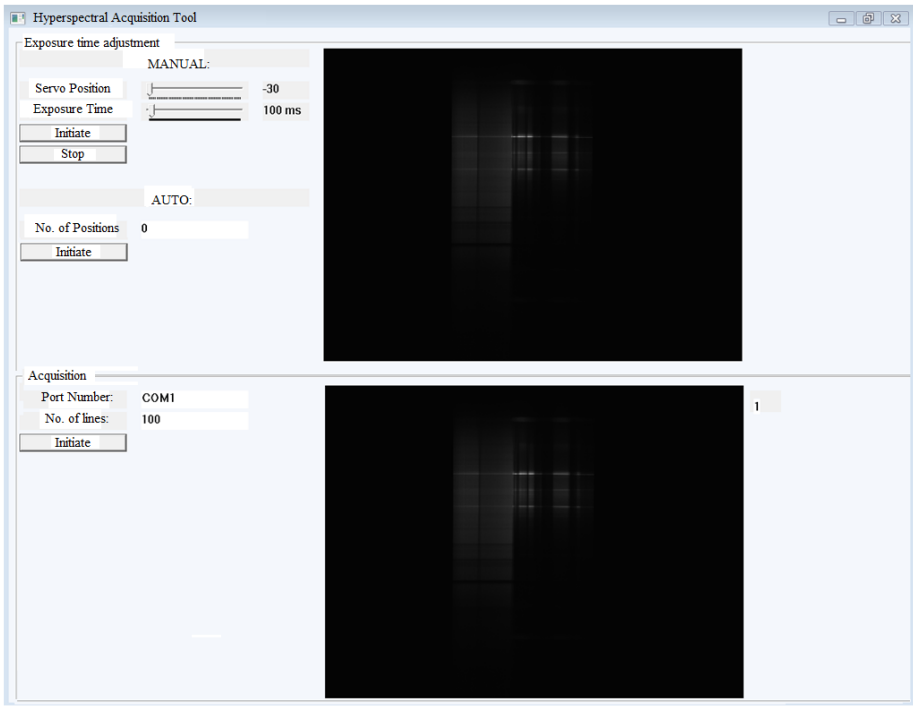

Figure 4.11: Capture of the acquisition tool interface

4.5.2 Visualization Tool

To provide a practical tool for the visual inspection of hyperspectral scenes, a visualization software tool has been implemented in Matlab. This tool enables the user to visualize the datacube projected on the $x-y$ and on the $y-\lambda$ planes, using a slider in order to modify the spectral band and the x value respectively. Additionally, the user can select a rectangle-shaped region of interest in order to inspect the spectra of the pixels located inside of it.

Fig. 4.12 shows a capture of the hyperspectral visualization tool.

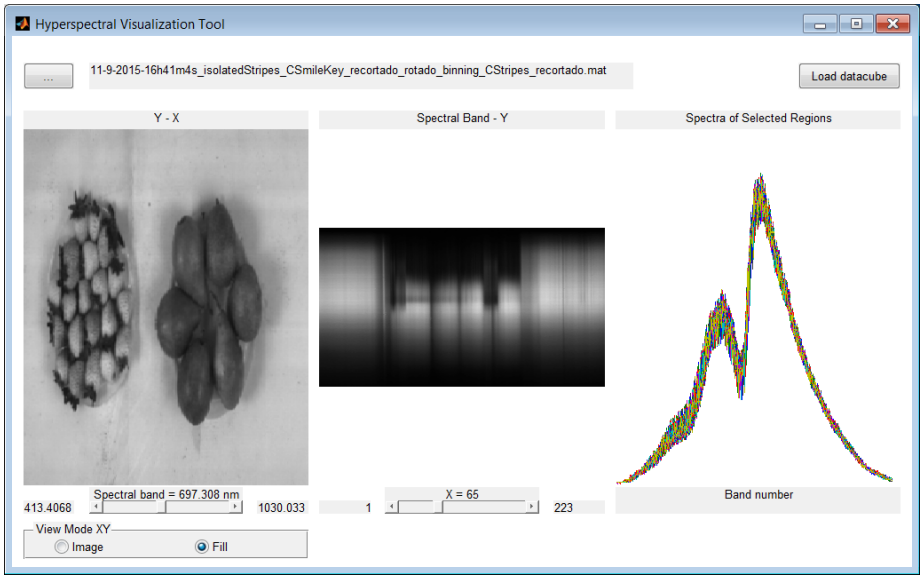

Figure 4.12: Capture of the visualization tool interface

4.6 Summary

This chapter has presented the actions carried out to make two prototypes of pushbroom hyperspectral imagers operational.

Firstly, the PHI V.1 hyperspectral camera has been equipped with an electro-mechanical module that enables the spatial scanning required to acquire a whole hyperspectral datacube. Along with this module, an appropriate control software and an acquisition tool have been implemented in order to make the acquisition process accessible to any type of user.

Secondly, a simple and affordable procedure has been proposed to characterize and calibrate the hyperspectral camera, as well as to correct the distortions associated with the optical elements of the imagers. The smile and keystone effect must be corrected once a spatio-spectral transformation has been estimated following the procedure presented in this work. This estimation should be performed periodically, and thus the suitability of the method due to its simplicity and repeatability. The proposed method for determining the spectral range of the sensors should be carried out after correcting the smile and keystone effect,

and again it is recommended to repeat this procedure from time to time. On the other hand, the correction of the stripping effect has been addressed following an automatic, simple and scene-independent approach.

Finally, a visualization tool has been provided to quickly and easily inspect the acquired hyperspectral images.

Chapter 5

Hyperspectral Image Repository

5.1 Introduction

In section 3.2.2 of the background chapter, a compendium of hyperspectral image databases found on-line was presented. That compilation revealed that, despite de fact that there are hundreds of hyperspectral images available, only a few of them have an associated ground truth.

This lack of publicly available repositories of labeled hyperspectral images leads to mainly three issues. The first one concerns the tendency of the hyperspectral community to focus on solving only some types of processing problems. That is, depending on the availability of hyperspectral scenes, scientists focus their algorithms toward one or another processing task. Secondly, processing algorithms may be highly skewed or biased towards the particular spatio-spectral characteristics of those scenes that have repeatedly been used, which does not guarantee the efficiency of the algorithms on a wider range of hyperspectral images. Finally, the shortage of labeled hyperspectral images and the difficulty in acquiring them have restricted the application of hyperspectral technology to new fields.

In order to alleviate the aforementioned problems, at the beginning of this thesis we considered it necessary to work in the construction of a repository of hyperspectral images with the following characteristics:

- The hyperspectral images should reflect different types of situations, scenes or cases of use, with the view of boosting the applicability of hyperspectral technology to different fields.
- The hyperspectral images should be categorized on the basis of spectral and spatial properties or features. Providing a set of hyperspectral images covering a wide range of spectral and spatial features would increment the reliability in the assessment of segmentation and classification algorithms.
- Real hyperspectral images should be properly labeled for segmentation and classification assessment purposes, which entails the acquisition of real images under controlled conditions and performing a careful labeling process.
- In order to provide an instrument to facilitate the training, adjustment, validation or testing of algorithms, synthetic hyperspectral images with particular characteristics should also be made available, or, more interestingly, a procedure for constructing synthetic hyperspectral images with greater or lesser complexity and particular spatial and spectral features depending on the user requirements should be provided.

Part of the work carried out in this thesis and summarized in this chapter has the main goal of creating a hyperspectral repository that fulfills these aspects. In order to manage the variety of hyperspectral scenes in the repository, firstly, it is necessary to establish a procedure that allows for the discrimination or categorization of hyperspectral scenes. This categorization should be based on both spectral and spatial properties of the real hyperspectral images since these lead to one type of segmentation or another. It would be also necessary to design a procedure for the construction of synthetic hyperspectral images that complies with the categorization system proposed for real hyperspectral images. Moreover, the creation of synthetic images should be easily controlled by any user that requires particular datasets for training and validating processing algorithms. Finally, both synthetic and real hyperspectral images should be

accurately labelled in order to ensure an effective assessment of segmentation or classification algorithms. All of this has been accomplished by using the following methodological approach:

1. A new method that takes into account both spatial and spectral characteristics of multidimensional images has been established to categorize hyperspectral images. As will be seen in section 5.2, this categorization basically consists in the parametrization of hyperspectral images using a reduced set of spatio-spectral descriptors.

2. An algorithm has been designed and implemented to create synthetic multidimensional images based on those spatio-spectral parametric descriptors. The idea is that the automatic creation of synthetic images reflecting particular characteristics simplifies and facilitates the adjustment and testing of processing algorithms.

3. Datasets of real hyperspectral images have been acquired using the two prototypes of hyperspectral pushbroom imagers built and calibrated at the Integrated Group for the Engineering Research of the University of a Coruña (GII).

4. All the real and synthetic hyperspectral images contained in the image repository, in addition to having been labeled for segmentation or classification purposes, have been described using the mentioned parametric categorization. The idea behind this initiative was to build a public expanding repository of hyperspectral scenes that combines a range of well categorized hyperspectral images of different nature and characteristics.

In order to illustrate how an image processing algorithm designer may take advantage of this hyperspectral image repository, let us consider a particular case of use. The designer needs to implement and test a system able to segment mature strawberries located in boxes mixed with fresh and mature fruits. The designer acquires a few hyperspectral images of this real scene and characterizes the problem following the parametric categorization presented in section 5.2 of this chapter. Then, the designer has two options for the selection of a training or testing image dataset: to pick similar hyperspectral images from the image repository or to create a set of synthetic hyperspectral images that reflect a

similar parametric categorization. In either case, the designer can proceed to adjusting or validating the segmentation algorithm using the selected datasets or as many automatically created images as are required.

In this work, several software utilities have also been implemented for the purpose of assisting a user in creating synthetic images by selecting the desired parametric categorization; categorizing real hyperspectral images based on parametric descriptors; and aiding in the manual labeling of real hyperspectral images.

5.2 Parametric Categorization of Hyperspectral Images

Within the framework of this work, the categorization of hyperspectral images has been conceived from the point of view of segmentation and classification tasks. The main goal of this categorization is to be able to describe multidimensional images in a parametric fashion on the basis of spatial and spectral characteristics that are relevant for segmentation or classification tasks.

With this objective in mind, a first descriptive analysis made us wonder which properties would lead a user to manually distinguish between segments or classes in an image. From our perspective, the distinction between classes is mainly based on the following aspects:

- Spectral relationship between pixels that belong to the same class, especially, between neighboring pixels.
- Spectral relationship between pixels that are associated to different regions.
- Geometry of the boundaries between regions (for example, rounded or rectilinear edges).

From this first rough description of spectral and spatial properties, we decided to follow a constructive procedure for the generation of multidimensional images that allowed us to reflect and tune the mentioned spatio-spectral aspects. That is, a new algorithm for the creation of multidimensional images has been designed based on six parameters: two related to spectral properties and four

related to geometrical characteristics of the boundaries between regions. Table 5.1 presents a brief description of each parametric descriptor that has been considered. Thus, the particular values of these parameters will be responsible for, on the one hand, conducting the synthetic images construction process and, on the other, providing a description or categorization of any multidimensional image.

Table 5.1: Description of the initial set of spatial and spectral parametric descriptors for the categorization of hyperspectral images

Name	Spectral Descriptor	Spatial Descriptor	Description
r_{max}	■		Averaged spectral distance between neighboring pixels belonging to the same region (averaged intra-class spectral distances)
$[s_{min} s_{max}]$	■		Minimum and maximum spectral distances among the averaged spectra of adjacent regions (inter-class spectral distances)
N		■	Number of different regions in the image
D_{max}		■	Related to the ruggedness of the borders that delimit different classes
eD		■	Related to the dispersion in size of regions in the image
Pr		■	Related to the dispersion in size of regions in the image

The first parametric descriptor is denoted by r_{max} and tries to reflect the spectral relationship between pixels that belong to the same class. In practice, r_{max} measures the averaged spectral distance between neighboring pixels (in a 3×3 spatial window) belonging to the same region. Thus, larger values of r_{max} would reflect more spectrally heterogeneous regions in hyperspectral images.

The spectral relationship between pixels that are associated to different regions is characterized by the $[s_{min}, s_{max}]$ interval. s_{min} and s_{max} denote the minimum and maximum spectral distances among the averaged spectra of adjacent regions, respectively. These parameters give information about the spectral proximity between pixels belonging to different regions.

Concerning the geometrical characteristics of multidimensional images, the N parameter directly indicates the number of different regions in the scene. The shape (more or less rounded edges) of the borders between regions is regulated by the D_{max} parameter, which indicates de maximum number of consecutive edge pixels that follows the same direction. On the other hand, the particular values of consecutive edge pixels that follow the same direction for each boundary trace in a image is regulated by a probability function parametrized using the eD and Pr descriptors. The variation of eD and Pr produces images with more or less dispersion in region size.

As the hyperspectral image parametric descriptors are intrinsically related to the creation procedure of multi-dimensional images, in the following section devoted to presenting the method for obtaining synthetic images, the meaning and role of each parameter will be described in detail and illustrated with several examples. Furthermore, section 5.4 will outline the procedure for estimating these parametric descriptors from real hyperspectral images.

5.3 Creation of Synthetic Hyperspectral Images

As mentioned in the introduction section, there was clearly a need for a source of hyperspectral images that facilitated the design, adjustment and validation of algorithms. Hence the decision to develop a procedure to create multi-dimensional images with specific spatial and spectral characteristics.

The method established for the creation of synthetic images is based on the six spatial and spectral parameters with 'descriptive meaning' of the previous section, which, in addition to providing parametric information for the construction process, themselves bring a categorization of the multidimensional image.

Before going into the detail of the creation process, let us introduce some advantages of the proposed method for creating synthetic multidimensional images:

- Once the six parametric descriptors have been fixed, the creation procedure is fully automatic, which allows obtaining synthetic datasets instantly.

- The complexity of the ground truth of the images can be regulated in a simple manner by just fixing the value of four parametric descriptors (N, D_{max}, Pr and eD).
- Based on two parametric descriptors ($[s_{min}, s_{max}]$ and r_{max}), the spectral relationship between pixels can be easily adjusted.
- Although the creation procedure has been designed for segmentation and classification purposes, slight variations can be introduced in order to adapt the created image datasets to other processing tasks, as will be shown in subsection 5.3.2.

Broadly speaking, the image creation procedure can be divided into three steps (Fig. 5.1). Firstly, a preliminary ground truth map is created. In this step, four parameters are involved: N, D_{max}, Pr and eD. Then, a global spectrum is assigned to each previously labeled region. The second step requires the determination of a range $[s_{min}, s_{max}]$, which is considered as a parameter. Finally, spectral variations are introduced to pixels belonging to the same region. In this step, the intensity of the spectral variations will be regulated by the r_{max} parameter.

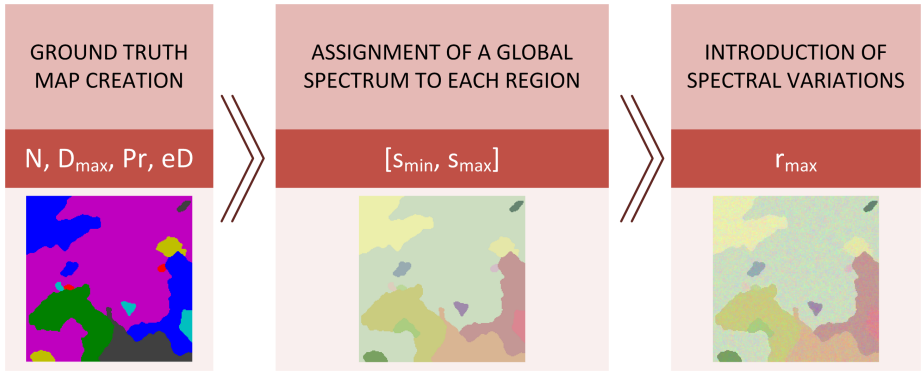

Figure 5.1: Steps involved in the creation of synthetic hyperspectral images

The following subsection presents a detailed description of each of the steps, showing the meaning of the spatial and spectral parameters and their influence over the appearance of the created synthetic image. A tool developed to assist a user to create synthetic images based on the selection of particular sets of parametric descriptors will also be presented. Subsection 5.3.2 outlines how

to derive benefit from the image creation procedure by adapting it to provide training or testing datasets for several types of processing tasks, such as change detection, denoising or temporal classification.

5.3.1 Creation process and parametrization

The construction of a synthetic image starts from the creation of the **ground truth map**. This process has been carried out by applying a snake-based tracing algorithm, in which the N, D_{max}, Pr and eD parameters are involved. The creation of the ground truth map follows this sequence:

1. A binary image, I, of all zeros is created. Then, a random seed (x_0, y_0) is selected and the value of $I(x_0, y_0)$ is set to one. A spatial direction is selected out of North, South, East, West, Northwest, Northeast, Southwest and Southeast. If, for instance, Northwest is selected, $I(x_0 + 1, y_0 - 1) = I(x_1, y_1)$ is set to one. The (x_0, y_0) and (x_1, y_1) coordinates are stored.

2. A new spatial direction is randomly selected out of three possible values depending on the last randomized spatial direction (see Fig. 5.2). The coordinates corresponding to the new spatial direction, (x_2, y_2), are stored and the value of $I(x_2, y_2)$ is updated, $I(x_2, y_2) = 1$. This procedure is repeated until the value of $I(x_i, y_i)$ equals 1 or (x_i, y_i) is out of the boundaries of the image.

3. From (x_0, y_0), the opposite direction to (x_1, y_1) is selected (Southeast in the example), and the corresponding value of the image is updated, $I(x_0 - 1, y_0 + 1) = I(x'_1, y'_1) = 1$. Again, the same procedure is repeated until $I(x'_i, y'_i)$ is equal to 1 or (x'_i, y'_i) are out of the boundaries of the image.

4. Once the previous step is executed, image I will be a trace of one-valued pixels. Using image I at this point, a label image of connected components denoted as L is created.

5. If the number of connected components is lower than the parameter N, a new spatial seed is randomly selected and a new line of one-valued pixels is traced on I. If not, the ground truth will be the labeled image L. Then, N will indicate the number of distinct regions in the image.

With the objective of obtaining borders delimiting different classes with more or less ruggedness, a variation in the second and third steps is introduced. To achieve more regular borders, instead of randomly selecting a new direction out of the three allowed ones, the algorithm can force the preservation of the last one selected. The last direction is kept for K steps following eq. 5.1:

$$\begin{aligned} & l = rand() \\ & p = rand() \\ K = & \begin{cases} D_{max} & \text{if } l < Pr \\ D_{max} \cdot p^{eD} & \text{otherwise} \end{cases} \end{aligned} \tag{5.1}$$

where D_{max} will determine the maximum number of steps in which the same direction is maintained for the selection of a new pair of coordinates, (x_i, y_i); Pr modifies the frequency with which K is equal or not to D_{max}; and eD determines the probability function in the calculation of K when $Pr = 0$.

Fig. 5.3 shows captures of the creation process of an example ground truth and a QR link to visualize an animation of the process in GIF format.

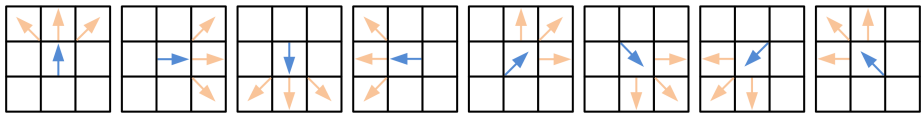

Figure 5.2: Allowed directions depending on the last selected one

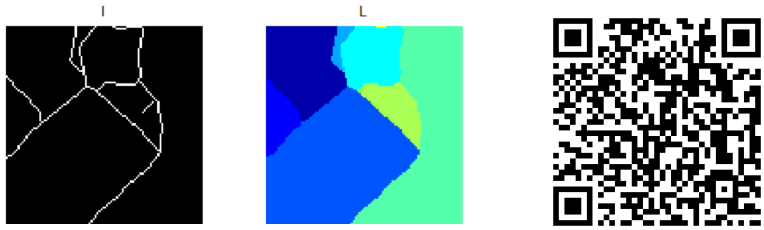

(a) (b)

Figure 5.3: (a) I and L images in the creation process of the ground truth, (b) QR link to visualize the creation process in GIF format

Summarizing, the N parameter indicates the number of different regions in the synthetic image and D_{max}, Pr and eD are related to the ruggedness of the borders that delimit different classes. The larger the value of D_{max}, the more rectilinear the boundaries between regions. On the other hand, the larger the value of Pr and eD, the more irregular the size of the regions in the image.

Figure 5.4: Multi-dimensional image with a spectral vector assigned to each region (left), multi-dimensional image with spectral variations (center), histograms of the neighboring spectral distances between pixels belonging to each different region (right)

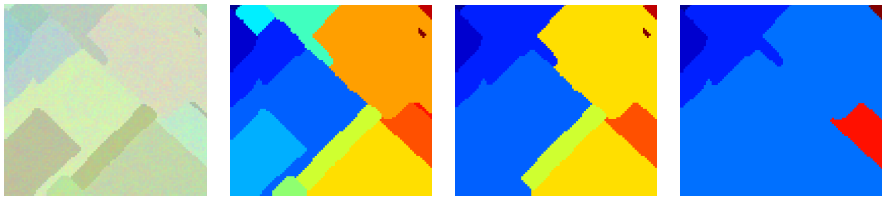

(a) (b) (c) (d)

Figure 5.5: Synthetic image created for testing or tuning segmentation and classification methods. (a) Multi-dimensional image, (b) ground truth #1, (c) ground truth #2, (d) ground truth #3

Despite the fact that these were the six parameters originally conceived, in order to reduce the number the geometric descriptors in the parametric characterization, Pr and eD were fixed to 0.5 and 1 respectively. This decision was based on a study of the influence of the variation of the parametric descriptors in relation with segmentation tasks. The results of that analysis (presented in chapter 6) revealed the negligible influence of these parameters over the segmentation and classification results of multidimensional images.

Continuing with the second step, the **global spectrum assignment** consists in associating the same spectral vector to all pixels belonging to the same region. The spectral vectors are assigned with the restriction of the normalized

spectral angle among the averaged spectra of adjacent regions having to be in the range from s_{min} to s_{max}. The normalized spectral angle (SA) between two spectral vectors, s_i and s_j, is defined as:

$$\alpha_{i,j} = \frac{2}{\pi} cos^{-1}\left(\frac{\sum s_i s_j}{\sqrt{\sum s_i^2}\sqrt{\sum s_j^2}}\right) \tag{5.2}$$

Thus, $[s_{min}, s_{max}]$ will adjust the averaged spectral similarity or discordance between pixels belonging to different and adjacent regions.

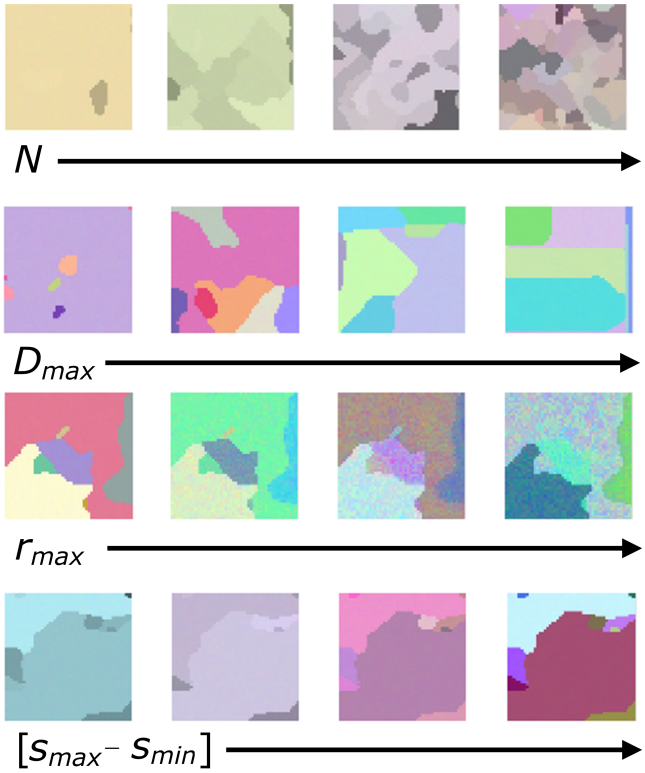

Figure 5.6: Synthetic multi-dimensional images. The influence of N, D_{max}, r_{max} and $[s_{min}, s_{max}]$ over the geometric and spectral aspects of the images can be appreciated

Finally, **spectral variations** are introduced to all pixels in the third step. The idea is to add spectral "noise" in such a way that the angular distances between neighboring pixels contained in a 3×3 spatial window follow a particular probability function. This parameter r_{max} represents the most frequent spectral

angle of the probability function under consideration. The picture on the left of Fig. 5.4 shows a multi-dimensional image once a different spectral vector has been assigned to each region when $s_{min} = 0.05$ and $s_{max} = 0.1$. The image in the center represents the multi-dimensional image after applying spectral variations when $r_{max} = 0.08$ and a Rayleigh distribution is considered. The histograms of the neighboring spectral distances between pixels belonging to each different region are plotted on the right graph of Fig. 5.4.

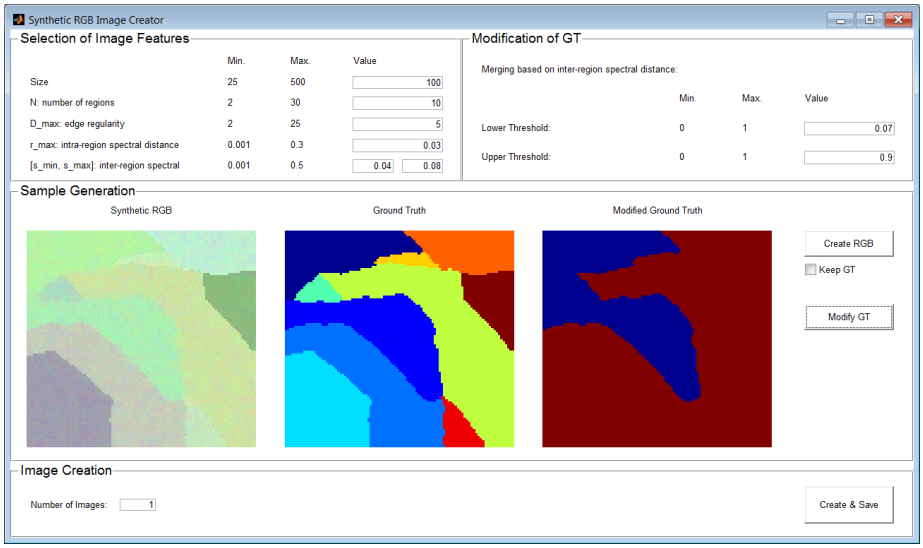

Figure 5.7: Capture of the interface of the RGB image Creator

Following this procedure, it is possible to construct synthetic images with parametrized geometric and spectral features. In order to illustrate the influence of the parameters, Fig. 5.6 shows synthetic multi-dimensional images created with different values of N, D_{max}, r_{max} and $[s_{min}, s_{max}]$, so that their effect over their geometric and spectral aspects can be observed.

With a view to provide a software utility to obtain RGB images created on the basis of this procedure, a tool has been created and distributed publicly[1]. This tool allows a user to have an unlimited source of datasets to validate

[1]The tool for the creation of synthetic images is available through downloadable MATLAB code at http://gii.udc.es/gii_hyperspectral_repository

or adjust segmentation and classification algorithms. Particularly, in this PhD thesis, synthetic RGB images (and their associated ground truths) created using this tool have been used as training datasets in an evolutionary algorithm.

In Fig. 5.7, a capture of the interface of the RGB image creator tool is shown. The user can select the size of the synthetic image, play around with the N, D_{max}, r_{max} and $[s_{min}, s_{max}]$ parameters and create variations of the ground truth map. The tool allows creating and saving in disk as many images as desired.

5.3.2 Target Processing Tasks

On the basis of the algorithm presented above for the generation of synthetic images and their ground truth maps, slight modifications can be introduced to exploit the method adapting it for the creation of datasets focused on different types of processing tasks. Let us describe this in greater detail task by task:

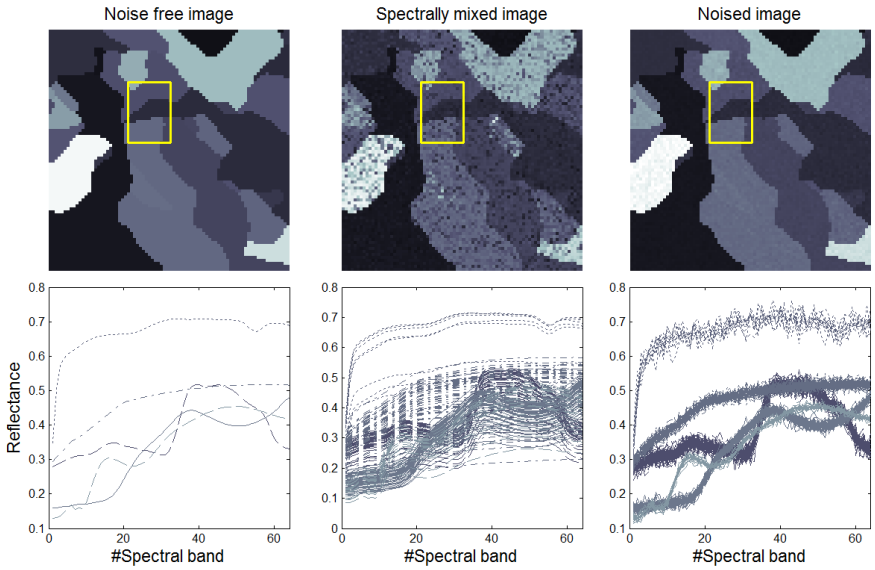

Figure 5.8: Synthetic image created for testing or tuning denoising methods. 17^{th} band of a noise-free, spectrally mixed and noised images are shown at the top. At the bottom, spectra of the yellow colored detailed area are plotted

- Segmentation and classification
  The procedure to follow is essentially the same as the one presented above. However, for certain applications, it could be interesting to rectify the ground truth map once the pair of multi-dimensional and ground truth images has been created. That would provide for the possibility, for instance, of tuning segmentation or classification methods in order to produce under/over-segmented results. Fig. 5.5 shows examples of different ground truth maps associated to the same multi-dimensional image. In this case, adjacent regions have been merged when the spectral angles between their averaged spectra are lower than a threshold value.

- Denoising
  In order to evaluate this task, it is necessary to have a noise-free version of a noisy image. This noise-free image could be considered as the multi-spectral image that is obtained after the *global spectrum assignment* step explained in the previous subsection. On the other hand, different types of noise models can be applied when the noise-free image version is being corrupted. Fig. 5.8 shows synthetic hyperspectral images created for testing or adjusting parameters of denoising methods considering two different types of noise.

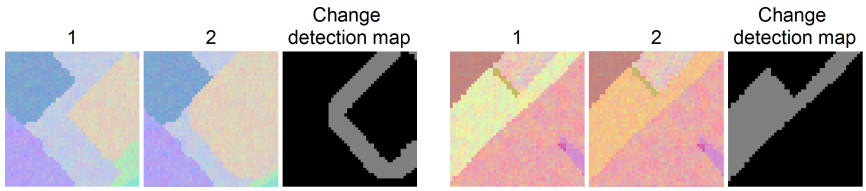

(a) (b)

Figure 5.9: Synthetic image created for testing or tuning change detection methods: (a) spatial change, (b) spectral change

- Change detection
  The change detection task consists in identifying pixels of two co-registered images that have experienced a temporal change in their spectra. Three different cases have been considered in this work: changes due to the spatial expansion or reduction of regions in the ground truth; changes due to spectral changes of pixels belonging to a region in the ground truth; and a combination of them. Fig. 5.9 shows examples of the first two cases.

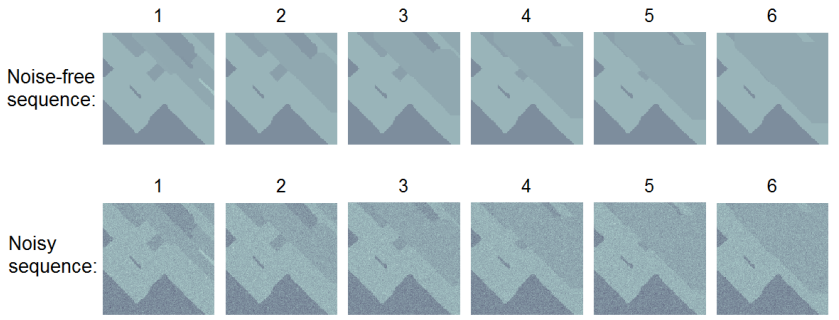

Figure 5.10: Noise-free and noisy synthetic image sequences created for testing or tuning temporal-denoising methods

- Temporal denoising
  An important preprocessing task is to filter the noise out of hyperspectral image sequences. To construct synthetic sequences of multi-dimensional noise-free and noisy images, firstly, a ground truth sequence is created in which some regions suffer a growth or decrease in size. Then, global spectrum vectors are assigned to each area, obtaining the noise-free image sequence. Afterwards, the noise-free sequence is corrupted using the selected noise model. Fig. 5.10 shows an example of noise-free and noisy sequences.

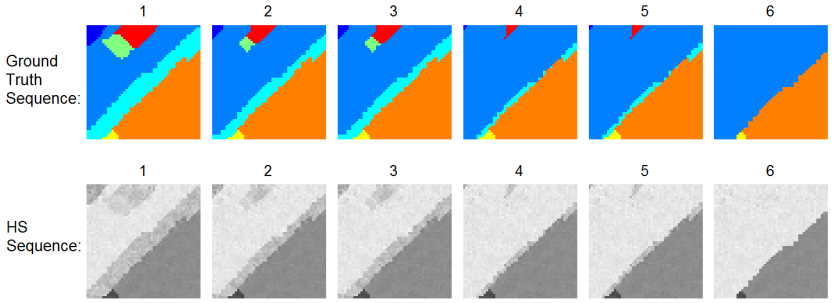

Figure 5.11: Synthetic image and ground truth image sequences created for testing or tuning multi-temporal segmentation/classification methods

- Temporal segmentation/classification
  Finally, sequences of multi-dimensional images in which some regions evolve in size or spectrum can be constructed. Again, it is possible to

adapt the ground truth map sequences depending on the requirements of the application. Fig. 5.11 shows both ground truth and hyperspectral images of a sequence composed of six frames.

5.4 Acquisition of Real Hyperspectral Images

It is a fact that the lack of publicly available repositories of real labeled hyperspectral images is a weak point for the generation of hyperspectral processing algorithms.

Part of the work carried out in this thesis seeks to provide a set of real cases in which hyperspectral images are associated to reliable ground truth maps, involving the controlled acquisition and a posterior precise labeling procedure. Furthermore, the idea is to have sets of diverse hyperspectral images, that is, the parametric categorization of the provided hyperspectral images should cover the space of parametric descriptors as fully as possible.

This section is devoted to presenting all the steps taken for real captures, from the acquisition of hyperspectral images using our own hyperspectral imagers to their publication on the hyperspectral image repository. These steps are summarized in figure 5.12 and enumerated in the following paragraphs.

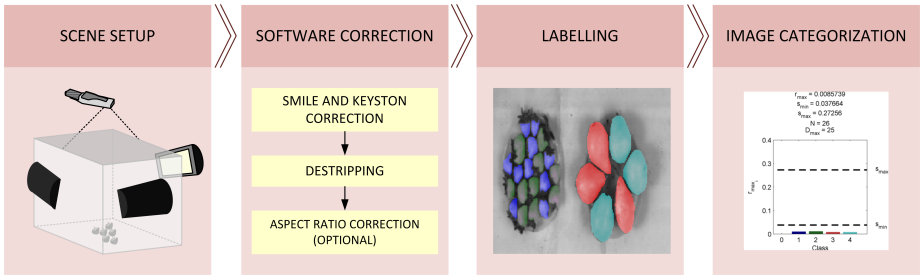

Figure 5.12: Steps in the process of preparing hyperspectral images for their inclusion in the image repository

1. **Scene Setup**
   One of the requirements that we imposed for the acquisition of real hyperspectral images was to carry it out in a controlled and supervised setting. In this regards, temporal variations of both the scene and the imager, such

as vibrations or instabilities, were minimized while maintaining the illumination source stable. Ensuring temporal and illumination stability would facilitate the software correction, characterization and labeling processes.

That was the reason we decided to acquire hyperspectral images indoors with the following setting (Fig. 5.13):

- The hyperspectral imager is located in a zenithal position with respect to the captured objects.
- The objects to be acquired are located inside a white box in order to unify and distribute light uniformly, reducing the shadow effect.
- Absence of direct natural light.
- Artificial light is used to illuminate de scene: we used commercial halogen lamps with very flat emission light spectrum within the range covered by the camera.

(a) (b)

Figure 5.13: Setup used for the acquisition of hyperspectral images indoors

The particular parameters involved in the acquisition process are summarized Table 5.2.

Table 5.2: Parameters involved in the acquisition process

Name	Value
Distance from imager to ground	1.32 m
Number of lines (along-track)	450
Sensor Resolution (along-track)	1392 pixels
Angle of view (along-track)	45°
Angle of view (across-track)	28.6°
Number of bands	342
Spectral Range	[413, 1030] nm
Pixel depth	8 bits

Using this setup, we have considered three different scenarios:

- Isolated objects over a light background. This scenario covers different types o fruits and vegetables with a grater or lesser degree of ripeness; food products with different hydration level; same type of food products but from different brands, such as potato chips, etc. In all cases, the ground truth consists in unlabeled background and labeled regions corresponding to different objects that appear in the scene. In such a scenario, the value of the parametric descriptor r_{max} is usually low due to the smooth texture of the objects that appear in this kind of captures. The values for the $[s_{min}, s_{max}]$ range can be easily adjusted by including objects with more or less similar averaged spectra. Finally, in order to increase or decrease the value of N, elements in the scene, such as pieces of fruit, would only have to be added or removed. Examples of this type of scenario are shown in images 1-4 of Fig. 5.14.
- Adjacent regions without a non-labeled ground truth. Each region is composed of a raw material or a mixture of different materials, creating this way regions with diverse spatial textures as shown in images 5-10 and 13-14 of Fig. 5.14. The parametric descriptors can be easily modified by including materials with rough or fine texture, varying this way the value of r_{max}. On the other hand, s_{min} could be minimized by mixing materials and s_{max} maximized including spectrally distant materials. N can be adjusted by incrementing the number of different regions in the scene and D_{max} will depend on the linearity of boundaries between regions, which can also be arranged when setting up the scene. The inclusion of spatial information in the segmentation process becomes relevant in the processing of this kind of images.
- Objects half-buried under materials of great heterogeneity and profuse texture (images 11-12 of Fig. 5.14). Also in this case, the spatial information becomes highly significant in the segmentation or classification of hyperspectral images acquired following this type of scenario. Since the overlying material may invade regions corresponding to the half-buried materials, the value of r_{max} will be typically high. The value of the $[s_{min}, s_{max}]$ range would depend on the selected objects as in the previous cases and the N value can be modified by

A comprehensive approach for the efficient acquisition and processing of hyperspectral images and sequences

Método integral para la adquisición y procesamiento eficiente de imágenes y secuencias hiperespectrales

Author/Autora: Blanca María Priego Torres

Doctoral Thesis / Tesis Doctoral / 2016

Advisor/Director:

Richard J. Duro Fernández

Programa Oficial de Doctorado en Computación[1]

[1]Programa regulado por el R.D. 1393/2007

incrementing or reducing the number of half-buried objects in the scene. However, the value of D_{max} would not be so easily controllable.

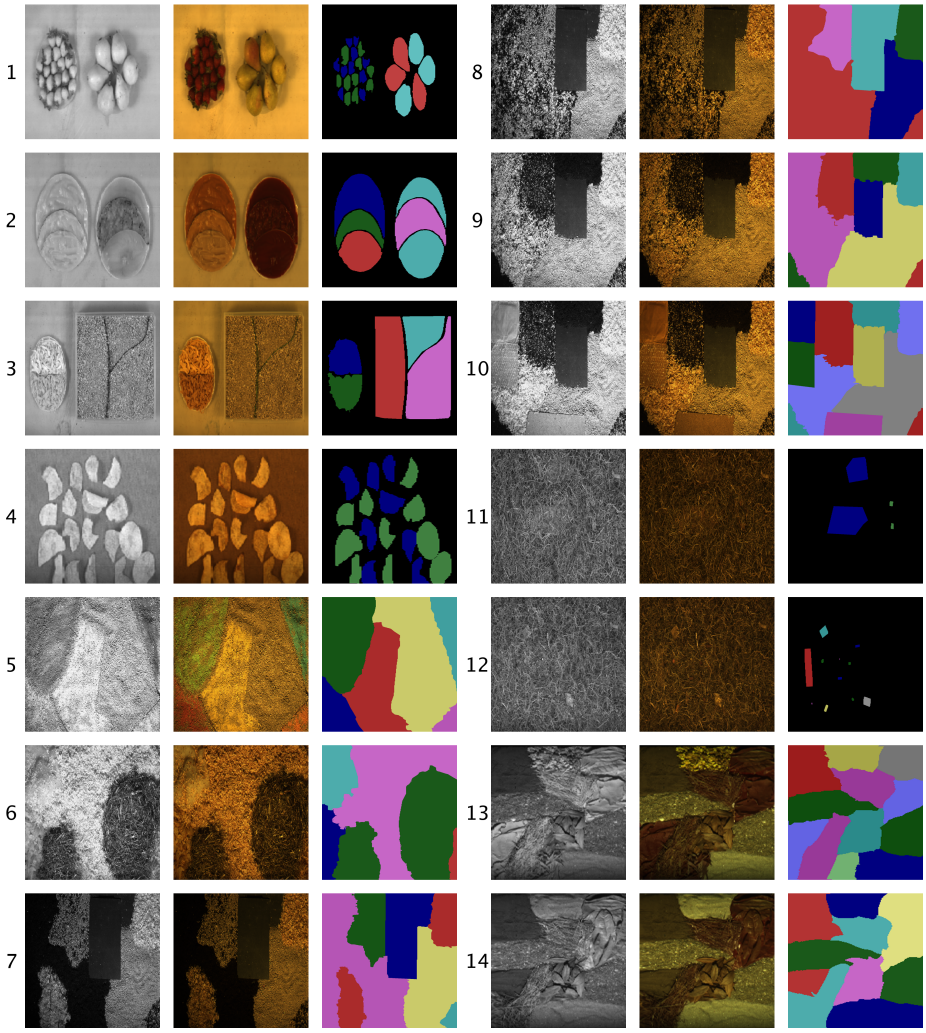

Figure 5.14: Some real scenes selected from the hyperspectral repository: the band of highest intensity, a RGB composite image and the ground truth are represented

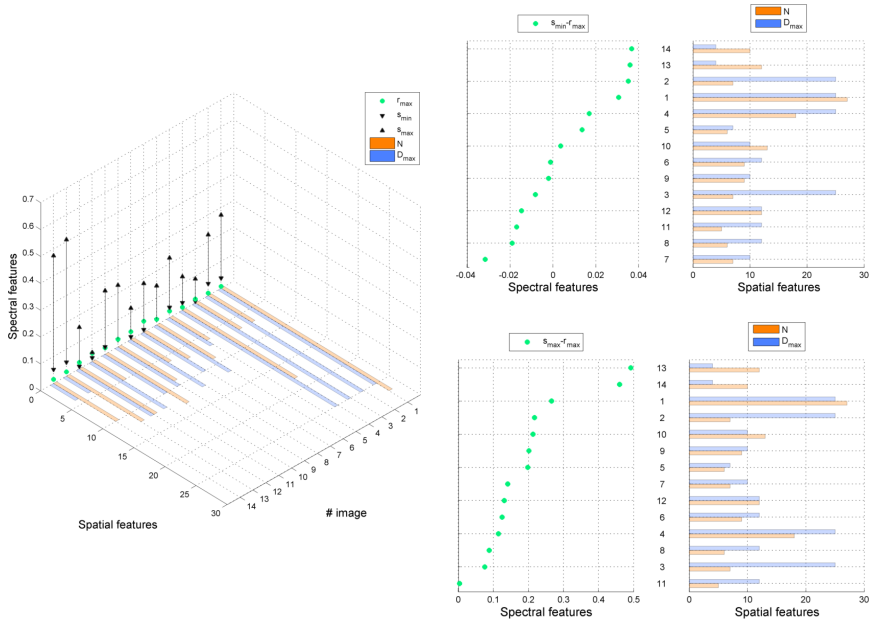

Figure 5.15: Spatio-spectral features of the hyperspectral scenes shown in Fig. 5.14

By following the guidelines of each scenario, we have acquired a set of hyperspectral scenes with a wide range of spatio-spectral parameter values. As it will be shown in section 6.6 of chapter 6, the parameters related to spectral features of hyperspectral images are more relevant in the case of segmentation and classification methods. Furthermore, the relationship between the $[s_{min}, s_{max}]$ and r_{max} parameters is highly significant for the difficulty of segmentation and classification tasks. Hence a considerable effort has been devoted to acquiring hyperspectral scenes that fully sweep the space of the $[s_{min}, s_{max}]$ and r_{max} parameters. Fig. 5.14 shows some real scenes included in the hyperspectral repository and Fig. 5.15 presents several representations of their estimated parametric descriptors.

2. **Software Correction**

   Once an image datacube has been acquired using the hyperspectral camera, some software corrections have been applied.

The first one deals with spatial and spectral PSF uniformities. Based on a previous calibration of the imager and following the procedure described in subsection 4.4.1 of chapter 4, smile and keystone effects were corrected by processing each spatio-spectral slice of the datacube following the along-track direction.

The next correction measure tries to remove the stripping effect. To suppress this scene-based effect the procedure described in subsection 4.4.3 of chapter 4 was applied to the hyperspectral image.

Then, if required, the spatial aspect ratio of the hyperspectral image was modified, so that the relationship between the two spatial dimensions corresponds to reality.

Summarizing, the corrected distortions were:

- Spatial and spectral PSF uniformities (smile and keystone).
- Spatio-spectral discontinuities (bad lines and stripping)
- Spatial aspect ratio correction.

On the other hand, the following aspects have been disregarded:

- Vignetting, because of the absence of instrumentation to allow the calibration and correction of this effect.
- Conversion from radiance to reflectance values, which has not been considered necessary.

3. **Labeling**
   The ground truth of the captured scenes was manually created. To aid in the manual labeling of hyperspectral images in a simple way, a software tool has been implemented. The objective is to support the user to conveniently, quickly and simply generate ground truth maps. The labeling process is polygon-based, so that vertex can be added and removed easily. Each region has an associated segmentation and classification label. Segmentation labels are all different from each other, whilst classification labels can be repeated from region to region.

4. **Image Categorization**
   In order to categorize hyperspectral images using the parametric descriptors presented in section 5.3, a procedure for estimating these spatio-spectral parameters has been adopted.

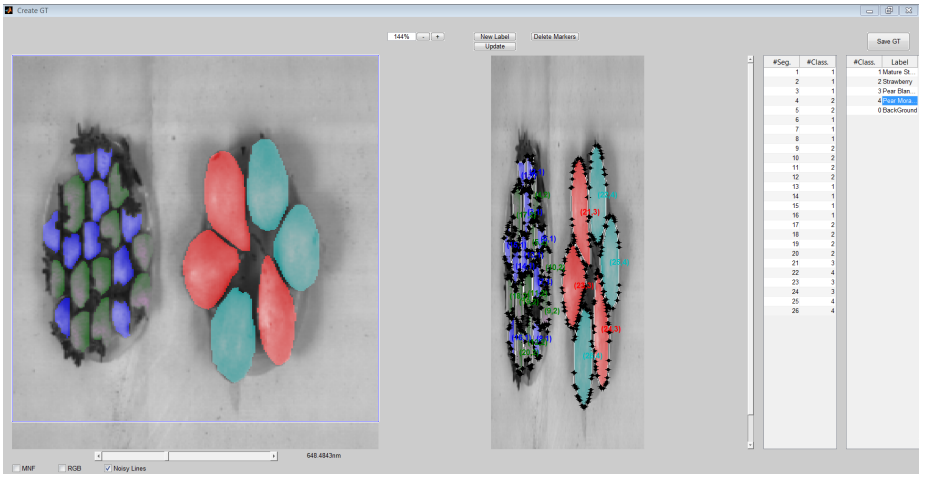

Figure 5.16: Capture of the interface of the Image Feature Estimation Tool

Firstly, an automatic selection of spectrally independent areas has been performed. A growing region algorithm is applied in order to establish several areas with uniform spectral characteristics. This growing algorithm starts with a randomly selected small seed area. Then, the spectral distances between all pixels (d_g) and only between neighboring pixels (d_n) within this area are obtained. After that, the 75^{th} percentile of d_g and d_n is calculated. The small seed area is allowed to grow if the $\frac{P_{75}(d_n)}{P_{75}(d_g)} < C_{th}$ condition is fulfilled, where $P_{75}(d_n)$ and $P_{75}(d_g)$ denotes the 75^{th} percentile of d_n and d_g respectively and C_{th} is a experimentally determined threshold value. Higher values of C_{th} will lead to more heterogeneous areas.

Once several regions have been identified, $[s_{min}, s_{max}]$ is obtained as the maximum and minimum spectral distance (spectral angle) between the averaged spectra between regions. On the other hand, r_{max} will be the weighted average of the most frequent spectral distance calculated from the spectral angles between neighboring pixels.

In order to estimate D_{max}, a first edge-detection step is applied to the hyperspectral image. The edge traces are analyzed and a histogram of the number of consecutive pixels that maintain the same direction is calculated. The obtained histogram is correlated with a database of predefined histograms with associated D_{max_k} values. The D_{max_k} value of the most

similar histogram from the database is selected for the D_{max} estimation. Finally, N is considered as a direct function of the percentage of edges in the image.

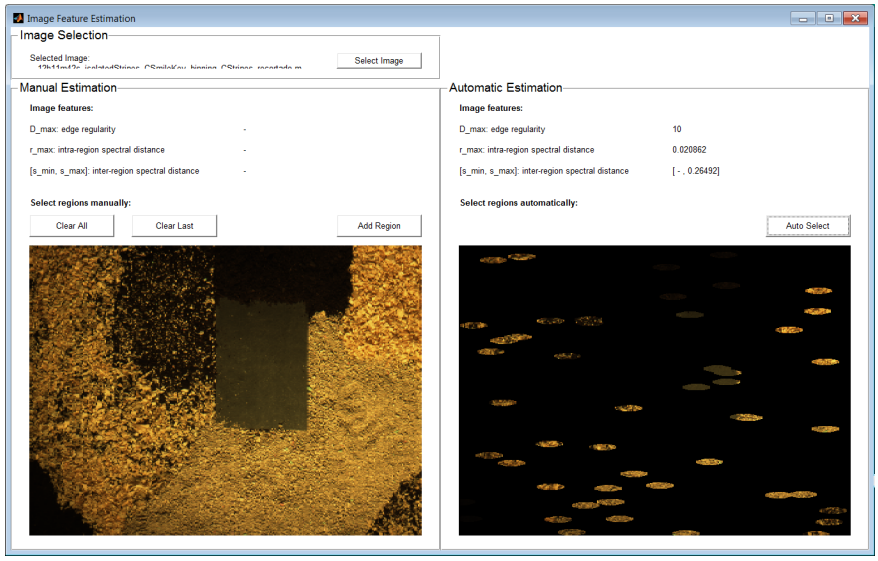

Figure 5.17: Capture of the interface of the Image Feature Estimation Tool

Furthermore, in an attempt to assist a user in the parameter estimation, another software tool has been developed and distributed publicly[2]. It consists in a graphical interface (Fig. 5.17) containing two different panels, labeled *Manual Estimation* and *Automatic Estimation*. Using the *Manual Estimation* panel, the user is in charge of selecting the coarse regions needed to estimate $[s_{min}, s_{max}]$ and r_{max}. Conversely, by means of the *Automatic Estimation* panel, the region selection is carried out automatically by the region-growing algorithm presented above.

[2]The tool for the estimation of feature parameters from real images is available through downloadable MATLAB code at http://gii.udc.es/gii_hyperspectral_repository

5.5 Hyperspectral Repository

Once the procedure for acquiring, preprocessing and categorizing real hyperspectral images and creating synthetic multidimensional images has been presented, this subsection describes the main contribution of this chapter, that is, the creation of a publicly available repository of synthetic and real hyperspectral images named *GII-HSEG repository*[3].

The GII-HSEG repository has been structured in three parts, made up of, respectively:

1. Synthetic hyperspectral images, created based on real spectral signatures [USGS] and following the procedure presented in section 5.3.1.
2. Real hyperspectral images, captured indoors under controlled illumination conditions and processed following the calibration and correction methods commented in the previous section and described in chapter 4.
3. Hyperspectral images provided by users, which must comply with some requirements in order to be accepted for their inclusion in the repository.

For each synthetically generated and real captured scene, an image package has been created including:

- An animation showing each band of the hyperspectral image in .GIF format.
- A RGB composite image of the datacube.
- A label image corresponding to the classification reference or ground truth.
- An image with a graphical description of the hyperspectral scene and its parametric categorization, such as the one shown in Fig. 5.18.
- A .mat (*MATLAB*) file containing the hyperspectral image itself, its associated ground truth image, the legend of the ground truth image, the wavelength range of the datacube, and the values of the estimated spatio-spectral parameters extracted following the procedure presented in section 5.4.

[3]Synthetic and real hyperspectral images are available at http://gii.udc.es/gii_hyperspectral_repository

- Information about the particular parameters involved in the acquisition process.

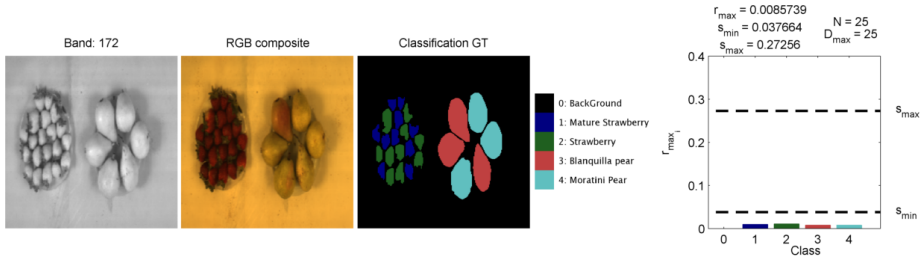

Figure 5.18: Graphical description of a hyperspectral image from the repository

Regarding the addition of external hyperspectral images to the repository, users must provide the following information about the image itself and the acquisition process: type and characteristics of the imager, similar to those shown in Table 5.2, type of illumination, ground truth and parametric categorization of the scene using the tool provided for that purpose (Fig. 5.16).

In a future version of the repository, social aspects would be added, such as comments about each scene or a scoring system for evaluating the usefulness of different scenes and the perceived quality of the ground truth labels.

5.6 Summary

This chapter sums up the tasks carried out in order to construct a repository of parametrized and labeled hyperspectral images.

A first analysis of real hyperspectral images has allowed the characterization of multi-dimensional images using only a few feature parameters that describe geometrical as well as local and global spectral aspects. Based on these features, an algorithm has been designed that enables constructing a single image or sequences of synthetic multi-dimensional images in an easy way. Furthermore, a tool for the creation of RGB images, with a simple and intuitive interface, has been created and made available for tuning or validating algorithms.

On the other hand, a set of hyperspectral images have been captured using a hyperspectral imager. All the acquired images have been corrected, labeled for classification purposes and described using the established feature parameters

presented in this chapter. The acquired images try to cover the space of spatial and spectral parameters in order to improve the assessment of segmentation and classification algorithms.

Moreover, two additional auxiliary tools have been implemented. The first one deals with feature parameter extraction from real hyperspectral images. Thanks to a simple graphical interface, any user can obtain a characterization based on spatial and spectral parameters. The second tool aids in the labeling of real images by means of polygon-based graphical objects.

Finally, the work carried out has allowed us to build a publicly available repository of hyperspectral images named GII-HSEG repository, which includes synthetically created and real hyperspectral images, which are accurately labeled and categorized, as well as hyperspectral scenes provided by users external to our research group.

Chapter 6

ECAS-II: An Approach for the Customized High-Dimensional Segmentation of Hyperspectral Images

6.1 Introduction

As introduced in the background chapter, addressing the segmentation and classification of hyperspectral images is still challenging. There are mainly three problems associated with these processing tasks. The first one is related to the fact that the segmentation of an image depends on the application and the needs of the user. For instance, the same scene of food products can be segmented into regions corresponding to different types of fruits, vegetables, etc. or into more detailed regions such as defects or ripe regions. This introduces a level of subjectivity linked to the interpretation of the data that needs to be contemplated in the process of implementing automatic classifiers. As a

consequence, classification algorithms should display the capability of adapting to meet the classification needs of different users or final applications, but this is not usually the case.

The second main issue concerns practical and operational problems. Capturing hyperspectral data and building reliable labelled datasets is costly in terms of economics, time and resources. That is why there are very few labelled hyperspectral datasets publicly available and they are not always too reliable in terms of their labels.

Finally, the inherent complexity of hyperspectral data introduces methodological difficulties. Hyperspectral images are highly correlated in the spatial and spectral dimensions, hence considering dependencies between neighboring pixels is desirable in the development of segmentation techniques. Furthermore, the segmentation and classification of hyperspectral data present high computing requirements. This is usually addressed by projecting the high dimensional image onto a lower dimension before segmenting in order to minimize the processing and hence the execution times, leading to the problem of possible loss of information. It is therefore desirable that processing algorithms be easily parallelizable for their implementation over hardware such as GPUs.

Bearing all of this in mind, a cellular automata based segmenter structure called Multi-Gradient based Cellular Automaton (MGCA) is proposed to segment multidimensional images without any projection of hyperspectral information onto lower dimensions. The behaviour of the MGCA depends, among other things, on a set of transition rules that need to be determined. In this work, an evolutionary based procedure called ECAS-II automatically provides those transition rule sets for MGCA segmenters adapted to particular segmentation needs as a function of a set of low dimensional training images in which the user expresses his segmentation requirements.

The application of the MGCA structure to a hyperspectral image provides a segmentation result that can serve as input to a subsequent classification stage, leading to a multi-stage classification procedure. This approach differs from the classification algorithms presented in the background chapter in that it does not provide as an output a labelled segmentation map or classification. Instead, it performs an image "regularization" or segmentation that is adapted to the particular segmentation level required by the user. Thus, its function is to adapt the hyperspectral image to a particular classification purpose. Once

the original hyperspectral image is transformed by the MGCA and thus fitted to a particular type of segmentation, any pixel-wise classification algorithm can be applied to label de regions of the image and, consequently, finalize the classification process.

For the examples shown in this chapter, we have selected for this classification stage a multi-class pairwise (one versus one) SVM classification algorithm, which is directly applied to the segmented data cube. Nevertheless, for this classification step, other suitable algorithms could be considered such as, for instance, Extreme Learning Machines (ELM) [Huang et al., 2006, Lopez-Fandino et al., 2015].

As a preview of the advantages of using ECAS-II and the MGCAs it generates for segmentation, this strategy is capable of simultaneously fulfilling the following aspects:

- It has the capacity of adapting to what the user desires contemplating the fact that there are multiple ways of segmenting the images.
- The training procedure is performed without having to resort to large training or labelled sets of real images. It makes use of a methodology that simplifies the training process by using low dimensional reference samples. Constructing high dimensional image segmenters from low dimensional training sets alleviates the problem of lack of labeled training images. These can be generated on line based on a parametric categorization of the desired segmentation extracted from a set of examples, as was described in chapter 5. As an added benefit, this methodology also reduces the expert knowledge requirements.
- It works with the complete spectral breadth of the images, avoiding projecting the spectral information onto lower dimensional spaces. In fact, it employs a distance measure to compare spectra that is independent of dimensionality.
- It presents intrinsically parallel low-level processing operations, making it attractive for its implementation in a concurrent fashion over hardware such as GPUs.

- This strategy has been tested over synthetic and real hyperspectral images and compared to state-of-the-art segmentation approaches over benchmark images in the area of remote sensing hyperspectral imaging, proving to be very competitive in terms of performances.

The remainder of this chapter is structured as follows. The MGCA structure considered in this paper is presented in the next section. Section 6.3 is devoted to the detailed description of the operation of the ECAS-II algorithm. Then, in section 6.4, we introduce how the training sets are constructed and in section 6.5, the classification algorithm that will be used for the purpose of comparing the results obtained to those found in the literature. Section 6.6 aims to analyse how the selection of the training images used to optimize the transition rules of the evolved CAs affects the performance of the resulting MGCAs in terms of segmentation error. Experimental results of the proposed classification algorithm are presented in section 6.7, including a performance comparison to other existing methods. Finally, some concluding remarks are summarized in section 6.8.

6.2 Multi-gradient based Cellular Automata

6.2.1 Cellular Automata

CAs were first proposed by Von Neumann et al. [1966] as a biologically inspired distributed computing paradigm. A CA consists of a regular one or multidimensional grid of cells, each characterized by a cell state. Basically, the CA is iteratively executed so that all cell states are repeatedly updated according to some transition rules. The particular rule to be applied to each cell in a given iteration is selected taking into account the current state of that cell and the states of the cells in its neighborhood.

The goal of this approach is for the CA to converge to a desired state after its execution during N iterations. The key to taking advantage of the great potential of CAs to achieve a particular purpose is to adequately conform its set of transition rules. Unfortunately, the determination of the appropriate rules for the automata is far from being a straightforward task, posing a great challenge to the algorithm designer. It would thus be desirable to be able to automate the process of determining the appropriate transition rules for

a particular purpose. This automatic rule selection has been addressed from many different perspectives by researchers in the CA community [Ganguly et al., 2003], being the most popular approach to use evolutionary techniques in order to obtain the transition rule set [Wang et al., 2011, Kauffmann and Piché, 2010].

Regarding the application of CAs to hyperspectral images, their potential has still hardly been explored. Some authors have designed CA structures to segment low dimensional images [Wang et al., 2011, Kauffmann and Piché, 2010, Gallego et al., 2011], and some authors have done some work in the high dimensional image processing area in terms of edge detection [Lee and Bruce, 2010] or image segmentation [Quesada-Barriuso et al., 2012]. However, in these cases, the set of transition rules were hand created ad-hoc and, in order to run them over hyperspectral data, the spectral information was usually projected onto a lower dimension using a PCT or MNF transformation.

6.2.2 General operation of MGCA

Focusing now on the particular implementation proposed in this thesis work, which has been called Multi-Gradient based Cellular Automata (MGCA), let us start by saying that in this case a cell of the automaton is placed over each pixel of the hyperspectral image and the state of the cell ($\boldsymbol{s_i}$) is given by an N-band spectrum, each band taking values in the range [0 1]. These cells are initialized with the spectra present in their assigned pixel. In fact, cells or pixels will be indistinctly mentioned when describing the operation of the CA. As a consequence, the state of the cell is vector valued, leading to a state space that is continuous and corresponds to the $\mathbb{R}^N$ positive vector space.

In what follows, the procedure for gradually and iteratively updating the state of all the cells of the CA making the global result converge towards a segmented image is described. This algorithm is summarized in Algorithm 1. The objective is to homogenize the spectra of each of the different regions into a narrow band of spectra so that any classification algorithm can then easily classify the different regions. It can be noticed here that the strategy contemplated for the CA operates over the whole pixel spectrum avoiding the projection of the multidimensional spectral information onto a lower dimension.

6.2.3 Spectral Distance Measure

In order to update the spectrum of each cell every iteration of the CA, one out of a set of M transition rules that controls the automaton behavior must be selected. This selection is performed based on the state of the spectrum of the cell and on the spectra of the $N_{Smax} \times N_{Smax}$ closest neighboring cells, where N_{Smax} is the maximum size considered for the spatial window centered over each cell.

To take into account the spectral information of the neighboring cells, it is necessary to establish a spectral distance measure. We have opted for the well-known spectral angle (SA), normalized between 0 and 1. The SA has been widely used as a spectral similarity measure for material identification [Keshava, 2004, Dennison et al., 2004] and the advantage of using it is its independence from the number of spectral components, which allows using the same CA over images of different spectral dimensionality. Moreover, the SA is also invariant to changes of scale which makes the method insensitive to changes in illumination. Thus, for a cell i, the normalized spectral angle, $\alpha_{i,j}$ with respect to its neighboring cell j is defined as:

$$\alpha_{i,j} = \frac{2}{\pi} cos^{-1} \left(\frac{\sum s_j s_i}{\sqrt{\sum s_j^2} \sqrt{\sum s_i^2}} \right) \tag{6.1}$$

where the summation is performed over the components of the state of s_i, i.e., the spectral dimension of a pixel.

6.2.4 Deciding on the appropriate update rule

As stated earlier, the CA applies a particular transition rule over each cell depending on the information from its neighborhood. The spectral angle is a rather low-level information source and here, to potentiate the descriptive power of the approach, we propose combining neighboring spectral measurements by means of the calculation of spatial gradients, $G_{N_{Si}}$. More specifically, the gradients are calculated taking into account the pixels contained in three different $N_S \times N_S$ cell windows, where $N_S = \{3, 5, 7\}$ (using the closest 8, 24 and 48 neighboring cells). Thus, each gradient will provide information on the intensity and direction of spectral changes in the image at different resolutions leading to a multi-gradient based decision process.

For each of the $N_S \times N_S$ windows, two bi-dimensional masks, $M_{X_{N_S}}$ and $M_{Y_{N_S}}$, are used to extract the spatial gradients:

$$\mathbf{G_{N_{S_i}}} = \left(G_{X_{N_{S_i}}}, G_{Y_{N_{S_i}}}\right), \quad N_S = \{3, 5, 7\} \tag{6.2}$$

$$G_{X_{N_{S_i}}} = \sum_{j=1}^{N_S \cdot N_S} \alpha_{i,j} \cdot M_{X_{N_{S_j}}}, \quad G_{Y_{N_{S_i}}} = \sum_{j=1}^{N_S \cdot N_S} \alpha_{i,j} \cdot M_{Y_{N_{S_j}}} \tag{6.3}$$

$$\begin{aligned}
M_{X_3} &= \tfrac{1}{2} \cdot \begin{bmatrix} -\frac{1}{2} & 0 & \frac{1}{2} \\ 1 & 0 & 1 \\ -\frac{1}{2} & 0 & \frac{1}{2} \end{bmatrix}, \quad M_{Y_3} = M_{X_3}^T \\
M_{X_5} &= \tfrac{10}{33} \cdot \begin{bmatrix} -\frac{1}{8} & -\frac{1}{5} & 0 & \frac{1}{5} & \frac{1}{8} \\ -\frac{1}{5} & -\frac{1}{2} & 0 & \frac{1}{2} & \frac{1}{5} \\ -\frac{1}{4} & -1 & 0 & 1 & \frac{1}{4} \\ -\frac{1}{5} & -\frac{1}{2} & 0 & \frac{1}{2} & \frac{1}{5} \\ -\frac{1}{8} & -\frac{1}{5} & 0 & \frac{1}{5} & \frac{1}{8} \end{bmatrix}, \quad M_{Y_5} = M_{X_5}^T \\
M_{X_7} &= \tfrac{361}{1527} \cdot \begin{bmatrix} -\frac{1}{18} & -\frac{1}{13} & -\frac{1}{10} & 0 & \frac{1}{10} & \frac{1}{13} & \frac{1}{18} \\ -\frac{1}{13} & -\frac{1}{8} & -\frac{1}{5} & 0 & \frac{1}{5} & \frac{1}{8} & \frac{1}{13} \\ -\frac{1}{10} & -\frac{1}{5} & -\frac{1}{2} & 0 & \frac{1}{2} & \frac{1}{5} & \frac{1}{10} \\ -\frac{1}{9} & -\frac{1}{4} & -1 & 0 & 1 & \frac{1}{4} & \frac{1}{9} \\ -\frac{1}{10} & -\frac{1}{5} & -\frac{1}{2} & 0 & \frac{1}{2} & \frac{1}{5} & \frac{1}{10} \\ -\frac{1}{13} & -\frac{1}{8} & -\frac{1}{5} & 0 & \frac{1}{5} & \frac{1}{8} & \frac{1}{13} \\ -\frac{1}{18} & -\frac{1}{13} & -\frac{1}{10} & 0 & \frac{1}{10} & \frac{1}{13} & \frac{1}{18} \end{bmatrix}, \quad M_{Y_7} = M_{X_7}^T
\end{aligned} \tag{6.4}$$

where $M_{X_{N_{S_j}}}$ and $M_{Y_{N_{S_j}}}$ represent the j^{th} elements of the gradient masks $M_{X_{N_S}}$ and $M_{Y_{N_S}}$ (horizontal and vertical masks respectively), and $\mathbf{G_{N_{S_i}}}$ denotes the gradient vector located at cell i, calculated considering the neighboring cells in a window of size $N_S \times N_S$.

Each gradient vector can be expressed as a modulus value, $|\mathbf{G_{N_{S_i}}}|$, and an angle value, $\phi_{N_{S_i}}$, defined as:

$$\begin{aligned}
|\mathbf{G_{N_{S_i}}}| &= \sqrt{G_{X_{N_{S_i}}}^2 + G_{Y_{N_{S_i}}}^2} \\
\phi_{N_{S_i}} &= \tan^{-1}\left(\frac{G_{Y_{N_{S_i}}}}{G_{X_{N_{S_i}}}}\right)
\end{aligned} \tag{6.5}$$

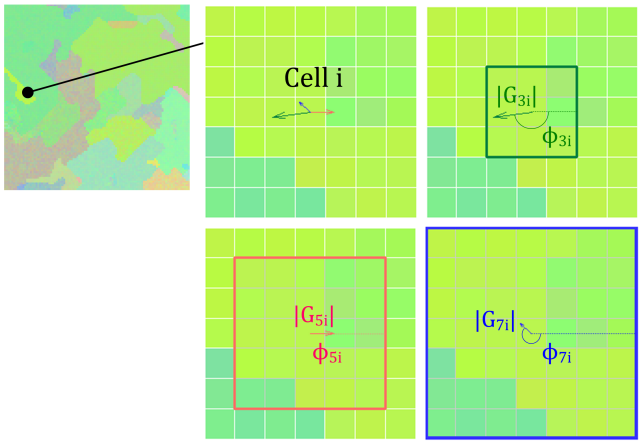

Figure 6.1: Extraction of the three gradient vectors, $G_{N_{Si}}$, with $N_S = \{3, 5, 7\}$, for a pixel from a RGB image.

The modulus, $|\mathbf{G_{N_{S_i}}}|$ is related to the intensity of the spectral change following the direction given by the angle, $\phi_{N_{S_i}}$, for window size N_S. To illustrate this, Fig. 6.1 shows an example of extracting the modulus and angle values for a cell from a RGB image. In this CA implementation, the values of the three moduli and angles, $(\mathbf{G_{3_i}}, \mathbf{G_{5_i}}, \mathbf{G_{7_i}}, \phi_{3_i}, \phi_{5_i}\phi_{7_i})$, are all the information that the CA collects from the neighborhood of a cell i in order to decide which transition rule to select and then apply.

On the other hand, in terms of the structure of the cellular automaton, the transition rule set that governs its behavior consists of a set of M rules, each one of them made up of 6 parameters, the first five corresponding to the condition and the last one to the action:

$$CA = \begin{Bmatrix} |\mathbf{G_{r_{3_1}}}| & |\mathbf{G_{r_{5_1}}}| & |\mathbf{G_{r_{7_1}}}| & \phi_{r_{5_1}} & \phi_{r_{7_1}} & \theta_{r_1} \\ \vdots & \vdots & \vdots & \vdots & \vdots & \vdots \\ |\mathbf{G_{r_{3_k}}}| & |\mathbf{G_{r_{5_k}}}| & |\mathbf{G_{r_{7_k}}}| & \phi_{r_{5_k}} & \phi_{r_{7_k}} & \theta_{r_k} \\ \vdots & \vdots & \vdots & \vdots & \vdots & \vdots \\ |\mathbf{G_{r_{3_M}}}| & |\mathbf{G_{r_{5_M}}}| & |\mathbf{G_{r_{7_M}}}| & \phi_{r_{5_M}} & \phi_{r_{7_M}} & \theta_{r_M} \end{Bmatrix} \tag{6.6}$$

It can be noticed that the encoding of the transition rules is a direct representation of three vector gradients. Subindex r is used here to avoid confusing rule parameters with the values of the gradient vectors extracted from the neighboring information of a cell. Now, if we select a representation where these three

vector gradients, as a group, are independent of angle rotations and reflections, only five parameters are required to represent the three vector set. One of the angles, in this case ϕ_{r3_k}, will always be taken as equal to 0. Fig. 6.2a (left) shows a geometrical representation of the condition parameters of a rule.

Each iteration of the CA, only one of these M rules is applied to each cell. To decide which one is selected, a comparison between the neighborhood information $(\mathbf{G_{3_i}}, \mathbf{G_{5_i}}, \mathbf{G_{7_i}}, \phi_{3_i}, \phi_{5_i}\phi_{7_i})$ and the first five parameters of each of the M rules $(|\mathbf{G_{r3_k}}|, |\mathbf{G_{r5_k}}|, |\mathbf{G_{r7_k}}|, \phi_{r5_k}, \phi_{r7_k})$ is carried out. For this comparison, the group of three gradient vectors represented by the condition parameters of that rule is rotated and reflected in such a way that the euclidean distance among the three pairs of gradient vectors is minimized.

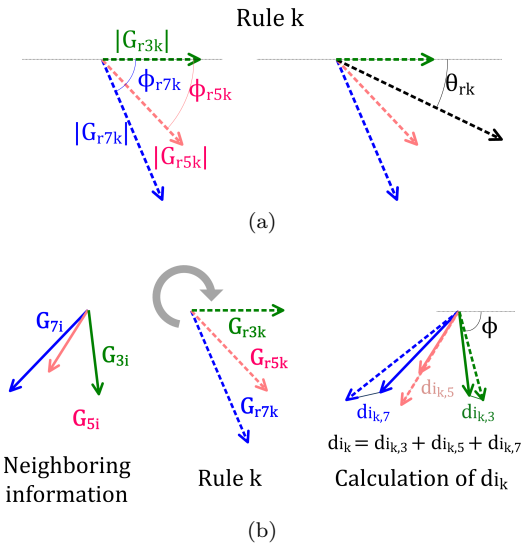

Figure 6.2: (a) Rule representation: (left) condition parameters and (right) action parameter; (b) comparison between the neighboring information of a cell i and the condition parameters of a rule k

The distance between the neighborhood and rule gradient vectors is calculated as the sum of the L^2 norms of the vector differences once the rule gradient vectors have been rotated and reflected:

$$d_{i_k} = \|\mathbf{G_{3_i}} - \mathbf{G'_{r3_k}}\| + \|\mathbf{G_{5_i}} - \mathbf{G'_{r5_k}}\| + \|\mathbf{G_{7_i}} - \mathbf{G'_{r7_k}}\| \tag{6.7}$$

where $\{\mathbf{G_{3_i}}, \mathbf{G_{5_i}}, \mathbf{G_{7_i}}\}$ are the gradient vectors of the cell under evaluation and $\{\mathbf{G'_{r3_k}}, \mathbf{G'_{r5_k}}, \mathbf{G'_{r7_k}}\}$ those of the gradient vectors representing rule k after rotating them an angle ϕ and, if necessary, reflecting them (Fig. 6.2b).

Summarizing, the process of selecting a rule consists in calculating the minimum distance d_{i_k} for each rule and selecting the rule, s, that provides the lowest value for the distance,

$$s = argmin_{k\in\{1,2,\ldots,M\}} d_{i_k} \tag{6.8}$$

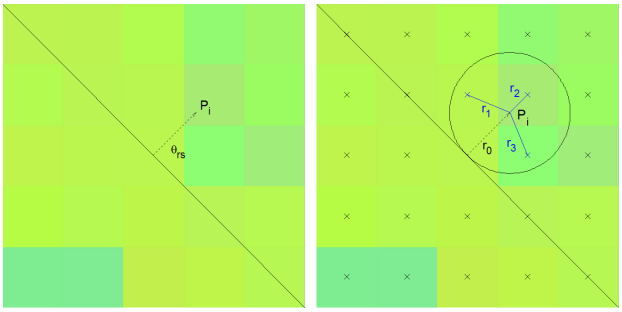

Figure 6.3: Selection of neighboring pixels for updating the state of the cell i

6.2.5 Updating the state of the CA

The last parameter of the selected rule contains the information required to update the state of cell i. The vector state of the cell will be modified by performing a weighted average of its vector state or spectrum and that of some of its neighbors. If we follow the direction given by $\phi + \theta_{r_s}$ for a distance of 1 pixel, where ϕ is the rotation angle of the selected rule, s, that was used to calculate the distance d_{i_k}, and θ_{r_s} is the last parameter of rule s, we will be at a point of the image, P_i (Fig. 6.3). The neighboring cells used to modify the spectrum of cell i will be located at a maximum distance of 1 pixel from P_i. Thus, the update of the state of cell i, $\mathbf{s'_i}$, will be given by the weighed average of the spectra of those cells and that of i:

$$\begin{gathered}\mathbf{s_i'} = \sum_{j=1}^{n} w_{ij} \cdot \mathbf{s_j} + w_i \cdot \mathbf{s_i} \\ w_{ij} = \frac{f_r(r_j)}{\sum_{j=1}^{n} f_r(r_j) + f_{th}}, \; w_i = \frac{f_{th}}{\sum_{j=1}^{n} f_r(r_j) + f_{th}} \\ f_r(r_j) = \begin{cases} f_{th} & \text{if } \frac{1}{r_j} > f_{th} \\ \frac{1}{r_j} & \text{otherwise} \end{cases}\end{gathered} \tag{6.9}$$

where $\mathbf{s_i'}$ is the updated spectrum of cell i; $\mathbf{s_i}$ represents the original spectrum of cell i; $\mathbf{s_j}$ is the spectrum of cell j which is a neighbor of cell i; n is the number of neighboring cells that will participate in the update of the state of cell i; r_j is the distance between the neighboring cell j and point P_i; w_{ij} is the weight associated to the spectrum of cell j; w_i is the weight associated to the spectrum of cell i; $f_r(r_j)$ is a function that assigns weights as a function of distance r_j.

Following this procedure, which is summarized in Algorithm 1, the CA is applied iteratively to the whole image producing a new hyperspectral cube every iteration. With the appropriate rules, the final hyperspectral cube will be a segmented version of the original one. Each region will be represented by a narrow range of spectra.

Algorithm 1 MGCA

Input: X: image of $m \times n$ pixels and N bands
Output: Y: segmented image of $m \times n$ pixels and N bands

1: **for** $p \leftarrow 1$ to K **do**
   ▷ K iterations
2: **for** $i \leftarrow 1$ to $n \cdot m$ **do**
3: Calculate $|\mathbf{G_{3_i}}|, |\mathbf{G_{5_i}}|, |\mathbf{G_{7_i}}|, \phi_{3_i}, \phi_{5_i}, \phi_{7_i}$ using the spectral angle values, α_{ij}
4: Select rule, s, by comparing the neighbouring information $|\mathbf{G_{3_i}}|, |\mathbf{G_{5_i}}|, |\mathbf{G_{7_i}}|, \phi_{3_i}, \phi_{5_i}, \phi_{7_i}$ with the first five parameters of the transition rules $|\mathbf{G_{r3_k}}|, |\mathbf{G_{r5_k}}|, |\mathbf{G_{r7_k}}|, \phi_{r5_k}, \phi_{r7_k}$
  ▷ Image rotation and reflection are considered
5: Update the state of the cell i using the last parameter of the selected rule
  ▷ A weighted spectral average of the spectrum of cell i and that of some of its neighbors is performed considering all the spectral bands
6: **end for**
7: **end for**

6.3 ECAS-II: Evolving the Cellular Automata

6.3.1 Introduction

ECAS, version I [Priego et al., 2013a] and II [Priego et al., 2015a,b], are evolutionary approaches for the generation of cellular automata (CA) based segmentation algorithms. They provide the parameters or transition rules that govern their operation and behavior.

There are several reasons for choosing evolutionary algorithms (EAs) as the optimization method for the creation of the transition rules. First, EAs do not make strong assumptions about the underlying fitness landscape. Second, EAs work on a population of solutions instead of a single point. This makes them less likely to get trapped in a local minimum when searching for the optimum set of transition rules.

As indicated, EAs operate over a population of individuals, data structures that encode the solutions to the problem. In each generation, a new population is created through the selection and variation of the individuals from the population in the previous generation as a function of their evaluation according to a cost or fitness function. This process is iterated until an individual with sufficient fitness (candidate solution) is found or when a previously selected computational limit is reached.

6.3.2 Differential Evolution

In particular, in this implementation of ECAS-II, we have chosen a Differential Evolution Algorithm (DE) [Storn and Price, 1997] in order to infer the set of transition rules that will govern the behavior of the CA. DE has proven to work efficiently for minimizing objective functions that are non-differentiable, non-continuous, non-linear, noisy, flat, multi-dimensional or present many local minima, constraints or stochasticity.

The most important components of the DE algorithm are:

- Representation (definition of the individuals): Each CA that makes up the DE population is encoded as a vector with $D = 6 \cdot M$ floating point values, which are a direct representation of the parameters shown in eq.

6.6. The values corresponding to $|\mathbf{G}_{\mathbf{r3_k}}|$, $|\mathbf{G}_{\mathbf{r5_k}}|$, and $|\mathbf{G}_{\mathbf{r7_k}}|$ belong to the $[0, \sqrt{2}]$ interval and those corresponding to ϕ_{r5_k}, ϕ_{r7_k} and θ_{r_k} are in the interval $[0, 2\pi]$.

- Population: NP D-dimensional parameter vectors $x_{i,G}, i = 1, 2, ..., NP$ are used as a population for each generation G. Defining a population implies indicating how many individuals make it up, that is, determining the population size. The initial vector population is chosen randomly and should cover the entire parameter space.

- Variation Operators: Mutation
  DE generates new parameter vectors by adding the weighted difference of two population vectors (individuals) to a third vector. This operation is called mutation. For each parameter vector, $x_{i,G}, i = 1, 2, ..., NP$, a mutant vector is generated according to: $v_{i,G+1} = x_{r_1,G} + F \cdot (x_{r_2,G} - x_{r_3,G})$ with integer, mutually different, random indexes $r_1, r_2, r_3 \in \{1, 2, ..., NP\}$ and $F > 0$. F is a real and constant factor $\in [0, 2]$ which controls the amplification of the differential variation $(x_{r_2,G} - x_{r_3,G})$.

- Variation Operators: Crossover
  In order to increase the diversity of the perturbed parameter vectors, crossover is introduced. To this end, new potential parameter vectors $u_{i,G+1} = (u_{1i,G+1}, u_{2i,G+1}, ..., u_{Di,G+1})$ are formed, following:

$$u_{ji,G+1} = \begin{cases} v_{ji,G+1} & \text{if } (randb(j) \leq CR) \text{ or } j = rnbr(i) \\ x_{ji,G} & \text{if } (randb(j) > CR) \text{ and } j \neq rnbr(i) \end{cases}$$
$$j = 1, 2, ..., D$$

  where $randb(j)$ is the jth evaluation of a uniform random number generator with outcomes $\in [0, 1]$. CR is the crossover constant $\in [0, 1]$, determined by the user; $rnbr(i)$ is a randomly chosen index $\in 1, 2, ..., D$ which ensures that $u_{i,G+1}$ gets at least one parameter from $v_{i,G+1}$.

- Selection: To decide if a potential parameter vector should become a member of generation $G+1$, $u_{ji,G+1}$ is compared to $x_{i,G}$. If $u_{ji,G+1}$ yields a smaller cost function value than $x_{i,G}$, then $x_{i,G+1}$ is set to $u_{ji,G+1}$, otherwise, the old value $x_{i,G}$ is retained. More details of this DE implementation can be found in Storn and Price [1997].

The key to the versatility of ECAS-II lies in how the individuals are evaluated and how the training image set is created. This is presented in the following two subsections.

6.3.3 Evaluation of Individuals and Fitness Function

In order to evaluate each individual (each MGCA), or calculate its fitness, we have chosen to determine how apt it is at segmenting a set of images that are provided together with the desired segmentation (ground truth). These images will be considered the training set, and, as commented later, should reflect the type of segmentation desired by the user. Every time the CA is evaluated, it is executed over a training image for a given number of iterations and the result is compared to its ground truth. In order to improve the evaluation process maximizing the generalization capabilities of the CA, and at the same time preventing circularity problems, each individual is evaluated using different images that can be either generated on-line or randomly selected from a pre-constructed image collection.

In ECAS-II, the cost function to be minimized using DE is defined as the maximum value of two error measurements: intra-class (e_{intra}) error and inter-class (e_{inter}) error:

$$e = max(e_{intra}, e_{inter}) \tag{6.10}$$

Before describing these error measurements, let us introduce some notation. Let $\mathcal{I} = \{x_p\}_{p=1}^{P\times Q}$ be the training image of size $P \times Q$ where x_p is a N-dimensional vector. Let $\mathcal{L}= \{l_p\}_{p=1}^{P\times Q}$ be the ground truth corresponding to this training image with $l_p \in S$, being $S = \{1,\ 2, \ldots, s_k,\ \ldots, M\}$ the set of different labels in $\mathcal{L}$. Let $\mathcal{R} = \{r_p\}_{p=1}^{P\times Q}$ with $r_p \in \{0, 1\}$ be a binary image characterizing each pixel of $\mathcal{L}$ as a border pixel, $\{0\}$, or an interior pixel, $\{1\}$. We can also consider $\mathcal{I}$ as the merging of regions with the same associated label, $\mathcal{I} = \bigcup_{k=1}^{M} B_k$, where $B_k = \{x_p \mid l_p = s_k\}$. B_k can also be divided into two subsets, one that only contains interior pixels and another one that only contains border pixels, taking into account the labelling in $\mathcal{L}$. Thus, $B_k = I_k \cup F_k$, where $I_k = \{x_p \mid l_p = s_k \wedge r_p = 1\}$ and $F_k = \{x_p \mid l_p = s_k \wedge r_p = 0\}$. F_k may be decomposed into $M-1$ subsets, $F_k = \bigcup_{k'=1}^{M} F'_{kk'}$ with $k' \neq k$, where $F'_{kk'}$ contains the pixels located in the borders between B_k and $B_{k'}$ (Fig. 6.4).

With this notation in mind, we can define the two types of errors. The intra-class error provides a measure of the homogeneity of the regions in the image, being a region a set of pixels that share the same label in the ground truth associated to the training image. This error is calculated as the maximum of two errors: the local intra-region error ($e_{local-intra}$) and the non-local intra-region error ($e_{nonlocal-intra}$):

$$e_{intra} = \max\left(e_{local-intra},\ e_{nonlocal-intra}\right) \tag{6.11}$$

Being the local intra-region error defined as:

$$e_{local-intra} = \frac{\sum_{k=1}^{M}\left[\sum_{x_p \in I_k}\left(\sum_{j=1}^{8}\frac{\alpha_{pj}}{8}\right)\right]}{\sum_{k=1}^{M}\#I_k} \tag{6.12}$$

where α_{pj} refers to the normalized spectral angle between a pixel x_p and its neighbor x_j and $\#I_k$ is the cardinality of subset I_k. The $e_{local-intra}$ error measures the local homogeneity of neighboring pixels that share the same label in $\mathcal{L}$. The local homogeneity for each I_k is defined as:

$$H_k = \frac{\sum_{x_p \in I_k}\left(\sum_{j=1}^{8}\frac{\alpha_{pj}}{8}\right)}{\#I_k} \tag{6.13}$$

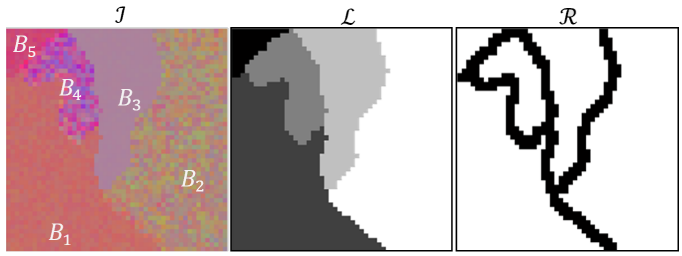

Figure 6.4: Synthetic RGB image, ground truth and edge image

On the other hand, to define the $e_{nonlocal-intra}$, a set of V pairs of pixels is randomly selected for each I_k subset, $\{x_{kv}, y_{kv}\} \in I_k$ with $v = \{1, 2, \ldots V\}$. Then, the $e_{nonlocal-intra}$ is defined as:

$$e_{nonlocal-intra} = \frac{\sum_{k=1}^{M}\left[\sum_{v=1}^{V}\frac{\alpha_{kv}}{V}\right]\Delta\ \#I_k}{\sum_{k=1}^{M}\#I_k} \tag{6.14}$$

where α_{kv} denotes the normalized spectral angle between x_{kv} and y_{kv}. The $e_{nonlocal-intra}$ error measures the spectral homogeneity among pixels which belong to the same region and are not necessarily neighbors.

Finally the inter-region error, e_{inter}, provides a measure of the dissimilarity of the different regions in the segmented image. To define the e_{inter} error, a set of U pairs of pixels are randomly selected for each $F'_{kk'} \cup F'_{k'k}$, $\{x_{ku}, y_{k'u}\}$, with $x_{ku} \in F'_{kk'}$ $x_{k'u} \in F'_{k'k}$, and $v = \{1, 2, \ldots V\}$.

$$e_{inter} = \frac{\sum_{k=1}^{M} \left[\sum_{k'=1}^{M} \frac{\sum_{u=1}^{U} f(\alpha_{kk'u},\ H_k,\ H_{k'}) \Delta \#B_{k'}}{U \Delta \sum_{k'=1}^{M} \#B_{k'}} \right] \Delta \#B_k}{\sum_{k=1}^{M} \#B_k} \tag{6.15}$$

$$f\left(\alpha_{kk'u},\ H_k,\ H_{k'}\right) = \begin{cases} 1 & if \quad \alpha_{kk'u} \leq \quad H_k + \ H_{k'} \\ 0 & if \qquad otherwise \end{cases} \tag{6.16}$$

where $\alpha_{kk'u}$ denotes the normalized spectral angle between x_{ku} and $y_{k'u}$.

Fig. 6.5a depicts a particular evolution of the fitness function when a MGCA is applied to a RGB image during 12 iterations. A GIF animation is also available following the QR link shown in Fig. 6.5b for visualizing the segmentation process.

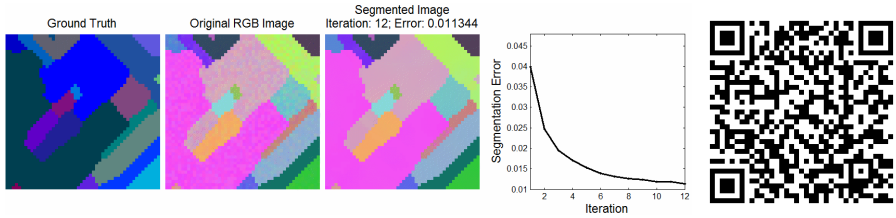

(a) (b)

Figure 6.5: (a) Segmentation process example with the evolution of the segmentation error after 12 iterations in the application of the MGCA and (b) QR link to visualize the segmentation process in GIF format

6.4 ECAS-II: Creating the training image dataset

In a first approximation, it may seem advantageous to select real hyperspectral images as training images for optimizing the transition rules of the CA in the evolutionary process. However, what happens in practice is that the number

of publicly available hyperspectral images is very limited, forcing us to perform the training process using always the same dataset. Furthermore, usually, the labelling of the available hyperspectral images is not entirely reliable, leading to skewed evaluations of the CAs. This makes a good case for using synthetic datasets that really reflect the type of segmentation that is desired. Furthermore, the fact that the application of the ECAS-II algorithm over an image is independent of its dimensionality, due to the use of the spectral angle as the distance measure among adjacent cells, can be exploited in order accelerate and simplify the evolutionary process. Thus, we will show that by using low dimensional images (RGB) in the training image datasets for the evolutionary process, computational complexity may be reduced due to the fact that, as long as the behavior in terms of Spectral Angle is preserved, the resulting CA will be valid for any dimensionality. This is a very powerful concept as, once the CA is evolved in whatever dimensionality, it can be applied to both low (RGB) or high dimensional (HS) images (Fig. 6.6 and 6.7).

The use of synthetic RGB images as training dataset for the DE algorithm entails the following benefits:

- Each synthetic RGB image is created with an associated fully reliable ground truth. This guarantees that the cost function output only depends on the evaluated CA.
- The creation of synthetic RGB images may be made completely automatic. This allows evaluating each individual with a different image created online, or by previously creating a large collection of synthetic RGB images and just picking one of them randomly at run-time.
- The controlled creation of synthetic RGB images together with appropriate ground truth values makes it feasible to train the CA in order to achieve any desired specialized segmentation algorithm.

With a view to adapt the behavior of the segmenter to the desired type of segmentation (coarse, detailed, or other), it is necessary to control and adjust the features of the RGB images used as training dataset in the evolutionary algorithm and their associated ground truths. To this end we have used the developed tool described in section 5.3.1 of chapter 5, that creates synthetic RGB images and their corresponding ground truths based on parametric descriptors which characterize their spectral and spatial properties.

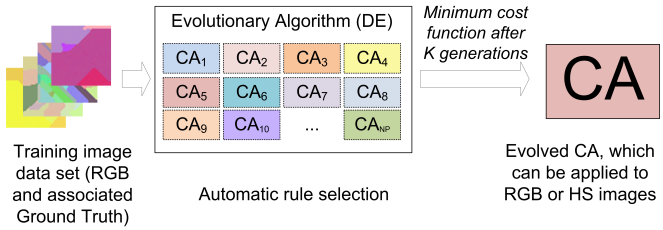

Figure 6.6: Diagram of the ECAS-II training process

Nevertheless, sometimes choosing the appropriate parameters for the type of segmentation a user requires may not be obvious. To solve this problem, the auxiliary tool described in section 5.4 of chapter 5 can be used. By providing this tool with a very small number of images and some indications about the type of segmentation the user desires, it is possible to obtain an automatic estimation of the N, D_{max}, r_{max} and $[s_{min}, s_{max}]$ parameters.

Summarizing, ECAS-II can modulate the MGCA transition rules depending of the features of the synthetic training images that are created, which have been adapted to the nature of the hyperspectral image type and to the sort of segmentation that is required.

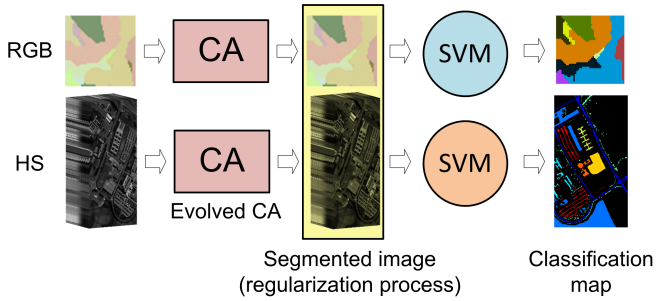

Figure 6.7: Diagram of the MGCA + SVM classification process

6.5 Classification step using SVM

To be able to compare the results of segmentation algorithms it is usually necessary to label the segmented regions, that is, to provide a complete classification of the image, as this is how the results are usually presented in the literature. In

the case of the approach presented here, to produce a final classification image from the segmented data, any pixel-wise classifier can be used. In the examples presented in this chapter, a SVM based pixel-wise classification is applied to the ECAS-II generated MGCA segmentation results (Fig. 6.7). This step is carried out using a multi-class pairwise (one versus one) SVM classification with the specific implementation found in Chang and Lin [2011]. For all the experiments, a Gaussian Radial Basis Function (RBF) kernel is used, and the parameters C and γ were determined by five-fold cross validation.

6.6 Influence of the training set on ECAS-II performance

This section provides an analysis of the performance of the ECAS-II method based on the parametric descriptors of the training image dataset used for optimizing the transition rules in the evolutionary process. The idea here is to analyse how the selection of certain spatio-spectral parameters for the training image dataset affects the segmentation behaviour of the evolved CA. In particular, this analysis aims to determine the combination of image parametric descriptors that the RGB training images should present so that the consequent evolved CA provides a minimum value of the cost function when it is applied to a benchmark set of synthetic images. That is which is the CA that provides the best generalization.

In order to perform this analysis, sets of training image datasets have been created, using different parametric descriptors in their construction process. The particular values of the descriptors for each dataset have been selected by sweeping each parameter aiming to cover a wide range of values in the parameter space.

Thus, 11 batteries of tests have been launched, resulting in 735 different evolved MGCAs (table 6.2). For each test, k, a particular training image dataset has been created using specific $N_k, D_{max_k}, r_{max_k}, Pr_k, eD_k$ and $[s_{min_k}, s_{max_k}]$ parameters. Using this synthetic dataset, the transition rules of the k^{th} CA are optimized by the evolutionary algorithm. Then, this evolved CA is applied to a benchmark set of synthetic images (Fig. 6.9) and an error value, e_k, is obtained by averaging the output of the cost function (eq. 6.10) computed over each image from the benchmark collection. An overview of the procedure followed

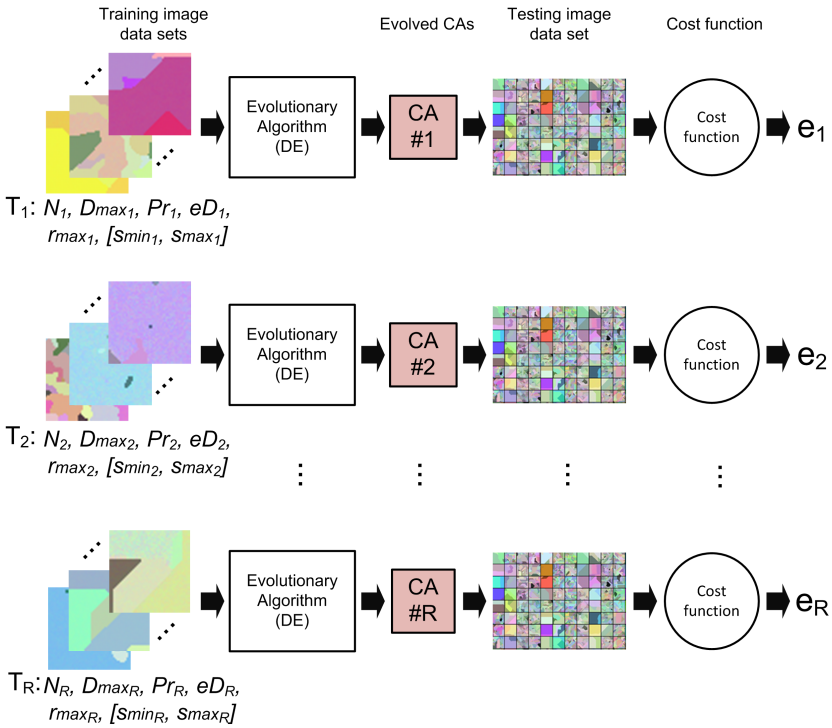

Figure 6.8: Overview of the procedure followed for the analysis of ECAS-II performance

for this study is shown in Fig. 6.8. The specific parameters of the DE algorithm used to evolve each CA are shown in Table 6.1 and the particular parametric descriptors used to create the training dataset associated with each battery of tests are shown in Table 6.2.

Table 6.1: Differential Evolution (DE) parameters

Number of parameters:	180 (30 $rules \times 6$ $parameters/rule$)
NP (Population Size):	100
CR (Crossover):	0.7
F (Mutation):	0.8
Stopping criterion:	Max. number of generations OR Min. cost function
Minimum cost function:	1e-6

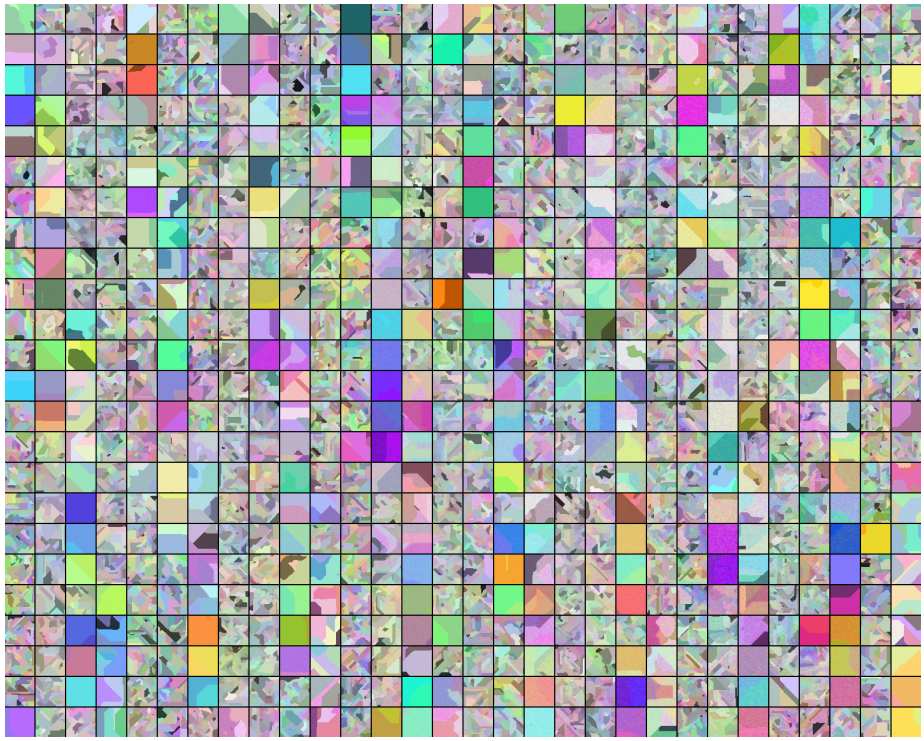

Figure 6.9: Benchmark set of synthetic images used to evaluate each k^{th} evolved MGCA

After this, we have carried out an analysis of which parametric descriptors, as well as the relationship between them, are more relevant in terms of the cost function. That is, which image feature parameters lead to a CA with a greater capacity to generalize when it is applied to the benchmark set. Only the most significant conclusions of this analysis are included here.

The first battery of tests (labelled as #1 in table 6.2) was obtained by sweeping r_{max} and $[s_{min}, s_{max}]$ and fixing the N, eD, Pr and D_{max} parameters in the creation of the training datasets. The y-axis of the left graph of Fig. 6.10 shows the averaged value of the cost function of each evolved CA once applied to the benchmark collection as a function of r_{max} and $[s_{min}, s_{max}]$. The absolute value of $[s_{min}, s_{max}]$ and r_{max} are represented using a two-headed arrow and a circle respectively, both of them situated at the same y-axis value. The right graph of Fig. 6.10 shows the same results except that the x-axis represents relative values of r_{max} and $[s_{min}, s_{max}]$. Observing these graphs,

we can infer that the numeric relation between r_{max} and $[s_{min}, s_{max}]$ is more relevant than the absolute value of these parameters. The CA generalises better when $r_{max} < s_{min}$. That is, when the averaged intra-class spectral distances between neighbouring pixels are lower than the minimum averaged inter-class spectral distance. Furthermore, if the condition $r_{max} < s_{min}$ is satisfied, the cost function value is lower if r_{max} approaches s_{min}. On the other hand, the worst results in terms of the cost function (higher values in eq. 6.10) are obtained when r_{max} is close to or greater than s_{max} in the images of the training dataset.

Table 6.2: Description of the batteries of tests launched for the analysis of the influence of the training set on ECAS-II performance

	r_{max}			$[s_{min}, s_{max}]$			N			D_{max}			eD			Pr		
#	From	To	Steps	From	To	Steps	From	To	Steps	From	To	Steps	From	To	Steps	From	To	Steps
1	0.01	1.5	15	0.03	1.1	9	15	15	1	15	15	1	1	1	1	0.5	0.5	1
				0.06	1.3	9												
2	0.03	0.03	1	0.04	0.04	1	5	45	5	3	50	6	1	1	1	0.5	0.5	1
				0.06	0.06	1												
3	0.03	0.03	1	0.04	0.04	1	15	15	1	15	15	1	1	100	7	0.1	0.9	7
				0.06	0.06	1												
4	0.005	0.2	3	0.04	0.1	2	15	15	1	15	15	1	1	100	3	0.1	0.9	3
				0.08	0.14	2												
5	0.03	0.03	1	0.04	0.1	4	15	15	1	15	15	1	1	100	3	0.1	0.9	3
				0.06	0.6	4												
6	0.05	0.05	1	0.06	0.06	1	5	45	2	1	50	4	1	100	3	0.1	0.9	3
				0.1	0.1	1												
7	0.03	0.2	5	0.04	0.1	2	5	45	3	20	20	1	1	100	3	0.5	0.5	1
				0.06	0.14	2												
8	0.005	0.2	4	0.04	0.1	3	15	15	1	1	50	3	50	50	1	0.1	0.9	3
				0.06	0.14	3												
9	0.005	0.06	7	0.04	0.04	1	5	45	5	15	15	1	1	1	1	0.5	0.5	1
				0.06	0.06	1												
10	0.005	0.06	6	0.04	0.04	1	5	45	5	3	50	3	1	1	1	0.5	0.5	1
				0.06	0.06	1												
11	0.005	0.06	6	0.04	0.1	3	15	15	1	3	50	2	1	1	1	0.5	0.5	1
				0.06	0.6	3												

The second battery of tests (labelled as #2 in table 6.2) fixes r_{max}, $[s_{min}, s_{max}]$, eD and Pr and sweeps N and D_{max} in the creation of the training datasets (Fig. 6.11). The results suggest that the use of training images with a low density of different regions or classes lead to CAs that provide lower values of the cost function once tested over the benchmark collection.

A third battery of tests (labelled as #3 in table 6.2) sweeps eD and Pr keeping the rest of the parameters fixed for the construction of the training datasets. As with the D_{max} parameter, variations of eD and Pr slightly affect the performance of the evolved MGCAs. As D_{max}, eD and Pr are closely interrelated and all of them are responsible for the geometry of the boundaries between regions, we have decided to fix eD and Pr with values of 1 and 0.5 respectively. This way, the process of creating training image datasets and estimating the parametric descriptors from real hyperspectral images becomes simpler and more manageable.

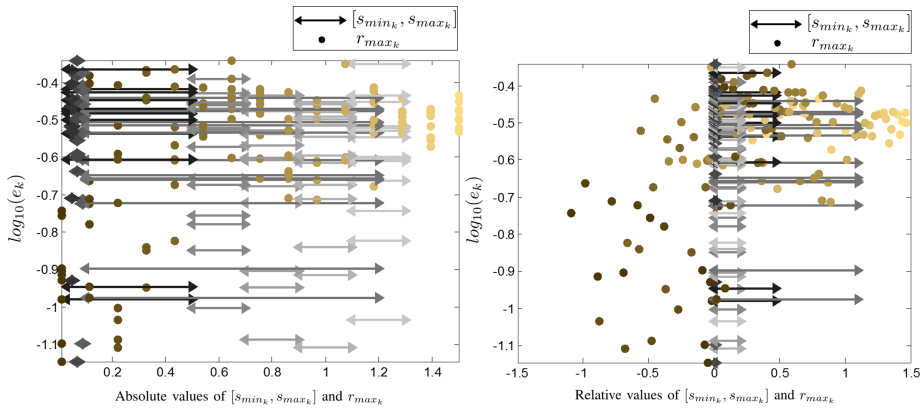

(a) (b)

Figure 6.10: Averaged value of the cost function of each evolved CA once applied to the benchmark collection as a function of r_{max} and $[s_{min}, s_{max}]$

Finally, the battery of tests labelled as #9 sweeps the r_{max} and N parameters, those labelled as #5, #10 and #11 sweep three out of the six parameters and the rest of the batteries of tests fix only 2 parameters. An analysis of the data produced by these tests have led to results that are quite coherent with those mentioned for the first three batteries of tests.

Summarizing, the above stated results and the ones obtained in the rest batteries of tests indicate that, in order to produce an evolved CA with enhanced capabilities for segmenting images from a benchmark data set, the following criteria or guidelines should be considered:

- Choose r_{max} lower than s_{min}.
- Choose $s_{min} - r_{max}$ positive and small.
- Keep the density of different regions, N, low .
- Changes in D_{max} do not substantially affect the results and eD and Pr may be fixed to 1 and 0.5 respectively due their low relevance in the MGCAs performance.

A comprehensive approach for the efficient acquisition and processing of hyperspectral images and sequences

Método integral para la adquisición y procesamiento eficiente de imágenes y secuencias hiperespectrales

Author/Autora: Blanca María Priego Torres

Doctoral Thesis / Tesis Doctoral / 2016

Advisor/Director:

Richard J. Duro Fernández

Programa Oficial de Doctorado en Computación[1]

[1]Programa regulado por el R.D. 1393/2007

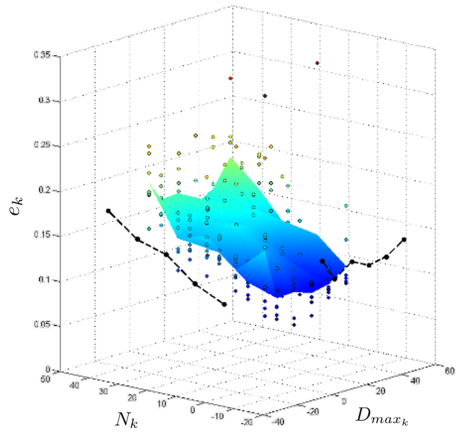

Figure 6.11: Averaged value of the cost function of each evolved CA once applied to the benchmark collection as a function of N and D_{max}

6.7 Application of ECAS-II generated MGCAs + SVM to hyperspectral images

To test the perfomance of the ECAS-II generated MGCA based segmentation algorithms, the whole strategy has been first applied to synthetic hyperspectral images to clearly demonstrate its validity in well controlled images. As a second step, the strategy was applied to well known real benchmark hyperspectral images in order to compare the results it produces to those of other algorithms found in the literature. Finally, the proposed algorithm has been tested using real hyperspectral images from the provided repository in order to consider image types and areas of the image parameter space that are usually ignored by the literature. It is important to note here that to perform comparisons, classification results are required. For this reason, the SVM classification step commented in section 6.5 has been added to the overall algorithm.

This section is organized as follows: in subsection 6.7.1, the ECAS-II generated MGCA (for simplicity we will refer to it as just ECAS-II) + SVM method is applied to synthetic hyperspectral images. This part is devoted to the demonstration of the impact of applying the ECAS-II method prior to the classification step over perfectly labelled multidimensional images. Afterwards, the capabilities of the CA are demonstrated with regards to how appropriately evolved CAs can adapt to different levels of segmentation, employing for this purpose also

synthetic hyperspectral images. Subsection 6.7.2 is focused on comparing the classification performance of the multistage ECAS-II + SVM algorithm to that of other existing techniques, when it is applied to real benchmark hyperspectral images. Finally, subsection 6.7.3 is devoted to demonstrating the suitability of the ECAS-II method for segmenting hyperspectral images coming from different scenarios, and contemplating other areas of the image parameters space using for this purpose real images from the our own repository.

The quality of the classification results has been computed using the quantitative metrics Overall Accuracy (OA), Average Accuracy (AA), Kappa coefficient (κ) and Class-specific accuracies (as defined in section 3.2.2 of chapter 3).

6.7.1 Application to synthetic hyperspectral images

This first experimental section is devoted to a quantitative analysis in order to demonstrate the capabilities of the ECAS-II method when applied to perfectly labelled and controlled multidimensional images. For this purpose, several images have been created synthetically. These test images have been constructed using five 64-band base spectra corrupted by noise, spectral mixtures and artifacts.

Fig. 6.12a displays the 13^{th} band of a synthetic image in which the pixels have been corrupted by a high level of random noise. A MGCA obtained using the ECAS-II algorithm is applied for 10 iterations to the noisy synthetic image and the resulting 13^{th} band is shown in Fig. 6.12b. The CA that was applied in this case was evolved using the parameters shown in Table 6.1. The SVM method has been trained using an extremely low number of reference samples, approximately 1 percent of each class. These training samples are marked with green dots in Fig. 6.12c. Additionally, Fig. 6.12d shows the classification map provided by the SVM method applied to the original synthetic image, and Fig. 6.12e the classification map when the SVM is applied to the segmented output provided by the CA. For both cases, misclassified pixels are marked with red dots. Table 6.3 permits noticing the improvement in terms of accuracy metrics introduced by the CA stage over the classification results using the raw SVM method.

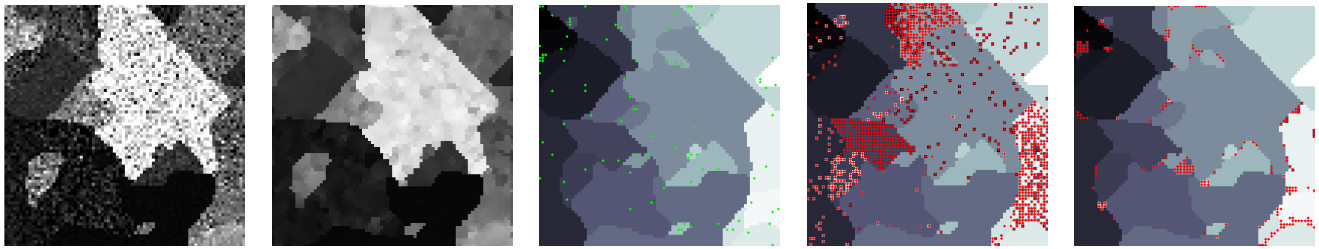

(a) (b) (c) (d) (e)

Figure 6.12: (a) 13^{th} band of a very noisy synthetic 64-band image. (b) 13^{th} band of the ECAS-II output, (c) Ground truth (green points represent training samples), (d) Classification produced by the SVM alone (red points represent misclassified pixels), (e) Classification produced by ECAS-II + SVM

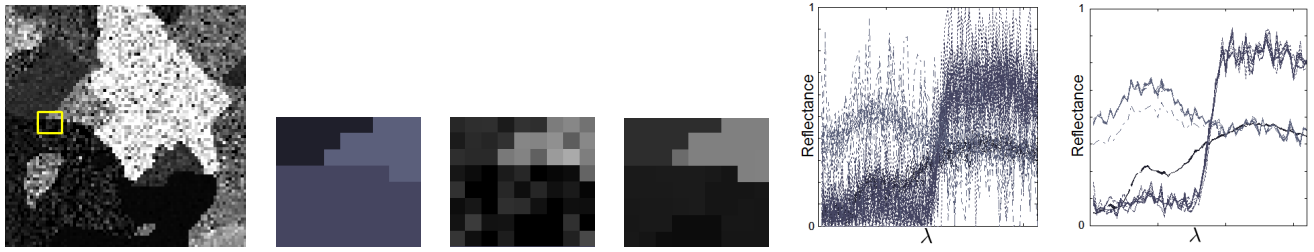

(a) (b) (c) (d) (e) (f)

Figure 6.13: (a) 13^{th} band of a very noisy synthetic 64-band image, (b) Detail (marked with a yellow square in Fig. 6.13a) of the associated ground truth, (c) 13^{th} band of the detailed area, (d) 13^{th} band of the ECAS-II output over the detailed area, (e) Spectra of pixels shown in 6.13c, (f) Spectra of pixels shown in 6.13d

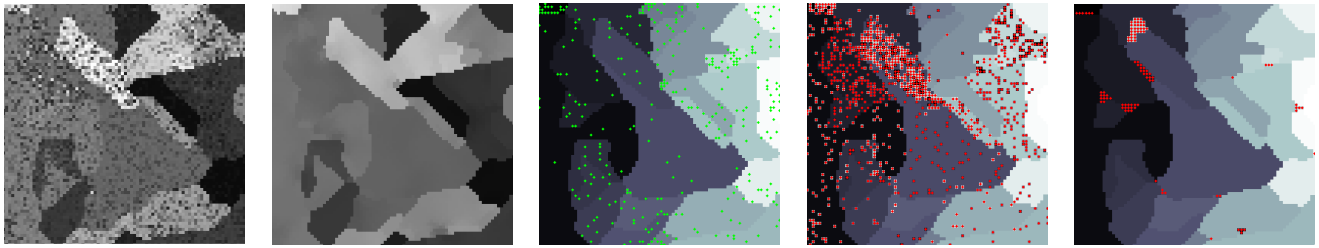

(a) (b) (c) (d) (e)

Figure 6.14: (a) 13^{th} band of a highly spectrally mixed synthetic 64-band image. (b) 13^{th} band of the ECAS-II output (c) Ground truth (green points represent training samples), (d) Classification produced using the SVM by itself (red points represent misclassified pixels), (e) Classification produced by ECAS-II + SVM

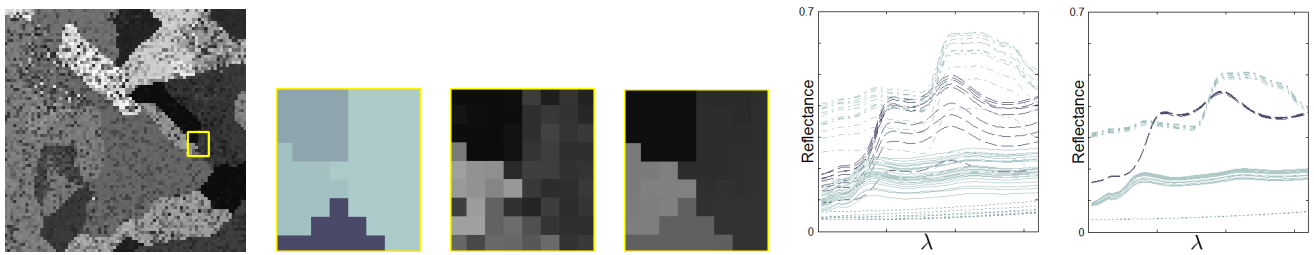

(a) (b) (c) (d) (e) (f)

Figure 6.15: (a) 13^{th} band of a highly spectrally mixed synthetic 64-band image, (b) Detail (marked with a yellow square in Fig. 6.15a) of the associated ground truth, (c) 13^{th} band of the detailed area, (d) 13^{th} band of the CA output over the detailed area, (e) Spectra of pixels shown in 6.15c, (f) Spectra of pixels shown in 6.15d

For the next experimental test, instead of adding random noise to corrupt the pixel spectra, we have created a synthetic 64-band image in which several spectra from a spectral database have been mixed to conform each pixel's spectrum. This situation is much more common, especially in remote sensing images, as it corresponds to endmember mixtures in pixels. The visual results for this test are shown in Fig. 6.14 and the classification accuracies obtained are indicated in Table 6.3. To better understand how the CA operates over this synthetic image, Fig. 6.15 depicts the effect of applying the CA over the spectra of pixels from a detailed area where four different regions intersect. Fig. 6.15e shows the original pixel spectra before the CA is applied. Fig. 6.15f represents the pixel spectra after 35 iterations in the CA application process.

Fig. 6.15f shows how the CA gradually modifies the pixel spectra until all pixels converge to some spectrum clusters. Thanks to this, as reflected in Fig. 6.15 and Table 6.3, the application of the CAs obtained using the ECAS-II algorithm simplifies the posterior classification stage and makes it more effective.

Table 6.3: Classification accuracies (%) for the raw pixel-wise SVM and the ECAS-II + SVM algorithm applied to the synthetic images shown in Fig. 6.12 and 6.14

Image	No of Training Samples	No of Test Samples	Metric	ECAS-II + SVM (%)	SVM (%)
Fig. 6.12	30	6370	OA	**96.96**	84.25
			AA	**93.02**	77.29
			κ	**96.65**	82.74
Fig. 6.14	309	6091	OA	**98.56**	84.40
			AA	**98.26**	80.73
			κ	**98.47**	83.24

Figure 6.16: Samples of the RGB dataset used to evolve CA #1 (left) and CA #4 (right) with the values of the parametric descriptors for the creation of the respective RGB image datasets

These first results support and validate the segmentation potential of the ECAS-II generated MGCA stage. These CAs have been produced using simple synthetic RGB image datasets for training and result in structures that when directly applied to multi-dimensional images produce satisfactory segmentations.

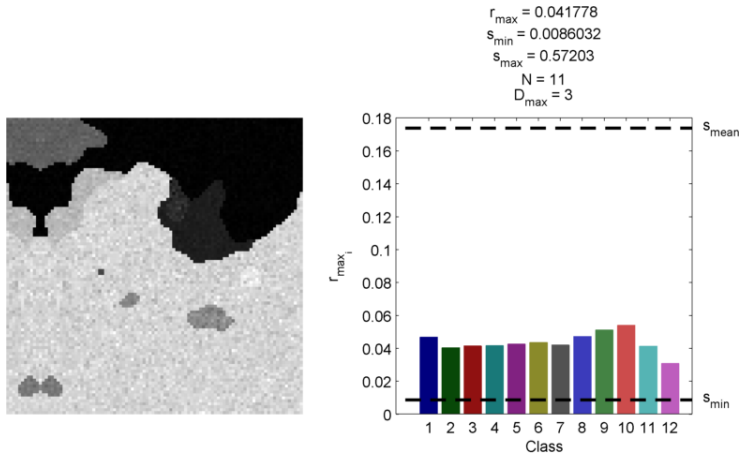

Figure 6.17: 20^{th} band of a synthetic 64-band image (left) and parametric descriptors of the original 64-band synthetic image (right)

In a third experiment, four different CAs, denoted as CA #1, CA #2, CA #3 and CA #4, have been evolved. Each evolution differs from the others in the set of RGB images used in the evaluation process. We will show below that the proper selection of the dataset for the evolutionary procedure will directly affect the kind of segmentation obtained when the CA is applied over RGB or hyperspectral images. The images of 6.16 present some samples of the RGB image dataset employed for the evolutionary processes to obtain the evolved CA #1 and CA #4. The text on the right of each image indicates the value of the parametric descriptors for the creation of the RGB image datasets used for evolving CA #1 and CA #4 respectively.

We will show below that the relation between intra-region spectral distance (r_{max}) and inter-region spectral distances ($[s_{min}, s_{max}]$) affects the segmentation result. That is, a RGB image dataset with a lower value of intra-region spectral distance will produce a CA that once applied to a RGB or hyperspectral image will result in a segmentation that contemplates fewer regions. On the other hand, a dataset with similar inter-region spectral distances that exhibits a

greater intra-region spectral distance will result in an evolved CA that produces more finely segmented images. Moreover, the proximity between intra-region and inter-region spectral distances in the RGB dataset also conditions the segmentation result after the application of the CA, as it was shown in section 6.6.

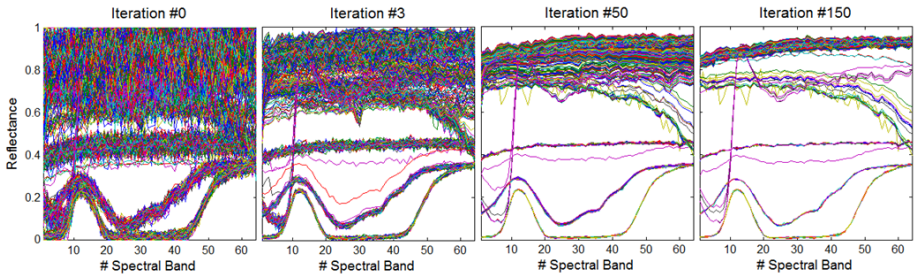

Figure 6.18: Evolution of the pixel spectra in the application of CA #2 on the synthetic hyperspectral image shown in Fig. 6.17

As testing dataset in this experiment, we have created a synthetic hyperspectral image set where the images contain 64 spectral bands (Fig 6.17). A total of 12 different spectral endmembers have been noised and blended taking into account spatial considerations. As a representation of the spatio-spectral characteristics of this synthetic hyperspectral image, the right graph of Fig. (Fig 6.17) shows its estimated parametric descriptors.

In the first place, to better understand how the CA operates over the images, Fig. 6.18 shows the evolution of the pixel spectra in the application of CA #2 to the synthetic hyperspectral image shown in Fig. 6.18. As previously indicated, the CA-based segmentation process consists in the gradual modification of the cell spectra until all pixels converge to some spectrum clusters. The first graph of Fig. 6.18 shows the original pixel spectra before CA #2 is applied. The other graphs of Fig. 6.18 represent the pixel spectra for different iterations in the CA application process. On the 150^{th} iteration, it is clear that the pixel spectra from the original synthetic image have been modified, making the detection of several spectral clusters easier.

Secondly, the four evolved CAs considered in this experiment have been applied to the example synthetic image. The segmentation results after 200 iterations in the CA process are shown in Fig. 6.19. It can be observed that each CA solves the segmentation task differently, merging or preserving spectrum clusters, leading to segmentations with different levels of detail.

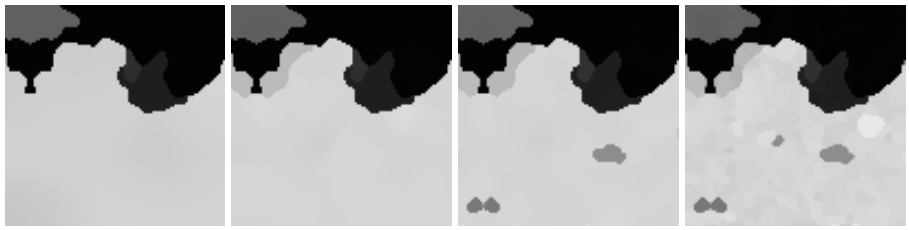

(a) (b) (c) (d)

Figure 6.19: 20^{th} band of the segmented synthetic image using CA #1 (a), CA #2 (b), CA #3 (c) and CA #4 (d).

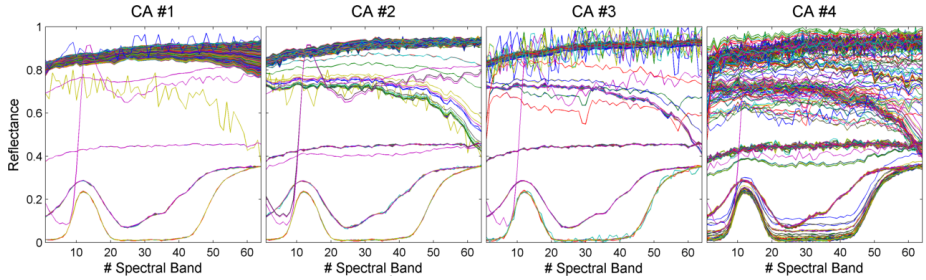

Figure 6.20: Pixel spectra after 200 iterations in the application of 4 different CAs to the synthetic image shown in Fig. 6.17

Fig. 6.20 shows the corresponding pixel spectra of the segmentations obtained in Fig. 6.19 after 200 iterations of the CAs. These graphs also exhibit the convergence of the original cell spectra to a different number of spectrum clusters depending on the specific CA that has been applied to the example image. As it can be observed in Fig. 6.19, CA #1 is the CA that produces a segmentation result with a smaller number of clusters, while in contrast, CA #4 is the CA that outputs a more detailed segmentation.

The results of this experiment support and validate one of the main goals of this work, that is, to establish a technique able to generalise the segmentation process, adapting the task to particular levels of segmentation.

6.7.2 Application to real benchmark hyperspectral images

Having tested the segmentation capabilities of the ECAS-II generated MGCAs, this section aims to verify their segmentation behavior over real images and to compare the performance of the approach to that of other methods extracted from the literature. To this end, three real hyperspectral scenes have been considered. The first hyperspectral image corresponds to the Pavia University scene. It is an image recorded by the ROSIS-03 satellite sensor. It has 115 bands and spatial dimensions of 610×340 pixels. The second hyperspectral image was captured by the AVIRIS sensor over Salinas Valley, CA, USA, and is composed of 224 bands with a spatial size of 512×217 pixels. Finally, the well-known Indiana scene is considered. It was recorded by the AVIRIS sensor over the Indian Pines test site in Northwestern Indiana. The Indiana scene has a spatial dimension of 145×145 pixels and 200-bands per pixel.

Before going into the application of ECAS-II to these scenes and the comparison of the results obtained to those published by other authors, as an illustration of the need to adapt the segmenting CA to the type of image and segmentation required, we are going to perform a parametric analysis of the spatio-spectral descriptors estimated from these images.

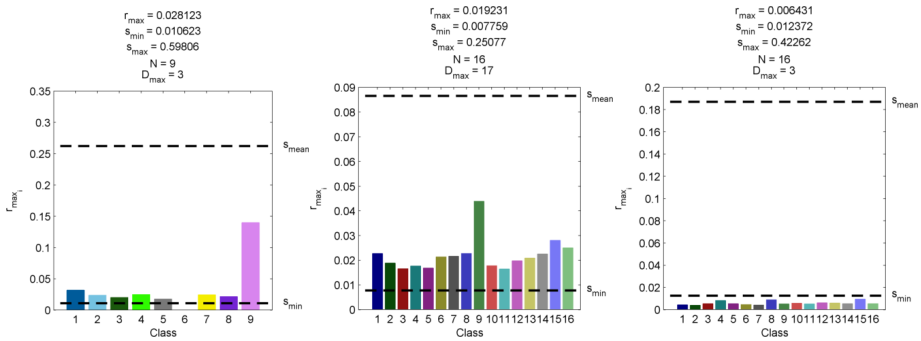

Figure 6.21: Representation of the values of the estimated spatio-spectral parameters extracted following the procedure presented in chapter 5 for Pavia (a), Indiana (b) and Salinas (c) scenes

The ground truth associated with each scene establishes the segmentation level desired by the user and the images themselves determine the type they belong to in terms of spectral and spatial characteristics, which are represented in Fig. 6.21 and estimated following the procedure described in chapter 5. The

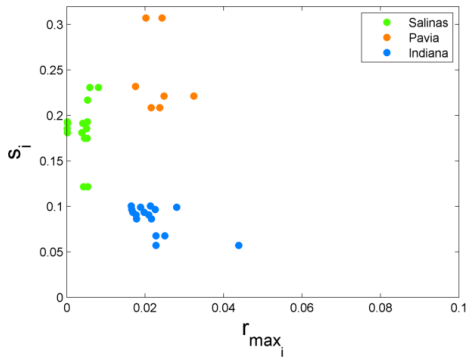

Figure 6.22: Averaged inter-class distance (y-axis) between each class and the rest of the classes vs. averaged intra-class distance (x-axis) of each class in terms of spectral angles normalized between 0 and 1 for Pavia, Indiana and Salinas scenes

four parametric descriptors are contemplated in Fig. 6.21 and each bar in these graphs represents the intra-spectral distance of each class individually. Additionally, Fig. 6.22 represents the averaged inter-class distance between each class and the rest of the classes vs. the averaged intra-class distance of each class for the Pavia, Indiana and Salinas scenes. In this graph it can be observed that the inter-class vs. intra-class distance points in terms of spectral angles normalized between 0 and 1 for each scene are located in different regions of the spectral parameter space. For example, the Salinas scene presents regions with low intra-class distances (r_{max_i}) and high inter-class distances (s_i), which presumably would make the segmentation or classification task easier. Conversely, the Indiana scene exhibits areas with relatively high intra-class distances compared to the inter-class distances, which may hinder the labeling for segmentation or classification methods.

It can be observed in these representations that each scene exhibits different combinations of parametric descriptors. It is our hypothesis that a CA that takes this into account will be better adapted to perform an improved segmentation leading to better classification performances when passed on to a subsequent classification stage.

Once the parametric descriptors that categorize a given type of hyperspectral image and segmentation process have been extracted, three different MGCAs have been trained using synthetic RGB images with feature parameters similar to those of the corresponding hyperspectral scenes. All the CAs were evolved using the parameters shown in Table 6.1 for the Differential Evolution algorithm:

each MGCA is made up of 30 rules, and each rule has 6 components, leading to a total of 180 real valued parameters in each chromosome; the Differential Evolution algorithm stops when the maximum number of generations (100) or a lower bound (1e-6) for the error used as fitness value is reached; the population size used was 100 in every case and the crossover and mutation probabilities were set to 0.7 and 0.8 respectively.

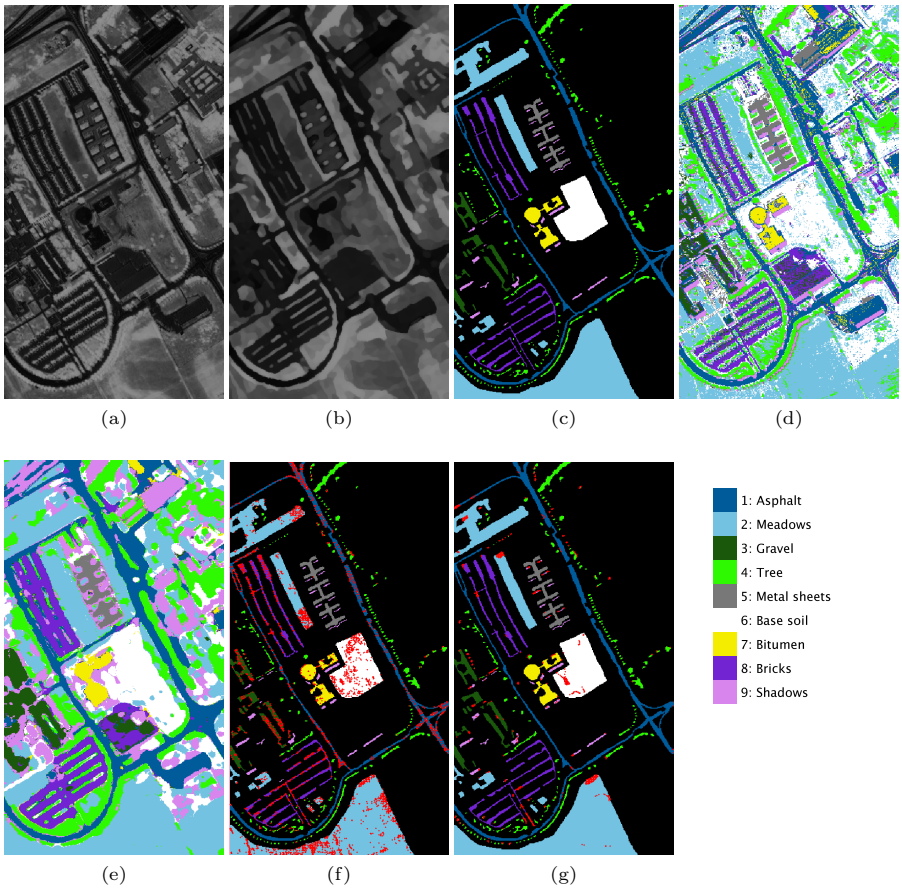

Figure 6.23: 2D transformation of the original scene (a) and of the ECAS-II segmented image (b), Ground Truth (c), SVM based classification applied to the original image (d) and to the ECAS-II segmented image (e), SVM based classification applied to the original scene showing only the labeled areas (red circles mark misclassified pixels) (f) and to the ECAS-II segmented image (g)

Before applying the SVM, the hyperspectral images were normalized with respect to the maximum spectral intensity found in the whole data cube. The specific C and γ parameters used for the SVM algorithm are indicated in Table 6.4. These have been selected by means of a fivefold cross validation procedure. Finally, the SVM for the classification of the Pavia image was trained using the number of samples shown in Table. 6.4, following the works of Tarabalka et al. [2010], Plaza et al. [2009b] and Lopez-Fandino et al. [2015]. The SVMs for classifying the Salinas and Indiana Scenes were trained using 10% of the samples for each class.

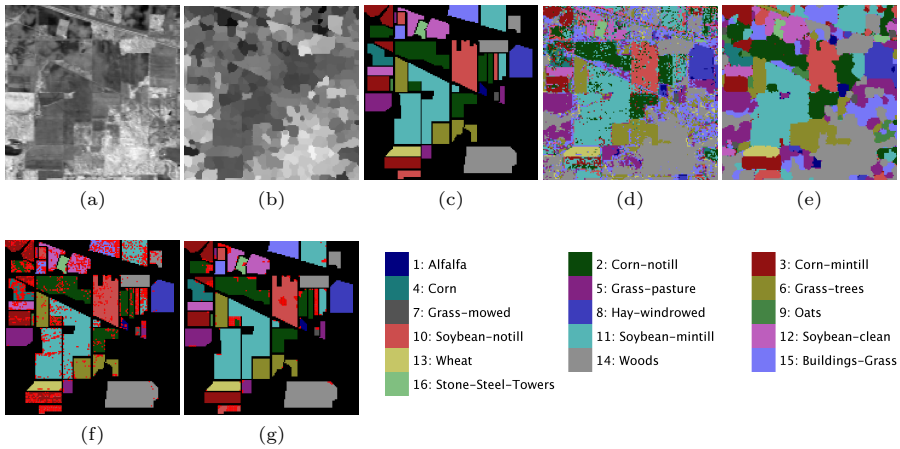

Figure 6.24: 2D transformation of the original scene (a) and of the ECAS-II segmented image (b), Ground Truth (c), SVM based classification applied to the original image (d) and to the ECAS-II segmented image (e), SVM based classification applied to the original scene showing only the labeled areas (red circles mark misclassified pixels) (f) and to the ECAS-II segmented image (g)

Fig. 6.23a, 6.24a and 6.25a show a 2D angular transformation of each original hyperspectral scene where each pixel corresponds to the angle between the spectrum of the pixel and a reference spectrum with all of its bands at the maximum value. Fig. 6.23b, 6.24b and 6.25b represent the 2D angular transformation after applying the MGCA obtained using ECAS-II. The ground truth of each scene is shown in Figs. 6.23c, 6.24c and 6.25c respectively. The final classification results for the raw SVM and ECAS-II + SVM algorithms are represented in Figs. 6.23d-6.23e, 6.24d-6.24e and 6.25d-6.25e. In all three cases it can be clearly appreciated that by introduing the MCGA stage in the processing of the images, the salt and pepper type noise resulting from the misclassified pixels of the pixel-wise SVM classification process that is present in

6.23d, 6.24d and 6.25d is drastically reduced. This is even more apparent in Figs. 6.23f-6.23g, 6.24f-6.24g and 6.25f-6.25g, where only pixels belonging to labelled areas are coloured. In these figures, we have indicated the pixels that were misclassified using red dots instead of providing the color corresponding to the class they were wrongly assigned to. These visual results show that the application of the ECAS-II MCGA prior to the SVM algorithm leads to a reduction of the misclassified pixels and that errors tend to take place in concentrated areas. The class specific accuracies for the raw pixel-wise SVM and the ECAS-II + SVM algorithms are presented in Table 6.4. From the quantitative results, it can be extracted that most of the classes experiment an improvement in terms of accuracy. In the case of the Pavia scene, the accuracy rise an average of 9.56% for 6 out of the 9 classes. The tree and metal sheets classes only suffer an accuracy decrement of only 1.80%. The accuracy for the shadow class from the Pavia scene is degraded (16.2%) by the application of ECAS-II. However, shadows are a controversial class because they do not represent a unique material by themselves (the class may include many different spectra), just different materials but with a low intensity spectrum. For the Indiana scene, the improvement in terms of class-specific accuracies after applying the ECAS-II is clear since 15 out of 16 classes saw an accuracy rise of 18.59% and only for the grass-mowed class the decrement is 0.03%. Finally, 12 classes of the Indiana scene increment their class-specific accuracy an averaged 2.33% while 4 classes see their accuracy decreased an averaged 0.95%. Is important to note that for the Salinas scene the result of applying the raw pixel-wise SVM is quite good, which restricts the margins for improvement for the ECAS-II.

To quantitatively compare the classification results obtained for these scenes to other approaches found in the literature, three reference algorithms have been selected. First, we have included in the comparison a purely spectral algorithm based on a pixel-wise SVM. In addition, we have considered three spatial-spectral algorithms. The first one is the EMP (extended morphological profiles) algorithm [Plaza et al., 2009b], the second one is a watershed transformation-based algorithm [Tarabalka et al., 2010], labeled as W-RCMG in Table. 6.5. The third algorithm is the V-ELM-1 implementation of ELM found in Lopez-Fandino et al. [2015]. We have restricted the comparisons between different methods to those with consistency in terms of the number of reference samples used for training the algorithms.

Table 6.4: Class specific accuracies (%) for the raw SVM and the ECAS-II + SVM algorithm applied to the Pavia, Indiana and Salinas Scenes

			Class-specific accuracies (%)	
	No of Training Samples	No of Test Samples	ECAS-II + SVM	SVM
PAVIA SCENE (SVM parameters: $C = 256$ $\gamma = 16$)				
1: Asphalt	548	6083	**99.34**	89.42
2: Meadows	540	18109	**99.94**	93.12
3: Gravel	392	1707	**98.24**	85.12
4: Tree	524	2540	95.59	**97.63**
5: Metal sheets	265	1080	97.59	**99.16**
6: Base soil	532	4497	**99.53**	92.75
7: Bitumen	375	955	**98.84**	92.04
8: Bricks	514	3168	**99.55**	85.63
9: Shadows	231	716	83.24	**99.44**
INDIANA SCENE (SVM parameters: $C = 512$ $\gamma = 0.5$)				
1: Alfalfa	5	41	**92.17**	55.12
2: Corn-notill	143	1285	**90.25**	78.35
3: Corn-mintill	83	747	**95.69**	65.03
4: Corn	24	213	**96.20**	57.75
5: Grass-pasture	49	434	**96.11**	89.54
6: Grass-trees	73	657	**98.55**	95.46
7: Grass-mowed	3	25	73.57	**73.60**
8: Hay-windrowed	48	430	**99.96**	97.40
9: Oats	2	18	**100**	56.67
10: Soybean-notill	98	874	**87.57**	72.31
11: Soybean-mintill	246	2209	**96.66**	83.29
12: Soybean-clean	60	533	**93.19**	67.58
13: Wheat	21	184	**98.44**	96.41
14: Woods	127	1138	**99.83**	94.85
15: Buildings-Grass	39	347	**97.04**	54.12
16: Stone-Steel-Towers	10	83	**88.60**	87.47
SALINAS SCENE (SVM parameters: $C = 512$ $\gamma = 8$)				
1: Weeds 1	201	1808	**100**	99.47
2: Weeds 2	373	3353	**99.88**	99.79
3: Fallow	198	1778	**100**	99.58
4: Fallow plow	140	1254	99.12	**99.35**
5: Fallow smooth	268	2410	**99.46**	98.88
6: Stubble	396	3563	99.80	**99.87**
7: Celery	358	3221	**99.78**	99.53
8: Grapes	1128	10143	**96.79**	88.84
9: Soil	621	5582	**99.88**	99.87
10: Corn	328	2950	**98.26**	96.89
11: Lettuce 4wk	107	961	**99.81**	99.15
12: Lettuce 5wk	193	1734	**100**	99.63
13: Lettuce 6wk	92	824	97.97	**99.54**
14: Lettuce 7wk	107	963	96.07	**98.03**
15: Vinyard untrained	727	6541	**93.27**	78.27
16: Vinyard trellis	181	1626	**99.46**	98.71

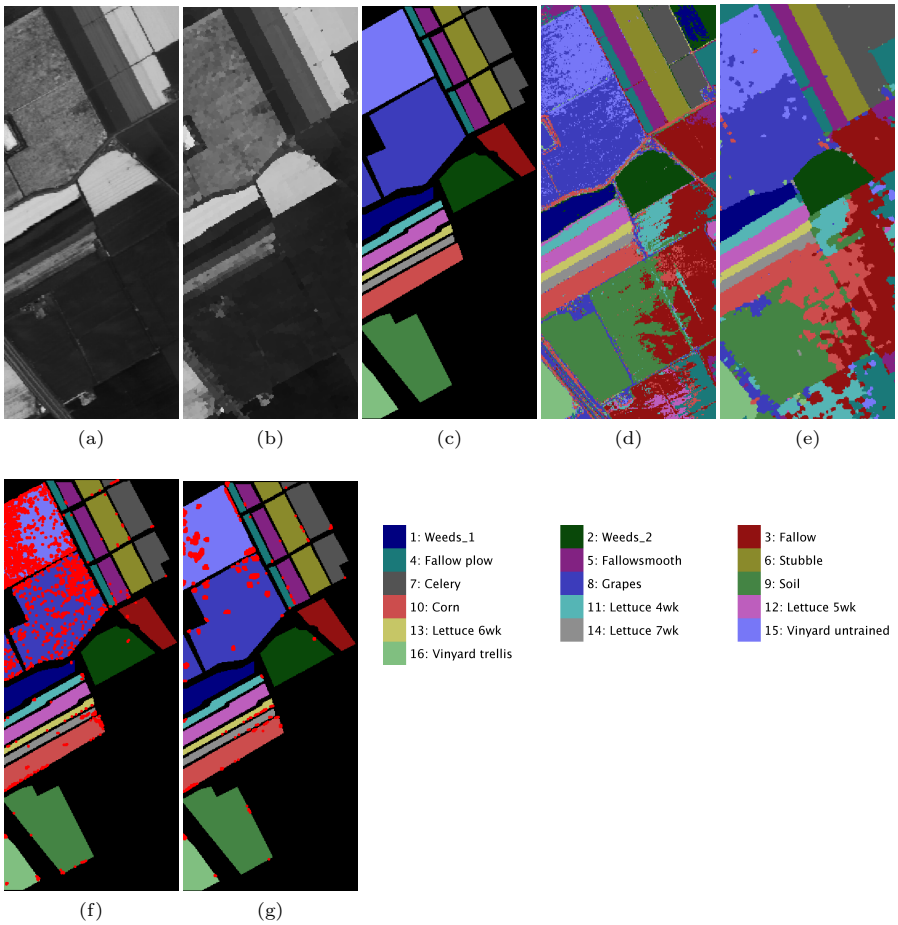

Figure 6.25: 2D transformation of the original scene (a) and of the ECAS-II segmented image (b), Ground Truth (c), SVM based classification applied to the original image (d) and to the ECAS-II segmented image (e), SVM based classification applied to the original scene showing only the labeled areas (red circles mark misclassified pixels) (f) and to the ECAS-II segmented image (g)

Table 6.5: Accuracy measurements (%) for different algorithms

	κ (%)	OA (%)	AA (%)
	PAVIA SCENE		
ECAS-II + SVM ($C = 256$, $\gamma = 16$)	**98.64**	**99.01**	**96.87**
SVM ($C = 256$, $\gamma = 16$)	89.43	92.16	93.00
SVM [Tarabalka et al., 2010] ($C = 128$, $\gamma = 0.125$)	75.86	81.01	88.25
W-RCMG [Tarabalka et al., 2010]	81.30	85.42	91.31
EMP [Plaza et al., 2009b]	96.05	97.07	96.79
V-ELM-1 [Lopez-Fandino et al., 2015]	95.00	96.66	95.92
	INDIANA SCENE		
ECAS-II + SVM ($C = 512$, $\gamma = 0.5$)	**94.48**	**95.12**	**93.99**
SVM ($C = 512$, $\gamma = 0.5$)	78.06	80.82	76.56
SVM [Tarabalka et al., 2010] ($C = 1024$, $\gamma = 2^{-7}$)	75.73	78.76	69.66
W-RCMG [Tarabalka et al., 2010]	91.39	92.48	77.26
	SALINAS SCENE		
ECAS-II + SVM ($C = 512$, $\gamma = 8$)	**97.87**	**98.09**	**98.72**
SVM ($C = 512$, $\gamma = 8$)	93.62	94.27	97.21

It can be observed that the ECAS-II technique followed by a SVM pixel-wise classification stage is the algorithm that provides the best classification accuracies in the three measures considered.

Finally, for each hyperspectral scene, ECAS-II is applied and the SVM is run using different percentages of samples for each class. Table 3 presents the quantitative improvement in terms of OA, AA and Kappa, showing that the ECAS-II segmentation algorithm improves the SVM results in every case, but, most importantly, even when the number of samples considered in the training process of the classification algorithm is very limited, which is a great advantage of the proposed method.

This subsection was aimed at comparing the performance of ECAS-II to that of other methods extracted from the literature using a set of widely used hyperspectral images. However, testing algorithms using only these scenes would not take into account the diverse casuistry of spectral and spatial characteristics that may appear in hyperspectral images. In order to verify that the results of applying the ECAS-II strategy are not skewed depending on the particular properties of these scenes, the following subsection is devoted to the validation of ECAS-II using hyperspectral images extracted from the GII-HSEG repository, which present different spectral and spatial features than the hyperspectral scenes processed hitherto.

Table 6.6: Improvement in accuracy measurements (%) when the CA is applied before the SVM classification algorithm.

		% of training samples				
		2	5	20	50	80
Pavia Scene	$\Delta OA(\%)$	**5.20**	4.97	4.37	3.52	3.00
	$\Delta AA(\%)$	2.87	**3.59**	3.20	2.82	2.29
	$\kappa(\%)$	**6.93**	6.61	5.79	4.67	3.98
Indiana scene	$\Delta OA(\%)$	**20.42**	17.72	10.62	7.68	9.24
	$\Delta AA(\%)$	**28.12**	18.71	9.25	8.66	10.35
	$\kappa(\%)$	**23.59**	20.32	12.12	8.77	10.56
Salinas Scene	$\Delta OA(\%)$	3.36	3.36	**4.16**	3.88	3.60
	$\Delta AA(\%)$	**2.03**	1.24	1.65	1.47	1.32
	$\kappa(\%)$	3.75	3.74	**4.63**	4.32	4.01

6.7.3 Application to real hyperspectral images from the GII-HSEG repository

This last experimental subsection has been included here with the purpose of validating the ECAS-II over hyperspectral images with different spatial and spectral parameter descriptors than those of the presented in the Salinas, Pavia and Indiana scenes. This would ensure that the ECAS-II strategy is valid independently of the type of hyperspectral images on which it is applied.

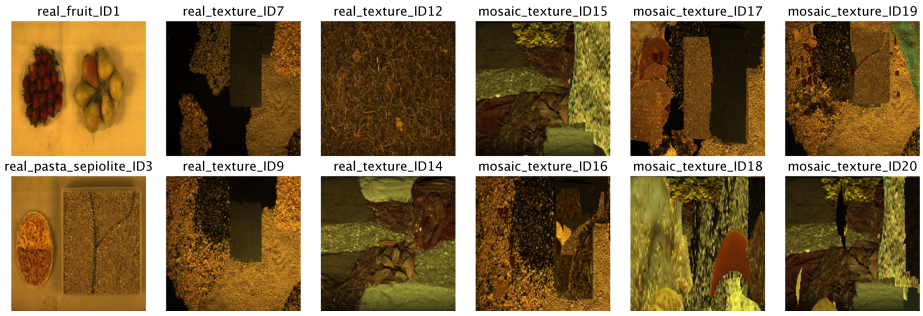

Figure 6.26: RGB false-color composition of hyperspectral images used in Fig. 6.27

Thus, this section is devoted to the application of the proposed method using as test images those extracted from our own repository, with the following threefold objective: firstly, to assess the validity of the ECAS-II method over hyperspectral images that exhibit different parametric descriptors than those of the benchmark images processed in the previous subsection; secondly, to

A comprehensive approach for the efficient acquisition and processing of hyperspectral images and sequences

Método integral para la adquisición y procesamiento eficiente de imágenes y secuencias hiperespectrales

Author/Autora: Blanca María Priego Torres

Doctoral Thesis / Tesis Doctoral / 2016

Advisor/Director:

Richard J. Duro Fernández

Programa Oficial de Doctorado en Computación[1]

[1]Programa regulado por el R.D. 1393/2007

check the necessity of including spatial information in processing algorithms by comparing the pixel-wise SVM with the ECAS-II + SVM performances; and finally, to validate the test use cases and test scenarios captured indoors using our hyperspectral imagers.

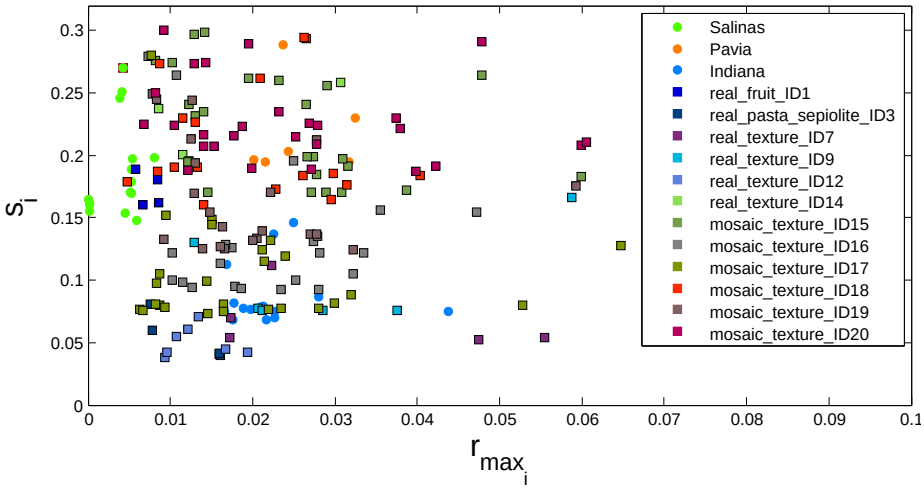

Figure 6.27: Averaged inter-class distance (y-axis) between each class and the rest of the classes vs. averaged intra-class distance (x-axis) of each class in terms of normalized spectral angle between 0 and 1 for Pavia, Indiana, Salinas scenes and selected images from the GII-HSEG repository

The images from the GII-HSEG repository cover different types of scenarios: isolated low-textured objects over a light background, isolated highly-textured regions over a light background, adjacent highly-textured regions without a common background and objects half-buried under materials of great heterogeneity and profuse texture. Fig. 6.27 graphically shows the spectral variations between different scenes, by representing the averaged intra-class distance of each class vs. the averaged inter-class distance between each class and the rest classes in terms of normalized spectral angle between 0 and 1 for the Pavia, Indiana, Salinas scenes and some images from the GII-HSEG repository (Fig. 6.26). In this graph it can be observed that the hyperspectral image labelled as *real_texture_ID7* exhibits high intra-class distances (r_{max_i}) keeping the inter-class distances (s_i) low. On the other hand, image *real_fruit_ID1* presents low spectral distances between pixels belonging to the same class but the spectral distance between pixels from different classes is quite high. The idea here was to select images aiming to complement the spectral parameter space. It can be noticed that there are no points in the spectral parameter

space for which $r_{max_i} > s_i$. This is because the difficulty of setting up a scene in which pixels belonging to a same class are more spectrally heterogeneous than the spectral differences between pixels from distinct classes. For a better grasp of Fig. 6.27, in Fig. 6.28 the spectra of some pixels belonging to the *real_texture_ID7*, *real_texture_ID12*, *mosaic_texture_ID15* and *mosaic_texture_ID20* scenes are shown. For each graph, the spectra of randomly selected pixels belonging to a certain class from the corresponding scene are plotted in color following the legend of Fig. 6.27, while the spectra from the remaining classes for the same scene are plotted in black. It is worth noting that, for example, in the case of the *real_texture_ID7* scene, the spectral distances between pixels belonging to the same selected class are almost the same as the ones with respect to pixels from the remaining classes, which is in line with a high value of r_{max_i} and a low value of s_i.

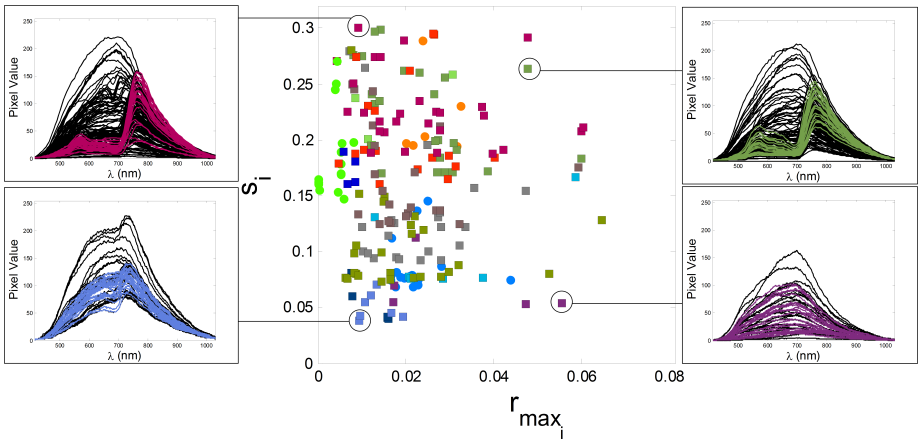

Figure 6.28: Spectra of pixels from the *real_texture_ID7*, *real_texture_ID12*, *mosaic_texture_ID15* and *mosaic_texture_ID20* scenes. For each graph, spectra of randomly selected pixels belonging to certain class from the corresponding scene are plotted in color following the legend of Fig. 6.27, while spectra from the remaining classes for the same scene are plotted in black.

From these twelve hyperspectral scenes, we have selected five images in order to assess the validity of the ECAS-II method. The spatial and spectral characteristics of the selected hyperspectral images are shown in Table 6.7. The spatial aspect ratio of the hyperspectral images has been modified leading to the spatial resolution shown in the second column of this table.

These images have been classified using a SVM algorithm with the specific C and γ parameters shown in Table 6.8 and these have been selected through a fivefold cross validation procedure. The SVM algorithm has been applied pixel-wise to the original datacube and to the segmented image provided by the ECAS-II. The SVM method has been trained and applied 10 times using different training samples. The averaged accuracy performances obtained are shown in Table 6.8.

Table 6.7: Spatial and spectral properties of the images selected from the GII-HSEG repository

Image	Spatial Resolution	N. spectral bands	Spectral Range (nm)	r_{max}	$[s_{min}, s_{max}]$	N	D_{max}
real_fruit_ID1	223×223	342	$[413, 1030]$	0.0086	[0.0380.272]	4	25
real_pasta_sepiolite_ID3	200×200	342	$[413, 1030]$	0.0142	$[0.0061, 0.089]$	6	25
real_texture_ID7	200×200	342	$[413, 1030]$	0.0416	$[0.0093, 0.1816]$	7	10
real_texture_ID9	200×200	342	$[413, 1030]$	0.0252	$[0.0262, 0.2293]$	9	10
real_texture_ID12	200×200	342	$[413, 1030]$	0.021	$[0.0090, 0.154]$	12	12

Table 6.8: Classification accuracies (%) for the raw SVM and the ECAS-II + SVM algorithm applied to real hyperspectral images from the GII-HSEG repository

	C	γ	No of Training Samples	No of Test Samples	κ (%)	OA (%)	AA (%)
real_fruit_ID1:							
SVM	512	0,0312	103	9884	82.76	87.41	86.18
SVM + ECAS-II					**87.47**	**90.85**	**89.31**
real_pasta_sepiolite_ID3:							
SVM	512	0,5	408	19886	71.60	78.86	81.24
SVM + ECAS-II					**91.73**	**93.83**	**93.92**
real_texture_ID7:							
SVM	512	0,5	803	39197	88.44	91.06	81.37
SVM + ECAS-II					**91.24**	**93.18**	**90.78**
real_texture_ID9:							
SVM	512	0,0312	804	39196	82.31	86.30	85.02
SVM + ECAS-II					**92.38**	**94.10**	**93.95**
real_texture_ID12:							
SVM	32	2	51	908	46.07	68.03	43.92
SVM + ECAS-II					**78.40**	**87.10**	**68.53**

In this section, the segmentation step has been carried out using three different evolved MGCAs, the first one to segment image *real_fruit_ID1*, the second one to segment image *real_pasta_sepiolite_ID3* and the third one to segment images *real_texture_ID7*, *real_texture_ID9* and *real_texture_ID12*.

Visual results for all the images are shown in Fig. 6.28. The images of Fig. 6.28a show the RGB false-color composition for each scene. Fig. 6.28b and 6.28c depict a 2D transformation of the original scenes and the segmentation results provided by ECAS-II. The ground truths are presented in Fig. 6.28c and their legends are displayed above the row corresponding to each scene. Fig. 6.28e and 6.28f represent the SVM based classification applied to both the original scene and the segmented one provided by ECAS-II. In these last images only the labeled areas are colored in gray and misclassified pixels are colored in red of varying intensity (a brighter red pixel means that it has been misclassified more times when the SVM algorithm has been repeatedly applied 10 times).

All the SVM results, applied to the original or segmented scenes, demonstrate that the selected use cases (discrimination between types of fruits, degree of ripeness, etc.) are appropriate to benefit from hyperspectral technology. The improvement that the ECAS-II segmentation step introduces in the accuracy performances depends on the spatial and spectral characteristics of the scene. When the regions exhibit high levels of spatio-spectral textures, the inclusion of spatial information is highly relevant in order to obtain better classification performances. This is more noticeable in images *real_pasta_sepiolite_ID3* and *real_texture_ID12*, where the increase in the accuracy measurements is $\Delta\kappa = 20.13\%$, $\Delta OA = 14.97\%$, $\Delta AA = 12.68\%$ and $\Delta\kappa = 32.33\%$, $\Delta OA = 19.07\%$, $\Delta AA = 24.61\%$ respectively. In image *real_pasta_sepiolite_ID3*, the difference between sepiolite and perfumed sepiolite classes is an added purple-colored component of much lower granularity that gives off the smell of the perfumed sepiolite and is responsible for the salt-and-pepper noise in the classification result of directly applying the SVM to the original scene. In image *real_texture_ID12*, the fact that objects are half-buried poses a further difficulty for the classification task, and that is the reason for the worst result in terms of accuracy performances for the SVM applied to the original image. However, the inclusion of spatial information by means of the ECAS-II segmentation step significantly improves the classification accuracies for this case.

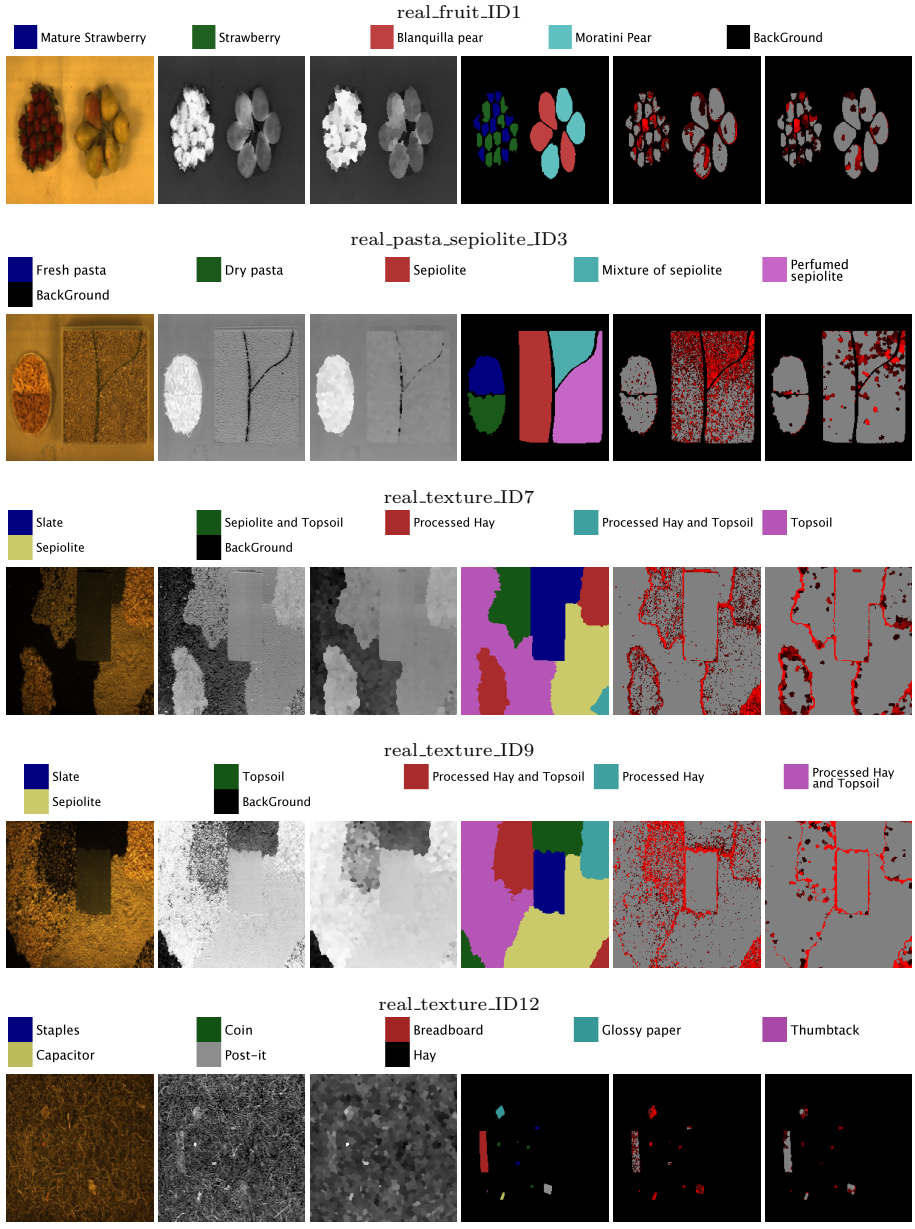

Figure 6.28: RGB false-color composition (a), 2D transformation of the original scene (b) and of the segmented image provided by ECAS-II (c), ground truth (d), SVM based pixel classification applied to the original scene (e) and to the segmented image provided by ECAS-II (f) showing only the labelled areas and marking misclassified pixels with red dots (a brighter red pixel means that it has been misclassified more times after applying the SVM algorithm 10 times)

6.8 Summary

This chapter has presented a strategy for the processing of hyperspectral images that solves the issues related to the segmentation of multidimensional data, particularly, the lack of appropriately labeled reference images, the user or application dependence of the required segmentation and the use of all the information provided by the high dimensionality of the images. This has been addressed following a methodology in which a dimension independent cellular automata based structure called Multi-Gradient based Cellular Automata (MGCA) has been proposed. Also an evolutionary approach, called ECAS-II, allows for generating the appropriate transition rules for MGCAs, using for this purpose low dimensional synthetic training images. These images, that reflect the same parametric categorization as the real images to be processed, can be picked from a synthetic image repository or created on-line following the procedure introduced in the previous chapter.

Regarding general issues of the proposed method, ECAS-II segmenters can operate over multi dimensional images with different numbers of spectral bands. In this work, the MGCAs used have been evolved using RGB images. After that, they have been applied to synthetic images consisting of 64 bands, as well to real hyperspectral images with different numbers of spectral bands (115, 200, 224 and 342 bands). In all cases, the performance results verify the applicability of the method to multi-dimensional images.

It is also important to note that the segmentation MCGAs obtained this way avoid projecting information onto lower dimensionalities during the segmentation process, which could lead to information loss. In fact, they work by modifying the whole spectrum as shown in Fig. 6.13 and Fig. 6.15, which illustrate that the effect is indeed a gradual spectral modification of pixels that belong to the same region, achieving this way spectral homogenization.

On the other hand, and regarding image dependent issues, the methodology followed to tune the transition rules of the MGCA makes it possible to obtain CA segmenters that can adapt to images with different spectral and spatial features. In all the test cases, the inclusion of the ECAS-II segmenters in the processing chain improves the classification accuracy results. The amount of improvement produced by the application of the ECAS-II generated MGCAs depends on the intrinsic characteristics of the images, as well as on the type of noise or artifacts present in the hyperspectral image being processed. In

this line, ECAS-II MGCA segmenters will be more efficient when spatial information is key to performing a more robust classification. This can be noticed in Table 6.5 (benchmark images) and in Table 6.8 (images captured with our own imager). From the benchmark hyperspectral images, the Indiana scene is the noisiest and lowest-resolution image considered in the experimental section and, consequently, for this image the inclusion of spatial information is crucial to perform an accurate segmentation and classification. For this reason, the increase in OA is about a 15% with respect to a raw classification for this scene. Concerning the images selected from the GII-HSEG image repository, images labeled as *real_pasta_sepiolite_ID3* and *real_texture_ID12* exhibit highly-textured regions and consequently the inclusion of the segmentation step provided by the ECAS-II algorithm results in a $\Delta OA = 14.97\%$ and $\Delta OA = 19.07\%$ increase respectively.

Additionally, the non-uniformities present in a hyperspectral image can derive from artifacts and noise in the acquisition process, changing lighting conditions or spectral mixtures. These non-uniformities are also highly relevant to the performance of the segmentation and classification process. In subsection 6.7.1, the ECAS-II method has been tested using synthetic hyperspectral images created with a high level of random noise and with a high level of spectral mixtures. In both cases, the classification performance (Table 6.3) is higher ($\Delta OA \approx 14\%$) when the ECAS-II MGCA step is introduced. These initial data indicate that performance is better in the case of spectral mixtures.

Finally, the algorithm has been compared to state-of-the-art classification methods by means of its application to the segmentation of real hyperspectral images. The accuracy results show that the ECAS-II + SVM algorithm outperforms the state of the art methods in all cases.

Chapter 7

4DCAF: A Temporal Approach for Denoising Hyperspectral Image Sequences

7.1 Introduction

This chapter deals with the preprocessing of hyperspectral image sequences as a previous step to other applications such as segmentation or classification tasks. In particular, the method proposed here is aimed at noise filtering or denoising of sequences that are significantly corrupted by noise. This problem is very common in some applications, especially when the spectral coverage of the data reaches the thermal domain.

Denoising or restoration of images is one of the most researched topics within the image processing field in the last two decades. Most of the algorithms that have been developed are focused on processing single images (2-D approaches) [Rudin et al., 1992, Portilla et al., 2003, Buades et al., 2005, Aharon et al., 2006, Luisier and Blu, 2008, Dabov et al., 2006], on denoising video sequences [Dabov et al., 2007, Priego et al., 2013b, Maggioni et al., 2013] or still hyperspectral

images [Peng et al., 2014, Renard et al., 2008, Liu et al., 2012, Lam et al., 2012, Liao et al., 2015, Salmon et al., 2014]. However, until recently, hyperspectral acquisition technology was not mature enough to enable the acquisition of temporal sequences of hyperspectral images. It is for this reason that, while there is an abundant literature on denoising (standard) video sequences or denoising (still) hyperspectral images, there are very limited contributions towards the denoising of whole hyperspectral image sequences.

Facing the problem of denoising hyperspectral image sequences, we found that this preprocessing task poses a challenge due to several factors. Firstly, the addition of temporal information makes the data more complex to process. A preliminary solution to this would be to work separately with frames or process the temporal sequence band by band. However, this would not take advantage of temporal or inter-band information diversity. On the other hand, the type of noise that corrupts the image sequences may vary from one sequence to another and spectral variations that are consequence of the temporal acquisition may appear. Thus, the denoising method should adapt to the particular characteristics of the hyperspectral scene, acquisition conditions and noise model. Concerning operational issues, just as for the segmentation case seen in the previous chapter, the availability of hyperspectral images sequences is extremely scarce, which makes the training and validation of denoising algorithms complex and cumbersome. Finally, taking under consideration that denoising is a preprocessing task, a desired characteristic of noise filtering methods is that they must be applied in real-time.

In view of the above, this chapter presents a strategy for the denoising of hyperspectral image sequences based on the application of a cellular automata structure called 4DCAF (4-dimensional cellular automata based filtering). The transition rules that govern the denoising behavior of the 4DCAF are tuned following an evolutionary process called ECAF (evolutionary method for obtaining cellular automata filters), fed by synthetic hyperspectral image sequences functioning as training datasets. These are created reflecting similar characteristics to those of the real image sequences to be denoised. The proposed method presents a solution for the denoising of hyperspectral image sequences, simultaneously meeting the following aspects:

- The method is able to adapt to hyperspectral image sequences exhibiting different spatial, spectral and temporal features, as well as to different types of noise that may corrupt the image sequences. This is addressed by using appropriate synthetic image sequences as training dataset for the evolutionary algorithm.
- The 4DCAF structure iteratively filters each frame of the sequence explicitly taking the temporal, spectral and spatial diversity into account.
- It presents intrinsically parallel low-level processing operations, which enables its implementation in a concurrent fashion over hardware such as GPUs.
- The proposed methodology outperforms several state-of-the-art algorithms on both simulated and real sequences.

The ECAF methodology was originally conceived to address the denoising of highly noised single-band image sequences. After validating its effectiveness, it was extended and adapted to the denoising of whole hyperspectral image sequences. This is why the following subsections describe both methods, denoting the CA-based filtering structures (CAF) for the spatio-temporal denoising of single-band and hyperspectral image sequences as st-CAF and 4DCAF, respectively. For both cases, the ECAF methodology for obtaining the CAF structures remains practically the same.

The remainder of this chapter is organized as follows. Section 7.2 introduces the proposed st-CAF and 4DCAF structures. Sections 7.3 and 7.4 present the procedure followed to determine the transition rules of the cellular automata based structures (ECAF), including the synthetic image sequence construction step. Sections 7.5 and 7.6 address the experimental results of applying the denoising algorithms over both synthetic and real image sequences. Finally, some concluding remarks are summarized in section 7.7.

7.2 Cellular Automata based Filtering

As introduced in the previous chapter, a cellular automaton is a spatially extended decentralized model made up of cells which communicate only with their neighbors and continuously update their state. If those cells represent

pixels and neighbors are assigned based on spatial, spatio-temporal or spatio-spectro-temporal distance measurements, the automaton recreates the effect of an image filter. Cellular automata have been widely used for the study of complex systems based on multicomponent models, but they have been extended for image filtering only in some preliminary works [Hernandez and Herrmann, 1996, Popovici and Popovici, 2002, Wang et al., 2004a, Selvapeter and Hordijk, 2009].

In this context, we present two novel CAF architectures, the spatio-temporal cellular automata-based filter (st-CAF), for single-band image sequence denoising, and the 4-dimensional cellular automata based filter (4DCAF), for the denoising of hyperspectral image sequences. The essential purpose of the proposed cellular automaton structures is to modify the intensity value or spectra of every cell so that after a number of iterations, every frame of the image sequence converges to a denoised version of it.

The rules that govern the behavior of CA-based filtering structures are automatically obtained through an evolutionary strategy named ECAF. Starting from a random rule set, the evolutionary process runs until it reaches a predefined performance and the resulting evolved cellular automaton, st-CAF or 4DCAF as the case may be, constitutes the noise reduction filter. These rules will be optimized to denoise image sequences coming from specific sources and corrupted by specific types of noise depending on the dataset used to determine the fitness of the rule set during the evolutionary process. Fig. 7.1 shows a schematic representation of the process.

7.2.1 General operation of st-CAF and 4DCAF

In particular, in st-CAF a cell of the automaton is placed over each pixel of the image sequence and the state of the cell is given by the gray-scale intensity value of this pixel (s_i), taking values in the range $[0, 1]$ (after a linear rescaling). In the case of a 4DCAF structure, a cell of the automaton is also situated over each pixel of the image sequence but the state of the cell ($\boldsymbol{s_i}$) is given by an N-band spectrum, taking values for each band in the range $[0, 1]$.

The CAF structure (st-CAF or 4DCAF) is executed K times over a section of the hyperspectral image sequence centered on a temporal single-band or hyperspectral frame f, whose cells are gradually modified converging towards a denoised version of it. Once a frame is properly denoised, the CAF is moved to the next frame, performing again the denoising operation.

The core of the operation of the CAF relies on the criteria which define the updating of the cell state. In both st-CAF and 4DCAF structures, this updating is based on one hand, on information on the intensity or spectral values of the $N_S \times N_S \times N_T$ closest neighboring cells, where N_S and N_T are the spatial and temporal size of the window in which every cell is centered. On the other hand, it depends on the set of updating/transition rules that control the automaton behavior.

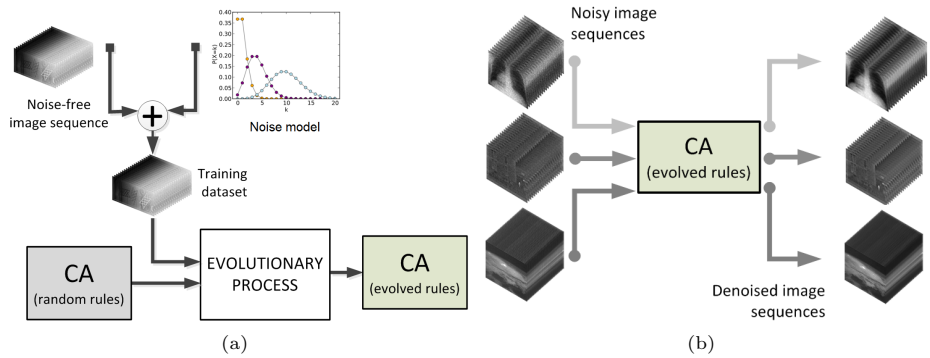

Figure 7.1: (a) Representation of the evolutionary process, ECAF, to automatically generate the CAF rule set which will perform the denoising of image sequences with particular features and (b) representation of the application of the st-CAF or 4DCAF structures on real noisy image sequences

Following the same reasoning as for the MGCA structure described in chapter 6 when dealing with hyperspectral images, in order to consider the spectral information of the neighboring cells when denoising image sequences by means of the 4DCAF structure, we have selected as distance measure the spectral angle (SA), normalized between 0 and 1. Thus, for a cell i corresponding to a pixel spectrum, the normalized spectral angle, $\alpha_{i,j}$ with respect to its neighboring cell j is defined as:

$$\alpha_{i,j} = \frac{2}{\pi} cos^{-1} \left(\frac{\sum \boldsymbol{s_j s_i}}{\sqrt{\sum \boldsymbol{s_j}^2} \sqrt{\sum \boldsymbol{s_i}^2}} \right) \tag{7.1}$$

where the summation is performed over the components of the state of $\boldsymbol{s_i}$, i.e., the spectral dimension of a pixel.

7.2.2 Deciding on the appropriate transition rule and updating the state of the CA

In st-CAF and 4DCAF, local information is extracted based on the gradient vector ($\mathbf{G}$) of the cell, taking into account the pixels contained in an $N_S \times N_S \times N_T$ 3-dimensional window. The use of gradient measurements has been widely used in the image processing field, mainly to address common tasks such as border detection, segmentation, classification or denoising since these gradient values will provide information about the strength and direction of intensity changes in each pixel of the image sequence, which is usually very relevant. The crux of the process is that the CAF structure, through the transition rule set, is able to distinguish between fluctuations among neighboring pixels due to real edges or noise and of applying the proper modifications in order to reduce noise without losing sharpness.

In order to calculate the gradient vector, three different 3-dimensional masks (Fig. 7.2) are applied to the pixel, obtaining this way three gradient components: G_X, G_Y and G_T.

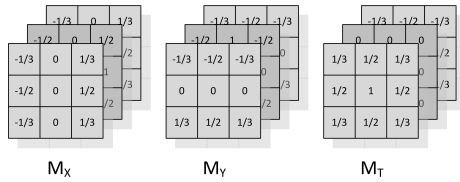

Figure 7.2: Gradient filter masks for $N_S = 3$ and $N_T = 3$. Closer neighbors are given a higher weight than pixels that are slightly further away from the pixel that is being filtered

When st-CAF is applied to a single-band image sequence, the $\mathbf{G} = (G_{X_{N_{S_i}}}, G_{Y_{N_{S_i}}}, G_{T_{N_{T_i}}})$ is calculated as:

$$
\begin{aligned}
G_{X_{N_{S_i}}} &= \sum_{j=1}^{N_S \cdot N_S \cdot N_T} s_j \cdot M_{X_{N_{S_j}}} \\
G_{Y_{N_{S_i}}} &= \sum_{j=1}^{N_S \cdot N_S \cdot N_T} s_j \cdot M_{Y_{N_{S_j}}} \\
G_{T_{N_{T_i}}} &= \sum_{j=1}^{N_S \cdot N_S \cdot N_T} s_j \cdot M_{T_{N_{T_j}}}
\end{aligned}
\tag{7.2}
$$

where $M_{X_{N_{S_j}}}$, $M_{Y_{N_{S_j}}}$ and $M_{T_{N_{T_j}}}$ represent the j^{th} elements of the gradient masks $M_{X_{N_S}}$, $M_{Y_{N_S}}$ and $M_{T_{T_S}}$ (horizontal, vertical and temporal masks respectively) and s_j is the intensity value of pixel j within the $N_S \times N_S \times N_T$ 3-dimensional window centered on pixel i.

On the other hand, the value of **G** when 4DCAF is applied to a hyperspectral image sequence is calculated as:

$$
\begin{aligned}
G_{X_{N_{S_i}}} &= \sum_{j=1}^{N_S \cdot N_S \cdot N_T} \alpha_{i,j} \cdot M_{X_{N_{S_j}}} \\
G_{Y_{N_{S_i}}} &= \sum_{j=1}^{N_S \cdot N_S \cdot N_T} \alpha_{i,j} \cdot M_{Y_{N_{S_j}}} \\
G_{T_{N_{T_i}}} &= \sum_{j=1}^{N_S \cdot N_S \cdot N_T} \alpha_{i,j} \cdot M_{T_{N_{T_j}}}
\end{aligned}
\tag{7.3}
$$

where $\alpha_{i,j}$ denotes the normalized spectral angle between a cell i and its neighboring cell j .

The modulus of the spatial projection of the gradient vector ($\rho_P = \sqrt{G_X^2 + G_Y^2}$) and the absolute value of the temporal component (G_T) are taken as the information the CAF needs in order to operate. Then, ρ_P is related to the intensity change in the spatial dimension, whereas G_T is associated with an intensity variation in the temporal dimension within a spatio-temporal $N_S \times N_S \times N_T$ 3-dimensional window. Additionally, a plane perpendicular to the gradient direction is defined based on this gradient vector in order to divide the neighborhood into two parts: a positive and a negative side (Fig. 7.3).

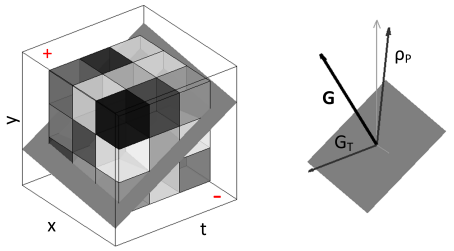

Figure 7.3: (Left) Example of spatio-temporal window when $N_S = 3$ and $N_T = 3$, including the plane defined by the gradient vector. Gray colored boxes represent pixel intensity values (for st-CAF) or spectral distances between neighboring pixels and the cell which is being evaluated (for 4DCAF). (Right) Gradient vector decomposition

Thus, when the CA is applied to a particular cell, the **G** vector is obtained and the positive and negative sides are identified. Based on this separation, a transition rule will decide which pixels on each side are going to participate in the modification of the cell state and how they are going to contribute to this cell state updating process.

Therefore, the CA is provided with a set of transition rules which consists of M rules and in every iteration of the CA structure, and for each pixel, one rule is selected to perform the updating.

The rules are made up of five parameters (2 state parameters + 3 updating parameters):

$$CA = \left\{ \begin{array}{ccccc} \rho_{r_{P_1}} & G_{r_{T_1}} & S_{r_{WS_1}} & T_{r_{WS_1}} & b_{r_1} \\ \vdots & \vdots & \vdots & \vdots & \vdots \\ \rho_{r_{P_k}} & G_{r_{T_k}} & S_{r_{WS_k}} & T_{r_{WS_k}} & b_{r_k} \\ \vdots & \vdots & \vdots & \vdots & \vdots \\ \rho_{r_{P_M}} & G_{r_{T_M}} & S_{r_{WS_M}} & T_{r_{WS_M}} & b_{r_M} \end{array} \right\} \tag{7.4}$$

$$\text{with} \left\{ \begin{array}{l} \rho_{P_{r_k}} \in [0,1] \\ G_{r_{T_k}} \in [0,1] \\ S_{r_{WS_k}} \in \{1,3,5,\ldots,N_S\} \\ T_{r_{WS_k}} \in \{1,3,5,\ldots,T_S\} \\ b_{r_k} \in [0,1] \end{array} \right.$$

where $\rho_{r_{P_k}}$ and $G_{r_{T_k}}$ are the state parameters (they define which pixels will use this rule) and are related to the spatial and temporal projection of the vector gradient; $S_{r_{WS_k}}$ and $T_{r_{WS_k}}$ denote the spatial and temporal size of the updating window which will define which pixels will be used to calculate the updated state of the current cell; b_{r_k} indicates the contribution of the considered pixels on the positive side and negative side to the updating process. Subindex r is used here to avoid confusing rule parameters with the values of the gradient vectors extracted from the neighboring information of a cell.

To decide which rule, out of the rule set, is selected, a comparison between the neighboring information (ρ_P and G_T) and the state parameters of each rule ($\rho_{r_{P_k}}$ and $G_{r_{T_k}}$) is performed. As mentioned before, ρ_P and G_T, are obtained from projections of a gradient vector calculated within a 3-dimensional spatio-temporal $N_S \times N_S \times N_T$ window, being the particular values of N_S and N_T fixed and set manually. The automaton selects the rule whose first two parameters $\left(\{\rho_{r_{P_1}}, G_{r_{T_1}}\}, \{\rho_{r_{P_2}}, G_{r_{T_2}}\}, \ldots, \{\rho_{r_{P_M}}, G_{r_{T_M}}\}\right)$ are most similar to $\{\rho_P, G_T\}$. The selected rule, q, establishes the spatial and temporal window size $\left(\{S_{r_{WS_q}}, T_{r_{WS_q}}\}\right)$ of the pixels that are taking part in the cell state updating process and the value of the updating parameter b_{r_q}.

Table 7.1: Differences between the st-CAF and 4DCAF methods

	st-CAF	4DCAF
Type of temporal image sequence	single-band	hyperspectral
Grid dimension	3D	4D
Cell state	$s_i(\mathbb{R})$	$\mathbf{s_i}(\mathbb{R}^N)$
Neighboring information	s_j	$\alpha_{i,j}$ (eq. 7.1)
Spatio-spectro-temporal gradients	$G_{X_{N_{S_i}}} = \sum_{j=1}^{N_S N_S N_T} s_j \cdot M_{X_{N_{S_j}}}$ $G_{Y_{N_{S_i}}} = \sum_{j=1}^{N_S N_S N_T} s_j \cdot M_{Y_{N_{S_j}}}$ $G_{T_{N_{S_i}}} = \sum_{j=1}^{N_S N_S N_T} s_j \cdot M_{T_{N_{S_j}}}$ (eq. 7.2)	$G_{X_{N_{S_i}}} = \sum_{j=1}^{N_S N_S N_T} \alpha_{i,j} \cdot M_{X_{N_{S_j}}}$ $G_{Y_{N_{S_i}}} = \sum_{j=1}^{N_S N_S N_T} \alpha_{i,j} \cdot M_{Y_{N_{S_j}}}$ $G_{T_{N_{S_i}}} = \sum_{j=1}^{N_S N_S N_T} \alpha_{i,j} \cdot M_{T_{N_{S_j}}}$ (eq. 7.3)
Updating process	$s_{i,t+1} = \bar{p}_{i,t} \cdot b_{r_q} + \bar{n}_{i,t} \cdot (1 - b_{r_q})$ (eq. 7.5)	$\mathbf{s_{i,t+1}} = \mathbf{\bar{p}_{i,t}} \cdot b_{r_q} + \mathbf{\bar{n}_{i,t}} \cdot (1 - b_{r_q})$ (eq. 7.6)

The updating process of the new cell state depends of the CAF structure considered. In the case of st-CAF, the new cell state is calculated as:

$$s_{i,t+1} = \bar{p}_{i,t} \cdot b_{r_q} + \bar{n}_{i,t} \cdot (1 - b_{r_q}) \tag{7.5}$$

where $s_{i,t+1}$ is the new state (intensity value) of cell i (pixel) which has been evaluated and $\bar{p}_{i,t}$ and $\bar{n}_{i,t}$ are the mean value of all the pixels contained in the positive and negative sides of the spatio-temporal window defined by $\left\{S_{r_{WS_q}}, T_{r_{WS_q}}\right\}$, respectively.

When the 4DCAF structure is applied, the updating formula becomes:

$$\mathbf{s_{i,t+1}} = \bar{\mathbf{p}}_{\mathbf{i,t}} \cdot b_{r_q} + \bar{\mathbf{n}}_{\mathbf{i,t}} \cdot (1 - b_{r_q}) \tag{7.6}$$

where $\mathbf{s_{i,t+1}}$ is the new spectrum of cell i and $\bar{\mathbf{p}}_{\mathbf{i,t}}$ and $\bar{\mathbf{n}}_{\mathbf{i,t}}$ denote the averaged spectra of all the pixels contained in the positive and negative sides of the spatio-temporal window defined by $\left\{S_{r_{WS_q}}, T_{r_{WS_q}}\right\}$.

This procedure is iteratively applied to all the cells of every frame producing, in the end, an updated and denoised –provided st-CAF or 4DCAF is properly tuned– image sequence.

Table 7.1 presents the main differences between the st-CAF and 4DCAF structures.

7.3 ECASF: Evolving the Cellular Automata

The efficiency of the proposed denoising method is subject to the set of transition rules that govern the behavior of the CAF structure. Setting the values of the parameters that make up the transition rules is a complex problem to solve manually. Similarly to the case of ECAS-II strategy, in order to obtain these rules in an automatic fashion, we have chosen an automatic optimization process in the form of an Evolutionary algorithm that encodes the CAF rule set (eq. 7.4). In this case, we have chosen a Genetic Algorithm (GA) in order to infer the set of transition rules. The decision of selecting a Genetic Algorithm instead of a Differential Evolutionary Algorithm was empirical.

7.3.1 Genetic Algorithm

Genetic Algorithms are basically search heuristics that mimic the process of natural selection. Their basic principles were established by Holland [1975] and since then have been widely used to generate solutions to multiple and diverse optimization problems.

GAs operate on a population of individuals, data structures that encode the sets of transition rules that make up the CAF structures. Each generation, a new offspring population is created through the selection, based on the evaluation of individuals according to a cost/fitness function, and the variation (recombination and mutation) of individuals from the previous population.

The main components of the GA algorithm are:

- Representation: Each CAF structure that makes up the GA population is encoded as a vector consisting of $D = 5 \cdot M$ floating point values in the $[0, 1]$ interval.
- Population: NP D-dimensional parameter vectors are used as a population for each generation G. The initial vector population is chosen randomly and should cover the entire parameter space.
- Selection: In the selection step, individual genomes are chosen from a population for later breeding. The particular selection algorithm used in this implementation of ECAF is denoted as *Stochastic Uniform*, implemented as follows:
  1. The fitness function is scaled for each individual.
  2. Each parent corresponds to a section of the line of length proportional to its scaled value.
  3. A random step size is chosen.
  4. The algorithm moves along the line in steps of equal size. At each step, the algorithm allocates a parent from the section it lands on.
- Genetic operators: The next step is to generate a second generation of solutions from those selected through a combination of genetic operators: crossover (recombination) and mutation.

The selected crossover function creates children by taking a weighted average of the parents. The weights associated to each parent are set by a single parameter, *Ratio*: $child = parent_1 + rand * Ratio * (parent_2 - parent_1)$.

Mutation introduces small random changes in the individuals of the population to create mutated children. Mutation provides genetic diversity and enables the genetic algorithm to search a broader space. The selected mutation function generates directions that are adaptive with respect to the last successful or unsuccessful generation.

Concerning the evaluation of individuals, the fitness of a prospective CAF is determined by running it over a training image sequence and comparing the result to the desired original one. The quality of the denoising obtained after applying the automaton is calculated using the mean squared error (MSE) between the original and denoised sequences.

When a st-CAF structure is being evaluated, the fitness function is given by:

$$MSE = \frac{1}{X \cdot Y \cdot F} \sum_{t=1}^{F} \sum_{x=1}^{X} \sum_{y=1}^{Y} [I(x,y,t) - I'(x,y,t)]^2 \tag{7.7}$$

where $I(x,y,t)$ and $I'(x,y,t)$ represent the intensity value of pixel (x,y) in frame t for the original and denoised sequences; X and Y are the spatial dimensions of the image and F is the number of frames of the sequences.

Conversely, the fitness function for a 4DCAF structure becomes:

$$MSE = \frac{1}{X \cdot Y \cdot N \cdot F} \sum_{f=1}^{F} \sum_{b=1}^{N} \sum_{x=1}^{X} \sum_{y=1}^{Y} [I(x,y,b,f) - I'(x,y,b,f)]^2 \tag{7.8}$$

where $I(x,y,b,t)$ and $I'(x,y,b,t)$ represent the b-band spectral value of pixel (x,y) in frame f for the original and denoised sequences; X and Y are the spatial dimensions of the image, N is the number of bands and F is the number of frames of the sequences.

Every time a prospective CAF needs to be evaluated, it is run over a training image sequence and the denoising result it obtains is compared to the noise-free image sequence.

Thus, how the ECAF adapts CAF structures in order to perform a satisfactory denoising task will strongly depend on how the training image set is selected or created. The creation process of the training image dataset is described in more detail in the next section.

7.4 ECASF: Creating the training image dataset

Evolving CA-based filtering structures capable of dealing with noise filtering effectively requires to provide the evolutionary algorithm with suitable training image sequence datasets that should reflect spatial, temporal and spectral (if it is the case) properties of the type of the real image sequences that is intended to denoise, as well as particular characteristics of the type of noise that corrupts those real sequences.

The steps followed for the creation of synthetic single-band and hyperspectral image sequences are summarized below:

1. Creation of the noise-free image sequence (*reference sequence*)
   In the case of creating the training image sequence dataset for evolving st-CAF structures, a set of F consecutive frames are created sharing a common background. This background contains pixels in ranges of low, medium and high intensity values. There are also spatial transitions between contiguous pixels (edges) with varying strength. Furthermore, some objects with sharp borders are superimposed on the background so that their position and orientation change frame by frame, creating that way temporal transitions among pixels belonging to different frames of the temporal sequence (Fig. 7.4a).
   The procedure followed to obtain a noise-free synthetic hyperspectral image sequence for evolving 4DCAF structures is based on the method for the creation of multidimensional synthetic images described in section 5.3.1 of chapter 5. Firstly, the ground truth of the first frame of the sequence is created by providing N and D_{max} parameters. The ground truth of subsequent frames are a modified version of the first frame by growing or decreasing some selected regions in size. Then, global spectrum vectors are assigned to each area with the same associated label, thus obtaining the noise-free or reference multidimensional image sequence (Fig. 7.20).

2. Corruption of the reference sequence with noise (*noisy sequence*)
   Once the noise-free image sequence is created, some signal-independent and/or signal-dependent noise is added to it. Ideally, a previous study of the real sequence to be denoised is carried out in order to approximate which noise model is affecting the real sequence. Then, the synthetic reference image is noised following the type of noise model that has been determined.

   The following model can be used to approximate both additive signal-dependent and signal-independent random noise:

$$\begin{aligned} g(x,y,b,t) &= f(x,y,b,t) + f(x,y,b,t)^{\gamma} \cdot u(x,y,b,t) + w(x,y,b,t) \\ &= f(x,y,b,t) + v(x,y,b,t) + w(x,y,b,t) \end{aligned} \tag{7.9}$$

   In eq. 7.9, g is the signal value for each pixel including noise, f is the corresponding signal value without noise and γ is the exponential parameter of the model and the only parameter it contains. Based on the value of γ the model will represent different types of noise. Finally, u and w are zero-mean random variables with variances σ_u^2 and σ_w^2.

   Those most frequent signal dependent-noise models considered in denoising applications [Kuan et al., 1985], due to their high presence in images, are film grain noise, multiplicative noise (speckle), and Poisson noise (also called shot or photon noise).

   Namely, for $1/3 \leq \gamma \leq 1/2$ the model represents a typical configuration of the so-called film-grain noise, which can be observed on digital images and appears when images initially recorded on photographic film are digitized. This noise is therefore modeled using an additive model considering one signal dependent noise source and one signal independent noise source that are based on Gaussian probability functions.

   Speckle noise is generated by coherent radiation as in the case of radars and synthetic aperture radars. A similar noise model is also present in ultrasounds, lasers and sonars. Speckle noise is described using a signal independent noise term but by means of a multiplicative model where the signal is multiplied by this noise term ($\gamma = 1$ in eq. 7.9). As a result, the

noise present in the corrupted image behaves as signal dependent noise and it is frequently modeled using zero mean additive noise with a variance obtained as a function of the uncorrupted signal at that point.

Finally, when an image system operates in low-light conditions a specific type of noise appears. This is produced due to the discrete nature of the process of detection of the radiance, which is performed counting the number of incident photons on the sensor during a period of time for its later conversion into photoelectrons. This type of noise is called photon noise or shot noise and, since it is generated by the sum of independent random occurrences of discrete events, it behaves following a Poisson distribution. The exponent γ takes a value of 0.5 in eq. 7.9. This will generate the term $\sqrt{f} \cdot u$ that will approximate the Poisson distribution component. As reflected in the approximation proposed, this makes the level of noise dependent on the brightness of the scene, and more specifically, it leads to the magnitude of the noise term growing with the square root of the average intensity of the signal. Accordingly, it is in the case of low light conditions when photon noise becomes more significant provided that there are no other sources of noise (the one associated to the electronic amplifier of the signal produced by the CCD, for instance) with higher average intensity. Photon noise is relevant when dealing with sensors that work with different exposure levels or sensor gains. Poor lighting conditions appear in many and diverse image processing applications: night vision for dynamic environments, X-ray fluoroscopic captures when used for real-time medical interventions, etc. and they are associated to sensors which can be divided into three main categories: X-Ray images, Infrared Images and conventional images obtained in low light conditions.

Particularly, in subsection 7.5.2 of this chapter, devoted to the application of st-CAF to synthetic single-band image sequences, st-CAF will deal with the denoising of real sequences corrupted by photon noise. Therefore, the training image sequence datasets will be noised using a Poisson-distributed noise model. For the creation of the synthetic image datasets, instead of considering an approximation for the Poisson noise as a zero-mean Gaussian noise with signal-dependent variance (eq. 7.9), we will corrupt the image sequences with a *parametrized Poisson-distributed noise model* (described below), allowing us to set the level of noise while preserving the Poisson distribution.

According to the Poisson probability function, the probability of obtaining any intensity value for the pixel with coordinates (i, j), $p^*(i, j)$, given that the original signal (without noise) intensity is $p(i, j)$, is obtained using eq. 7.10.

$$P[p^*(i,j); p(i,j)] = \frac{p(i,j)^{p^*(i,j)} e^{-p(i,j)}}{p^*(i,j)!} \tag{7.10}$$

Note that eq. 7.10 unequivocally sets a noise distribution for each signal value without any possibility of parameterizing the noise model (for instance, due to different sensors or gains). In order to introduce a parametrization within the standard deviation assigned to each signal value while preserving the Poisson distribution (variance proportional to the expected signal value), a change of variable is introduced to include a proportionality factor, as shown in eq. 7.11. Accordingly, the new expected value will be $C \cdot p(i, j)$ and the new standard deviation will be $\sigma = \sqrt{C \cdot p(i, j)}$.

$$P[p^*(i,j); p(i,j), C] = \frac{(C \cdot p(i,j))^{p^*(i,j)} e^{-C \cdot p(i,j)}}{p^*(i,j)!} \tag{7.11}$$

In eq. 7.11, p^* denotes the noisy signal, p the original signal, and C represents a proportionality factor.

Normalizing to the original range of the signal, an equivalent distribution may be obtained where the deviation with the proportionality factor can be controlled:

$$p^{*,n}(i,j) = p^*(i,j)/C \tag{7.12}$$

being $p^{*,n}(i, j)$ the finally normalized signal. As a result and including it in the noise model used, a new parametrized Poisson model is obtained in eq. 7.13.

$$P[p^{*,n}(i,j); p(i,j), C] = \frac{(C \cdot p(i,j))^{C \cdot p^{*,n}(i,j)} e^{-C \cdot p(i,j)}}{(C \cdot p^{*,n}(i,j))!} \cdot C \tag{7.13}$$

This normalization will scale the expected value and variance linearly:

$$E\{p^{*,n}(i,j)\} = p(i,j) \tag{7.14}$$

$$\sigma^2\{p^{*,n}(i,j)\} = p(i,j)/C \tag{7.15}$$

Thus, using this formulation the variance of the signal is parametrized with this proportionality factor C. Fig. 7.4 displays examples of single-band frames created, with different values for the proportionality factor C.

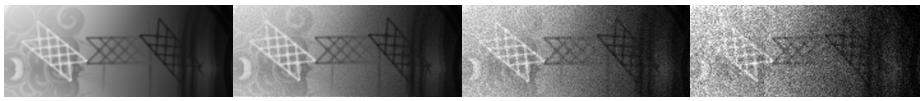

(a) (b) (c) (d)

Figure 7.4: (a) Original noisy frames: (b) with $C = 2000$, (c) with $C = 600$ and (d) with $C = 75$, from a automatically generated synthetic image sequence

7.5 Application of st-CAF to image sequences

This section is devoted to testing the performance of the ECAF generated st-CAF structures. The performance quantification of the denoising filter requires the availability of a benchmark of real image sequences, including both noise-free (ground truth) and signal-dependent noisy data, in order to achieve a reliable evaluation of the denoising algorithm. However, it is quite difficult to collect this kind of image benchmark, and an evidence of that is the lack of repositories of real image sequences found on-line. An accepted approach to estimate how good the denoising algorithm is, relies on the generation of a set of synthetic image sequences similar to the real image sequences we are interested in denoising, corrupting each image by a given noise model. Afterwards, the denoising algorithm is applied to the sequence and finally, an evaluation is carried out by comparing the synthetic noise-free image sequence to the denoised one. This is the procedure followed in subsection 7.5.1, where a quantitative analysis of the performance of the denoising method has been performed using synthetic single-band image sequences.

In subsection 7.5.2, the denoising performance of the evolved st-CAF structures is qualitatively evaluated using real highly noisy single-band image sequences corrupted by Photon noise. Additionally, in order to reduce the intrinsic arbitrariness and imprecision of this evaluation and to improve its reliability, two novel visualization procedures are proposed.

Both subsections present the experimental results obtained comparing the proposed algorithm to the ST-GSM [Varghese and Wang, 2010] and VBM3D [Dabov et al., 2007] methods.

7.5.1 Validation of st-CAF over synthetic single-band image sequences

This first experimental section seeks to carry out a quantitative analysis to demonstrate the capabilities of the st-CAF structure and the ECAF evolutionary process to denoise image sequences.

Next subsection 7.5.2 will present the results of the application of the st-CAF structure over real single-band image sequences dominated by additive Poisson-distributed quanta noise. Thus, in this subsection we have decided to create a synthetic image sequence also corrupted by this type of noise model. In order to create a test synthetic image sequence, we have selected an X-ray image with very little noise, which is taken as noise-free, and following the procedure described in section 7.4, the image sequence is noised following a parametrized Poisson-distributed noise.

Table 7.2: Genetic Algorithm (GA) and CAF parameters

Name	Value
(Genetic Algorithm)	
Number of parameters:	75 (15 $rules \times 5$ $parameters/rule$)
NP (Population Size):	200
Elite count (number of individuals that are guaranteed to survive to the next generation):	$0.05 \times NP$
CR (Fraction of the next generation, other than elite children, that are produced by crossover):	0.8
$Ratio$ (Crossover):	0.7
Stopping criterion:	Max. number of generations
(CAF)	
N_S	7
N_T	7

On the other hand, the training image sequence dataset used in the evolutionary ECAF procedure is shown in Fig. 7.4. This training dataset is completely different in terms of content from the test dataset that was generated from the X-Ray images, although they both share the same noise model. The fact that the st-CAF has been evolved using a dataset that is different from the one employed for the experimental results is quite meaningful in terms of the generalization capabilities of the method. Some relevant technical specifics

of the ECAF procedure and st-CAF structures used are summarized in table 7.2. The st-CAF structure evolved using the mentioned training dataset and the evolutionary parameters of table 7.2 will represent the CA-based filter used to denoise image sequences in this section.

In order to provide a basis for comparison, the synthetic sequence has been denoised using VBM3D, STGSM and st-CAF. A proportional factor of $C = 50$ has been used to corrupt by noise the image sequence. A noisy frame of the sequence is shown in Fig. 7.5a, as well as the denoised results after applying the three denoising methods (Fig. 7.5b-7.5d). A GIF animation is also available following the QR link shown in Fig. 7.11a for visualizing the denoising process.

In order to quantitatively compare our algorithm to VBM3D and STGSM, the peak signal noise ratio (PSNR) for all the denoised frames of the synthetic sequence has been represented in Fig. 7.6a. The PSNR is defined as the ratio between the maximum possible power of a signal and the power of corrupting noise that affects the fidelity of its representation, $PSNR = 10 \cdot \log(\frac{MAX_I^2}{MSE})$, where MAX_I^2 is the maximum possible power of the spectral values and MSE is the mean squared error defined in eq. 7.7 and eq. 7.8.

The comparison of Fig. 7.6a shows that the improvement obtained by using st-CAF is clear which is also noticeable by visual inspection in Fig. 7.5, where the reduction in noise is patent without detriment of the structures of the image. The first three frames present a lower PSNR due to the lack of temporal information associated with the initial steps of the process.

(a) (b) (c) (d) (e)

Figure 7.5: (a) Original frame from a synthetic image sequence, (b) noisy frame corrupted by additive Poisson noise with C=50, denoised frame using (c) VBM3D, (d) STGSM and (e) st-CAF

To further evaluate st-CAF, another experiment has been carried out in which each denoising algorithm was applied to a set of synthetic image sequences corrupted by Poisson-distributed noise with different values of C ranging from

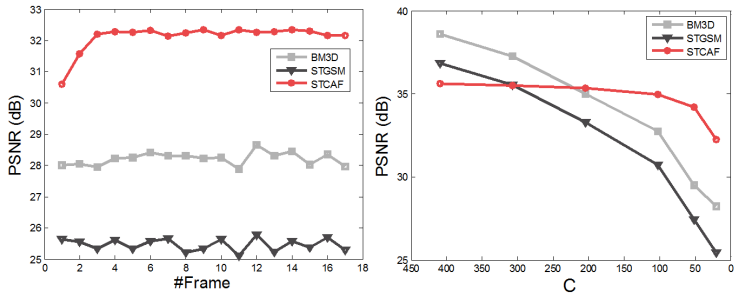

(a) (b)

Figure 7.6: (a) Per-frame PSNR comparison of the proposed st-CAF, VBM3D and STGSM applied to a synthetic image sequence corrupted by additive Poisson noise with C=50, (b) PSNR comparison of the proposed st-CAF, VBM3D and STGSM as a function of noise level

450 to 20, that is, different noise levels (Fig. 7.6b). The purpose of this test was to analyze the sensitivity of the three denoising methods to the gain factor C, which is inversely proportional to the noise variance for a given mean intensity value of the signal, as formulated in eq. 7.15. The results show, on the one hand, that st-CAF achieves quite stable PSNR values when the denoised image sequences are corrupted using C values larger than 100. As C decreases below 100, VBM3D and STGSM results suffer an appreciable PSNR loss, whereas the PSNR in the case of st-CAF only exhibits a slight decrease.

Therefore, for images which a C value under approximately 200, st-CAF outperforms both the VBM3D and STGSM algorithms, that is to say, at medium and high noise levels, st-CAF offers better denoising results while for low levels of noise, ($C > 200$), the behavior is slightly poorer than the other two algorithms.

Furthermore, performing a visual analysis of a selected denoised frame (Fig. 7.5), a qualitative observation reveals that st-CAF reduces the noise more significantly in light regions without losing sharpness, avoiding blurring existing structures in the original image sequence.

Finally, in order to have a better insight of the operation of the three methods, a global representation of the process is shown in Fig. 7.7 by displaying each denoised pixel value vs. its original correspondence from the corrupted synthetic image sequence. It can be observed in the case of VBM3D and STGSM that the denoised values get on average further away from the original pixel val-

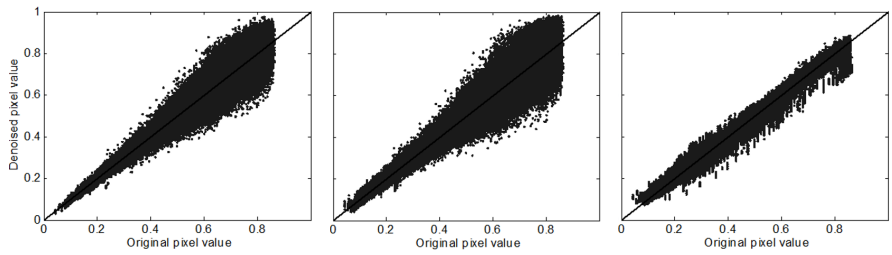

(a) (b) (c)

Figure 7.7: Denoised pixel values vs. noisy pixel values from the corrupted synthetic image sequence after applying VBMD (a), STGSM (b) and st-CAF algorithms (c).

ues as the intensity of the pixel grows. These algorithms denoise the sequence considering that the noise level is signal independent, and as consequence, as reflected in Fig. 7.6, the performance of these algorithms depends on the pixel intensity range of the denoised image. However, in the case of st-CAF, the noise reduction is more uniform for the whole intensity interval, which explains its better performance for high noise levels. Both the VBM3D and STGSM algorithms require as a first step an estimation of the noise level of the image sequence, which has been obtained in this work using a standard algorithm. As in this case we are dealing with Poisson-distributed noise, the estimated noise level will only fit the real noise in a pixel intensity interval.

7.5.2 Application of st-CAF to real single-band image sequences

Further tests have been carried out over real sequences of images corresponding to IR, X-Ray and low light conventional image sequences to provide a fully realistic validation of the suitability of the method.

Previous to the application of the denoising method, for each type of image sequence, a study of the noise model has been carried out in order to construct the synthetic training image dataset for the evolutionary ECAF strategy. Then, the appropriately evolved st-CAF structure has been applied to denoise the real sequences.

On the other hand, as mentioned, the use of real images suffers from the lack of a ground truth (denoised sequence) against which to measure the performance of the denoising. It implies that the evaluation of the results has to be carried out by means of some type of visual inspection. The most common and straight-forward procedure to perform this visual inspection consists in the qualitative observation and comparison of some of the frames of the sequences denoised by different methods. In order to reduce the intrinsic arbitrariness and imprecision of this evaluation and to improve its reliability a new representation is proposed. It consists in a 2D representation which plots the intensity fluctuations (first derivative) between contiguous pixels on the vertical axis, and on the X-axis, a sequence of pixels which were selected following a spatio-temporal zigzag direction (marked with red circles in the left image of Fig. 7.15 and Fig. 7.18) which smoothly temporally and spatially-wise traverses the sequence.

The following subsections show the analysis of the noise model affecting X-ray, IR and low illuminated image sequences, and the visual results of denoising the sequences through the application of the st-CAF, VBM3D and STGSM methods, as well as by means of the two novel representation techniques.

X-Ray Image sequences

The first temporal images under consideration are two real sequences of low-dose X-ray images, which have been provided by Thales Electro Devices. The first sequence (Fig. 7.8a) shows a high-dose low-abdominal X-ray image and the second one (Fig. 7.8c) shows a similar X-ray image sequence but corrupted by medium noise.

In order to perform an analysis of the type of noise model that affects these sequences, we have represented in Fig. 7.8b and 7.8d the variance (σ) versus the intensity (μ) of the pixels from the sequences. The σ and μ values shown in these figures were obtained by means of a temporal average of selected frames without motion or objects moving. The circles in these graphs represent the density of elements in each range of intensity that exhibit a certain noise variance value. A text label in each graph indicates the slope of the regression line, the inverse of this value, that is, the value of factor C and also the correlation coefficient of the linear regression, R. It can be noticed that the noise/signal representation fits the model shown in eq. 7.13 perfectly (R coefficient is close to 1).

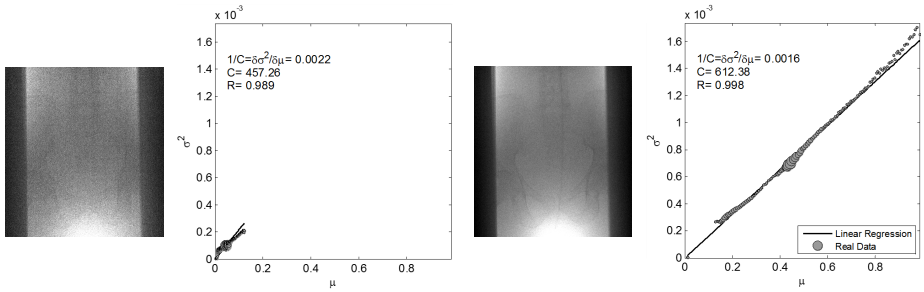

(a) (b) (c) (d)

Figure 7.8: (a) Frame of a highly noisy real X-ray sequence and (b) representation of the noise variance vs. intensity signal value, (c) frame of a medium noisy real X-ray sequence and (d) representation of the noise variance vs. intensity signal value

Since the image sequences are corrupted by noise following a Poisson-distributed model, the same st-CAF structure that was evolved for subsection 7.5.1 will be used to denoise the X-ray sequences.

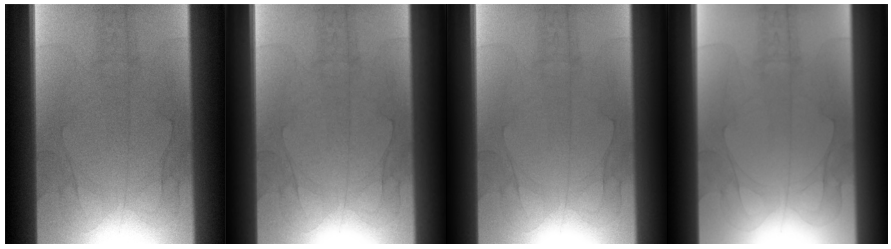

(a) (b) (c) (d)

Figure 7.9: (a) Frame of a medium noisy real sequence, denoised frame using: (b) VBM3D, (c) STGSM and (d) st-CAF

After the application of the algorithms and comparing the resulting images (frames of Fig. 7.9 and 7.10 and GIF animations following the QR link shown in Fig. 7.11), it is easy to visually perceive that VBM3D and STGSM introduce artifacts and the denoising is appreciably poorer than when applying the st-CAF method, which is consistent with the quantitative results obtained using synthetic sequences when the image sequence is corrupted by high noise levels.

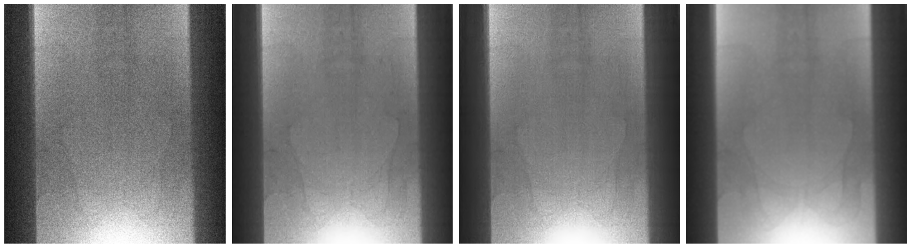

(a) (b) (c) (d)

Figure 7.10: (a) Frame of a highly noisy real sequence, denoised frame using: (b) VBM3D, (c) STGSM and (d) st-CAF

(a) (b) (c) (d)

Figure 7.11: QR link to visualize the temporal denoising in GIF format of a synthetically generated sequence (a), a highly (b) and medium (c) noisy X-ray sequences and a IR real sequence (d)

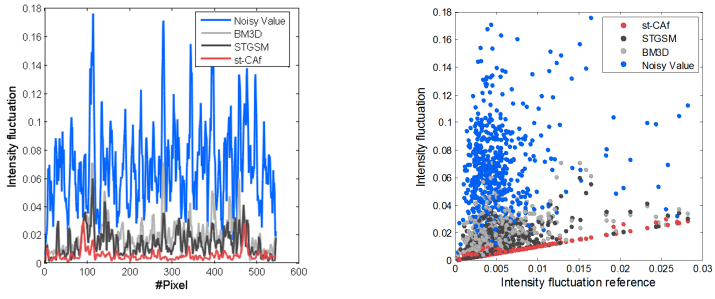

(a) (b)

Figure 7.12: (a) Intensity fluctuation (first spatio-temporal derivative) from the noisy and denoised sequences used also in Fig. 7.10 for the pixels selected following a spatio-temporal zigzag direction. The right figure shows the values presented in (a) but sorted in the X-axis in ascending order according to the minimum intensity fluctuation selected from the noisy and denoised values.

Fig. 7.12a shows the results using the new 2D representation. Fig. 7.12b plots four curves, one for the noisy intensity fluctuation, and three for the denoised intensity fluctuations, revealing that the st-CAF result presents lower intensity variations compared to BM3D and STGSM results, which also validates the proposed denoising method.

IR image sequences

In this experiment, we seek to validate the st-CAF algorithm applied to an IR image sequence also corrupted by Poisson-distributed quanta noise. We have obtained this IR image sequence from online repositories (AIC Thermal/Visible Night-time Dataset) [Conaire et al., 2006] and it captures a night scene in an urban area.

Fig. 7.13 shows that on poorly illuminated areas the Poisson-distributed quanta noise model fits the noise with a certain value of factor C, while on more illuminated areas, this dependence changes, increasing the C value. Thus, different values of C characterize the gain of the sensor over the pure Poisson distribution.

Again, the st-CAF structure used to denoise the IR sequence is the same as the one evolved for subsection 7.5.1.

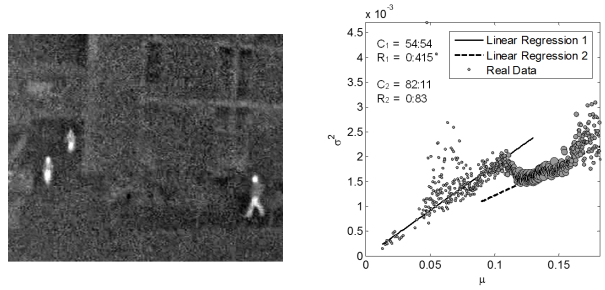

(a) (b)

Figure 7.13: Frame of a highly noisy real IR image sequence (a) and its corresponding noise variance vs. intensity signal value graph (b)

Fig 7.14 shows a frame of the sequence before and after being denoised by the three methods and following the QR link of Fig. 7.11d, a GIF animation of the denoising process can be observed. Additionally, Fig. 7.15 shows the results

using the new 2D representation. When comparing the denoising results, it is easy to visually perceive the denoising improvement of st-CAF over VBM3D and STGSM: the background areas are more homogeneous while the structures and edges are preserved sharp. On the other hand, in the 2D representation is noticeable that the intensity variations in neighboring pixels are lower in the st-CAF denoising compared to BM3D and STGSM results, validating also for this case the CAF-based filtering method.

(a) (b) (c) (d)

Figure 7.14: (a) Frame of a noisy IR real sequence, denoised frame using: (b) VBM3D, (c) STGSM and (d) st-CAF

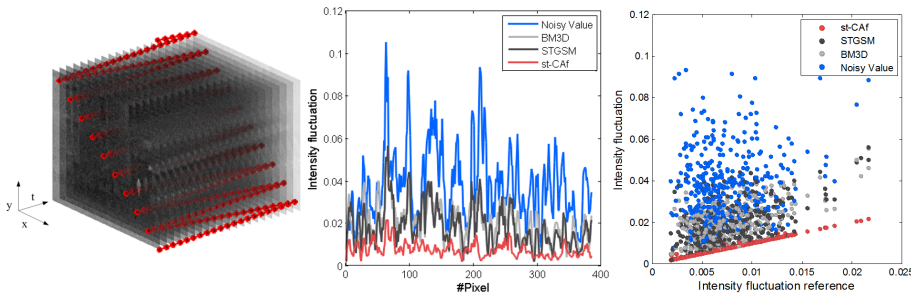

(a) (b) (c)

Figure 7.15: (a) Temporal sequence with the selected pixels represented by red circles; (b) Intensity fluctuation (first spatio-temporal derivative) from noisy and denoised sequences (Fig. 7.14) for the pixels selected following the spatio-temporal zigzag direction marked with red circles; (c) Same values presented in (b) but sorted in the X-axis in ascending order according to the minimum intensity fluctuation selected from the noisy and denoised values

Image sequences under low light conditions

The last test takes a space shuttle observation sequence under low-light conditions from the STS-58 Columbia mission (Fig. 7.16). For this case, the σ-μ representation seems not to be clearly fitted to a Poisson-distributed quanta noise model. However, the regression coefficient (R) is quite high due to the different density of elements in each range of intensity. Hence, the st-CAF structure used to denoise the IR sequence is also the same as the one evolved for subsection 7.5.1.

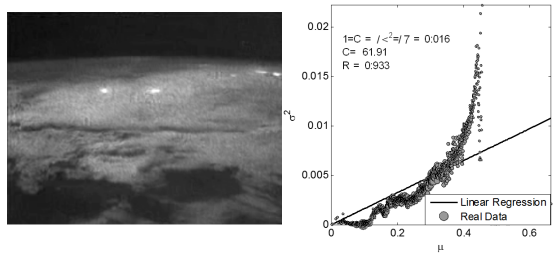

(a) (b)

Figure 7.16: Frame of a very noisy real image sequence acquired under low light conditions (a) and its corresponding noise variance vs. intensity signal value graph (b)

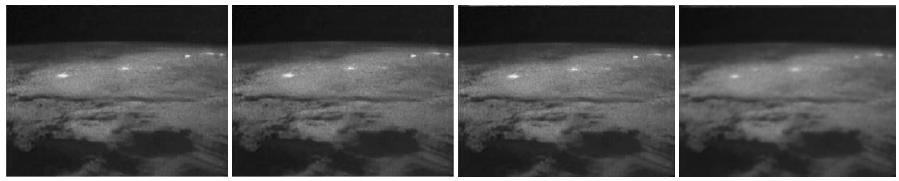

(a) (b) (c) (d)

Figure 7.17: (a) Frame of a noisy real sequence under low light conditions, denoised frame using: (b) VBM3D, (c) STGSM and (d) st-CAF

Fig. 7.17 and Fig. 7.18 show the results after applying the three denoising algorithms. Again, st-CAF seems to reduce the noise local intensity variations in homogeneous areas (neighboring pixels with no or low changes in the intensity values). The representation of local intensity variations (Fig. 7.18) also shows in this experiment that st-CAF keeps the intensity variations in neighboring pixels lower, leading to a better denoising result.

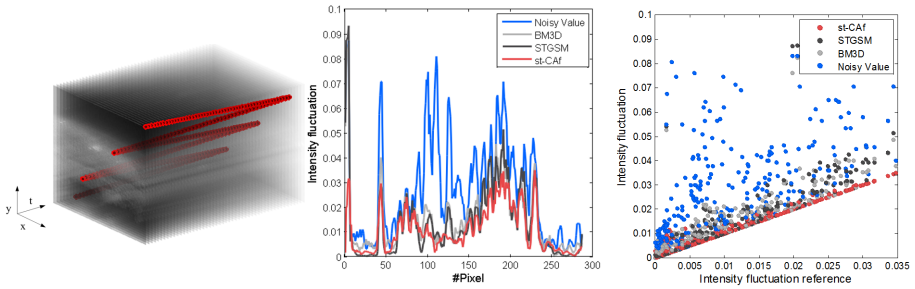

(a) (b) (c)

Figure 7.18: (a) Temporal sequence with the selected pixels represented by red circles; (b) Intensity fluctuation (first spatio-temporal derivative) from noisy and denoised sequences (Fig. 7.17) for the pixels selected following the spatio-temporal zigzag direction marked with red circles; (c) Same values presented in (b) but sorted in the X-axis in ascending order according to the minimum intensity fluctuation selected from the noisy and denoised values

7.6 Application of 4DCAF to image sequences

This section is devoted to the presentation of the experimental results obtained from applying the 4DCAF structure and to its comparison to recent successful methods from the state of the art. This comparison has been carried out using both synthetic and real hyperspectral image sequences. All the state-of-the-art methods cited in section 7.1 have been tested over the hyperspectral sequences considered in this work. From all the results, only those that provided better performances are shown here. Thus, the methods selected for comparisons are K-SVD [Aharon et al., 2006], BM3D [Dabov et al., 2007], BM4D [Maggioni et al., 2013] and DNTDL (Decomposable Nonlocal Tensor Dictionary Learning for MS) [Peng et al., 2014], respectively.

K-SVD and BM3D treat each frame and spectral band separately. This has been called frame-wise band-wise (fw-bw) processing, whereas BM4D and DNTDL are applied frame-wise (fw).

7.6.1 Validation of 4DCAF over synthetic hyperspectral image sequences

This subsection addresses the quantitative validation of the 4DCAF method obtained from the ECAF evolutionary strategy by applying the CAF structure to a synthetic hyperspectral image sequence.

Before the application of the 4DCAF structure over the synthetic hyperspectral image sequence, the set of transition rules that define its behavior have been evolved using the ECAF evolutionary method, feeding the evaluation step of the genetic algorithm with training datasets created synthetically.

On the other hand, the synthetic image sequence created for validation purposes will be noised following the same estimated noise model exhibited by the real test image sequence shown in subsection 7.6.2. Thus, before corrupting both the training dataset employed in the ECAF method and the validation synthetic hyperspectral image, it will be necessary to estimate the noise model of the real hyperspectral image sequence referred in subsection 7.6.2.

The analysis of the type of noise model that affects the real sequence has been carried out by representing the variance (σ) versus the averaged intensity value (μ) for each spectral band of the sequence (Fig. 7.19). Both σ and μ values were obtained considering values in a spatial window of a 3×3 pixels and a temporal window of 25 frames for regions in the image sequence without moving objects. The radius of the circles in these graphs represent the density of pixels in each range of intensity that presents a certain noise variance value. Fig. 7.19 shows the noise analysis for three selected spectral bands. The value of the linear regression coefficient, R, is shown in the title of each graph presenting a good fit to the linear models.

In order to construct each training image sequence used as input for the evolutionary algorithm, firstly, a ground truth map sequence was created. Then, a real spectral signature [USGS] was associated to each labeled region of the ground truth map sequence, thus creating the reference or noise-free hyperspectral image sequence. After that, each band of the reference sequence was corrupted using the following model:

$$g(x, y, b, t) = f(x, y, b, t) + (p_2(b) + p_1(b) \cdot f(x, y, b, t))^{\frac{1}{2}} \cdot u(x, y, b, t) \quad (7.16)$$

where g denotes the spectral value being noised, f is the corresponding signal value without noise; u is a zero-mean random variable with standard deviation 1; and p_2 and p_1 are the offset and the slope of the linear regression fit for each band b, respectively.

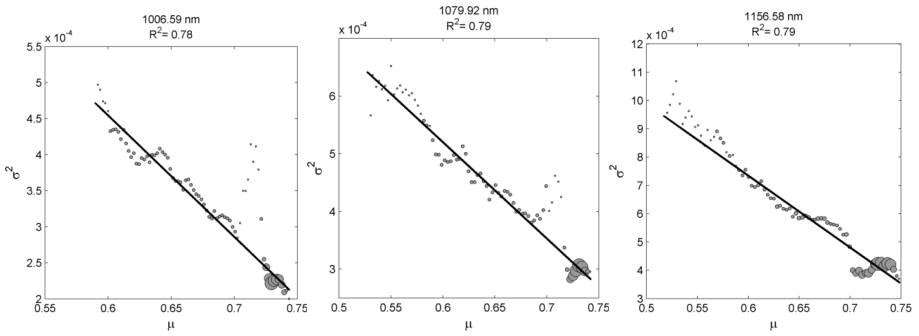

(a) (b) (c)

Figure 7.19: Noise variance vs. intensity signal value graph for the 1006.59 nm (a), 1079.92 nm (b) and 1156.58 nm (c) bands of the real hyperspectral image shown in Fig. 7.25

Regarding the synthetic image sequence used for validating the 4DCAF structure, the creation process differs from the training dataset in the selection of the spectral signatures for creating the noise-free hyperspectral image sequence. The spectral signatures (composed of 129 bands) have been extracted from the real sequence presented in subsection 7.6.2 using the following procedure: firstly, N pixel spectra have been selected from the real sequence aiming to be as spectrally different as possible from one another (in terms of spectral angle), where N is the number of different labels found in the ground truth image sequence; then, these N spectra have been filtered achieving a smoothed effect. The reference image sequence has been corrupted following the same procedure as indicated for the construction of the training hyperspectral image sequence dataset.

The technical specifics of the ECAF procedure and 4DCAF structures used are summarized in table 7.2 and captures of the training datasets are shown in Fig. 7.20.

The 4DCAF structure evolved using the mentioned training dataset and the evolutionary parameters of table 7.2 will represent the multidimensional CA-based filter used to denoise both the synthetic sequence of this subsection and the real sequence of the subsequent subsection.

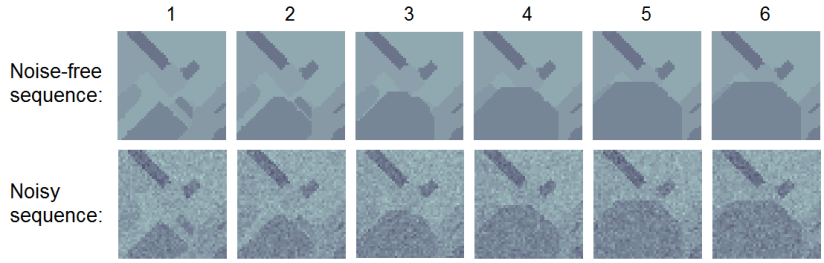

Figure 7.20: One band of noise-free and noisy synthetic hyperspectral image sequences used as training data set for the ECAF evolutionary strategy

Turning now to the evaluation of the performances of the algorithms, we have obtained four quantitative picture quality indices (PQI), including peak signal-to-noise ratio (PSNR), structure similarity (SSIM) [Wang et al., 2004b], feature similarity (FSIM) [Zhang et al., 2011] and spectral angle mapper (SAM) [Yuhas et al.].

The 4DCAF structure was been applied directly to the synthetic sequence, while in the case of the other methods, before the application of fw-bw-KSVD, fw-bw-BM3D, fw-DNTDL and fw-BM4D, the hyperspectral sequence was transformed using a variance-stabilizing transformation (VTS) [Starck et al., 1998].

Quantitative and visual results are shown in Table 7.3 and Fig. 7.21 respectively. Additionally, following the QR link of Fig. 7.24a, a GIF animation of the denoising process can be observed. The picture quality indices demonstrate that the proposed method is able to efficiently operate over noisy hyperspectral image sequences consistently providing values for the indices that are much better than those given by the other methods. On the other hand, the spectral bands from a selected frame of the sequence represented in Fig. 7.21 show that 4DCAF reduces the noise and preserves small structures and edges sharp.

Fig. 7.22 depicts the absolute deviation between the reference and the denoised spectral images of a selected frame from the synthetic hyperspectral image sequence shown in Fig. 7.21. It can be observed that fw-bw-KSVD and fw-BM4D introduce spot-type noise. Moreover, the denoising quality provided

by the fw-BM4D method is band-dependent, as it can clearly be noticed for the 853.3 nm spectral band. The fw-bw-BM3D method produces a blurring effect on the edges while at the same time presenting two-dimensional noise fluctuations. The behavior in flat areas is quite good for the fw-DNTDL denoising result but heavy speckle-type noise is present close to the borders. Finally, the 4DCAF method provides the best result in terms of flat areas, low deviation and preservation of sharpness close to the edges.

The graphs in Fig. 7.23 show the per-frame and per-band PSNR, SSIM and FSIM quality indices of the proposed 4DCAF, fw-bw-KSVD, fw-bw-BM3D, fw-DNTDL and fw-BMd4D methods applied to the synthetic hyperspectral image sequence under analysis. Regarding the per-frame representation, 4DCAF outperforms the other four methods after the first two frames of the sequence in terms of PSNR, SSIM and FSIM. As with the st-CAF applied to a single-band sequence, the loss of quality in the first frames is due to the lack of temporal information associated with the initial steps of the process. On the other hand, observing the per-band representation, it can be noticed that the denoising performances vary from band to band for all the methods, exhibiting the 4DCAF method the best quality values for all the spectral bands. Furthermore, considering the SSIM and FSIM indices, the fluctuations between bands are much lower for the 4DCAF result.

Table 7.3: PQI comparison of the proposed 4DCAF, fw-bw-KSVD,fw-bw-BM3D, fw-DNTDL and fw-BM4D applied to a synthetic image sequence corrupted by signal dependent noise

Method	PSNR	SSIM	FSIM	SAM
fw-bw-KSVD [Aharon et al., 2006]	41.36	0.972	0.932	0.010
fw-bw-BM3D [Dabov et al., 2007]	42.85	0.976	0.924	0.009
fw-DNTDL [Peng et al., 2014]	44.99	0.983	0.971	0.006
fw-BM4D [Maggioni et al., 2013]	44.01	0.984	0.958	0.010
4DCAF	**49.62**	**0.993**	**0.982**	**0.003**

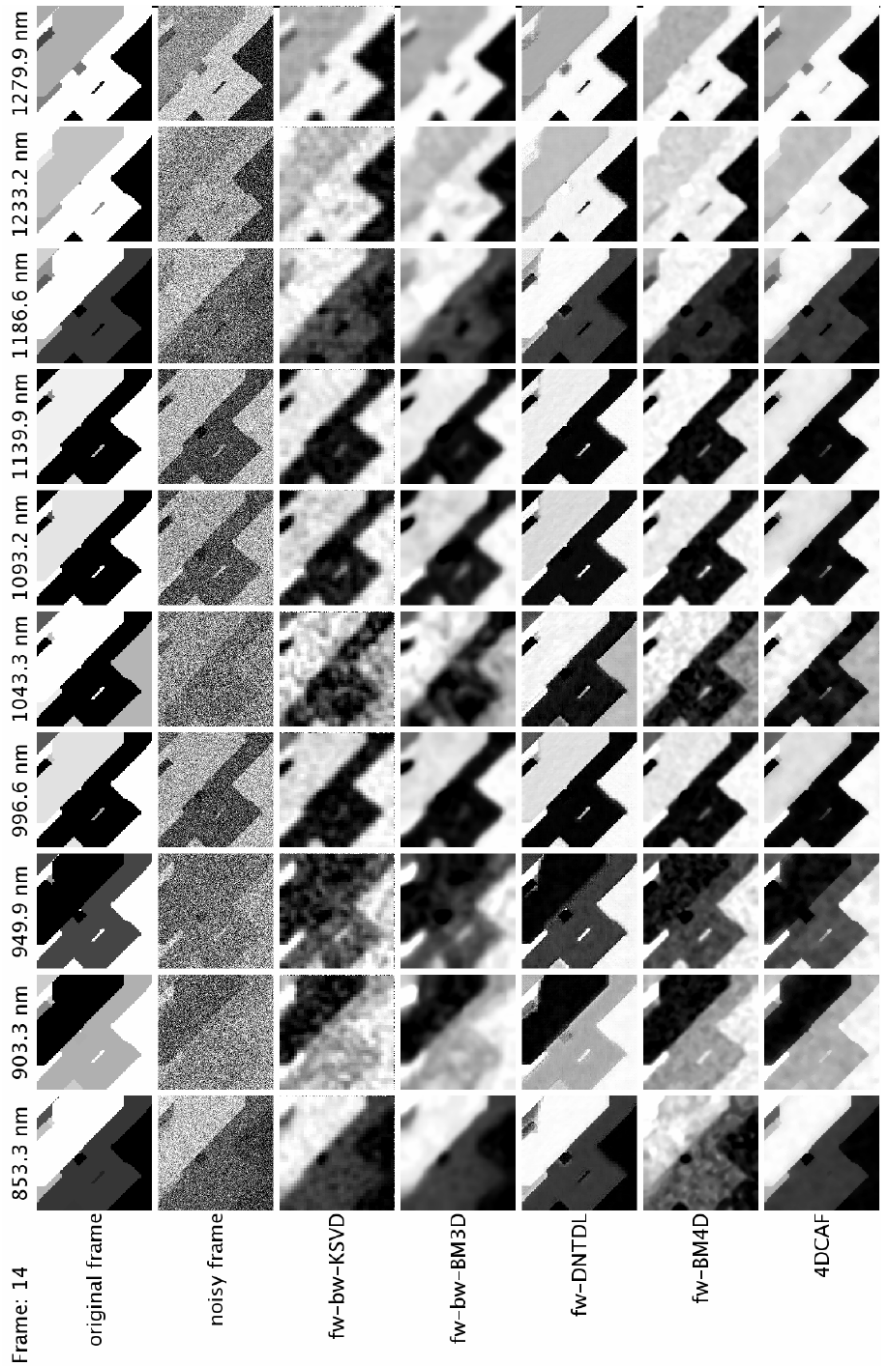

Figure 7.21: Original, noisy and denoised images of a selected frame from a synthetic hyperspectral image sequence. Only ten bands (out of 129) are shown

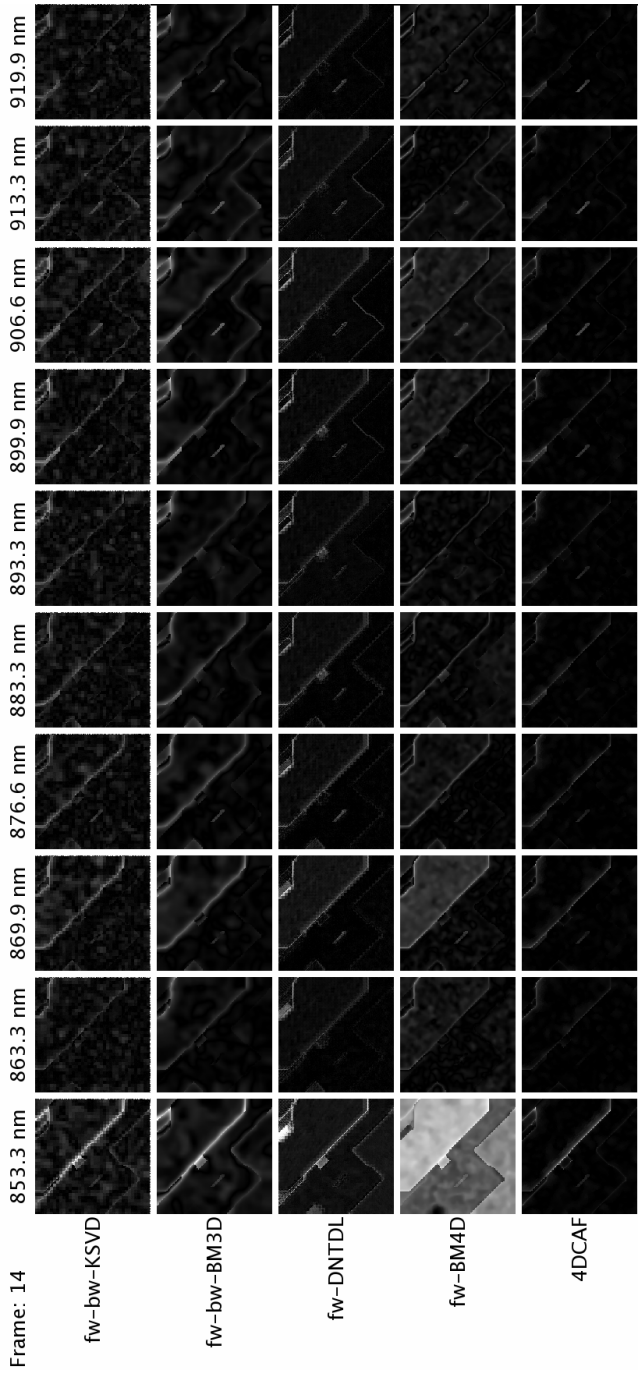

Figure 7.22: Absolute deviation between the reference and the denoised images of a selected frame from the synthetic hyperspectral image sequence shown in Fig. 7.21. Only ten bands (out of 129) are shown

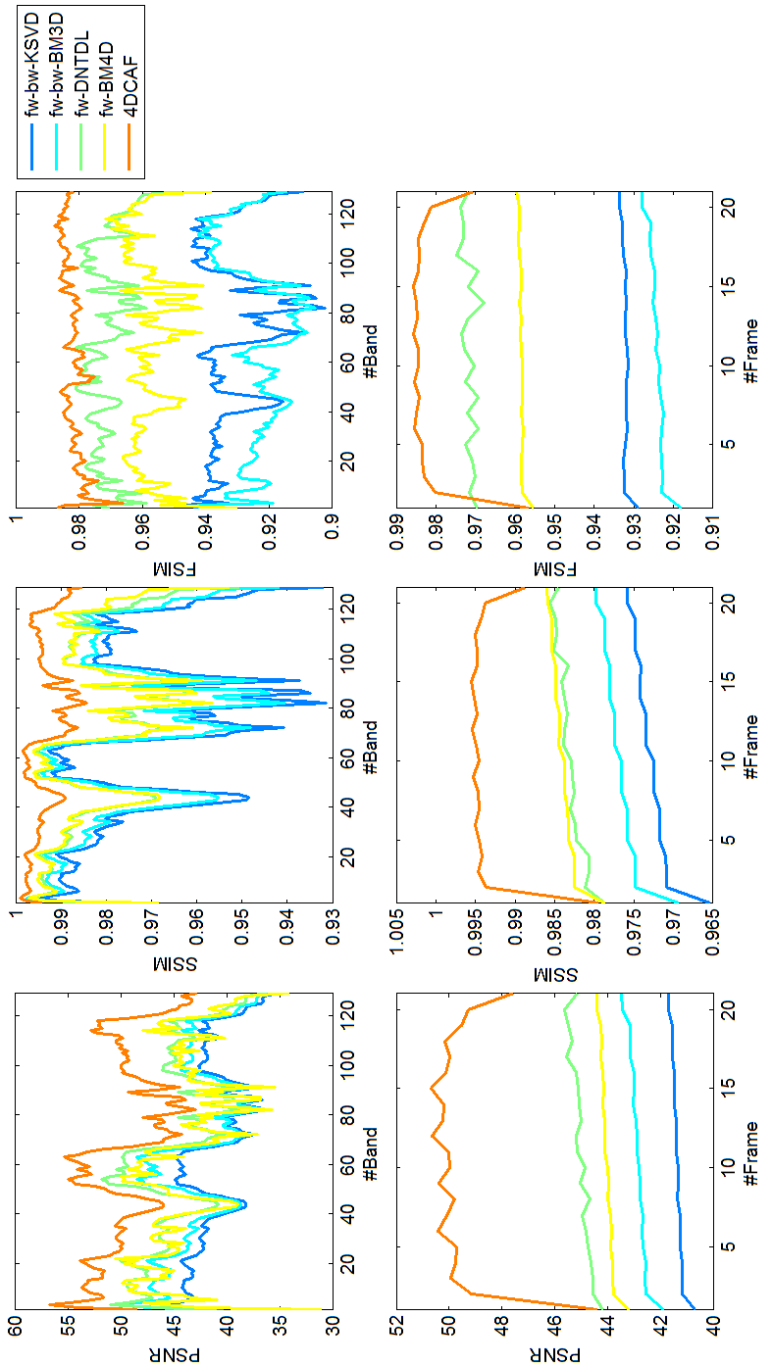

Figure 7.23: Per-frame and per-band PSNR, SSIM and FSIM comparison of the proposed 4DCAF, fw-bw-KSVD, fw-bw-BM3D,fw-DNTDL, and fw-BMd4D methods applied to the synthetic hyperspectral image sequence shown in Fig. 7.21

7.6.2 Application of 4DCAF to real hyperspectral image sequences

Once the proposed method has been validated over synthetic sequences, we have applied our algorithm to a real hyperspectral image sequence of a dispersion of a chemical plume acquired by a LWIR sensor. The sequence consists of 25 frames, each one containing 129 spectral bands in the $[853, 1.280]$ nm range. For this sequence, since a noise-free version of it is not available, a first evaluation of the denoising has to be performed visually. Fig. 7.25 demonstrates that the 4DCAF method produces the most satisfactory result: the background appears more homogeneous, whereas the shape of the plume looks sharper than in the case of the other methods. A GIF animation of the denoising process can be observed following the QR link shown in Fig. 7.24b.

Also for assessing the denoising of real hyperspectral image sequences, we have considered a 2D representation (Fig. 7.26b) which plots the fluctuations in terms of spectral angle between contiguous pixels belonging to a string of pixels selected following a spatio-temporal zigzag direction (marked with red circles in the left image of Fig. 7.26a) which traverse the sequence temporally and spatially-wise. Furthermore, Fig. 7.26c) plots the same values presented in Fig. 7.26b but sorted in the X-axis in ascending order according to the minimum spectral angle fluctuation selected from the noisy and denoised pixels. Both 2D representations reveal that the variations between contiguous pixels, in terms of spectral angle, are lower when the 4DCAF structure is applied compared to the rest of considered denoising methods.

(a) (b)

Figure 7.24: QR link to visualize the temporal denoising in GIF format applied to the synthetic hyperspectral image sequence shown in subsection 7.6.1 (a) and the real hyperspectral image sequence presented in subsection 7.6.1

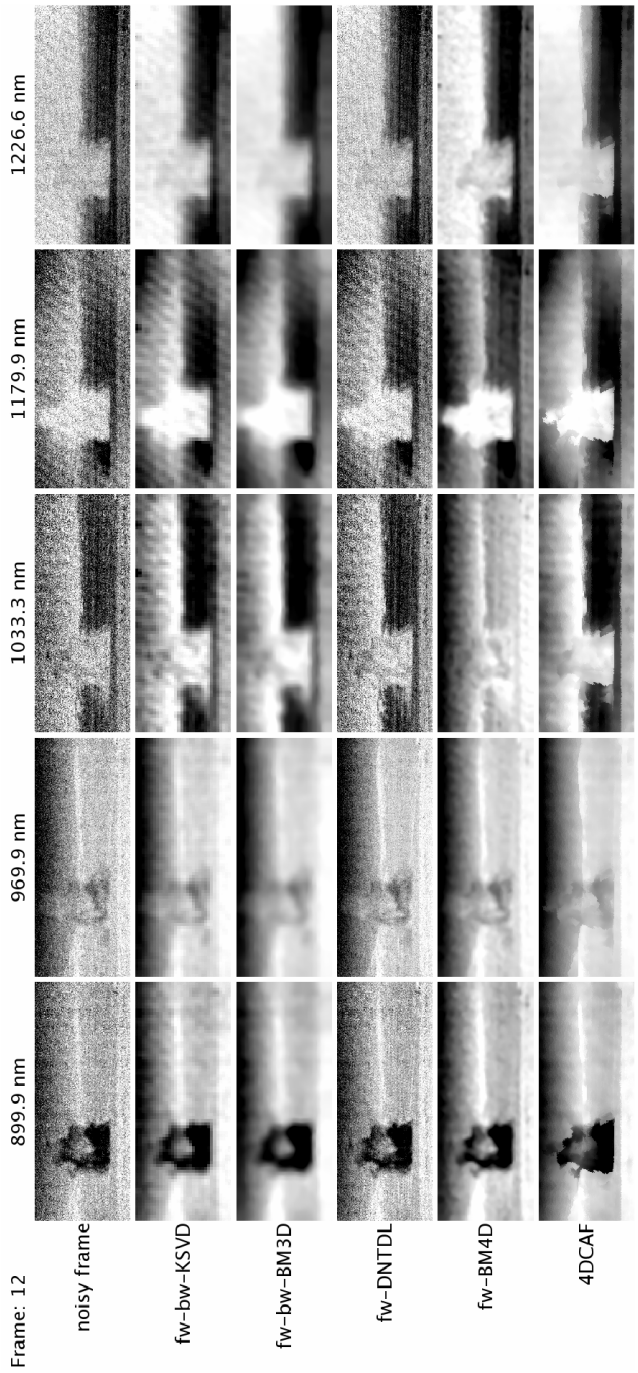

Figure 7.25: Noisy and denoised images of a selected frame from a real hyperspectral image sequence representing a chemical plume. Only five bands (out of 129) are shown

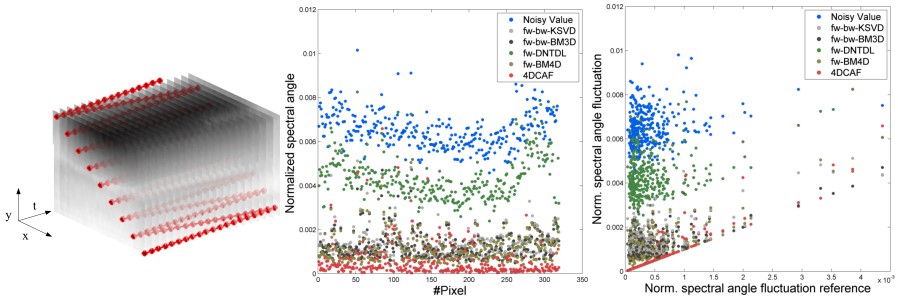

(a) (b) (c)

Figure 7.26: (a)Temporal sequence (only one band is shown) with the selected pixels represented by red circles; (b) Intensity fluctuation (spectral angle distances) from noisy and denoised sequences (Fig. 7.25) between contiguous pixels selected following the spatio-temporal zigzag direction marked with red circles; (c) Same values presented in (b) but sorted in the X-axis in ascending order according to the minimum spectral angle fluctuation selected from the noisy and denoised values

7.7 Summary

This work has presented a strategy for the denoising of single-band and hyperspectral image sequences. The proposed method deals with some issues associated to the denoising problem: the lack of available noised and noise-free image sequences to validate and train algorithms; the adaptability of methods to different types of noise that may corrupt the sequences; and the joint processing of temporal, spatial and spectral information, taking into account the inter-dimensional diversity.

In order to solve these problems, a methodology made up of a CA-based filtering structure (st-CAF and 4DCAF for processing single-band and hyperspectral sequences, respectively) and an evolutionary approach, denoted as ECAF, allows for obtaining a suitable set of rules that conform to the processing task. The adaptation of the CAF to properly perform the denoising considering a particular type of noise model is carried out by an evolutionary technique after appropriately selecting the noisy image sequences used to evaluate the individuals of the population. Therefore, an advantage of the ECAF method is its versatility for adjusting the rule set of the CAF structure in an automatic manner to the noise model exhibited by the image source by only modifying the training image sequences.

The particular application case considered for the denoising of single-band image sequences through the st-CAF structure deals with frames corrupted by signal dependent noise, in particular, by photon noise. In order to quantify the level of noise associated with the source of a noisy image sequence, we have introduced a proportionality factor, C, in the photon model, which is inherently defined parameterless. This allows characterizing the intensity of the noise and will serve to analyze the efficiency of the denoising methods regarding the level of corruption of the image sequences.

The st-CAF structure performance has been compared to state-of-the-art denoising methods by applying them to synthetic and real image sequences coming from low-dose X-ray, infrared and low light visible imaging conditions. The results of denoising synthetic image sequences show that the st-CAF algorithm outperforms in terms of PSNR the state of the art methods in the most difficult situations, this is, where the signal to noise ratio drops. To validate the st-CAF method over datasets of real image sequences, all of which do not have an associated noise-free ground truth, a new method for the denoising evaluation has been presented. This evaluation method has complemented the evaluation performed by simple visual inspection. This results obtained over real image sequences validated those obtained denoising synthetic image sequences.

On the other hand, the 4DCAF structure has been validated over synthetic and real hyperspectral image sequences. To that end, an analysis of the noise model that affects the real sequence has been performed. The estimated noise model has been used to corrupt synthetic images created for the validation of the method. After the application of the evolved 4DCAF structure, the performances are excellent when compared to alternative state of the art filtering strategies, both from a quantitative perspective, as observed on synthetic sequences, and from a qualitative point of view using visual analysis on real hyperspectral sequences featuring the release and dispersion of a gas plume.

In addition to the successful performance, an important perspective of this work is related to its potential for efficient parallel implementations. Since the proposed method is based on cellular automata, it can be easily implemented by distributing it over high speed GPU based platforms, thus increasing significantly its suitability to be used in real time applications.

Chapter 8

Conclusions and Future Work

This chapter concludes the thesis presenting a general discussion on the major results and providing an outlook for future work.

Summary and discussion

In this thesis, we have firstly contributed to the hyperspectral field with procedures for the automatic acquisition of hyperspectral images using imagers developed at out research group, providing methods for the calibration and correction of the hyperspectral datacubes from distortions. Secondly, we have created and made public a hyperspectral repository of well categorized and labeled images. Finally, we have designed and implemented processing techniques based on computational intelligence that facilitate the application of hyperspectral technology to new areas.

With respect to the first issue, in chapter 4 we have made operational two low-cost prototypes of pushbroom hyperspectral imagers. The first prototype has been endowed with an electro-mechanical module and software tools that enable the system to spatially scan a scene in order to automatically construct and visualize a complete hyperspectral datacube. Additionally, we have designed

and implemented simple and affordable methods to characterize, calibrate and correct images acquired with these two hyperspectral imager prototypes. These methods have dealt with the simultaneous correction of the keystone and smile effect, as well as with the scene-based stripping distortion. The proposed methods have revealed to be low-cost, simple and repeatable, desirable features since calibration and characterization methods should be applied periodically.

The creation of the GII-SEG repository of hyperspectral images has been addressed in chapter 5. The hyperspectral repository has been made publicly available and contains sets of synthetically created and real hyperspectral images, as well as scenes provided by users external to the GII research group. A novel feature of this repository is that, in addition to properly labeling the hyperspectral images, each scene has been categorized by a few feature parameters that describe geometrical and local/global spectral aspects. Additionally, an algorithm for the creation of synthetic hyperspectral images has been designed based on those geometrical and spectral features, which enables the construction of single images or sequences of multi-dimensional images quickly and easily. This repository becomes a useful aid for the training and testing of processing methods.

Finally, two processing strategies based on computational intelligence techniques have been designed and implemented for the processing of still and sequences of hyperspectral images.

The first processing strategy consists in a segmentation approach based on a CA structure called Multi-Gradient based Cellular Automata (MGCA), whose behavior depends on a predefined set of transition rules. The effect of applying the MGCA over a multi-dimensional image is to gradually modify the spectra of pixels belonging to the same region until a spectral homogenization is achieved. In order to adjust the transition rules that direct the behavior of the CA, a methodology called ECAS-II based on evolutionary algorithms, has been designed. Through ECAS-II, the appropriate transition rules for MGCAs are generated using low dimensional synthetic training images created from the parametrization of certain characteristics of the real images to be processed.

The proposed segmentation method addresses some issues related to the processing of multi-dimensional images. It solves the problem of projecting spectral information onto lower dimensionalities by jointly processing the spatial and spectral information through algorithms based on cellular automata (CA).

Furthermore, the intrinsic structure of CAs can be easily implemented over high speed GPU based platforms, significantly increasing their suitability for real time applications. On the other hand, the segmentation behavior of the CA structure can be adjusted following a evolutionary procedure through the use of synthetically created images that avoids the problem of the lack of appropriately labeled reference images for training the algorithm.

The performance of the MGCA segmenters evolved using the ECAS-II methodology has been tested in terms of accuracy metrics after the inclusion of the segmentation step in a multistage SVM-based classification approach (ECAS-II + SVM). Experimental results obtained with the application of the proposed method over synthetic and real hyperspectral images revealed that the method is able to adapt to hyperspectral images exhibiting different types of noise or artifacts. Furthermore, the amount of improvement depends on the intrinsic characteristics of the images, as well as on the types of noise or artifacts present in the hyperspectral image being processed. Actually, the ECAS-II generated MGCAs prove to be more efficient when spatial information is key to performing a more robust classification. The proposed method improves the raw SVM-based classification accuracy results when it is applied to synthetic multidimensional images, benchmark hyperspectral images and real images extracted from the GII-SEG repository. Additionally, the algorithm has been compared to state-of-the-art classification methods applied to benchmark images showing that the ECAS-II + SVM algorithm outperforms the state of the art methods in all cases.

The second processing strategy deals with the denoising of single-band and hyperspectral image sequences through the design and application of CA-based filtering structures (called st-CAF and 4DCAF for processing single-band and hyperspectral sequences, respectively). In the application of the st-CAF or 4DCAF filters, the intensity values or spectra of each pixel are modified so that after a number of iterations, every frame of the image sequence converges to a denoised version of it. The transition rules that solve the denoising problem adapted to a particular type of noisy sequence are adjusted by an evolutionary-based methodology denoted as ECAF. The evaluation step of the evolutionary algorithm is fed by synthetic image sequences created on-line that exhibit the same type of noise as the real sequences to be denoised. This solves the problem of the shortage of real sequences for training algorithms.

The performances of evolved st-CAF and 4DCAF structures have been compared to state-of-the-art denoising methods by applying them to synthetic and real image sequences coming from low-dose X-ray, infrared and low light visible imaging conditions, for the case of single-band image sequences, and synthetic hyperspectral and real hyperspectral image sequences whose spectral coverage reaches the infrared domain. The quantitative results of applying the denoising methods to synthetic image sequences show that the proposed method outperforms in terms of PSNR, SSIM, FSIM and SAM the filtering strategies that are considered state of the art, especially when the signal to noise ratio is very low. To complement the evaluation by visual inspection of real image sequences without associated noise-free ground truths, a novel representation has been presented for validation purposes. The results of using this representation over real image sequences also validated those obtained denoising synthetic image sequences.

Summing-up, in this thesis work, operational and methodological solutions for the acquisition and processing of hyperspectral images have been proposed, analyzed and validated with the underlying aim of promoting hyperspectral technology to new areas and for their intended use by expert or non-expert users.

Future work

This dissertation presents innovative methodologies that contribute to a more extended use of hyperspectral technology in many real world applications. Even though the proposed methodologies represent progress in the hyperspectral field, the experiments carried out and the results obtained lead to the opening of potential improvements for future research. In what follows, we provide a list of future research topics that would extend the work accomplished in this PhD thesis:

- In terms of the line addressed in chapter 4, the next steps would imply the adaptation of the second prototype of pushbroom imager using complementary hardware and software to make it operational from unmanned areal vehicles (UAVs). This would enable the acquisition of outdoor images considering new target applications, such as environmental control, precision agriculture or surveillance.
- Further steps could be taken to expand the GII-SEG repository described in chapter 5 with new still or temporal captures, aiming at solving new tasks such as anomaly detection, unmixing, change detection, temporal denoising or temporal classification. Furthermore, it would be valuable to add social aspects, such as comment boxes or a scoring systems for evaluating the usefulness of different scenes.
- Concerning the CA-based methods presented in chapters 6 and 7, further work should be conducted in order to test the CA-based segmentation and denoising structures with additional scenes and analysis scenarios.
- A new research line could be focused on the extension of the CA-based segmentation algorithm to deal with sequences of hyperspectral images, with the purpose of making temporal classification algorithms more robust.
- It would be valuable to evaluate the improvement of the CA-based temporal denoising method presented in chapter 7 with respect to some applications, such as classification and segmentation performances or spectral unmixing.

- Finally, a new research line could address the analysis of the computational complexity of the CA-based methods and the hardware optimizations related to parallel computing and their efficient partitioning for exploiting high performance computing architectures, such as commodity graphic processing units (GPUs).

Several of these topics will be addressed in the context of a national and cooperative project initiated in 2016, titled SIMMAP: acquisition and processing of semi-remote sensing images.

Appendix A

Resumen en Castellano

Las imágenes hiperespectrales se forman a partir de la adquisición de cientos de bandas espectrales estrechas y contiguas, derivándose para cada elemento de imagen un espectro completo de radiancia o reflectancia dentro de un determinado rango espectral. La tecnología hiperespectral explota el hecho de que los materiales reflejan la radiación electromagnética de forma distinta en función de su forma y composición molecular, dando lugar a patrones diferenciados en longitudes de onda específicas. Esta particularidad conlleva una gran capacidad para extraer información relevante de los materiales presentes en una escena en base a sus propiedades espectrales. En la actualidad, el potencial de esta tecnología da lugar a una sólida y activa línea de investigación, contando con un amplio respaldo en la literatura científica de los últimos 25 años.

El concepto de tecnología hiperespectral surgió en la década de los 80 a partir del desarrollo del sensor hiperespectral Airborne Visible-Infrared Imaging Spectrometer (AVIRIS) por parte del Jet Propulsion Laboratory/NASA [Goetz et al., 1985]. De ahí que en sus comienzos su aplicación se enfocara principalmente en el campo de la sensorización remota, realizándose la adquisición de imágenes desde instrumentos a bordo de satélites o aerotransportados. Desde entonces, el campo hiperespectral ha experimentado un rápido crecimiento gracias a los avances de hardware asociados con los sensores hiperespectrales, lo que ha supuesto nuevos retos para la comunidad científica en cuanto al desarrollo de algoritmos para la representación, procesamiento y análisis de datos. Paralelamente y con relación a los avances tecnológicos en la adquisición de imagen

digital, en los últimos diez años han aparecido diseños de hiperespectrómetros comerciales de menor tamaño que han abierto nuevos dominios de aplicación de la tecnología hiperespectral. Si bien la filosofía en el desarrollo de sensores hiperespectrales sobre plataformas aerotransportadas o satélites descansa en mejorar la resolución y precisión espectro-espacial manteniendo en la adquisición el mayor rango espectral posible, de manera que en función de la aplicación final se seleccione una porción concreta del espectro, la filosofía en el desarrollo de sensores comerciales se apoya en el diseño e implementación de cámaras hiperespectrales cuyas características espectrales, espaciales y temporales se adapten lo máximo posible a una determinada aplicación final.

La tecnología hiperespectral presenta un gran potencial en cuanto a su aplicabilidad a nuevos campos. Sin embargo, existen hoy en día contextos en los cuales su empleo es aún poco factible. Para promover la difusión y popularización de esta tecnología, se han de solventar algunas limitaciones existentes actualmente, entre ellas:

- Los sensores hiperespectrales disponibles comercialmente son aún hoy en día relativamente engorrosos y caros, requiriendo un grado elevado de conocimientos y experiencia para producir resultados adecuados.
- Se han generado pocas bases de datos de imágenes hiperespectrales tomadas en tierra accesibles de forma pública, lo que, por un lado, ha condicionado el diseño de algoritmos, y por otro, ha restringido la visión de aplicabilidad de la tecnología a otros campos.
- El estado del arte sobre las técnicas de procesamiento y análisis de los datos hiperespectrales está altamente enfocado al procesamiento de imágenes aisladas y capturadas desde plataformas aerotransportadas. Las imágenes adquiridas a grandes distancias tienen como característica una baja resolución espacial, por lo que la mayor parte de las técnicas que se han desarrollado para el procesamiento de las mismas se centran en la extracción de *endmembers*, es decir, en la estimación de contribuciones de distintos materiales sobre cada píxel de la imagen. Prueba de ello es el resultado de realizar las búsquedas *"hyperspectral and (endmembers or unmixing)"* y *"hyperspectral and segmentation"* en la base de datos bibliográfica Scopus. El número de documentos publicados entre los años 2010 y 2014 en relación con la extracción de endmembers resulta 4.23 veces mayor que con respecto a los documentos que presentan métodos de segmentación.

Sin embargo, en el procesamiento y análisis de imágenes capturadas con una mayor proximidad a la escena, el análisis combinado espacio-espectral pasa a adquirir un mayor protagonismo en las técnicas de procesamiento.

- De los métodos existentes en la bibliografía que consideran un enfoque espacio-espectral, es notable la carencia de técnicas que, aun llevando a cabo tareas de tipo general tales como segmentación, detección de anomalías, clasificación, etc., propongan una metodología para su adaptación a los requerimientos concretos de un usuario en una determinada aplicación final. Por ejemplo, al efectuar una tarea de segmentación, es deseable disponer de una metodología que permita ajustar el funcionamiento del algoritmo segmentador a un nivel de detalle concreto en cuanto a la delimitación de regiones en la imagen de análisis.

- Un alto porcentaje de los algoritmos propuestos basan su funcionamiento en la extensión o extrapolación de métodos concebidos para el procesamiento de imágenes en escala de gris o RGB recurriendo a proyecciones de los datos hiperespectrales a dimensionalidades más bajas, lo que supone un desaprovechamiento de la riqueza de información contenida en este tipo de imágenes. Se precisa por tanto de técnicas de carácter general que exploten la naturaleza multidimensional inherente a las imágenes hiperespectrales y que se ajusten a las necesidades específicas de cada tipo de aplicación/usuario.

- Por último, es escasa la labor investigadora dedicada al procesamiento y análisis de la evolución temporal de características espacio-espectrales presentes en secuencias de imágenes hiperespectrales. En muchos casos, una imagen estática no proporciona información suficiente para resolver problemas de clasificación, segmentación, detección de anomalías, etc., encontrándose la información relevante en las variaciones espacio-espectrales que se producen en el transcurso del tiempo.

Es nuestra visión que para que se extienda el uso de esta tecnología se requiere de un impulso en tres direcciones principales: la compactación e integración hardware a través del desarrollo de nuevos dispositivos más manejables y desplegables, con bajo mantenimiento, simplicidad en su calibración, puesta en marcha y toma de datos; la simplificación en el procesamiento de imágenes hiperespectrales, de manera que se extraiga la información o características deseadas de forma lo más automatizada posible; y finalmente, con el objeto de

unificar y hacer más riguroso el campo, es necesario seguir una metodología para la validación de métodos o herramientas, lo que conlleva disponer de material hiper-fotográfico adecuadamente etiquetado así como de criterios que permitan una apropiada comparación de las técnicas desarrolladas.

En este contexto, el objeto de esta Tesis doctoral es aportar al campo hiperespectral instrumentación y un conjunto de técnicas de procesado de imágenes hiperespectrales basadas en inteligencia computacional que permitan extender el rango de uso de esta tecnología, haciéndola más accesible y ubicua.

En el marco de esta línea de investigación, por un lado, se ha tratado la adaptación y puesta en marcha de dos prototipos de sensores hiperespectrales, los cuales se han utilizado para crear un repositorio de imágenes para la validación y testeo de algoritmos. Por otra parte, se han abordado en este trabajo las tareas de procesamiento de imagen por medio de la integración de técnicas de inteligencia computacional, afrontando dos cuestiones generales:

- Proporcionar una metodología que permita la obtención automática de elementos de procesado espacio-espectrales multidimensionales, especialmente segmentadores, computacionalmente eficientes, lo más eficaces posibles y adaptados a los requisitos de procesado requeridos por los usuarios.
- Estudiar y proponer aproximaciones que permitan el análisis de secuencias de imágenes hiperespectrales considerando los aspectos espaciales, espectrales y temporales de forma intrínseca.

Así, el trabajo desarrollado se ha dividido en tres bloques principales:

A través del primer bloque de trabajo, mayormente de carácter hardware, se continúa la línea de investigación emprendida en el Grupo Integrado de Ingeniería de la UDC sobre el desarrollo de sistemas hiperespectrales compactos para la adquisición de imágenes hiperespectrales. En una primera etapa de esta línea, se diseñó e implementó un prototipo de sensor portátil, de elevada sensibilidad y bajo ruido, concebido para aplicaciones con requerimientos de alta fiabilidad espacial y espectral. Posteriormente, se ha desarrollado un segundo prototipo de cámara hiperespectral, también portátil, más ligera, económica y de bajo mantenimiento, pero con menores exigencias en cuanto a calidad de imagen (ruido espectral, distorsión, etc.). De esta manera, disponer de ambos dispositivos permite cubrir la aplicabilidad de la tecnología hiperespectral sobre

multitud de campos en función de las características de la escena o del tipo de procesamiento a efectuar. En este marco, la labor realizada en este trabajo doctoral ha consistido en adecuar estos dispositivos para facilitar su modo de empleo parte de usuarios no expertos. Para ello se han desarrollado herramientas para la simple e intuitiva calibración semiautomática de los dispositivos, así como para una fácil adquisición y visualización de imágenes. Las cámaras hiperespectrales desarrolladas pertenecen a la tecnología tipo *pushbroom*, con la que se consigue capturar información espectral sobre una única línea espacial, siendo necesario habilitar un sistema para llevar a cabo el barrido espacial que permita obtener el cubo hiperespectral de datos completo. En este aspecto, la labor realizada en este trabajo estriba en proporcionar dos mecanismos, junto con los sistemas de control y sincronización asociados, para efectuar el mencionado barrido espacial.

El segundo bloque de trabajo está dedicado a la creación de un repositorio de imágenes hiperespectrales reales capturadas con los hiperespectrómetros previamente desarrollados y acondicionados. Esta labor surge de la necesidad de disponer de imágenes y secuencias hiperespectrales reales para el testeo de los algoritmos desarrollados. Además, supone un respaldo de material hiper-fotográfico, aliviando con ello la actual carencia de librerías benchmark de imágenes para el testeo y validación de algoritmos. El repositorio creado cuenta con imágenes hiperespectrales sintéticas y reales. Para la generación de imágenes sintéticas se ha desarrollado una herramienta software siguiente un procedimiento basado en características espaciales y espectrales. En cuanto a las imágenes reales, éstas se han adquirido usando los prototipos de cámaras desarrolladas tras haber sido calibradas. Un aspecto relevante de este repositorio es que todas las imágenes se han caracterizado en base a propiedades espaciales y espectrales, lo que facilita la elección de una imagen u otra para entrenar o validar algoritmos. El repositorio se ha hecho público[1] bajo una licencia Creative Commons Atributtion & Share alike.

Por último, el tercer bloque de trabajo está dedicado al diseño e implementación de algoritmos basados en inteligencia computacional para el procesamiento de imágenes hiperespectrales. El desarrollo de los mismos parte de un conjunto de cinco exigencias previamente impuestas para satisfacer su posterior aplicabilidad en distintos ámbitos:

[1] El repositorio de imágenes hiperespectrales sintéticas y reales está disponible en http://gii.udc.es/gii_hyperspectral_repository

- Su procesamiento ha de ser de carácter genérico (segmentación, clasificación, detección de bordes, etc.), en contraposición a algoritmos *ad-hoc*, para su acomodación a distintos tipos de necesidades.
- El funcionamiento de los métodos ha de basarse en un conocimiento adquirido a través de un aprendizaje guiado por un usuario, lo que supone evidentes ventajas de flexibilidad y adaptabilidad.
- Se apoyarán en una metodología que simplifique el proceso de entrenamiento/aprendizaje de los algoritmos, reduciendo el coste y tiempo computacional, así como facilitando el alcance de los mismos a usuarios no expertos.
- En el procesamiento de las imágenes, ha de explotarse la naturaleza multidimensional inherente a las mismas, evitando la proyección de la información espectral a un espacio de menor dimensionalidad.
- Se basarán en estructuras susceptibles de ser procesadas concurrentemente en hardware de alto rendimiento, como por ejemplo, GPUs (*General Purpose Unit*).

Teniendo en cuenta estas premisas, en primer lugar hemos tratado el problema de la segmentación de imágenes hiperespectrales a través de la transformación de los cubos hiperespectrales en versiones más significativas y fáciles de tratar por tareas de procesamiento posteriores, como por ejemplo, clasificación o detección de anomalías. Hemos abordado este problema mediante la aplicación de *autómatas celulares (CA)*, motivados por su adaptabilidad a las cinco condiciones planteadas inicialmente. Por tanto, en esta primera fase, se procesan imágenes hiperespectrales estáticas, basándose la técnica propuesta en el procesamiento de información espacio-espectral de forma conjunta. Una vez diseñado y validado este primer método, en una segunda fase, hemos incrementado la complejidad del procesamiento multidimensional mediante la incorporación de información temporal en el procesamiento de secuencias de imágenes, extendiendo el algoritmo anteriormente desarrollado. En este segundo caso, hemos considerado la reducción de ruido en secuencias de imágenes multidimensionales, utilizando para ello autómatas celulares y teniendo en cuenta la diversidad interdimensional mediante el procesamiento conjunto de información espacial, espectral y temporal.

Los CA son modelos de sistemas no lineales, descentralizados y espacialmente estructurados, compuestos por celdas distribuidas en una región del espacio, las cuales únicamente se comunican con otras celdas locales o vecinas. Cada celda define un autómata y el estado del mismo depende de su estado en instantes de tiempo previos y del estado de las celdas situadas en su vecindad, en base a un conjunto de reglas de transición. El quid para lograr un determinado objetivo mediante la ejecución de los CA consiste en seleccionar adecuadamente el conjunto de reglas de transición, de manera que tras sucesivos cambios de estado de las celdas que constituyen el CA, se genere el comportamiento deseado.

Por lo tanto, el reto en el empleo de los CA para efectuar una tarea concreta estriba en fijar el conjunto apropiado de reglas con las que determinar su comportamiento global. Esto implica resolver el denominado *problema inverso*, esto es, deducir un conjunto de reglas locales a partir de un comportamiento global dado, lo cual es extremadamente complejo. El problema inverso se ha abordado desde diversos puntos de vista por investigadores de la comunidad dedicada al análisis de CA [Ganguly et al., 2003], siendo el método más popular y eficaz el uso de técnicas evolutivas para obtener el conjunto de reglas.

Sin embargo, en el estado del arte, la evolución de las reglas para llevar a cabo tareas complejas como segmentación o clasificación, sólo se ha efectuado sobre imágenes de baja dimensionalidad [Gallego et al., 2012, Wang et al., 2011, Kauffmann and Piché, 2010], mientras que para imágenes de alta dimensionalidad, únicamente se ha tratado la selección de reglas mediante algoritmos evolutivos para tareas más simples como el problema de detección de bordes [Lee and Bruce, 2010]. En la mayoría de trabajos dedicados al procesamiento de imágenes basados en CA, las reglas de transición se fijan de forma manual y *ad-hoc*.

En este trabajo proponemos un método de segmentación basado en autómatas celulares, cuyas peculiaridades y que ventajas se resumen en:

- En cada iteración del CA sobre los píxeles de la imagen se conserva la multidimensionalidad del cubo de datos, es decir, no se produce una proyección del espectro sobre otra base vectorial de menor dimensionalidad. De esta manera se evita simplificar el cómputo a expensas de la pérdida de información contenida en la dimensión espectral. La segmentación se consigue por tanto modificando iterativa y gradualmente el espectro asociado a cada celda del CA, de forma que tras un número de

iteraciones, el cubo de datos converge a clusters espectrales claramente diferenciados, presentando todos los píxeles pertenecientes a una misma región o cluster un espectro similar.

- El comportamiento del CA al ser aplicado sobre una imagen hiperespectral depende de una fase previa de aprendizaje a través del empleo de algoritmos evolutivos. Esto permite obtener distintos tipos de segmentadores, con los que se consiguen diferentes niveles de segmentación en función de los requerimientos de la aplicación final.

- Para la fase aprendizaje de reglas mediante algoritmos evolutivos proponemos una metodología que evita un entrenamiento costoso computacionalmente, así como el uso de imágenes multidimensionales reales. Esta metodología consiste en las extracción de parámetros característicos referentes al tipo de imagen y segmentación asociada que se pretende emular; posteriormente, la creación de imágenes sintéticas de baja dimensionalidad coherentes con los parámetros extraídos; y por último, el uso de estas imágenes sintéticas como conjuntos de datos de entrenamiento para el algoritmo evolutivo. Los pasos de esta metodología son totalmente automáticos y pueden ser ajustados sin dificultad por un usuario no experto.

- Al ser los CA modelos intrínsecamente distribuidos, son susceptibles de ser fácilmente implementados sobre plataformas de alto rendimiento, incrementando significativamente su idoneidad para ser usados en aplicaciones con requerimientos de tiempo real.

El segundo método que se propone en esta tesis doctoral es un primer paso en la inclusión de la dimensión temporal en el procesamiento conjunto espacio-espectral, lo que requiere extender el método previamente desarrollado basado en autómatas celulares. En este caso, el CA efectúa un filtrado de ruido sobre una secuencia completa de imágenes multidimensionales. La introducción de la dimensión temporal en el procesamiento supone una mejora en la tarea de reducción ruido, ya que la correlación temporal entre fotogramas supone una nueva fuente de información a explotar por los algoritmos.

En el procesamiento de secuencias de imágenes hiperespectrales, las celdas del autómata celular se distribuyen en tres dimensiones, apareciendo entonces relaciones de vecindad entre celdas tanto en el plano espacial como en el plano temporal. El método de reducción de ruido difiere del de segmentación en la

codificación de las reglas que rigen el funcionamiento del autómata celular, en cómo los estados de las celdas se actualizan y en el procedimiento seguido para determinar el conjunto de reglas de transición que constituyen el CA.

El método de reducción de ruido basado en CA cumple con los cinco requerimientos planteados inicialmente. Las principales características del método se resumen en los siguientes puntos:

- El método de filtrado de ruido procesa cada fotograma de la secuencia de imágenes hiperespectrales teniendo en cuenta explícita y conjuntamente la información espectral, espacial y temporal.
- Las reglas de transición que componen el CA se seleccionan siguiendo una metodología basada en algoritmos evolutivos, permitiendo conseguir CA adaptados a secuencias de imágenes hiperespectrales con características espaciales y espectrales particulares y a distintos tipos de fuentes de ruido.
- La adaptación de las reglas de transición de los CA a las características de las secuencias y modelos de ruido se consigue mediante la construcción de imágenes de entrenamiento sintéticas apropiadas para la fase de evaluación de individuos de la población en la ejecución del algoritmo evolutivo. Este proceso es totalmente automático una vez que se identifica el modelo de ruido que afecta a la imagen real a filtrar.
- El método basado en CA se ejecuta sobre imágenes a través de operaciones fácilmente paralelizables, lo que permite la implementación de manera concurrente sobre GPUs.

Ambos métodos propuestos para la segmentación y reducción de ruido de imágenes estáticas y secuencias de imágenes hiperespectrales, respectivamente, se han comparado con algoritmos extraídos del estado del arte, demostrando que, tanto cuantitativa como cualitativamente, los resultados de los métodos basados en CA mejoran los obtenidos con el resto de técnicas consideradas.

Appendix B

Mirror movement and image capture timing control

Arduino is an open-source prototyping platform based on easy-to-use hardware and software. Its microcontroller has been programmed to govern the control in the acquisition. The main steps involved in the capture of a whole hyperspectral data cube are:

1. To initiate the capture of a datacube, a signal arrives to the Arduino from the PC, specifying the exposure time for each single spatio-spectral image and the number of lines to acquire in the spatial scanning.
2. A direct communication between the Arduino and the camera starts:
   (a) The Arduino sends a 5V TTL pulse to begin triggering the camera.
   (b) Two signals *sync A* and *sync B* are monitored to control the timing. *Sync A* and *sync B* indicate the readout time of the camera and the exposure pulse, respectively (Fig. B.1a). Then,
      - Once the exposure time is finished for a single image, the Arduino sends a signal to the servomotor in order to reach the next angular position.

- Once the readout time is finished, the Arduino triggers the camera again.

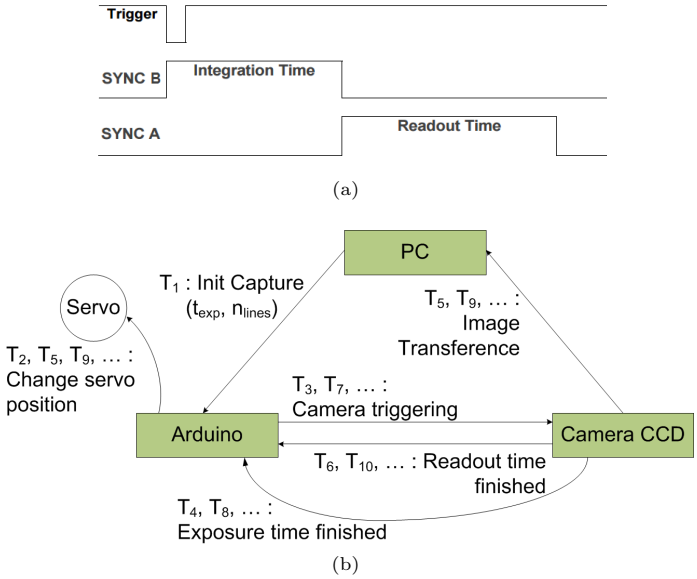

Figure B.1: (a) External trigger signal timing, (b) Control State Diagram

Thus, following the procedure shown in B.1b, n_{lines} partial spatio-spectral images are acquired. From these partial captures, a whole datacube can be built.

References

Michal Aharon, Michael Elad, and Alfred Bruckstein. K-svd: An algorithm for designing overcomplete dictionaries for sparse representation. *IEEE Transactions on Signal Processing*, 54(11):4311–4322, 2006.

M.L.G. Althouse. Least squares subspace projection approach to mixed pixel classification for hyperspectral images. *IEEE Transactions on Geoscience and Remote Sensing*, 36(3):898–912, 1998.

AVIRIS. Free aviris standard data products. http://aviris.jpl.nasa.gov/data/free_data.html

Corey Baker, Rick L Lawrence, Clifford Montagne, and Duncan Patten. Change detection of wetland ecosystems using landsat imagery and change vector analysis. *Wetlands*, 27(3):610–619, 2007.

András Bárdossy and Luis Samaniego. Fuzzy rule-based classification of remotely sensed imagery. *IEEE Transactions on Geoscience and Remote Sensing*, 40(2):362–374, 2002.

Marion F. Baumgardner, Larry L. Biehl, and David A. Landgrebe. 220 band aviris hyperspectral image data set: June 12, 1992 indian pine test site 3, 2015.

Andreas Baumgartner, Peter Gege, Claas Köhler, Karim Lenhard, and Thomas Schwarzmaier. Characterisation methods for the hyperspectral sensor hyspex at dlr's calibration home base. In *SPIE Remote Sensing*, pages 85331H–85331H. International Society for Optics and Photonics, 2012.

Bayspec. http://www.bayspec.com

Jon Atli Benediktsson, Martino Pesaresi, and Kolbeinn Amason. Classification and feature extraction for remote sensing images from urban areas based on morphological transformations. *IEEE Transactions on Geoscience and Remote Sensing*, 41(9):1940–1949, 2003.

Jón Atli Benediktsson, Jón Aevar Palmason, and Johannes R Sveinsson. Classification of hyperspectral data from urban areas based on extended morphological profiles. *IEEE Transactions on Geoscience and Remote Sensing*, 43 (3):480–491, 2005.

José M. Bioucas-Dias, Antonio Plaza, Nicolas Dobigeon, Mario Parente, Qian Du, Paul Gader, and Jocelyn Chanussot. Hyperspectral unmixing overview: Geometrical, statistical, and sparse regression-based approaches. *IEEE Journal of Selected Topics in Applied Earth Observations and Remote Sensing*, 5 (2):354–379, 2012.

T Blaschke. Towards a framework for change detection based on image objects. *Göttinger Geographische Abhandlungen*, 113:1–9, 2005.

Bodkin. http://www.bodkindesign.com

Francesca Bovolo, Silvia Marchesi, and Lorenzo Bruzzone. A framework for automatic and unsupervised detection of multiple changes in multitemporal images. *IEEE Transactions on Geoscience and Remote Sensing*, 50(6):2196–2212, 2012.

D. H. Brainard. Hyperspectral image data. http://scyllarus.research.nicta.com.au/data/

Brimrose. http://www.brimrose.com

Antoni Buades, Bartomeu Coll, and Jean-Michel Morel. A non-local algorithm for image denoising. In *Computer Vision and Pattern Recognition, 2005 IEEE Computer Society Conference on*, volume 2, pages 60–65. IEEE, 2005.

James B Campbell. *Introduction to remote sensing*. CRC Press, 2002.

Gustavo Camps-Valls and Lorenzo Bruzzone. Kernel-based methods for hyperspectral image classification. *IEEE Transactions on Geoscience and Remote Sensing*, 43(6):1351–1362, 2005.

Gustavo Camps-Valls and Lorenzo Bruzzone. *Kernel methods for remote sensing data analysis*. John Wiley & Sons, 2009.

Gustavo Camps-Valls, Luis Gómez-Chova, Javier Calpe-Maravilla, Emilio Soria-Olivas, José David Martín-Guerrero, and J Moreno. Support vector machines for crop classification using hyperspectral data. In *Pattern recognition and image analysis*, pages 134–141. Springer, 2003.

Gustavo Camps-Valls, Luis Gómez-Chova, Javier Calpe-Maravilla, José David Mart'ın-Guerrero, Emilio Soria-Olivas, Luis Alonso-Chordá, and José Moreno. Robust support vector method for hyperspectral data classification and knowledge discovery. *IEEE Transactions on Geoscience and Remote Sensing*, 42(7):1530–1542, 2004.

Gustavo Camps-Valls, Luis Gomez-Chova, Jordi Muñoz-Marí, Joan Vila-Francés, and Javier Calpe-Maravilla. Composite kernels for hyperspectral image classification. *Geoscience and Remote Sensing Letters*, 3(1):93–97, 2006.

Hervé Carfantan and Jérôme Idier. Statistical linear destriping of satellite-based pushbroom-type images. *IEEE Transactions on Geoscience and Remote Sensing*, 48(4 PART 1):1860–1871, 2010.

Ayan Chakrabarti and Todd Zickler. Statistics of real-world hyperspectral images. In *Computer Vision and Pattern Recognition , 2011 IEEE Conference on*, pages 193–200. IEEE, 2011.

Chein-I Chang. Further results on relationship between spectral unmixing and subspace projection. *IEEE Transactions on Geoscience and Remote Sensing*, 36(3):1030–1032, 1998.

Chein-I Chang, Xiao-Li Zhao, Mark LG Althouse, and Jeng Jong Pan. Least squares subspace projection approach to mixed pixel classification for hyperspectral images. *IEEE Transactions on Geoscience and Remote Sensing*, 36 (3):898–912, 1998.

Chih-Chung Chang and Chih-Jen Lin. Libsvm: A library for support vector machines. *ACM Transactions on Intelligent Systems and Technology*, 2(3): 27, 2011.

Gang Chen, Geoffrey J Hay, Luis MT Carvalho, and Michael A Wulder. Object-based change detection. *International Journal of Remote Sensing*, 33(14): 4434–4457, 2012.

Jinsong Chen, Yun Shao, Huadong Guo, Weiming Wang, and Boqin Zhu. Destriping CMODIS data by power filtering. *IEEE Transactions on Geoscience and Remote Sensing*, 41(9 PART II):2119–2124, 2003.

Emmanuel Christophe. Hyperspectral data compression tradeoff. In *Optical Remote Sensing*, pages 9–29. Springer, 2011.

CI Systems. http://www.ci-systems.com

M. A. Cochrane. Using vegetation reflectance variability for species level classification of hyperspectral data. *International Journal of Remote Sensing*, 21 (10):2075–2087, 2000.

Ciarán O Conaire, Noel E O'Connor, Eddie Cooke, and Alan F Smeaton. Comparison of fusion methods for thermo-visual surveillance tracking. In *Information Fusion, 2006 International Conference on*, pages 1–7, 2006.

Cubert. http://cubert-gmbh.de

Kostadin Dabov, Alessandro Foi, Vladimir Katkovnik, and Karen Egiazarian. Image denoising with block-matching and 3d filtering. In *Electronic Imaging 2006*, pages 606414–606414. International Society for Optics and Photonics, 2006.

Kostadin Dabov, Alessandro Foi, and Karen Egiazarian. Video denoising by sparse 3d transform-domain collaborative filtering. In *Proc. 15th European Signal Processing Conference*, volume 1, page 7, 2007.

Mauro Dalla Mura, Jon Atli Benediktsson, Björn Waske, and Lorenzo Bruzzone. Extended profiles with morphological attribute filters for the analysis of hyperspectral data. *International Journal of Remote Sensing*, 31(22):5975–5991, 2010.

SPECIM Hyperspectral Image Dataset. https://sites.google.com/site/hyperspectralcolorimaging/dataset/general-scenes

Curtiss Davis, Jeffrey Bowles, Robert Leathers, Daniel Korwan, T Valerie Downes, William Snyder, W Rhea, Wei Chen, John Fisher, Paul Bissett, and Robert Alan Reisse. Ocean PHILLS hyperspectral imager: design, characterization, and calibration. *Optics express*, 10(4):210–221, 2002.

Philip E Dennison, Kerry Q Halligan, and Dar A Roberts. A comparison of error metrics and constraints for multiple endmember spectral mixture analysis and spectral angle mapper. *Remote Sensing of Environment*, 93(3):359–367, 2004.

Wei Di, Lei Zhang, David Zhang, and Quan Pan. Studies on hyperspectral face recognition in visible spectrum with feature band selection. *IEEE Transactions on Systems, Man and Cybernetics, Part A: Systems and Humans*, 40 (6):1354–1361, 2010.

Qian Du and Chein-I Chang. An interference rejection-based radial basis function neural network for hyperspectral image classification. *Neural Networks, 1999. IJCNN '99. International Joint Conference on*, 4:2698–2703 vol.4, 1999.

Qian Du and Chein-I Chang. A linear constrained distance-based discriminant analysis for hyperspectral image classification. *Pattern Recognition*, 34(2): 361–373, 2001.

Eba Japan. http://www.ebajapan.jp

Evk. http://www.evk.biz

Nicola Falco, Jón Atli Benediktsson, and Lorenzo Bruzzone. Spectral and spatial classification of hyperspectral images based on ica and reduced morphological attribute profiles. *IEEE Transactions on Geoscience and Remote Sensing*, 53 (11):6223–6240, 2015.

Mathieu Fauvel, Yuliya Tarabalka, Jon Atli Benediktsson, Jocelyn Chanussot, and James C Tilton. Advances in spectral-spatial classification of hyperspectral images. *Proceedings of the IEEE*, 101(3):652–675, 2013.

Giles M Foody. On the compensation for chance agreement in image classification accuracy assessment. *Photogrammetric Engineering and Remote Sensing*, 58(10):1459–1460, 1992.

David H Foster, Kinjiro Amano, Sérgio Nascimento, and Michael J Foster. Frequency of metamerism in natural scenes. *Journal of the Optical Society of America A – Optics Image Science and Visio.*

Andrei Fridman, Gudrun Hø ye, and Trond Lø ke. Resampling in hyperspectral cameras as an alternative to correcting keystone in hardware, with focus on benefits for the optical design and data quality. *Proceedings of SPIE, Infrared Imaging Systems: Design, Analysis, Modeling, and Testing XXIV*, 8706:870602, 2013.

F. L. Gadallah, F. Csillag, and E. J. M. Smith. Destriping multisensor imagery with moment matching. *International Journal of Remote Sensing*, 21(12): 2505–2511, 2000.

Paul Gader, Alina Zare, Ryan Close, J Aitken, and G Tuell. Muufl gulfport hyperspectral and lidar airborne data set. *University of Florida, Gainesville, FL, Tech. Rep. REP-2013-570*, 2013.

Josune Gallego, Carmen Hernandez, and Manuel Graña. A morphological cellular automata based on morphological independence. *Logic Journal of IGPL*, page jzr003, 2011.

Josune Gallego, Carmen Hernandez, and Manuel Graña. A morphological cellular automata based on morphological independence. *Logic Journal of IGPL*, 20(3):617–624, 2012.

Gamaya. http://gamaya.com

Niloy Ganguly, B Sikdar, Andreas Deutsch, Geoffrey Canright, and P Chaudhuri. A survey on cellular automata, centre for high performance computing, dresden university of technology. Technical report, Technical Report 9, 2003.

J. C. Garcia and J. Moreno. Removal of noises in CHRIS/PROBA images: Application to the SPARC campaign data. *European Space Agency, (Special Publication) ESA SP*, (578):24–28, 2004.

Ashish Ghosh, Niladri Shekhar Mishra, and Susmita Ghosh. Fuzzy clustering algorithms for unsupervised change detection in remote sensing images. *Information Sciences*, 181(4):699–715, 2011.

Gilden photonics. http://www.gildenphotonics.com

Alexander FH Goetz, Gregg Vane, Jerry E Solomon, and Barrett N Rock. Imaging spectrometry for earth remote sensing. *Science*, 228(4704):1147–1153, 1985.

Luis Gómez-Chova, Luis Alonso, Luis Guanter, Gustavo Camps-Valls, Javier Calpe, and José Moreno. Correction of systematic spatial noise in push-broom hyperspectral sensors: application to CHRIS/PROBA images. *Applied optics*, 47(28):F46–F60, 2008.

J Anthony Gualtieri and Robert F Cromp. Support vector machines for hyperspectral remote sensing classification. In *The 27th AIPR Workshop: Advances in Computer-Assisted Recognition*, pages 221–232. International Society for Optics and Photonics, 1998.

J.A. Gualtieri and S. Chettri. Support vector machines for classification of hyperspectral data. volume 2, pages 813–815, 2000.

Kerri J Guilfoyle, Mark L Althouse, and Chein-I Chang. A quantitative and comparative analysis of linear and nonlinear spectral mixture models using radial basis function neural networks. *IEEE Transactions on Geoscience and Remote Sensing*, 39(10):2314–2318, 2001.

Nathan Hagen, Robert T Kester, Liang Gao, and Tomasz S Tkaczyk. Snapshot advantage: a review of the light collection improvement for parallel high-dimensional measurement systems. *Optical Engineering*, 51(11):111702–1, 2012.

Matthew C Hansen and Thomas R Loveland. A review of large area monitoring of land cover change using landsat data. *Remote sensing of Environment*, 122:66–74, 2012.

Joseph C. Harsanyi and Chein I. Chang. Hyperspectral image classification and dimensionality reduction: An orthogonal subspace projection approach. *IEEE Transactions on Geoscience and Remote Sensing*, 32(4):779–785, 1994.

HeadwallPhotonics. http://www.headwallphotonics.com

Gonzalo Hernandez and Hans J Herrmann. Cellular automata for elementary image enhancement. *Graphical Models and Image Processing*, 58(1):82–89, 1996.

HICO. The hyperspectral imager for the coastal ocean. http://hico.coas.oregonstate.edu/datasearch/data-search-basic.php

John H Holland. *Adaptation in natural and artificial systems: an introductory analysis with applications to biology, control, and artificial intelligence.* U Michigan Press, 1975.

Philip J Howarth and Gregory M Wickware. Procedures for change detection using landsat digital data. *International Journal of Remote Sensing*, 2(3): 277–291, 1981.

Chengquan Huang, Kuan Song, Sunghee Kim, John RG Townshend, Paul Davis, Jeffrey G Masek, and Samuel N Goward. Use of a dark object concept and support vector machines to automate forest cover change analysis. *Remote Sensing of Environment*, 112(3):970–985, 2008.

Guang-Bin Huang, Qin-Yu Zhu, and Chee-Kheong Siew. Extreme learning machine: theory and applications. *Neurocomputing*, 70(1):489–501, 2006.

Gordon P Hughes. On the mean accuracy of statistical pattern recognizers. *Information Theory, IEEE Transactions on*, 14(1):55–63, 1968.

Masroor Hussain, Dongmei Chen, Angela Cheng, Hui Wei, and David Stanley. Change detection from remotely sensed images: From pixel-based to object-based approaches. *International Journal of Photogrammetry and Remote Sensing*, 80:91–106, 2013.

Imec. http://www2.imec.be

Qiong Jackson, David Landgrebe, et al. An adaptive classifier design for high-dimensional data analysis with a limited training data set. *IEEE Transactions on Geoscience and Remote Sensing*, 39(12):2664–2679, 2001.

Qiong Jackson, David Landgrebe, et al. Adaptive bayesian contextual classification based on markov random fields. *IEEE Transactions on Geoscience and Remote Sensing*, 40(11):2454–2463, 2002.

Nathaniel P. Jacobson, Maya R. Gupta, and Jeffrey B. Cole. Linear fusion of image sets for display. *IEEE Transactions on Geoscience and Remote Sensing*, 45(10):3277–3288, 2007.

Jurij Jemec, Franjo Pernuš, Boštjan Likar, and Miran Bürmen. Push-broom hyperspectral image calibration and enhancement by 2D deconvolution with a variant response function estimate. *Optics Express*, 22(22):27655, 2014.

Wei Ji, Jia Ma, Rima Wahab Twibell, and Karen Underhill. Characterizing urban sprawl using multi-stage remote sensing images and landscape metrics. *Computers, Environment and Urban Systems*, 30(6):861–879, 2006.

X. Jia and J.A. Richards. Segmented principal components transformation for efficient hyperspectral remote-sensing image display and classification. *IEEE Transactions on Geoscience and Remote Sensing*, 37(1 II):538–542, 1999.

Xiuping Jia, John Richards, et al. Efficient maximum likelihood classification for imaging spectrometer data sets. *IEEE Transactions on Geoscience and Remote Sensing*, 32(2):274–281, 1994.

Suming Jin and Steven A Sader. Comparison of time series tasseled cap wetness and the normalized difference moisture index in detecting forest disturbances. *Remote sensing of Environment*, 94(3):364–372, 2005.

R Johnson and ES Kasischke. Change vector analysis: a technique for the multispectral monitoring of land cover and condition. *International Journal of Remote Sensing*, 19(3):411–426, 1998.

JPL. Information processing group. free hyperspectral standard data products.

Claude Kauffmann and Nicolas Piché. Seeded nd medical image segmentation by cellular automaton on gpu. *International journal of computer assisted radiology and surgery*, 5(3):251–262, 2010.

Nirmal Keshava. Distance metrics and band selection in hyperspectral processing with applications to material identification and spectral libraries. *IEEE Transactions on Geoscience and Remote Sensing*, 42(7):1552–1565, 2004.

Hugh H Kieffer. Detection and correction of bad pixels in hyperspectral sensors. In *SPIE's 1996 International Symposium on Optical Science, Engineering, and Instrumentation*, pages 93–108. International Society for Optics and Photonics, 1996.

M Kosec, M Burmen, D Tomazevic, F Pernus, and B Likar. Characterization of a spectrograph based hyperspectral imaging system. *Optics Express*, 21(10): 12085–12099, 2013. ISSN 10944087.

FA Kruse, AB Lefkoff, JW Boardman, KB Heidebrecht, AT Shapiro, PJ Barloon, and AFH Goetz. The spectral image processing system (sips)—interactive visualization and analysis of imaging spectrometer data. *Remote Sensing of Environment*, 44(2):145–163, 1993.

Darwin T Kuan, Alexander Sawchuk, Timothy C Strand, Pierre Chavel, et al. Adaptive noise smoothing filter for images with signal-dependent noise. *IEEE Transactions on Pattern Analysis and Machine Intelligence*, (2):165–177, 1985.

Antony Lam, Imari Sato, and Yuuki Sato. Denoising hyperspectral images using spectral domain statistics. In *Pattern Recognition, 2012 21st International Conference on*, pages 477–480. IEEE, 2012.

David A Landgrebe. *Signal theory methods in multispectral remote sensing*, volume 29. John Wiley & Sons, 2005.

Kurt C Kc C Lawrence, B Park, Wr R Windham, and C Mao. Calibration of a pushbroom hyperspectral imaging system for agricultural inspection. *Transactions of the American Society of Agricultural Engineers*, 46(2):513–521, 2003.

Robert Leathers, Trijntje Downes, and Richard Priest. Scene-based nonuniformity corrections for optical and SWIR pushbroom sensors. *Optics express*, 13(13):5136–5150, 2005.

Matthew A Lee and Lori Mann Bruce. Applying cellular automata to hyperspectral edge detection. In *Geoscience and Remote Sensing Symposium (IGARSS), 2010 IEEE International*, pages 2202–2205. IEEE, 2010.

Antoine Lefebvre, Thomas Corpetti, and Laurence Hubert-Moy. Object-oriented approach and texture analysis for change detection in very high resolution images. In *Geoscience and Remote Sensing Symposium, 2008 IEEE International*, volume 4, pages IV–663. IEEE, 2008.

Karim Lenhard, Andreas Baumgartner, and Thomas Schwarzmaier. Independent laboratory characterization of neo hyspex imaging spectrometers vnir-1600 and swir-320m-e. *IEEE Transactions on Geoscience and Remote Sensing*, 53(4):1828–1841, 2015.

Jun Li, Prashanth Reddy Marpu, Antonio Plaza, Jose M Bioucas-Dias, and Jon Atli Benediktsson. Generalized composite kernel framework for hyperspectral image classification. *IEEE Transactions on Geoscience and Remote Sensing*, 51(9):4816–4829, 2013a.

Qingli Li, Xiaofu He, Yiting Wang, Hongying Liu, Dongrong Xu, and Fangmin Guo. Review of spectral imaging technology in biomedical engineering: achievements and challenges. *Journal of biomedical optics*, 18(10):100901–100901, 2013b.

Chien-Sheng Liao, Joon Hee Choi, Delong Zhang, Stanley H Chan, and Ji-Xin Cheng. Denoising stimulated raman spectroscopic images by total variation minimization. *The Journal of Physical Chemistry C*, 119(33):19397–19403, 2015.

Guoqing Lin, Robert E. Wolfe, and Masahiro Nishihama. Npp viirs geometric performance status. In *SPIE Optical Engineering + Applications*, pages 81531V–81531V. International Society for Optics and Photonics, 2011.

Sicong Liu, Lorenzo Bruzzone, Francesca Bovolo, and Peijun Du. Hierarchical unsupervised change detection in multitemporal hyperspectral images. *IEEE Transactions on Geoscience and Remote Sensing*, 53(1):244–260, 2015a.

Sicong Liu, Lorenzo Bruzzone, Francesca Bovolo, Massimo Zanetti, and Peijun Du. Sequential spectral change vector analysis for iteratively discovering and detecting multiple changes in hyperspectral images. *IEEE Transactions on Geoscience and Remote Sensing*, 53(8):4363–4378, 2015b.

X Liu and RG Lathrop Jr. Urban change detection based on an artificial neural network. *International Journal of Remote Sensing*, 23(12):2513–2518, 2002.

Xuefeng Liu, Salah Bourennane, and Caroline Fossati. Denoising of hyperspectral images using the parafac model and statistical performance analysis. *IEEE Transactions on Geoscience and Remote Sensing*, 50(10):3717–3724, 2012.

LLa instruments GmbH. http://www.lla-instruments.com

Javier Lopez-Fandino, Pablo Quesada-Barriuso, Dora B. Heras, , and Francisco Arguello. Efficient ELM-Based techniques for the classification of hyperspectral remote sensing images on commodity GPUs. *IEEE Journal of Selected Topics in Applied Earth Observations and Remote Sensing*, 8(6):2884 – 2893, 2015.

Dengsheng Lu and Qihao Weng. A survey of image classification methods and techniques for improving classification performance. *International journal of Remote sensing*, 28(5):823–870, 2007.

Florian Luisier and Thierry Blu. Sure-let multichannel image denoising: interscale orthonormal wavelet thresholding. *IEEE Transactions on Image Processing*, 17(4):482–492, 2008.

Matteo Maggioni, Vladimir Katkovnik, Karen Egiazarian, and Alessandro Foi. Nonlocal transform-domain filter for volumetric data denoising and reconstruction. *IEEE Transactions on Image Processing*, 22(1):119–133, 2013.

Farid Melgani and Lorenzo Bruzzone. Support vector machines for classification of hyperspectral remote-sensing images. In *Geoscience and Remote Sensing Symposium, 2002 IEEE International*, volume 1, pages 506–508. IEEE, 2002.

Géegoire Mercier and Marc Lennon. Support vector machines for hyperspectral image classification with spectral-based kernels. In *Geoscience and Remote Sensing Symposium, 2003 IEEE International*, volume 1, pages 288–290. IEEE, 2003.

Middleton spectral vision. http://www.middletonspectral.com

Thomas S Moon and Erzsebet Merenyi. Classification of hyperspectral images using wavelet transforms and neural networks. In *SPIE's 1995 International Symposium on Optical Science, Engineering, and Instrumentation*, pages 725–735. International Society for Optics and Photonics, 1995.

Giovanni Motta, Francesco Rizzo, and James A Storer. *Hyperspectral data compression*. Springer Science & Business Media, 2006.

Pantazis Mouroulis and Michael M. McKerns. Pushbroom imaging spectrometer with high spectroscopic data fidelity: experimental demonstration. *Optical Engineering*, 39(3):808, 2000.

MultiSpec. Hyperspectral images.

Allan A Nielsen, Knut Conradsen, and James J Simpson. Multivariate alteration detection (mad) and maf postprocessing in multispectral, bitemporal image data: New approaches to change detection studies. *Remote Sensing of Environment*, 64(1):1–19, 1998.

Allan Aasbjerg Nielsen. The regularized iteratively reweighted mad method for change detection in multi-and hyperspectral data. *IEEE Transactions on Image Processing*, 16(2):463–478, 2007.

Vanessa Ortiz-Rivera, Miguel Vélez-Reyes, and Badrinath Roysam. Change detection in hyperspectral imagery using temporal principal components. In *Defense and Security Symposium*, pages 623312–623312. International Society for Optics and Photonics, 2006.

CA Párraga, Gavin Brelstaff, Tom Troscianko, and IR Moorehead. Color and luminance information in natural scenes. *JOSA A*, 15(3):563–569, 1998.

Yi Peng, Deyu Meng, Zongben Xu, Chenqiang Gao, Yi Yang, and Biao Zhang. Decomposable nonlocal tensor dictionary learning for multispectral image denoising. In *Computer Vision and Pattern Recognition, 2014 IEEE Conference on*, pages 2949–2956. IEEE, 2014.

Martino Pesaresi and Jon Atli Benediktsson. A new approach for the morphological segmentation of high-resolution satellite imagery. *IEEE Transactions on Geoscience and Remote Sensing*, 39(2):309–320, 2001.

Photon Etc. http://www.photonetc.com

a Plaza, Javier Plaza, Abel Paz, and S Sánchez. Parallel Hyperspectral Image and Signal Processing. *IEEE Signal Processing Magazine*, 28(May):119–126, 2011.

Antonio Plaza, Pablo Martinez, Javier Plaza, and Rosa Perez. Dimensionality reduction and classification of hyperspectral image data using sequences of extended morphological transformations. *Geoscience and Remote Sensing, IEEE Transactions on*, 43(3):466–479, 2005.

Javier Plaza, Antonio Plaza, Rosa Perez, and Pablo Martinez. On the use of small training sets for neural network-based characterization of mixed pixels in remotely sensed hyperspectral images. *Pattern Recognition*, 42(11):3032 – 3045, 2009a.

Javier Plaza, Antonio J Plaza, and Cristina Barra. Multi-channel morphological profiles for classification of hyperspectral images using support vector machines. *Sensors*, 9(1):196–218, 2009b.

Gerrit Polder, Gerie W a M Van Der Heijden, L. C Paul Keizer, and Ian T. Young. Calibration and characterisation of imaging spectrographs. *Journal of Near Infrared Spectroscopy*, 11(3):193–210, 2003.

Robert Gilmore Pontius Jr and Marco Millones. Death to kappa: birth of quantity disagreement and allocation disagreement for accuracy assessment. *International Journal of Remote Sensing*, 32(15):4407–4429, 2011.

Adriana Popovici and Dan Popovici. Cellular automata in image processing. In *Fifteenth International Symposium on Mathematical Theory of Networks and Systems*, volume 1, 2002.

Javier Portilla, Vasily Strela, Martin J Wainwright, and Eero P Simoncelli. Image denoising using scale mixtures of gaussians in the wavelet domain. *IEEE Transactions on Image Processing*, 12(11):1338–1351, 2003.

B Priego, F Bellas, and RJ Duro. Ecas-ii: A hybrid algorithm for the construction of multidimensional image segmenters. In *Neural Networks, 2015 International Joint Conference on*, pages 1–8. IEEE, 2015a.

B. Priego, R. J. Duro, J. Lopez-Fandino, D. B. Heras, and Arguello F. Evolutionary cellular automata based approach to high-dimensional image segmentation for gpu projection. In *Neural Networks, 2016 International Joint Conference on*, pages 1594–1600. IEEE, 2016.

Blanca Priego, Daniel Souto, Francisco Bellas, and Richard J Duro. Hyperspectral image segmentation through evolved cellular automata. *Pattern Recognition Letters*, 34(14):1648–1658, 2013a.

Blanca Priego, Miguel Angel Veganzones, Jocelyn Chanussot, Carole Amiot, Abraham Prieto, and Richard Duro. Spatio-temporal cellular automata-based filtering for image sequence denoising: Application to fluoroscopic sequences. In *Image Processing, 2013 20th IEEE International Conference on*, pages 548–552. IEEE, 2013b.

Blanca Priego, Francisco Bellas, and Richard J Duro. Evolving cellular automata to segment hyperspectral images using low dimensional images for training. In *Bioinspired Computation in Artificial Systems*, pages 117–126. Springer, 2015b.

Pablo Quesada-Barriuso, Francisco Argüello, and Dora Blanco Heras. Efficient segmentation of hyperspectral images on commodity gpus. In *Advances in Knowledge-Based and Intelligent Information and Engineering Systems (Frontiers in Artificial Intelligence and Applications)*, volume 243, pages 2130–2139, 2012.

Nadine Renard, Salah Bourennane, and Jacques Blanc-Talon. Denoising and dimensionality reduction using multilinear tools for hyperspectral images. *Geoscience and Remote Sensing Letters*, 5(2):138–142, 2008.

Resonon. http://www.resonon.com

Rikola. http://www.rikola.fi

C. Rodarmel and J. Shan. Principal component analysis for hyperspectral image classification. *Surveying and Land Information Science*, 62(2):115–122, 2002.

Paul L Rosin and Efstathios Ioannidis. Evaluation of global image thresholding for change detection. *Pattern Recognition Letters*, 24(14):2345–2356, 2003.

Leonid I Rudin, Stanley Osher, and Emad Fatemi. Nonlinear total variation based noise removal algorithms. *Physica D: Nonlinear Phenomena*, 60(1): 259–268, 1992.

Joseph Salmon, Zachary Harmany, Charles-Alban Deledalle, and Rebecca Willett. Poisson noise reduction with non-local pca. *Journal of Mathematical Imaging and Vision*, 48(2):279–294, 2014.

D. Schläpfer, M. Schaepman, S. Bojinski, and a. Börner. Calibration and validation concept for the airborne PRISM experiment (APEX). *Canadian Journal of Remote Sensing*, 26(5):455–465, 2000.

Daniel Schläpfer, Jens Nieke, and Klaus I. Itten. Spatial PSF nonuniformity effects in airborne pushbroom imaging spectrometry data. *IEEE Transactions on Geoscience and Remote Sensing*, 45(2):458–468, 2007.

Scyllarus. http://scyllarus.research.nicta.com.au/data/

Jebaraj P Selvapeter and Wim Hordijk. Cellular automata for image noise filtering. In *Nature & Biologically Inspired Computing, 2009 World Congress on*, pages 193–197. IEEE, 2009.

S Serneels, MY Said, and EF Lambin. Land cover changes around a major east african wildlife reserve: the mara ecosystem (kenya). *International Journal of Remote Sensing*, 22(17):3397–3420, 2001.

Ashbindu Singh. Review article digital change detection techniques using remotely-sensed data. *International journal of remote sensing*, 10(6):989–1003, 1989.

Torbjørn Skauli. An upper-bound metric for characterizing spectral and spatial coregistration errors in spectral imaging. *Optics express*, 20(2):918–933, 2012.

Torbjørn Skauli and Joyce Farrell. A collection of hyperspectral images for imaging systems research. In *IS&T/SPIE Electronic Imaging*, pages 86600C–86600C. International Society for Optics and Photonics, 2013.

Specim. http://www.specim.fi

Spectir. Free data samples. http://www.spectir.com/free-data-samples/

Ram Srinivasan, Michael Cannon, and James White. Landsat data destriping using power spectral filtering. *Optical Engineering*, 27(11):271193–271193, 1988.

Jean-Luc Starck, Fionn D Murtagh, and Albert Bijaoui. *Image processing and data analysis: the multiscale approach*. Cambridge University Press, 1998.

Rainer Storn and Kenneth Price. Differential evolution–a simple and efficient heuristic for global optimization over continuous spaces. *Journal of Global Pptimization*, 11(4):341–359, 1997.

Douglas Stow. Geographic object-based image change analysis. In *Handbook of applied spatial analysis*, pages 565–582. Springer, 2010.

Lixin Sun, Robert Neville, Karl Staenz, and H. Peter White. Automatic destriping of Hyperion imagery based on spectral moment matching. *Canadian Journal of Remote Sensing*, 34(1), 2008.

Surfaceoptics. http://surfaceoptics.com

Xiaoli Tang, William A Pearlman, et al. Scalable hyperspectral image coding. In *2005 IEEE International Conference on Acoustics Speech and Signal Processing Proceedings*, pages 401–404, 2005.

Yuliya Tarabalka, Jón Atli Benediktsson, and Jocelyn Chanussot. Spectral–spatial classification of hyperspectral imagery based on partitional clustering techniques. *IEEE Transactions on Geoscience and Remote Sensing*, 47(8): 2973–2987, 2009.

Yuliya Tarabalka, Jocelyn Chanussot, and Jon Atli Benediktsson. Segmentation and classification of hyperspectral images using watershed transformation. *Pattern Recognition*, 43(7):2367–2379, 2010.

Tattile. http://www.tattile.com

Prasad S Thenkabail, John G Lyon, and Alfredo Huete. *Hyperspectral remote sensing of vegetation*. CRC Press, 2011.

James C Tilton, Yuliya Tarabalka, Paul M Montesano, and Emanuel Gofman. Best merge region-growing segmentation with integrated nonadjacent region object aggregation. *IEEE Transactions on Geoscience and Remote Sensing*, 50(11):4454–4467, 2012.

Daniel Tomowski, Manfred Ehlers, and Sascha Klonus. Colour and texture based change detection for urban disaster analysis. In *Urban Remote Sensing Event (JURSE), 2011 Joint*, pages 329–332. IEEE, 2011.

G Turk. Map evaluation and chance correction, 2002.

UPV/EHU. Hyperspectral remote sensing scenes. grupo de inteligencia computacional de la universidad del país vasco.

USGS. Digital spectral library.

G. W a M Van Der Heijden and C. a. Glasbey. Calibrating spectral images using penalized likelihood. *Real-Time Imaging*, 9(4):231–236, 2003.

Gijesh Varghese and Zhou Wang. Video denoising based on a spatiotemporal gaussian scale mixture model. *IEEE Transactions on Circuits and Systems for Video Technology*, 20(7):1032–1040, 2010.

Anthony J Viera, Joanne M Garrett, et al. Understanding interobserver agreement: the kappa statistic. *Fam Med*, 37(5):360–363, 2005.

John Von Neumann, Arthur W Burks, et al. Theory of self-reproducing automata. *IEEE Transactions on Neural Networks*, 5(1):3–14, 1966.

D Wang, NM Kwok, X Jia, and G Fang. A cellular automata approach for superpixel segmentation. In *Image and Signal Processing (CISP), 2011 4th International Congress on*, volume 2, pages 1108–1112. IEEE, 2011.

Hai-ming Wang, Shi-de Guo, and Dao-heng Yu. A new ca method for image processing based on morphology and coordinate logic [j]. *Application Research of Computers*, 1:081, 2004a.

Zhou Wang, Alan C Bovik, Hamid R Sheikh, and Eero P Simoncelli. Image quality assessment: from error visibility to structural similarity. *IEEE Transactions on Image Processing*, 13(4):600–612, 2004b.

Xingping Wen and Xiaofeng Yang. Change detection from remote sensing imageries using spectral change vector analysis. In *Information Processing, 2009 Asia-Pacific Conference on*, volume 2, pages 189–192. IEEE, 2009.

Ximea. http://www.ximea.com

Fei Yuan, Kali E Sawaya, Brian C Loeffelholz, and Marvin E Bauer. Land cover classification and change analysis of the twin cities (minnesota) metropolitan area by multitemporal landsat remote sensing. *Remote sensing of Environment*, 98(2):317–328, 2005.

Roberta H Yuhas, Joseph W Boardman, and Alexander FH Goetz. Determination of semi-arid landscape endmembers and seasonal trends using convex geometry spectral unmixing techniques. *Summaries of the 4th Annual JPL Airborne Geoscience Workshop*.

Silvano Di Zenzo, Stephen D DeGloria, R Bernstein, and Harwood G Kolsky. Gaussian maximum likelihood and contextual classification algorithms for multicrop classification experiments using thematic mapper and multispectral scanner sensor data. *IEEE Transactions on Geoscience and Remote Sensing*, (6):815–824, 1987.

Lin Zhang, Lei Zhang, Xuanqin Mou, and David Zhang. Fsim: a feature similarity index for image quality assessment. *IEEE Transactions on Image Processing*, 20(8):2378–2386, 2011.

Weiqi Zhou, Austin Troy, and Morgan Grove. Object-based land cover classification and change analysis in the baltimore metropolitan area using multitemporal high resolution remote sensing data. *Sensors*, 8(3):1613–1636, 2008.

Zolix. http://www.zolix.com.cn

List of Figures

List of Tables

Glossary

4DCAF 4 Dimensional Cellular Automata-based Filtering.

ANN Artificial Neural Networks.

AP Attribute Profiles.

C^{2}VA Compressed Change Vector Analysis.

CA Cellular Automata.

CAF Cellular Automata-based Filtering.

CV Change Vector.

CVA Change Vector Analysis.

DE Differential Evolution Algorithm.

EA Evolutionary Algorithm.

ECHO Extraction and Classification of Homogeneous Objects.

EMAP Extended Morphological Attribute Profiles.

EMP Extended Morphological Profiles.

FSIM Feature Similarity Index.

FWHM Full Width at Half Maximum.

GA Genetic Algorithm.

GCP Geometric Control Points.

GPU Graphic processing Units.

HSCVA Hierarchical Spectral Change Vector Analysis.

HSeg Hierarchical Segmentation.

HSI Hyperspectral Imaging.

ICA Independent Component Analysis.

INS Inertial Navigation System.

IR-MAD Iterative Re-weighted Multivariate Alteration Detection.

KT Kauth-Thomas Transformation.

LCDA Linearly Constrained Discriminant Analysis.

LCTF Liquid Crystal Tunable Filter.

LDA Linear Discriminant Analysis.

MAD Multivariate Alteration Detection.

MGCA Multi-Gradient based Cellular Automaton.

ML Maximum-Likelihood.

MNF Minimum Noise Fraction.

MP Morphological Profile.

MRF Markov Random Field.

MSI Multispectral Imaging.

OBCD Object-Based Change Detection.

OSP Orthogonal Subspace Projection.

PCA Principal Component Analysis.

PCB Printed Circuit Board.

PCT Principal Component Transformation.

PGP Prism-Grating-Prism.

PHI Pushroom Hyperspectral Imagers.

PQI Picture Quality Indices.

PSF Point Spread Function.

PSNR Peak Signal-to-Noise Ratio.

RGB Red-Green-Blue Color Model.

RS Remote Sensing.

S^{2}VA Sequential Spectral Change Vector Analysis.

SA Spectral Angle.

SAM Spectral Angle Mapper.

SiRF Spatial Response Function.

SMLR Sparse Multinomial Logistic Regression.

SNR Signal-to-Noise Ratio.

SRF Spectral Response Function.

SSIM Structure Similarity Index.

st-CAF Spatio-temporal Cellular Automata-based Filtering.

SVM Support Vector Machine.

SVM-CKs Support Vector Machine with Composite Kernels.

UAV Unmanned Aerial Vehicle.

VS Vertical Stripping.